uOttawa

L'Université canadienne
Canada's university

FACULTÉ DES ÉTUDES SUPÉRIEURES ET POSTDOCTORALES

uOttawa

L'Université canadienne
Canada's university

FACULTY OF GRADUATE AND POSTDOCTORAL STUDIES

Pu Wang

AUTEUR DE LA THÈSE / AUTHOR OF THESIS

Ph.D. (Physics)

GRADE / DEGREE

Department of Physics

FACULTÉ, ÉCOLE, DÉPARTEMENT / FACULTY, SCHOOL, DEPARTMENT

Magnetic Properties and Mössbauer Spectroscopy of Novel Alloys

TITRE DE LA THÈSE / TITLE OF THESIS

Z. Stadnik

DIRECTEUR (DIRECTRICE) DE LA THÈSE / THESIS SUPERVISOR

CO-DIRECTEUR (CO-DIRECTRICE) DE LA THÈSE / THESIS CO-SUPERVISOR

EXAMINATEURS (EXAMINATRICES) DE LA THÈSE / THESIS EXAMINERS

R. Dunlap

G. Oakham

E. Fortin

L. Ramunno

Gary W. Slater

Le Doyen de la Faculté des études supérieures et postdoctorales / Dean of the Faculty of Graduate and Postdoctoral Studies

Magnetic properties and Mössbauer spectroscopy of novel alloys

Pu Wang

Thesis submitted to the

Faculty of Graduate and Postdoctoral Studies

In partial fulfillment of the requirements

For the Doctor of Philosophy degree in Physics

Department of Physics

Faculty of Science

uOttawa

L'Université canadienne
Canada's university

University of Ottawa

Your file Votre référence
ISBN: 978-0-494-59494-0
Our file Notre référence
ISBN: 978-0-494-59494-0

Abstract

This thesis is an experimental study of structural and magnetic properties, and hyperfine interactions in crystalline alloys Cu_2GdIn, CrNiP, CrNiAs, $EuCu_2Si_2$, Cr_2FeSe_4 and icosahedral quasicrystals $Al_{60}Cr_{19.9}Fe_{0.1}Ge_{20}$, $Ag_{50}In_{36}Gd_{14}$, $Zn_{77}Fe_7Sc_{16}$.

The Heusler alloy Cu_2GdIn is shown to crystallize in the $L2_1$ crystal structure (space group $Fm\bar{3}m$) with a lattice constant of 6.6643(3) Å. It is an antiferromagnet with the Néel temperature of 9.6(1) K, the effective magnetic moment of 7.98(4) μ_B per Gd atom, and the paramagnetic Curie temperature of –41.2(9) K. Its Debye temperature is 229(5) K.

The alloys CrNiP and CrNiAs crystallize, respectively, in the Co_2P-type structure (space group *Pnma*) and the Fe_2P-type structure (space group $P\bar{6}2m$), with the lattice parameters a = 5.7965(1) Å, b = 3.5337(1) Å, c = 6.8123(2) Å, and a = 6.1128(2) Å, c = 3.6585(1) Å. CrNiP is shown to be a three-dimensional Heisenberg ferromagnetic with the Curie temperature of 142.9(6) K, whereas CrNiAs is demonstrated to be a mean-field ferromagnet with the Curie temperature of 171.9(1) K. A long standing controversy concerning the Ni magnetic moment in these alloys is solved unequivocally: Ni atoms carry a magnetic moment of 0.14 μ_B in CrNiP and 0.15(3) μ_B in CrNiAs. The Debye temperatures of CrNiP and CrNiAs are, respectively, 261(3) K and 221(1) K.

$EuCu_2Si_2$ is one of the first Eu-based alloys in which intermediate valence behavior of Eu was observed. It is demonstrated here that there are no valence fluctuations of Eu in this alloy: Eu atoms are divalent in the temperature range 2–300 K. The Debye temperature of $EuCu_2Si_2$ is shown to be 236(4) K.

Cr_2FeSe_4 is found to have antiferromagnetism with weak ferrimagnetism due to the two different distortions of the octahedral Cr^{3+} and the octahedral Fe^{2+}. A negative magnetization is found in a magnetic field of 5 Oe and below due to the coercive-field magnetization reversal. The magnetization reversal disappears in a magnetic field larger than 65 Oe.

The icosahedral quasicrystals $Al_{60}Cr_{19.9}Fe_{0.1}Ge_{20}$, $Ag_{50}In_{36}Gd_{14}$, and $Zn_{77}Fe_7Sc_{16}$ are shown to have a primitive six-dimensional Bravais lattice with a six-dimensional lattice constant of 6.558(2) Å, 7.805(2) Å, and 8.087(1) Å, respectively. $Al_{60}Cr_{19.9}Fe_{0.1}Ge_{20}$ is a paramagnet with the effective magnetic moment of 0.312(3) μ_B per Cr/Fe atom. Its Debye temperature is 463(15) K. The temperature dependence of the electrical conductivity of $Al_{60}Cr_{19.9}Fe_{0.1}Ge_{20}$ is well accounted for quantitatively by theories of quantum interference effects. $Ag_{50}In_{36}Gd_{14}$ and $Zn_{77}Fe_7Sc_{16}$ are shown to be spin glasses with the spin freezing temperature of 4.25(5) K and 7.75(2) K, respectively. The hyperfine magnetic fields at ^{155}Gd and ^{57}Fe nuclei in $Ag_{50}In_{36}Gd_{14}$ and $Zn_{77}Fe_7Sc_{16}$ are shown to set in at temperatures larger than the corresponding freezing temperatures. The frequency dependence of the freezing temperature in $Zn_{77}Fe_7Sc_{16}$ is shown to be equally well accounted for by the Vogel-Fulcher law and the power law. Analysis of the aging effects observed in $Zn_{77}Fe_7Sc_{16}$ leads to a major finding that the nature of the spin-glass state in this quasicrystal is fundamentally different from that of a canonical spin glass. The Debye temperatures of $Ag_{50}In_{36}Gd_{14}$ and $Zn_{77}Fe_7Sc_{16}$ are, respectively, 199(2) K and 443(8) K.

Acknowledgments

I would like to give my thanks first to my supervisor, Professor Z. M. Stadnik. It is him who showed me the spectacular world in the field of the solid state physics. I have benefited a lot from his enormous knowledge and experience in this field. He also encouraged and supported me to apply my previous knowledge and experience to a daily research so that I can have a good understanding to the topics I studied from the bottom to the top. His endless patience and help accompanied me to go through all the difficulties I encountered during my graduate studies. His financial support also enabled me to concentrate on my research.

It was my honor to meet Professor G. Lamarche and work with him since the beginning of my study. I learned many experimental techniques and relevant theories in low-temperature physics from him. His thorough understanding of a DC SQUID magnetometry helped me to repair a 25-year old Quantum Design (QD) Magnetic Property Measurement System (MPMS) with which most of the experimental magnetic data presented in this thesis were obtained. He and his wife showed me the basic sample-making methods and helped me to design and construct an electric programmable furnace, which greatly improved the sample making repeatability and the quality of the synthesized samples.

The qualified technicians in the mechanical workshop worked closely with me on creating the parts for the existing experimental apparatus and the newly designed systems. Their delicate craftsmanship and rich experience ensured the quality of the obtained experimental results.

I also greatly appreciate the support from the Department of Physics. It provided me a trouble-free environment in which the regular research activities could be carried on.

Last but not least, I would like to thank my families. Their love and dedicated support made me focus on my work. I would like to share my achievements with them.

Statement of originality

The author states that the work presented in this PhD thesis constitutes, to the best of his knowledge, new and original research in the field of physics. In accordance with the nature of graduate studies, all of the author's work was done under the direct and close supervision of his research supervisor, Professor Zbigniew M. Stadnik. The specific contributions of the author are as follows.

Paper I. I designed the study, synthesized the alloy, performed all the measurements, evaluated all the experimental data, and wrote the first draft of the paper.

Paper II. I carried out all the measurements, except for ^{61}Ni Mössbauer measurements, analyzed all the experimental data, and assisted in writing the paper.

Paper III. I conducted all the measurements, except for ^{61}Ni Mössbauer measurements, evaluated all the experimental data, and assisted in writing the paper.

Paper IV. I made all ^{151}Eu Mössbauer measurements, analyzed all Mössbauer spectra, and wrote the first draft of the paper.

Paper V. My contributions to the magnetic, the DTA and the resistivity measurements were very useful in the writing of the paper. I also participated actively in the interpretation of results.

Paper VI. I synthesized the quasicrystal, carried out all the measurements, evaluated all the experimental data, and wrote the first draft of the paper.

Paper VII. I participated in performing and analyzing the magnetization measurements and the ^{151}Gd Mössbauer measurements, and assisted in writing the paper.

Paper VIII. I conducted and analyzed the dc magnetization measurements, analyzed the ac susceptibility measurements, participated in conducting and analyzing the ^{57}Fe Mössbauer measurements, and assisted in writing the paper.

List of publications

This is a paper-format PhD thesis. It is based on work reported in the following papers:

I. P. Wang and Z.M. Stadnik.

Magnetic properties and ^{155}Gd Mössbauer spectroscopy of the rare-earth Heusler compound Cu_2GdIn.

J. Phys.: Condens. Matter, **19**, 346235 (2007).

II. Z.M. Stadnik, P. Wang, N. Jansen, D. Walcher, P. Gütlich, and T. Kanomata.

Magnetic properties and ^{61}Ni Mössbauer spectroscopy of the ternary phospide CrNiP.

J. Phys.: Condens. Matter, **20**, 285227 (2008).

III. Z.M. Stadnik, P. Wang, N. Jansen, D. Walcher, P. Gütlich, and T. Kanomata.

Magnetization and ^{61}Ni Mössbauer effect study of the ternary arsenide CrNiAs.

J. Phys.: Condens. Matter, **20**, 325230 (2008).

IV. Z.M. Stadnik, P. Wang, J. Żukrowski, and B.K. Cho.

Absence of charge fluctuations of europium in metallic single crystals of $EuCu_2Si_2$.

Hyperfine Interact., **169**, 1295 (2006).

V. G. Lamarche, I. Bulyzhenkov, P. Wang, M. Quintero, and A.-M. Lamarche.

Low-field negative magnetization and coercive-field magnetization reversal in transition metal chalogenides; Cr_2FeSe_4 magnetic structure from neutron diffraction.

J. Phys. Chem. Solids, 69, 884 (2008).

VI. Z.M. Stadnik and P. Wang.

Physical properties of icosahedral quasicrystal $Al_{60}Cr_{19.9}Fe_{0.1}Ge_{20}$.

J. Phys.: Condens. Matter, **18**, 8363 (2006).

VII. Z.M. Stadnik, K. Al-Qadi, and P. Wang.

Magnetic properties and ^{155}Gd Mössbauer spectroscopy of the icosahedral quasicrystal $Ag_{50}In_{36}Gd_{14}$.

J. Phys.: Condens. Matter, **18**, 8363 (2006).

VIII. K. Al-Qadi, P. Wang, Z.M. Stadnik, and J. Przewoźnik.

A structural, magnetic and Mössbauer spectral study of the icosahedral quasicrystal $Zn_{77}Fe_7Sc_{16}$.

Phys. Rev. B, submitted.

Introduction

Magnetic moments in crystalline solids have a variety of long-range arrangements, ranging from simple ferromagnetic to complex helical ones [1]. One of the aims of this thesis was to gain some insight into the magnetic moment arrangements in four crystalline alloys: Cu_2GdIn, CrNiP, CrNiAs, and Cr_2FeSe_4.

One of the fundamental parameters of a magnetic alloy is a local magnetic moment associated with each magnetic atom in the alloy [1]. There has been a long-standing controversy concerning the Ni magnetic moment in CrNiP and CrNiAs alloys [2-4]. Another aim of this thesis was to unambiguously resolve this controversy.

In 1984, Shechtman and his colleagues announced the discovery of the first quasicrystalline material (quasicrystal) [5]. This new metallic phase revealed five-fold rotational symmetry which is incompatible with any crystalline structure [6]. One of the central issues in the physics of quasicrystals is the possibility of the existence of long-range magnetic order in these alloys. Initial intuition suggests that quasiperiodicity necessarily leads to frustration and is therefore incompatible with long-range magnetic order; a magnetic ordering in a form of a spin-glass state [1] is expected. However, various theoretical models dealing with magnetism in quasicrystals indicate [7] the possibility of the existence of long-range magnetic order in these alloys. The aim of this thesis is to search for such a long-range magnetic order and to determine the nature of the magnetic ordering in three icosahedral quasicrystals: $Al_{60}Cr_{19.9}Fe_{0.1}Ge_{20}$, and recently discovered $Ag_{50}In_{36}Gd_{16}$ and $Zn_{77}Fe_7Sc_{16}$.

The electrical resistivity of quasicrystals is much larger than that of the corresponding crystalline and/or amorphous alloys of similar composition and their temperature dependence is

opposite to that of metallic alloys [6]. One of the aims of this thesis was to account for the temperature dependence of the electrical resisitivity of the $Al_{60}Cr_{19.9}Fe_{0.1}Ge_{20}$ quasicrystal by theories of quantum interference effects.

The ternary alloy $EuCu_2Si_2$ is one of the first Eu-based alloys in which the valence fluctuation of Eu was observed. There have been recently reports claiming that, in fact, no Eu valence fluctuations in this alloy occur [8, 9]. The aim of this thesis was to convincingly resolve this dispute.

This thesis is organized in the following way. In Chapter 1 a review of crystal structure and magnetic properties of solids, a theory of Mössbauer spectroscopy and the electrical resistivity of disordered alloys is presented. Chapter 2 describes in detail the sample synthesis methods and the experimental techniques used in this study. Chapters 3-9 contain the published and submitted papers that are the publication work upon which this thesis is based. Chapter 10 summarizes the results of this thesis.

References

1. M. Getzlaff, *Fundamentals of Magnetism* (Springer-Verlag, Berlin, 2008).
2. J.B. Goodenough, J. Solid State Chem. **7**, 428 (1973).
3. S. Ishida, T. Takiguchi, S. Fuji, and S. Asano, Physica B **217**, 87 (1996).
4. J. Toboła, S. Kaprzyk, D. Fruchart, M. Backmann, P. Wolfers, and R. Fruchart, J. Alloys Comp. **262-263**, 65 (1997).
5. D. Shechtman, I. Blech, D. Gratis, and J.W. Cahn, Phys. Rev. Lett. **53**, 1951 (1984).

6. *Physical Properties of Quasicrystals*, edited by Z.M. Stadnik (Springer-Verlag, Berlin 1999).
7. Z.M. Stadnik, K. Al-Qadi, and P. Wang, J. Phys.: Condens. Matter **19**, 326208 (2007), and references therein.
8. P.G. Pagliuso, J.L. Sarrao, J.D. Thompson, M.F. Hundley, M.S. Sercheli, R.R. Urbano, C. Rettori, Z. Fisk, and S.B. Oseroff, Phys. Rev. B **63**, 092406 (2001).
9. J.-S. Rhyee, B.K. Cho, and H.C. Ri, J. Appl. Phys. **93**, 8346 (2003).

List of figures

List of tables

Table of contents

Chapter 1 Theoretical background

1.1 Crystal structures of solids

1.1.1 Fundamental crystallography

In solid state physics, the solids can be classified into crystalline materials, amorphous materials, and quasicrystalline materials. The atomic arrangement in a crystalline solid exhibits a long-range positional order. The atoms in amorphous materials are randomly arranged. The quasicrystalline materials form an ordered pattern that fill all the space but lack a translational symmetry.

1.1.1.1 Single crystals

In a crystalline solid, the atoms, molecules, ions, or building blocks are arranged in an orderly repeating pattern extending in three dimensional space. This is a statement for a crystalline material from the crystallography point of view. These particles appear in a clearly defined geometrical relationship to each other. In crystallography, the layout of the particle positions in a crystalline solid is called a Bravais lattice, which consists of a finite array of points repeating periodically in 3D (three dimensions). The smallest repeatable identical unit in a Bravias lattice is called a unit cell. The lengths of the edges and the angles between the edges in a unit cell are called the lattice parameters. Figure 1 gives the schematic drawing of a unit cell with the lattice parameters.

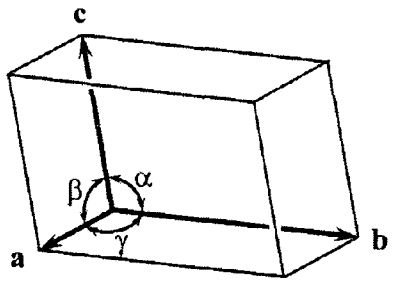

Figure 1. The lattice parameters in a unit cell [1].

The choice of unit cell might not be unique. One structure can be represented by different types of unit cells which can be converted between each other. In order to express the distribution of the atoms in a unit cell, **a**, **b**, and **c** can be used as unit vectors to form a crystallographic coordinate system. *X*, *Y*, and *Z* are the normalized lengths of a point in 3D in a unit cell along the **a**, **b**, and **c** directions starting from the origin. α, β, and γ indicate the angles between the **a**, **b**, and **c** unit vectors.

The crystallographic point group is a set of symmetry operations which consist of rotations and reflections from which the same geometric symmetry can be achieved by moving each point of the crystal while keeping one point fixed. There are five allowed rotations in crystal structures, i.e., $2\pi/1$, $2\pi/2$, $2\pi/3$, $2\pi/4$, $2\pi/6$. The symbols of the rotations are 1, 2, 3, 4, and 6, respectively. Similarly, the symbols for the reflection operations are $\bar{1}$, $\bar{2}$ ($\bar{2} \equiv m$), $\bar{3}$, $\bar{4}$, and $\bar{6}$. The possible crystallography point group operations that can occur in conventional crystals are listed in Table 1 [2-4], and the geometric rotation and inversion operations are illustrated in Table 2.

Table 1 The possible 1, 2, 3, 4, and 6 fold symmetry operations in a single crystal [4].

Rotation n	1	2	3	4	6
Reflection	$\bar{1}$	($\bar{2}\equiv$) m	$\bar{3}$	$\bar{4}$	$\bar{6}$
n with parallel reflection planes (mirror)	m	2mm	3m	4mm	6mm
n with normal 2-fold axis		222	32	422	622
n with mirror normal to n		2/m	(3/m ≡ $\bar{6}$)	4/m	6/m
n with parallel planes			$\bar{3}$m	$\bar{4}$2m	$\bar{6}$m2
n with normal and parallel planes		mmm		4/mmm	6/mmm

Table 2. The geometric rotation and inversion operations of 1, 2, 3, 4, and 6 fold symmetries [4].

	rotation	inversion
1 fold	 360°	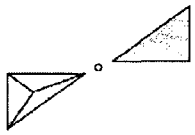
2 fold	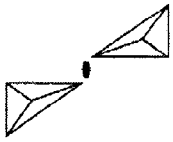 180°	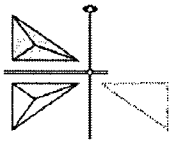
3 fold	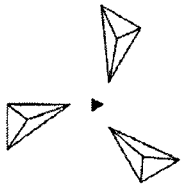 120°	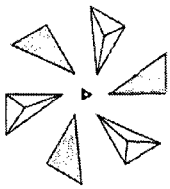
4 fold	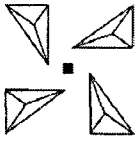 90°	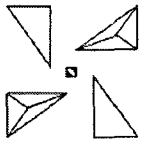
6 fold	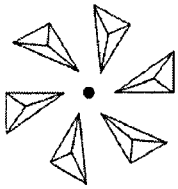 60°	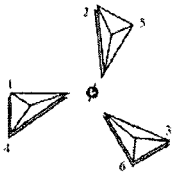

The PG (plane group) is a set of operations which consists of rotations, inversion, reflections, translations, or the combinations of these, from which the same periodic structure in a plane is unchanged. Based on the following three criteria, the SGs (space group) and PGs can be classified in three dimensions: 1) according to the crystallographic point group, there are 32 crystal classes [5]; 2) according to crystal families, 230 SGs can be classified into six categories: triclinic, monoclinic, orthorhombic, tetragonal, hexagonal, and cubic; 3) according to crystal systems, the classification collects the PGs into seven categories: triclinic, monoclinic, orthorhombic, tetragonal, trigonal, hexagonal, and cubic [5]. The classification based on the combination of the Bravias lattices and the crystal classes is listed in Table 3[5-7].

Table 3. The single crystal classification that combines the Bravias lattices and the crystal classes.

Systems(7)	**Independent lattice parameters**	**Crystal classes(32)**	**Bravais lattices(14)**				
			P	**C**	**I**	**F**	**R**
Cubic	a=b=c α=β=γ=90°	$m\bar{3}m$, $m\bar{3}$, $\bar{4}3m$, 432, 23					
Tetragonal	a=b, c α=β=γ=90°	$4/mmm$, $\bar{4}2m$, $4mmm$, 422, $4/m$, $\bar{4}$, 4					
Hexagonal	a=b, c α=β=90°, γ=120°	$6/mmm$, $6mm$, $\bar{6}m2$, 622, $6/m$, $\bar{6}$, 6					
Trigonal	a=b, c α=β=90°, γ=120°	$\bar{3}m$, $3m$, 32, $\bar{3}$, 3					
Orthorhombic	a, b, c α=β=γ=90°	mmm, $mm2$, 222			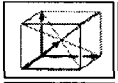		
Monoclinic	a, b, c α=γ=90°, β (+cyclic perm.)	$2/m$, m, 2					
Triclinic	a, b, c α, β, γ	$\bar{1}$, 1					

The SG (space group) is a mathematical description of the symmetry inherent in the crystal structure of a solid. The crystallography SG symbol contains two parts; the first one characterizes the Bravais lattice whereas the second one characterizes the crystal class [3].

The complete "Lattice" symbols can be found in Table 3. The symbol for the crystal class consists of three elements c c c, which are similar to the ones give in Tab 1. In order to describe a plane in a solid lattice in a crystalline solid, a crystallographic coordinate system which consists of a crystallographic basis (basis vectors are lattice vectors) and a crystallographic origin (origin at a centre of symmetry or a point of high site symmetry) [3] is used. With a clearly defined coordinate system, the crystallographic planes are defined as a set of planes that intersect all lattice points. The planes in one set are parallel to each other and equally spaced. The distance between the adjacent planes is the *d*-spacing. The specific set of planes can be described using three integer indices *h*, *k*, and *l*, which are called Miller indices. They are a symbolic vector representation for the orientation of a crystallographic plane in a crystal lattice and are defined as the reciprocals of the fractional intercepts which the plane makes with the crystallographic axes [8].

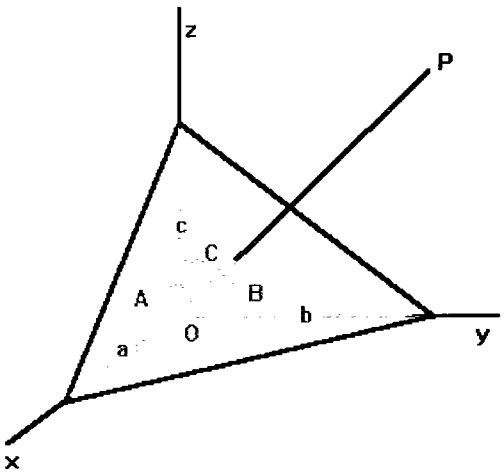

Figure 2. The intercepts of the plane along the unit cell axes [8].

The Miller indices can be determined with following steps: first, determine the intercepts of the plane along the unit cell axes in terms of lattice constants; second, take the reciprocals of the intercepts and clear the fractions; lastly, reduce the reciprocals to the lowest terms. Figure 2 demonstrates the concept of determining the indices. In order to illustrate and understand the relevant mathematical relationships and the diffraction geometry lattice, the concept of a reciprocal lattice, which was introduced by Ewald in 1921, became an important tool. The elementary translations in the reciprocal lattice are defined as [9]:

$$a^* = \frac{b \times c}{V}, b^* = \frac{c \times a}{V}, c^* = \frac{a \times b}{V}, d^*_{hkl} = \frac{1}{d_{hkl}}, \quad (1)$$

where V is the volume of the unit cell and d is the d-space between the neighboring parallel planes.

In a unit cell, atoms might appear in the equivalent positions that can be expressed by the symmetry operations (e.g. reflection, rotation, inversion, and translation). Symbolic and algebraic methods are employed to describe these operations. The symbolic description includes the finite symmetry operations which are performed based on the origin and the crystallographic axes, and the infinite operations which are performed based on the glide planes and the screw axes. The combined algebraic treatment can be written in the form [10]:

$$\begin{pmatrix} x' \\ y' \\ z' \end{pmatrix} = \begin{pmatrix} r_{11} & r_{12} & r_{13} \\ r_{21} & r_{22} & r_{23} \\ r_{31} & r_{32} & r_{33} \end{pmatrix} \begin{pmatrix} x \\ y \\ z \end{pmatrix} + \begin{pmatrix} t_1 \\ t_2 \\ t_3 \end{pmatrix}, \tag{2}$$

where x', y', and z' indicate the resulting vectors, the matrices r_{ij} and t_i correspond to the symmetry operations, and the x, y, and z are the original vectors.

One of the most widely used crystallographic notations of atomic positions and the equivalent positions is Wyckoff code, which can be found in the international crystallography tables. A Wyckoff position is a point belonging to a set of points for which site symmetry groups are conjugate subgroups of the space group [11]. Some RR (Rietveld refinement) programs use the Wyckoff notations to identify the individual atoms in a unit cell, whereas other programs take the real x, y, and z values of a specific atom in a predefined unit cell coordinate system.

By knowing the structure of crystals and its mathematical interpretation, one would like to investigate the real 3D structure of atoms and/or molecules. The atomic radii range from a few tenths of an angstrom to a few angstroms. They are a thousand times smaller than the wavelengths of visible light (roughly from 4000 to 7000 Å). A wavelength to observe the structure of a solid at an atomic level is that of x-ray which are commensurate with both atomic sizes and the shortest inter-atomic distances. The index of refraction of x-ray is close to 1 for all

materials. Therefore, x-rays cannot be focused by a lens to form the image of small objects such as atoms. However, the diffraction pattern of a crystal is a transformation of the crystal structure into reciprocal space, and the 3D crystal structure can be restored by transforming the diffraction pattern back into direct space.

1.1.1.2 Quasicrystals

In conventional crystallography the five-fold symmetry, which was discovered by Dan Shechtman in 1982 [3], is forbidden. A simple understanding of quasiperiodic structures, which describe the structure of QCs (quasicrystals) from a crystallographic point of view, is given by the structural description of a quasilattice with two or more different unit cells, its symmetry, and decoration with atomic clusters [12]. Differing from the glasses and the crystalline materials, the QC structure can be generated by a nonrandom procedure, however, its unit blocks cannot be repeated in a long-range periodic order. The most successful QC models are: the Penrose model, the glass model, and the random-tiling model.

The basis of the Penrose model is a Fibonacci series. A Fibonacci series consist of the successive numbers: $u_0=0$, $u_1=1$, $u_n=u_{n-1}+u_{n-2}$, where n in the subscript of u and n is an integer. The value of u_{n-1}/u_n converges to the value of the golden mean, $\tau=1.618033$ when n is large. The Fibonacci series can also be expressed in power form: $\tau^0=1$, $\tau^1=\tau$, $\tau^n=\tau^{n-1}+\tau^{n-2}$, etc. In a 2D system, the Fibonacci series can be written:

$$\begin{pmatrix} u_{k+1}+u_k \\ u_{k+1} \end{pmatrix} = \begin{pmatrix} 1 & 1 \\ 1 & 0 \end{pmatrix} \begin{pmatrix} u_{k+1} \\ u_k \end{pmatrix}, \tag{3}$$

By replacing u_{n+1} with L, and u_n with S, Equation (3) can be written as [13]:

$$\begin{pmatrix} L+S \\ S \end{pmatrix} = \begin{pmatrix} 1 & 1 \\ 1 & 0 \end{pmatrix} \begin{pmatrix} L \\ S \end{pmatrix}, \tag{4}$$

where L represents 'long' and S represents 'short'. From equation (4), one can obtain the Fibonacci series when $\lim_{n\to\infty} \frac{u_{n+1}}{u_n} = \tau$ (Table 4):

Table 4. The developed Fibonacci series [14].

Series	Number of	
	L	S
L	1	0
LS	1	1
LSL	2	1
LSLLS	3	2
LSLLSLSL	5	3
.	.	.
.	.	.
.	u_{n+1}	u_n

The Fibonacci series in a 2D Penrose tiling is shown in Figure 3.

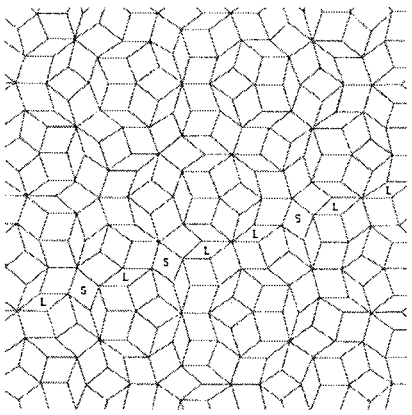

Figure 3. 2D Penrose tiling with marked Fibonacci series.

One can find that the Fibonacci series and the purely randomized L and S sequence are similar to each other. This fact leads to the glass model of QC which suggests that the short-range ordered clusters are purely randomized over longer distances. The broadened peaks found in QC x-ray powder diffraction spectrum proved this hypothesis. From the thermodynamics point of view, the QCs are assumed to be stabilized by a configurational entropy originating from the short-range ordered clusters. A good agreement between the random-tiling model and the experimental results can be achieved by tuning the entropic parameters.

Experimentally, the pentagonal ($\bar{5}$, 5m, 52, $5/m \equiv \overline{10}$, and $\bar{5}m$ according to the missed 5 fold symmetries in Tab.1), octagonal (8/mmm), decagonal (10/mmm), dodecagonal (12/mmm), and i (icosahedral) ($m\bar{3}\bar{5}$) [14, 15] symmetries are found in powder x-ray diffraction patterns. Figure 4 gives the recently solved i-QC structure of the binary compound $YbCd_{5.7}$ [15], one of the very few stable QCs.

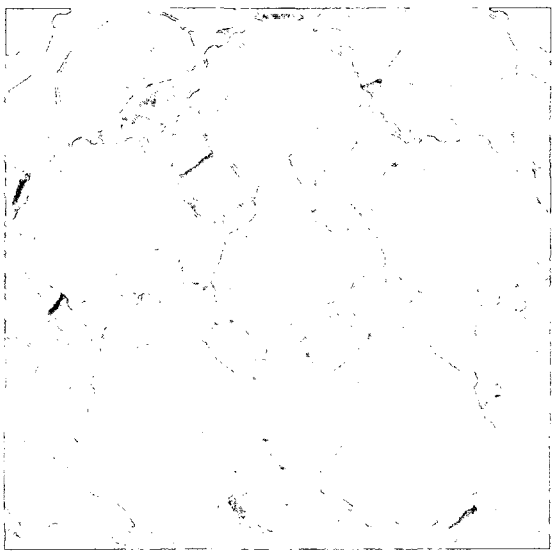

Figure 4. The i-QC structure of $YbCd_{5.7}$.

It can be seen from Figure 4 that three building units with unique atomic decorations are arranged quasiperiodically and fill the space.

1.1.1.3 Approximants

Based on crystallographic classification, approximants belong to the class of crystalline materials. The fundamental clusters (building blocks) of an approximant are clusters that consist of many atoms, rather than that of single atoms in a single crystal, and they are arranged in a long-range periodic order. In general, the building blocks of an approximant and a QC are similar to each other. This makes the physical properties of the two types of materials. The 1/1 approximant only consists of one type of cluster, whereas the 2/1 approximant consists of two types. The schematic 3D structure is shown in Figure 5.

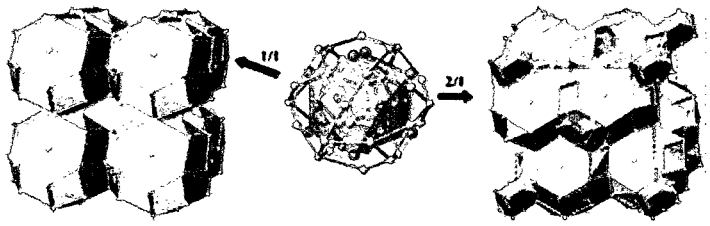

Figure 5. The schematic 3D structure of the 1/1 and 2/1 approximants.

1.1.1.4 Amorphous materials

The amorphous alloys are also called glasses. Their constituents (atoms or molecules) are arranged in a randomly packed fashion that is similar to the constituent arrangement in a liquid in frozen state. This implies that the amorphous solids have to be prepared with an extremely rapid quenching method. Compared to crystalline materials, amorphous solids normally possess higher electrical resistivity and lower density. They also look shinier and feel more ductile.

1.1.2 X-ray powder diffraction

The engineering realization of x-ray diffractometer is discussed in chapter 2. The geometry of diffraction by lattices can be illustrated by Braggs' law. As shown in Figure 6, an incident front of waves with parallel propagation vectors is reflected by the planes (*hkl*) like mirror reflection. The path differences between the beams reflected by the neighboring planes are determined by $\Delta = d_{hkl} \sin\theta$.

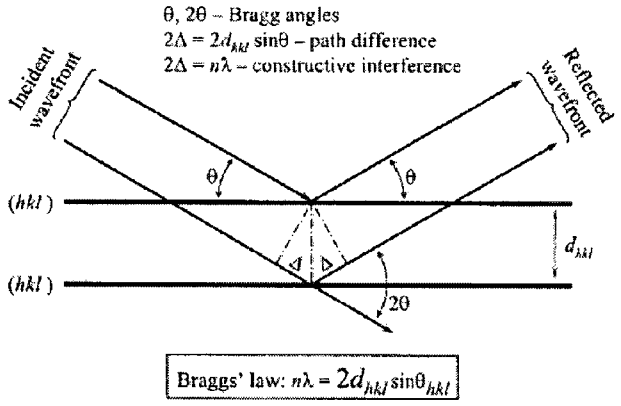

Figure 6. The geometric illustration of Bragg's law [16].

The constructive interference can be observed only when the relation $2\Delta = n\lambda$ is satisfied, where n is an integer and λ is the wavelength of the incident wave-front. These physical and geometrical analyses result in the Braggs' law equation [16]:

$$2d_{hkl} \sin\theta_{hkl} = n\lambda. \tag{5}$$

In reciprocal space, the incident and scattered wave vectors can be defined as the inverse of the wavelength assuming there is no energy loss of the x-rays during the diffraction process:

$|\mathbf{k}_0| = |\mathbf{k}_1| = 1/\lambda$. The angle between $\mathbf{k}_0$ and $\mathbf{k}_1$ is 2θ. The circle in Figure 7 indicates the Ewald's sphere in the case of 2D reciprocal lattice.

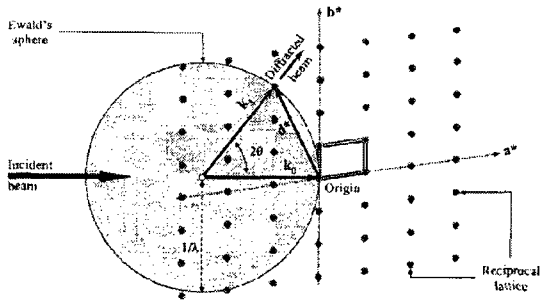

Figure 7. The visualization of diffraction using the Ewald's sphere with radius 1/λ and the 2D reciprocal lattice [17].

If the wave-vectors $\mathbf{k}_0$ and $\mathbf{k}_1$ originate from the same point in the reciprocal space with the unit vectors $\mathbf{a}^*$ and $\mathbf{b}^*$, the constructive diffraction can be observed along $\mathbf{k}_1$ direction only when the difference vector between $\mathbf{k}_0$ and $\mathbf{k}_1$ is equal to $\mathbf{d}^*$ ($|\mathbf{d}^*|=1/d_{hkl}$). For polycrystalline or pulverized specimens, the particles' orientation in the x-ray irradiated area is completely randomized.

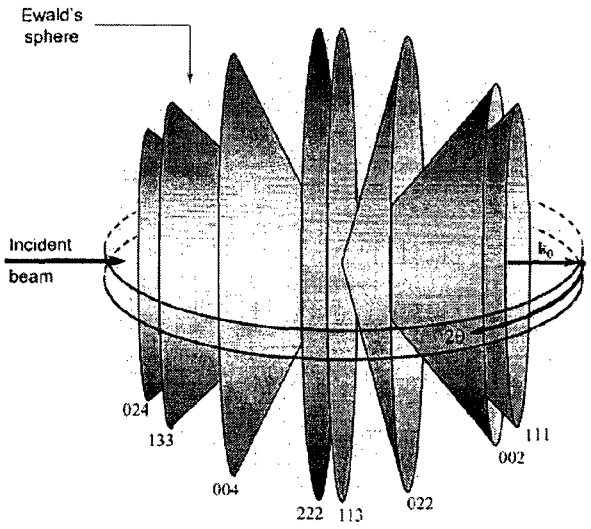

Figure 8. The schematic of the powder diffraction cones produced by a pulverized sample [18].

Therefore, the constructive diffraction can only be detected at those 2θ angles that satisfy the relations mentioned above. Figure 8 illustrates the powder diffraction in 3D reciprocal space. Note that the intensities of the constructive $\mathbf{k}_1$ cones are not discriminated. The intensities of the real x-ray powder diffraction spectrum are relative and depend on many factors, such as Lattice parameters, preferred orientation, x-ray absorption, porosity of the specimen, and the geometry and configuration of the x-ray diffractometer. The shape and width of the x-ray diffraction peaks are related to the crystallinity, disorder, defects, grain size, strain, and stress of the specimen, the spectral purity, the geometry, and beam condition of the diffractometer.

1.1.3 Neutron diffraction

The neutron diffraction is a complementary technique to the x-ray powder diffraction. First, the similarity in wavelength of a neutron source used in a neutron diffraction measurement at room temperature (1.45 Å) [19] and the x-ray radiation ($K\alpha_1$: 1.54 Å) makes the neutron diffraction a suitable method for exploring the structure information in a solid. Second, the neutron is an atomic particle which has no electric charge [20, 21] and its mass is 2000 times larger than that of an electron. The neutrons interact with the atoms in a sample via nuclear rather than electrical forces, and the nuclear force is considered to be a short range interaction on the order of a few femtometers. This makes the neutron scattering less sensitive to the electric charge than x-ray or electron scattering [20]. Last, the moment carried by a neutron gives rise to the magnetic Bragg scattering in a magnetic field produced by the unpaired electrons. Therefore, the direction and magnitude of the magnetization inside a solid can be studied [20].

1.1.3.1 Nuclear scattering wavelength

The de Broglie wavelength of neutron is given:

$$\lambda = \frac{h}{mv}, \tag{6}$$

where λ is the wavelength, m is the mass, v is the velocity, and h is the Planck's constant. Assuming that neutrons act as an ideal gas, the RMS (root-mean-square) velocity can be evaluated by using Maxwell-Boltzmann distribution:

$$E = \frac{1}{2}mv^2 = \frac{3}{2}kT, \tag{7}$$

From equation (6) and (7), the wavelength of neutrons at temperature T can be calculated as [22]:

$$\lambda^2 = \frac{h^2}{3mkT}, \tag{8}$$

Equation (8) shows that the wavelength of neutrons at 300 K is 1.54 Å.

1.1.3.2 Nuclear scattering cross-section

The interactions between the neutrons and the nucleus during the scattering process are considered as short-range interactions. The results of the scattering process can be expressed in terms of a quantity know as a cross-section. In the polar coordinates, the partial differential cross-section can be defined as [23]:

$$\frac{d^2\sigma}{d\Omega dE'} = \frac{\begin{array}{c}number\ of\ neutrons\ scattered\ per\ second\ into\ a\ small\ solid\ angle \\ d\Omega\ in\ the\ direction\ \theta,\phi\ with\ final\ energy\ between\ E'\ and\ E'+dE'\end{array}}{\Phi d\Omega dE'}. \tag{9}$$

Defining a neutron with wavevector $\boldsymbol{k}$ incident on a sample with a wavelength λ, expressing the wavefunction of the neutron by ψ_k and of the scattering system by χ_λ, the final state wavevector

and scattering system by k' and λ', respectively, the general expression for the partial differential cross-section is [24]:

$$\frac{d^2\sigma}{d\Omega dE'} = \frac{k'}{k}\left(\frac{m}{2\pi\hbar^2}\right)^2 |\langle k'\lambda'|V|k\lambda\rangle|^2 \delta(E_\lambda - E_{\lambda'} + E - E'), \tag{10}$$

where V is the potential of the scattering system. The mathematical expression of this potential can be written as a delta function, which is known as Fermi pseudopotential:

$$V(r) = \frac{2\pi\hbar^2}{m} b\delta(r), \tag{11}$$

where b is the scattering length.

1.1.3.3 Magnetic scattering

Since neutrons carry a spin, the microscopic magnetic structure can be revealed by studying the interaction between the spin and the magnetic moment in a sample. In the case of magnetic scattering, equation (10) can be re-written as:

$$\left(\frac{d^2\sigma}{d\Omega dE'}\right)_{mag} = N\frac{k'}{k}\left(\frac{\gamma r^0}{2}\right)^2 g^2 \left|\vec{F}(\vec{Q})\right|^2 e^{-2W} S_{mag}(\vec{Q},\omega), \tag{12}$$

where γ is a constant (γ=1.913), e^{-2W} is the Debye-Waller factor, $\vec{F}(\vec{Q})$ is a Fourier transform of the spin density, also known as the magnetic form factor, and $S_{mag}(\vec{Q},\omega)$ is the scattering function. The expression of $S_{mag}(\vec{Q},\omega)$ is [25]:

$$S_{mag}(\vec{Q},\omega) = \frac{1}{2\pi\hbar}\int_{-\infty}^{\infty} dt \sum_{\alpha,\beta}(\delta_{\alpha,\beta} - \hat{Q}_\alpha \hat{Q}_\beta \sum_j e^{i\hat{Q}r_j}) \langle S_0^\alpha(0) S_j^\beta(t)\rangle e^{-i\omega t}, \tag{13}$$

where α and β refer to x, y, and z, and S_j^β is the β component of the spin of the j^{th} magnetic ion.

Other than the short-range interactions found in neutron scattering process only, the diffraction theories of neutron scattering and x-ray scattering are essentially the same. Therefore, the Rietveld Refinement analysis method can be applied to both scattering techniques.

1.1.4 Rietveld refinement

In order to refine and confirm the precise structural information of the crystalline specimen and eliminate device related errors from the x-ray powder diffraction spectrum, the Rietveld method (whole-profile) is employed in the data analysis. To apply the RR (Rietveld Refinement) analysis, the following procedure is followed [26]: 1) data collection, 2) background determination, 3) peak-shape selection, 4) profile parameters refinement, 5) structural parameters refinement, 6) restraints usage, 7) the result and discussions.

1.1.4.1 Data collection

In most modern laboratories, the x-ray powder diffractometers based on Bragg-Brentano geometries are used to obtain the raw x-ray spectrum. The following factor has to be taken into consideration in getting accurate data. First, the mechanical precision of the 2θ relations of the diffractometer is critical in getting high quality raw spectra for RR analysis. This factor is determined by the device manufacture. However, certain mathematical treatments can be used to further reduce such types of system errors, i.e., correcting the 2θ scale based on the spectrum obtained from mixing a standard sample with the specimen and applying the zero offset by software. The standard laboratory diffractometers are equipped with ADS (automatic divergence slits) which can greatly improve the SNR (signal-to-noise-ratio). However, the standard RR analysis software only accepts the spectrum obtained with FDS (fixed divergence slits). The two types of spectra can be converted by software. The x-ray penetration depths are different from sample to sample. The thickness of the pulverized sample has to be carefully calculated and

prepared to ensure the correct 2θ geometry. The grain of the sample might possess a preferred orientation that can lead to incorrect intensity measurements. This can be solved or alleviated by rotating the sample while taking the measurement and paying attention during the sample preparation, although the RR software allows refinement of a preferred-orientation parameter. In principle, monochromatic x-ray radiation is the ideal source, which makes synchrotron radiation the best candidate. Conventional x-ray sources are generated from impacts of high-energy electrons with a copper target. By filtering out unwanted radiations, only the $K\alpha_1$, $K\alpha_2$ lines, and some minor background x-rays remain.. RR programs can also take the doublet source into consideration in data analysis.

1.1.4.2 Background determination

Backgrounds could come from the x-ray sources, the sample tray or environmental interferences. They can be removed from the raw spectrum by subtracting a refined multi-degree polynomial or an empirical function that describes the specific background the best.

1.1.4.3 Peak-shape selection

The peak shapes are a function of both the sample (domain size, stress/strain, and defects) and the instrument (radiation source, geometry, and slit sizes) and they vary as a function of 2θ. The most widely used peak shape for x-ray is a pseudo-Voigt approximation of a Voigt function. The pseudo-Voigt function is simply a combination of Lorenzian and Gaussian components in the ratio $\eta/(1-\eta)$, where η is the pseudo-Voigt mixing parameter [26]. In general, the Gaussian component tends to dominant at low angles and the Lorentzian at high angles. RR programs give the user the right to choose the peak shape function. Satisfactory result can be obtained by trial and error and the relevant parameters can be refined by the programs.

1.1.4.4 Profile parameters refinement

When the structural model is incomplete, the calculated intensities might deviate significantly from the observed ones. In this case, the structure-free approach referred to as the Le Bail refinement (Le Bail *et al.*, 1988) [26] can be used to obtain a satisfactory fit. The prerequisite for getting a good improvement is to refine the SG, the unit-cell parameters (a, b, c, α, β, and γ), and the 2θ correction (which includes both the zero offset and the deviations in 2θ caused by displacement of the sample from the centre of the 2θ circle) [26]. Once good agreement between the lattice parameters and 2θ is achieved, the FWHM (full width at half maximum) of the Gaussian component, as a function of 2θ, can be written in a form proposed by Caglioti *et al.* [27],

$$\mathrm{FWHM}^2 = U\tan^2\theta + V\tan\theta + W, \tag{14}$$

and that of the Lorentzian component can be written as

$$\mathrm{FWHM} = X\tan\theta + Y/\cos\theta. \tag{15}$$

The FWHM parameters X and Y of the Lorentzian component can be easily refined for high-resolution data. The Gaussian parameters U, V, and W should be constrained under some circumstances to avoid nonphysical results. The Le Bail refinement might result in a good match between the generated profiles and the experimental ones without correct structural parameters. However, the lattice parameters obtained from the Le Bail refinement can be used to refine the structural parameters in the complete whole-profile refinement.

1.1.4.5 Structural parameters refinement

The structural refinement should be performed with the correct structural model and all atomic positions. If the structural model is incomplete and some atomic positions are missing,

one can generate a difference Fourier map, which represents the difference electron density, by subtracting the electron density generated from the starting model from the one calculated from the experimental spectrum. The difference Fourier map can be used to calculate the missing atomic positions and complete the structural model.

By completing all the preparations mentioned above, one can start refining the structure of the sample by comparing the generated profiles with the experimental ones. The least-squares residual functions can refine the specified parameters by minimizing the difference between the generated profiles and the experimental spectrum. In most cases, only 2-5 least-squares cycles are performed at a time to prevent the divergence of the refined parameters [26]. There are two criteria to monitor the progress of a refinement: the value of GOF (goodness of the fit) and the range of the refined parameters. If the GOF value ($\geq$1) is smaller than that of the previous refinement, it means that the refined parameters are converging for this round. After a set of least-squares cycles, the range of each parameter has to be carefully examined, i.e., the refinement could result in a negative of the square of a real variable. The adjustment of the atomic position parameters can affect the relative peak intensities. The thermal parameters, which are highly correlated with the scale and occupancy parameters, are related to background correction and peak broadening. It is advised to start the refinement of the structural parameters with the positions of the heavier atoms and then the lighter ones. Other refinements, such as refinements of the anisotropic parameters, are also possible to improve the overall reliability of the RR when a high quality spectrum is used. An acceptable structural refinement can require a hundred cycles or more for a sample with medium complexity in its structure [26]. It is unavoidable to roll back to previous refinement and then adjust the refinement controls for a

better result. The refinements done by different persons might differ from each other depending on the experience and sequence of the refinement controls used by the individuals.

1.1.4.6 Restraints usage

The RR is performed by assuming the main structure and most of the atomic position parameters are correct. However, the situation is different from sample to sample. Sometimes, fine refinement of atomic positions is required. For example, the occupancies of two different types of atoms on two atomic positions can be refined by the RR programs with the restraint that the sum of the occupancies is 1. The geometric and chemical restraints, if used carefully, can enhance a considerable refinement.

1.1.4.7 The results and discussions

There are many RR programs available on the market. The interface and detailed operations are different from one to another. In general, the sequence of RR can be summarized as: 1. Import the raw spectrum to the RR program; 2. Apply the 2θ correction and the zero offset compensation, if possible; 3. Convert the spectrum from ADS mode to FDS mode if necessary; 4. Determine and refine the background; 5. Input the SG, the lattice parameters, and the complete structural information of the sample; 6. Carefully control the parameters to be refined by following the principles mentioned above, monitor the result after each set of least-squares cycles, adjust the refinement controls, and redo current or proceed to the next refinement; 7. Evaluate the validity of the result and implement special setting, i.e., apply damping factors when the refined parameters cannot converge as needed; 8. Add the second phase or more phases if necessary and repeat the procedures 5-7 until a satisfactory result is obtained; 9. Output the results, do the quantitative analysis for different phases, and evaluate the results.

The RR method is a powerful tool to extract the structural details from the powder diffraction data for the crystalline materials. With sufficiently high quality data and carefully planned processes, about 200 structural parameters can be refined with great success [26].

1.2 Magnetic properties

1.2.1 Introduction

Based on their magnetic properties, solids can be classified into the following categories: diamagnetic, paramagnetic, ferromagnetic, antiferromagnetic, ferrimagnetic, and spin glass.

Each of the above six categories will be discussed in details in this section. The first five categories are based on traditional magnetic classification method. The magnetic properties of these five conventional materials are represented in Figure 9.

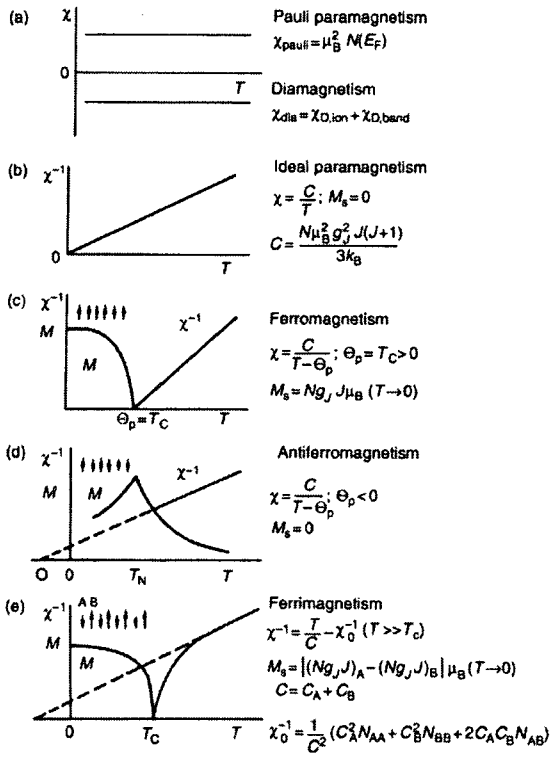

Figure 9. The summary of the temperature dependence of the magnetization M, the inverse magnetic susceptibility $1/\chi$ in various types of magnetic materials [28].

The history- and aging-related effects make the temperature-dependent magnetic properties of a spin glass different from the other five categories. The theoretical models of spin glass will be discussed in section 1.2.8.

1.2.2 Diamagnetism

Diamagnetism is a very weak form of magnetism that is only exhibited in the presence of an external magnetic field. It is the result of the changes in the orbital motion of electrons due to the external magnetic field. The induced magnetic moment is very small and in a direction opposite to that of the applied field. When placed between the poles of a strong electromagnet, diamagnetic materials are attracted towards regions where the magnetic field is weak. The

diamagnetism can be understood qualitatively by the Lenz's law of electricity. When the magnetic flux enclosed in a current loop changes, the induced current in this loop tends to weaken the change [29].

Assuming there are Z electrons in an atom, the susceptibility per cm^3 can be estimated by Langevin's equation [29]:

$$\chi = -N\frac{e^2}{6mc^2}\sum_{i=1}^{z}\overline{r_i^2}, \tag{16}$$

where N is the number of atoms per cm^3, $\overline{r^2}$ is the mean square of the distance between the nucleus. It can be seen from equation (16) that the diamagnetic susceptibility is always negative (the term $\overline{r_i^2}$ is always positive). Diamagnetism exists in all matter. Since $\overline{r_i^2}$ will slightly vary with temperature, χ is also temperature dependent, although this temperature dependent effect is very small.

1.2.3 Paramagnetism

Paramagnetism is the tendency of the atomic magnetic dipoles, due to quantum-mechanical spin, in a material that is otherwise non-magnetic to align with an external magnetic field. This alignment of the atomic dipoles with the magnetic field tends to strengthen it, and is described by a relative magnetic permeability greater than unity (or, equivalently, a small positive magnetic susceptibility).

In 1895, Pierre Curie showed a relationship between the susceptibility and the absolute temperature for certain class of materials which are known as paramagnetic materials:

$$\chi = \frac{C}{T}, \tag{17}$$

where C is a constant. This relation is the so-called Curie's law [30].

The quantum mechanical basis of magnetism can be simply understood as below. Each atom has a principle quantum number n with n=1, 2, 3.... which corresponds to the electrons occupying the K, L, M... shells. The value of the orbital angular momentum quantum number l ranges from 0 to n-1. The electrons with the orbital angular quantum number l are considered as s (l=0), p (l=1), d (l=2), f (l=3),... electrons. The angular momentum of an electron can be calculated with $\hbar\sqrt{l(l+1)}$. The magnetic quantum number m_l ranges from $-l$ to l. Each m_l indicates a specific direction which is known as the quantization direction in accordance to the applied magnetic field. The spin quantum number m_S which has the allowed values 1/2 and -1/2 describes the component of the electron spin along the external magnetic field direction. The relations of the quantum numbers in the vector form are $\vec{L} = \sum_i \vec{l_i}$, $\vec{S} = \sum_i \vec{s_i}$, and $\vec{J} = \vec{L} + \vec{S}$, where $\vec{J}$ is the total angular momentum and its values are in the range of:

$$J=(L\text{-}S),\ (L\text{-}S+1),\ \text{to}\ (L+S\text{-}1),\ (L+S). \tag{18}$$

Therefore, the total magnetic dipole momentum of an atom can be evaluated as:

$$\vec{\mu} = -g_J \mu_B J, \tag{19}$$

where μ_B is the Bohr magneton, g_J is the Landé spectroscopic g-factor and it has the form: $g_J = 1 + \frac{J(J+1)+S(S-1)-L(L+1)}{2J(J+1)}$ [31]. The magnetization M of the system is a statistical average of the magnetic moment of each state by the probability that this state is occupied along the applied magnetic field direction. By applying the definition of the magnetic susceptibility $\chi = M/H$, the derived magnetic susceptibility is given:

$$\chi = \frac{N\mu_0 g^2 J(J+1)\mu_B^2}{3kT} = \frac{C}{T}, \tag{20}$$

where $C = \frac{N\mu_0 g^2 J(J+1)\mu_B^2}{3k}$. Equation (20) proves the Curie's law from the quantum mechanics point of view [32]. However, the distribution of different quantum states varies with the system

temperature. The quantum states in equation (20) should be modified by taking the thermal effect into account to reflect the real magnetic susceptibility of the system. The temperature dependent magnetizations of a few typical paramagnetic complex slats are illustrated in Figure 10.

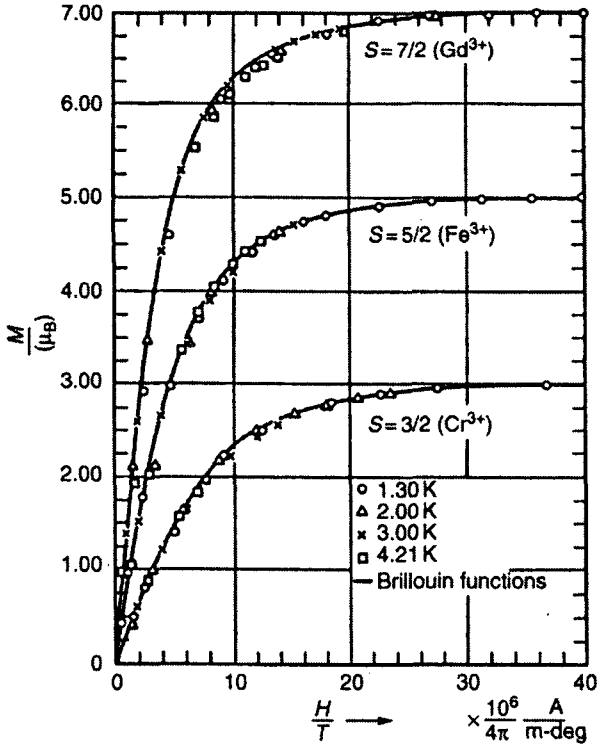

Figure 10. The magnetization M (in μ_B/atom) of a few paramagnetic complex salts containing Gd^{3+}, Fe^{3+}, and Cr^{3+} plotted *vs.* $\mu_0 H/T$ (in T/K) [33].

1.2.4 Magnetically ordered states

A high magnetization is observed in magnetically ordered materials even without the presence of an external magnetic field. These materials are characterized by a SM (spontaneous magnetization). The SM vanishes at temperatures higher than a particular value T_C, which is the Curie temperature.

The phenomenological and the quantum-mechanical origin of SM are the Weiss field (molecular-field) and the Heisenberg exchange interaction (quantum-mechanical exchange

interaction), respectively. The existence of SM indicates that the magnetic field intensity of the magnetic dipoles in the substance is much larger than that of the externally applied magnetic field. The difference is known as the Weiss field or the molecular-field and takes the form:

$$\overrightarrow{H_T} = \vec{H} + \overrightarrow{H_m} = \vec{H} + N_W \vec{M}, \tag{21}$$

where $\overrightarrow{H_T}$ is the total magnetic field acting on a given dipole, $\overrightarrow{H_m}$ is the so-called molecular field, and N_W is the molecular-field constant [34]. The enormous molecular-field was left unexplained by Weiss model until quantum mechanics was applied. In general, the Heisenberg model takes into account the interactions between the spins on the nearest-neighbors and a larger number of surrounding atoms. Its exchange Hamiltonian has the form [35]:

$$H_{exch} = -\sum_{i \neq j} I_{ij} \overrightarrow{S_i} \overrightarrow{S_j}, \tag{22}$$

where I_{ij} are the exchange integrals between the spins located on sites i and j. By considering only the interactions between the spins on the nearest-neighboring atoms and assuming there are Z magnetic nearest-neighbor atoms, with equation (21), equation (22) can be written as [36]:

$$H_{exch} = \frac{-ZJ_{nn}(g-1)^2 \vec{\mu} \cdot \langle \vec{\mu} \rangle}{g^2 \mu_B^2} = -\mu_0 \vec{\mu} \cdot \overrightarrow{H_m}, \tag{23}$$

where $\overrightarrow{H_m} = \frac{ZJ_{nn}(g-1)^2 \langle \vec{\mu} \rangle}{g^2 \mu_B^2}$. Therefore, the phenomenological Weiss field model finds its quantum-mechanical proof [37].

The origin of the interaction between two electrons in the same atom is the same as that of the interaction between two electrons in two neighboring atoms. This interaction can be considered as the direct exchange interaction. It can lead to parallel and anti-parallel spin states. The direct exchange interaction can result in a strong interaction especially for 3d metals due to the overlaps between the neighboring 3d-electron charge clouds. A ratio r_{ab}/r_d found by Slater in 1930 is highly correlated to this exchange interaction, where r_{ab} is the inter-atomic distance and

r_d is the radius of the incompletely filled d shell [38]. The Bethe-Slater curve which describes the empirical relationship between the exchange interaction and the ratio r_{ab}/r_d is illustrated in Figure 11 schematically. The theoretical basis of this relationship remains unclear despite its success in separating the ferromagnetic 3d elements from the anti-ferromagnetic elements.

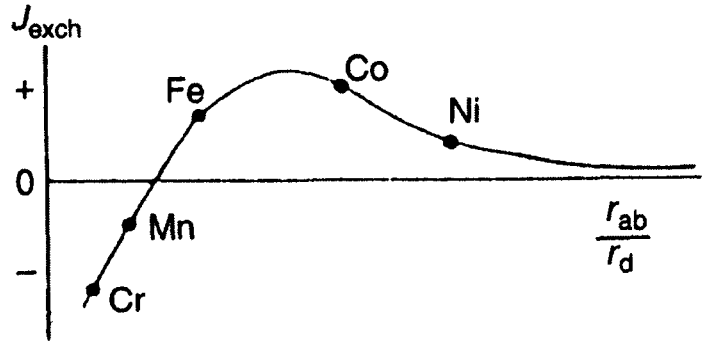

Figure 11. The Bethe-Slater curve describing the variation of the exchange constant with inter-atomic separation r_{ab} and radius r_d of the incompletely filled d shell [38].

1.2.5 Ferromagnetism

1.2.5.1 The theory

A material with high magnetic permeability which imposes little resistance to orientation in the presence of an applied magnetic field, such as iron, steel, and nickel, is a ferromagnetic substance. If all magnetic dipoles in a system are aligned in accordance to the applied magnetic field, the maximum magnetic moment can be derived from summing the magnetic dipole moments (equation (19)) of N atoms [38]:

$$M(0) = Ng\mu_B J. \tag{24}$$

Similarly, the magnetization of the sample at a given temperature can be written as [38]:

$$M(T) = Ng\mu_B J B_J(x), \tag{25}$$

where $$x = \frac{Jg\mu_B H}{kT}, \tag{26}$$

and $$B_J = \frac{2J+1}{2J}\coth\frac{2J+1}{2J}x - \frac{1}{2J}\coth\frac{x}{2J}, \tag{27}$$

where B_J is the Brillouin function. For a given ferromagnetic material, the H in equation (26) should be replaced by H_T (equation (21)), thus, the susceptibility can be written as [39]:

$$x = \frac{Jg\mu_B}{kT}(H + N_W M). \tag{28}$$

For H=0, the following relationship can be derived from equation (24) and equation (25) [38]:

$$\frac{M(T)}{M(0)} = B_J(x) = \frac{kT}{NN_W g^2\mu_B^2 J^2}. \tag{29}$$

From equation (28), one has $x \ll 1$ at high temperatures. Thus, the Brillouin function can be evaluated as [40]:

$$B_J(x) \approx \frac{J+1}{3J}x - \frac{J+1}{3J}\frac{2J^2+2J+1}{30J^2}x^3. \tag{30}$$

One can introduce a parameter T_C which can be defined as [40]:

$$T_C = \frac{Ng^2\mu_B^2 J(J+1)}{3k}N_W. \tag{31}$$

Thus, equation (29) can be simplified to [40]:

$$\frac{M(T)}{M(0)} = \frac{J+1}{3J}\left(\frac{T}{T_C}\right)x. \tag{32}$$

The $M(T)/M(0)$ *vs.* x and the $M(T)/M(0)$ *vs* T/T_C curves are shown in Figure 12 and Figure 13, respectively.

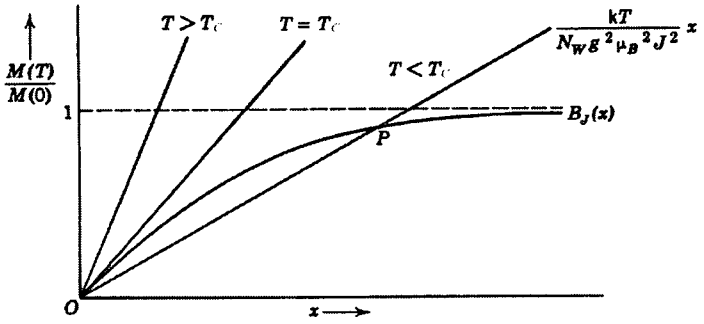

Figure 12. The illustration of the spontaneous magnetization at a given temperature T [40].

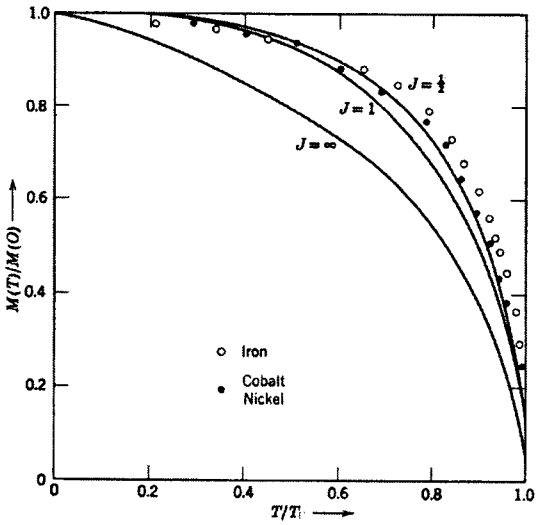

Figure 13. The spontaneous magnetization as a function of temperature. the curves are the analytical solution and the points represent the experimental data [40].

At temperatures above the Curie point T_C, the SM vanishes. For a small externally applied magnetic field, the saturation effects can be ignored. The magnetization can be derived from equation (25) and equation (27):

$$M = \frac{Ng\mu_B(J+1)}{3}x, \tag{33}$$

where the x is given by equation (28). Using the definition of the magnetic susceptibility $\chi = M/H$, equation (28) becomes:

$$\chi = \frac{C}{T-\theta}, \tag{34}$$

where $C = \frac{Ng^2\mu_B{}^2J(J+1)}{3k}$ and $\theta = N_W \frac{Ng^2\mu_B{}^2J(J+1)}{3k} = N_W C$. Equation (34) is the so-called Curie-Weiss law which describes the temperature dependent magnetic susceptibility of the ferromagnetic materials at temperatures higher than the Curie point. The temperature dependency of the reciprocal of the susceptibility above T_C is illustrated in Figure 14.

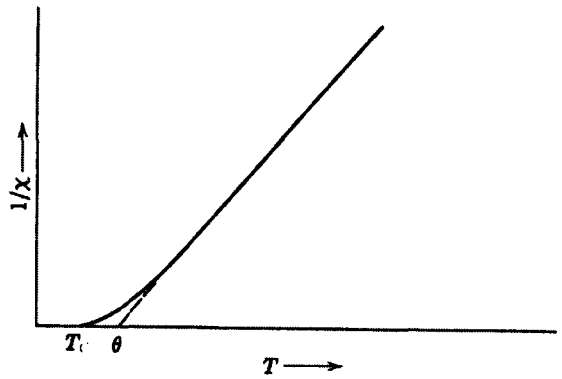

Figure 14. The illustration of the temperature dependency of the reciprocal of the susceptibility of a ferromagnetic material above the Curie point. T_C is the ferromagnetic Curie point and θ is the paramagnetic Curie point [41].

1.2.5.2 Arrott plot

The precise determination of the Curie temperature is of great interest in analyzing the magnetic properties of a ferromagnetic sample. A method proposed by A. Arrott in 1957 shows that a linear relationship between the terms M^3 and H or M^2 and H/M for a ferromagnetic sample in the limit of small applied magnetic field around the Curie point can be found based on the mean-field approximation [42].

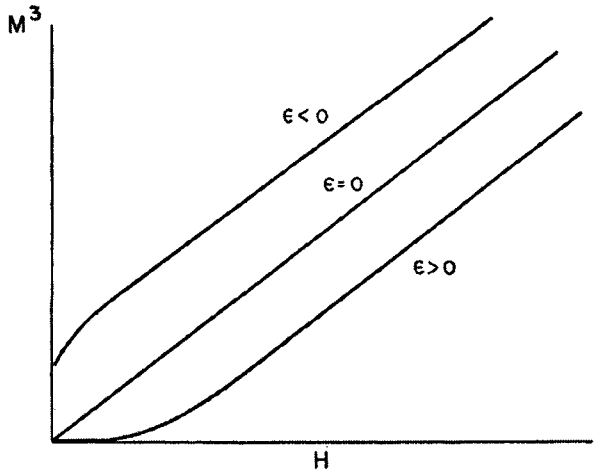

Figure 15. Magnetization cubed vs field for temperatures just below the Curie point ($\epsilon < 0$), at the Curie point ($\epsilon = 0$), and just above the Curie point ($\epsilon > 0$) [42].

As can be seen in Figure 15, the curve M^3 *vs* H at Curie temperature is linear and its linear extrapolation passes through the origin, where $\epsilon = 1 - \frac{T_C}{T}$. The isotherms above and below the Curie point are somewhat nonlinear.

1.2.5.3 Modified Arrott plot

For samples that deviate from the mean-field theory, a modified model which introduces the critical exponential parameters γ and β can be used to accommodate this deviation. This model is the so-called modified Arrott plot and its general expression is given by [43]:

$$\left(\frac{H}{M}\right)^{1/\gamma} = \frac{T-T_C}{T_1} + \left(\frac{M}{M_1}\right)^{1/\beta}, \tag{35}$$

where T_1 and M_1 are constants. As the temperature approaches T_C and the applied field is close to zero, the following four relations can be used to determine the parameters γ, β, and T_C:

$$\lim_{H\to 0}\left(\frac{H}{M}\right) = \left(\frac{T-T_C}{T_1}\right)^{\gamma}, T > T_C, \tag{36}$$

where

$$\frac{H}{M} = |M/M_1|^{\delta-1}, T = T_C, \tag{37}$$

and $$\lim_{H\to 0} M = \left(\frac{T_C - T}{T_2}\right)^{\beta}, T < T_C, \quad (38)$$

and $$\delta - 1 = \gamma/\beta. \quad (39)$$

The isotherms in the $M^{1/\beta}$ *vs.* $(H/M)^{1/\gamma}$ plane show good linearity and the one at the Curie point passes through the origin [43]. The modified Arrott plot can effectively overcome the influence of the applied magnetic field and thermal effects [43]. The linearity of the isotherms of the modified Arrott method can be clearly seen in Figure 16.

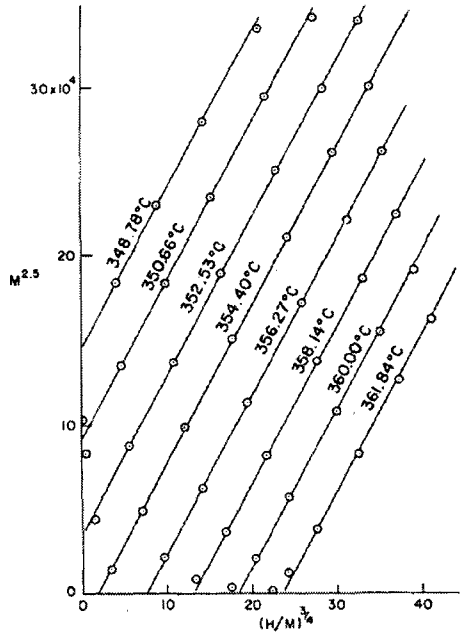

Figure 16. The illustration of the modified Arrott plot in the $M^{1/\beta}$ *vs.* $(H/M)^{1/\gamma}$ plane from equation (35) [43].

1.2.6 Antiferromagnetism

In materials that exhibit antiferromagnetism, the spins of magnetic electrons align in a regular pattern with neighboring spins pointing in opposite directions. This is the opposite of ferromagnetism. Generally, antiferromagnetic materials exhibit antiferromagnetism at a low temperature, and become disordered above a certain temperature. This transition temperature is

called the Néel temperature above which the material typically becomes paramagnetic.

An antiferromagnetic material can be considered as two overlapped sub-lattices, denoted by A and B. The magnetic moments are identical in magnitude in each sub-lattice, whereas their orientations are anti-parallel [44]. This arrangement can be seen in Figure 17.

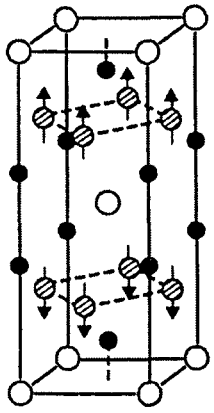

Figure 17. The arrangement of the magnetic moments in the unit cell of an antiferromagnetic material, YMn_2Ge_2. The open circles represent the Y atoms, the dashed circles the Mn atoms, and the black circles the Ge atoms [44].

This makes the total magnetism of an antiferromagnet zero at absolute zero temperature. Based on the postulated model above, the fields acting on the two sub-lattices can be written separately as:

$$\vec{H}_A = \vec{H} + N_{AA}\vec{M}_A + N_{AB}\vec{M}_B, \tag{40}$$

$$\vec{H}_B = \vec{H} + N_{BA}\vec{M}_A + N_{BB}\vec{M}_B. \tag{41}$$

where N_{AA}=N_{BB}=N_1, N_{AB}=N_{BA}=N_2, and $N_1 \neq N_2$ [44].

From equation (40), equation (41), and the description above, the absolute values of M_A and M_B are the same [44]:

$$|M_A| = |M_B| = \frac{1}{2}NgJ\mu_B. \tag{42}$$

In a similar manner to the derivation done in the ferromagnetic section, one can find:

$$\chi = \frac{C}{T-\theta_p}, \tag{43}$$

where $C = \frac{N\mu_0 g^2 J(J+1)\mu_B{}^2}{3k}$, $\theta_p = \frac{1}{2}C(N_1 + N_2)$, and $T_N = \frac{1}{2}C(N_1 - N_2)$, where T_N is the Neel temperature and it is different from θ_p in equation (43). At temperatures above T_N, the Curie Weiss law is still valid.

1.2.7 Ferrimagnetism

A ferrimagnetic material is one in which the magnetic moment of the atoms on different sublattices oppose as in antiferromagnetism but the opposing moments are unequal and a spontaneous magnetization remains [45]. This happens when the sublattices consist of different materials or ions (such as Fe^{2+} and Fe^{3+}).

In ferrimagnetic materials, the magnitude of the magnetic moments of the A and B sub-lattices are different. Similar to the antiferromagnetic materials, the arrangement of the magnetic moments in the unit cell in a ferrimagnetic material can be illustrated in Figure 18:

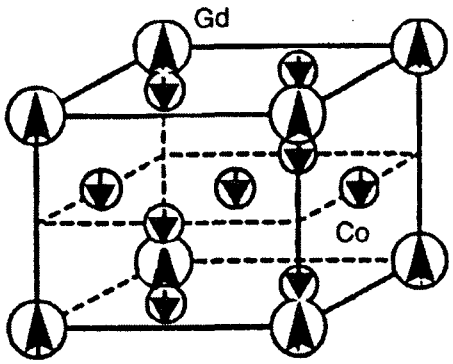

Figure 18. The magnetic moment arrangement in the unit cell of $GdCo_5$ [45].

At temperatures higher than the Curie point, the Curie Weiss law is still valid, whereas the magnetic susceptibility behavior at temperatures lower than T_C are generally more complex. Assuming the applied magnetic field H is zero, the expression for the temperature dependent SM

is given by:

$$M(T) = |M_A(T) - M_B(T)|, \tag{44}$$

$$M_A(T) = \frac{C_A}{T}(N_{AA}M_A + N_{AB}M_B), \tag{45}$$

$$M_B(T) = \frac{C_B}{T}(N_{BB}M_B + N_{BA}M_A), \tag{46}$$

$$C_A = \frac{N_A g_A{}^2 \mu_B{}^2 J_A(J_A+1)}{3k}, \tag{47}$$

$$C_B = \frac{N_B g_B{}^2 \mu_B{}^2 J_B(J_B+1)}{3k}. \tag{48}$$

From equation (44) to equation (48), one can tell that the A and B sub-lattice components are highly correlated. The Curie point of a ferrimagnetic substance can be calculated as [46]:

$$T_C = \frac{1}{2}(C_A N_{AA} + C_B N_{BB}) + \frac{1}{2}\sqrt{(C_A N_{AA} - C_B N_{BB})^2 + 4C_A C_B N_{AB} N_{BA}}. \tag{49}$$

1.2.8 Spin glass

1.2.8.1 Introduction

Spin glass refers to a magnetic state of a system in which the interactions between the magnetic moments are "in conflict" with each other due to disorder so that the spins order in a non-periodic fashion - they "freeze" into *random* directions. Additionally, the state is characterized by very slow equilibration after perturbation and significant history-dependence [46].

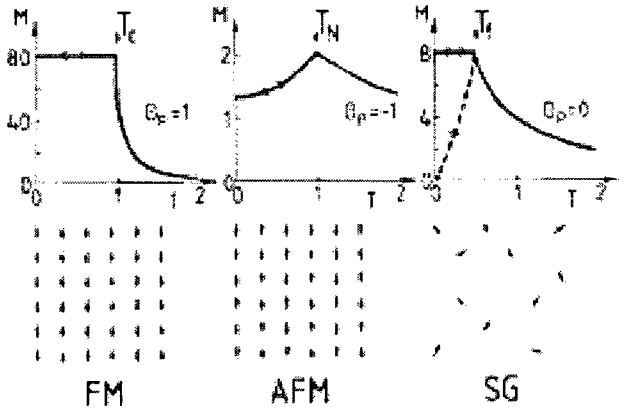

Figure 19. Comparison of the magnetization and their magnitude for (a) a ferromagnet, (b) an anti-ferromagnet, and (c) a spin glass in the limit of small applied magnetic field. For spin glass, the solid line indicates the FC (field cooled) curve and the dash line indicates the ZFC (zero field cooled) curve [46].

The schematic magnetizations and their relative magnitudes of a ferromagnet, an anti-ferromagnet, and a spin glass are compared in Figure 19, where the measurements are done in a small applied magnetic field.

1.2.8.2 Spin glass and the EA (Edwards-Anderson) model

As indicated by the name, the term spin glass implies that the spin orientation in a spin glass is similar to the pattern of the randomly packed atoms in glasses. At temperatures above T_f (known as freezing temperature), the magnetic moments of spin glass can be estimated by the Curie-Weiss's law. Depending on the magnetic history, the magnetization splits into two curves, the FC (field-cooled) and ZFC (zero-field-cooled) at temperatures lower than T_f.

In 1975, Edwards and Anderson proposed a statistical method based on mean-field theory to study the disordered spin system. The Hamiltonian is given by [47]:

$$\mathcal{H} = -\sum_{ij} J_{ij} S_i S_j - g\mu_B \sum_i S_i, \tag{50}$$

where S_i and S_j are the Ising-like spin variables for nearest neighboring pairs (i, j) and J_{ij} is the random interaction factor of the spin pair (i, j) which has a Gaussian distribution:

$$P(J_{ij}) \propto exp\left[-\frac{(J_{ij}-J_0)}{2\Delta J^2}\right], \tag{51}$$

where the mean J_0 is smaller than ΔJ. The couplings between the spin pair (i, j) are ferromagnetic if $J_{ij} > 0$, and are antiferromagnetic if $J_{ij} < 0$ [37]. The time correlated spin distribution function at temperatures lower than T_f can be written as:

$$q_{EA} = \lim_{t\to\infty}[\langle S_i(t)S_i(0)\rangle_T]_{av}, \tag{52}$$

where $\langle ... \rangle_T$ is the statistical average of a given set of interactions and $[...]_{av}$ is an average over the distribution of interactions (= configurational average) [47]. This time correlation makes spin glass different from the paramagnetic materials and gives spin glass a "memory" effect. A partition function Z is introduced to calculate the free energy [48]:

$$[F] = -T[lnZ] = -T\int \prod_{ij} dJ_{ij} P(J_{ij}) lnZ. \tag{53}$$

In the thermodynamic limit where an infinite number of atoms are considered, the free energy per degree of freedom $f(\boldsymbol{J}) = F(\boldsymbol{J})/N$ can be treated the same as its mean value $[f]$. This is the so-called self-averaging property of the free energy. Comparing with the calculation of the configurational average $[lnZ]$, the value of $[Z^n]$ can be obtained with ease. One can prepare n replicas of the original system, and $[lnZ]$ can be calculated with the relation [48]:

$$[lnZ] = \lim_{n\to 0}\frac{[Z^n-1]}{n}. \tag{54}$$

This technique is the so-called replica method. Since the analytical solution of EA-Ising model is not conclusive, numerical simulations using Monte Carlo methods are used to evaluate the

validity of this model and reach fairly good agreement with the experimental data is obtained [49].

1.2.8.3 The SK (Sherrington-Kirkpatrick) model

The SK model extends the EA model in the infinite-range limit. The Hamiltonian can be written as [50]:

$$\mathcal{H} = -\sum_{i<j} J_{ij} S_i S_j - h \sum_i S_i, \tag{55}$$

Similarly, the Gaussian distribution function of the interaction has the form [50]:

$$P(J_{ij}) \propto \frac{1}{J} exp\left[-\frac{N}{2J^2}\left(J_{ij} - \frac{J_0}{N}\right)^2\right]. \tag{56}$$

The normalization can be done by letting [50]:

$$[J_{ij}]_{av} = \frac{J_0}{N}, \ [(\Delta J_{ij})^2]_{av} = \frac{J^2}{N}. \tag{57}$$

The original solution by using the replica method of the SK model shows that the low-temperature phase is characterized by a single order parameter q_{SK} [51]:

$$q_{SK} = [\langle S_i \rangle_T^2]_{av}, \tag{58}$$

where $q_{SK} \propto 1 - T/T_f$, $q_{SK}(T)$ vanishes at the finite temperature T_f, and is unity at T=0. The phase transition at T_f is given by [51]:

$$\chi(T) = \frac{C}{T}(1 - q_{SK}). \tag{59}$$

The solution was shown later on by de Almeida and Thouless (AT) to be unstable down a line in the H-T plane terminating at T=T_f for H=0, and varying for small field as [51]:

$$\frac{\delta T_f(H)}{f} = \left(\frac{3}{4}\right)^{\frac{1}{3}} \left(\frac{H}{f}\right)^{2/3}, \tag{60}$$

with $\delta T_f = T_f(H-0) - T_f(H)$.

1.2.8.4 Other models and claims

The AT instability represents an essential physics of spin-glass. A correction was made by Parisi in 1979 with a whole-order-parameter function $q(x)$ (equation (58)) in the range $0 \leq x \leq 1$ below the AT line. This model predicts that $q(x)$ has many minima at temperatures below T_f with a result derived from numerical simulation without meaningful explanation [51]. With the other two approaches, the characteristics of the phase below the AT line in the SK model were clarified. The first approach is the combination of the replica method and the self-similar replica symmetry breaking proposed by De Dominicis in 1983. For the second approach, the $q(x)$ is given by a dynamical formulation where the parameter x is related to a set of time scales [51]. The TAP (Thouless, Anderson, and Palmer) model shows that the magnetization of spin-glasses has many minima (solutions) in the phase space for a particular set of J_{ij}. In the thermodynamic limit $N \to \infty$, the minima are stable at finite temperatures in which they are separated from each other by an energy barrier the height of which diverges [51].

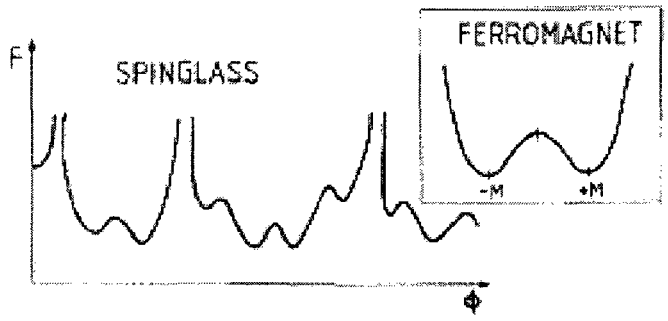

Figure 20. The schematic plot of the free energy F of a spin glass as a function of a phase-space coordinate ϕ which measures the projection of the considered state on a particular ordered state. The inset shows the situation in an Ising ferromagnet for comparison [51].

The distribution function $q(x)$ is static and can be estimated by the average from equilibrium statistical mechanics without the magnetic field [52]:

$$q_{EA} = \lim_{t\to\infty} \lim_{N\to\infty} q(t), \tag{61}$$

and

$$q = \lim_{\bar{H}\to 0} \lim_{N\to\infty} \lim_{t\to\infty} q(t). \tag{62}$$

The time dependent autocorrelation function is given [52]:

$$q(t) = [\langle S_i(0)S_i(t)\rangle_{t'}]_{av}, \tag{63}$$

where the time average $\langle ... \rangle_{t'}$ is performed over the observation time. It can be seen that the presence of a magnetic field breaks the spin reversal symmetry. The spectrum of relaxation time $\tau(x)$ is a function of x. The distribution function $q(x)$ reaches two extremes, in the shortest time limit where x=1 and in the longest time limit where x=0 as:

$$q(x) = \begin{cases} q_{EA} & x = 1 \\ q & x = 0 \end{cases}. \tag{64}$$

The SK model is non-ergodic below $T_f(H)$ and $q(x)$ is close to time independent in the thermodynamic limit $N\rightarrow\infty$. The Monte Carlo simulation gives [52]:

$$\begin{aligned} 1-q_{EA}(T) &\propto T^2 \\ \tilde{\chi}(T) = \frac{C}{T}(1-q_{EA}) &\propto T \end{aligned} \quad for\, T \ll T_f. \tag{65}$$

In the range $T>T_f$, one has:

$$\begin{aligned} 1-q(T) &\propto T \\ \chi_{eq}(T) = \frac{C}{T}(1-q) &= const \end{aligned} \tag{66}$$

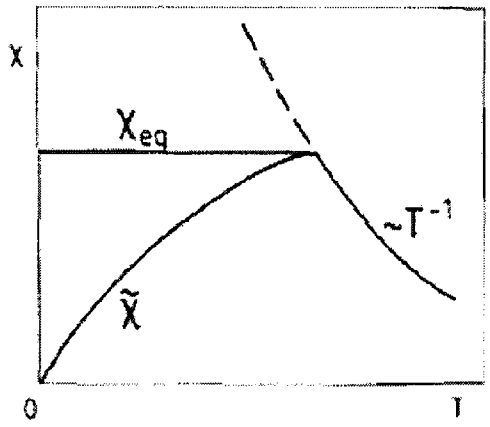

Figure 21. The predicted susceptibility by equation (65) and (66) *vs.* temperature by SK model with infinite-range interactions [52].

The Parisi order parameter function $q(x)$ is related to overlap functions between different minima with $0\leq x\leq 1$ [52]:

$$q_{12} = \frac{1}{N}\sum_i \langle S_i^1\rangle\langle S_i^2\rangle. \tag{67}$$

The distribution function $P(q)$ is the derivative of the inverse function $x(q)$. One can find that there are restrictions on the values the overlaps can take. The physics origin of these restrictions is the ultrametric space which arises from a hierarchical structure of multi-minima in phase space.

1.2.8.5 ZFC and FC

The magnetic histories can be seen from the temperature dependent magnetic susceptibility curves in the ZFC (zero-field-cooled) and the FC (field-cooled) processes. The sample is cooled to the lowest temperature that is lower than T_f (low enough that satisfies the relation $T \ll T_f$) in zero applied magnetic field. Then, its magnetic moments are measured with the presence of a small field from the lowest temperature to a temperature above T_f. This is the ZFC procedure. The FC procedure is to measure the magnetic moments of the sample in a small external magnetic field as a function of temperature from below to above T_f. The ZFC procedure is irreversible while the FC procedure is reversible and time-dependent. The measured ZFC and FC curves of $Zn_{77}Fe_7Sc_{16}$ are shown in Figure 22.

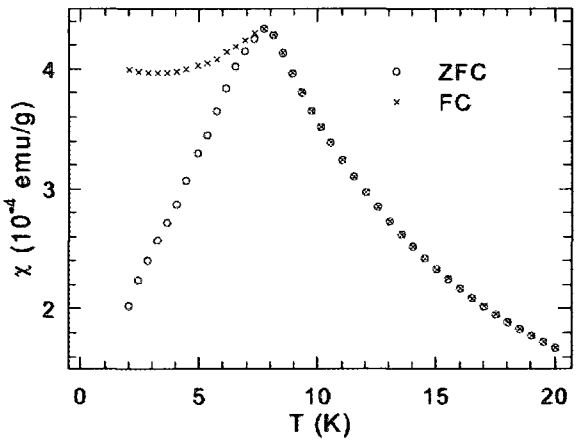

Figure 22. The measured ZFC and FC curves with an applied magnetic field 50 Oe.

1.2.8.6 IRM and TRM

Two types of remnant magnetization which depend on the magnetic history can be observed with the presence of a small magnetic field, the TRM (thermoremnant magnetization) and the IRM (isothermal remnant magnetization). The TRM is measured in the following manner. The sample is quickly cooled in a magnetic field from a temperature above T_f to a temperature $T \ll T_f$ and is kept in the field for a certain waiting time t, and then, the field is removed. The measured magnetization decreases as a function of time. For an IRM measurement, the sample is cooled in a zero field to a temperature below T_f, then, the field is turned on. After keeping the sample in the field for a certain waiting time t, the field is removed. The magnetization is measured as a function of time. For small fields, one has $IRM(H, T)<TRM(H, T)$. For large fields, both *IRM* and *TRM* saturate to the same value M_{rs}. This is illustrated in Figure 23 [53].

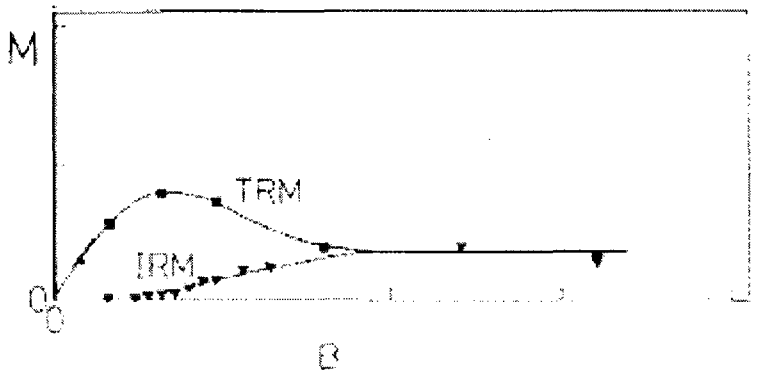

Figure 23. The schematic magnetization of IRM and TRM vs magnetic field [53].

The "spin clouds" model proposed by Tholence and Tournier in 1974 shows good agreement with the experimental data of spin glass and is given by:

$$\frac{\partial M_r}{\partial \ln(t)} = \frac{1}{\ln(t) - \ln(\tau_0)} \cdot T \cdot \frac{\partial M_r}{\partial T}, \tag{68}$$

where τ_0 is some intrinsic time constant and M_r is the remnant magnetization [54]. The aging effects can be clearly seen in Figure 24.

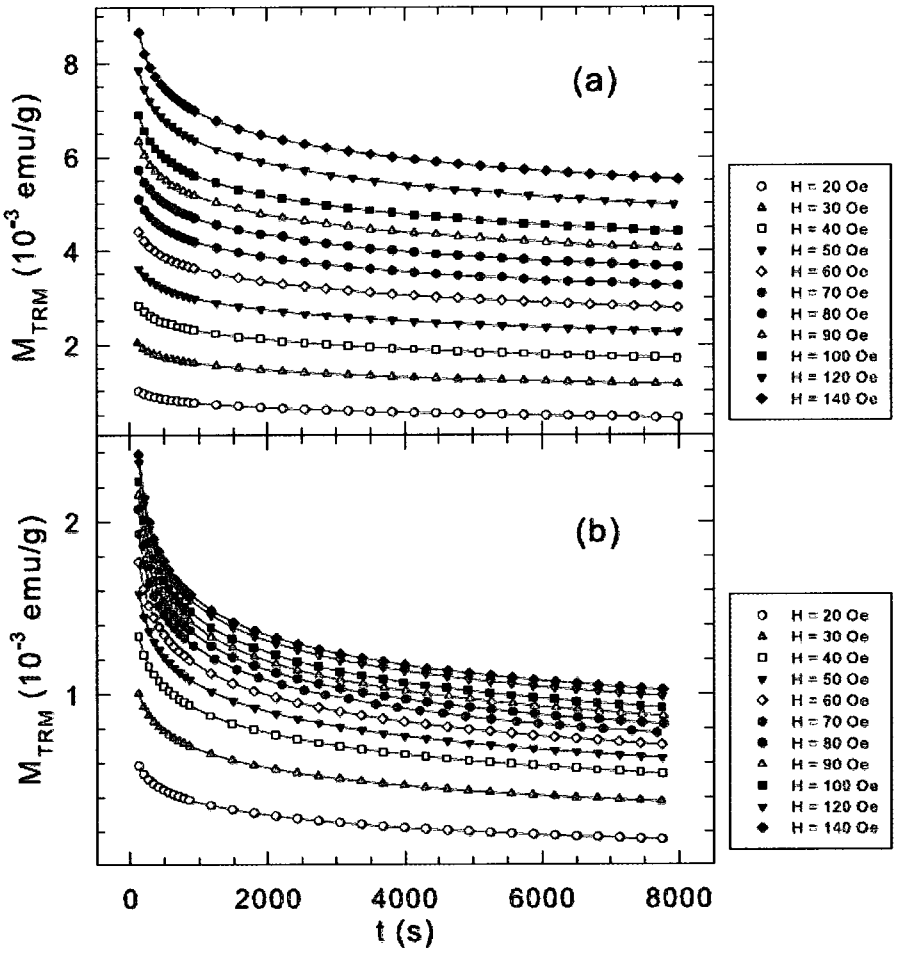

Figure 24. The TRM measurement of $Zn_{77}Fe_7Sc_{16}$.

Although some agreement between the proposed models and the experimental results can be obtained, the physical basis of TRM and IRM are still controversial.

1.3 Mössbauer spectroscopy

1.3.1 Introduction

The scientific name of Mössbauer spectroscopy is recoil-free nuclear resonance absorption. The γ-ray is used in obtaining a Mössbauer spectrum. This measuring technique is highly sensitive to energy changes of the order of 10^{-8} eV and has extreme sharpness of tuning [55].

1.3.2 Recoil-free nuclear resonance absorption

The γ-ray emission and absorption processes can be described with energy and momentum conservation laws. The atom will gain a recoil energy E_R by emitting a γ-ray with E_γ for a given energy difference E_0 between two energy levels of this atom. In accordance with the energy conservation law, the sum of E_R and E_γ is equal to E_0, $E_0 = E_R + E_\gamma$. In accordance with the momentum conservation law, the absolute value of the recoil momentum and the emitted γ-ray momentum are equal, whereas their propagation directions are anti-parallel. The energy of the γ-ray emitted from a moving atom is shifted by: $E_D = vE_\gamma/c$ [56], where v is the velocity of the atom along the γ-ray propagation direction and c is the speed of light. Taking the energy conservation law and the Doppler Effect into account, the energy relationship of the emission processes can be written as: $E_\gamma = E_0 - E_R + E_D$ [56]. By using the ideal gas model, and considering that the movement of the atoms is isotropic, the mean kinetic translational energy per degree of freedom of an atom is: $E_k = \frac{1}{2}k_B T = \frac{M}{2\overline{v^2}}$, where k_B is the Boltzmann constant and $\overline{v^2}$ is the mean square velocity in the propagation direction of the γ-ray. Therefore the Doppler broadening caused by the thermal energy E_k can be estimated as: $D_T \approx 2\sqrt{E_k E_R}$. The absorption processes are similar to the emission ones: $E_\gamma = E_0 + E_R - E_D$ [56]. The phenomena of resonance between the

emission and the absorption may occur when the γ-rays involved in both processes have the same frequencies. In a solid, the atoms can be treated as solid balls located at joints in a 3D lattice and represented by springs connecting their nearest neighbors. In quantum mechanics, the lattice vibration energy is quantized. By replacing the average energy in classical theory by the quantized energy E_t which is described by phonons, one can write: $E_t = h\nu_E\left(n+\frac{1}{2}\right) = \hbar\omega_E\left(n+\frac{1}{2}\right)$ [57], where n is the quantum number, h is the Planck's constant, ν_E and ω_E are the frequency and the angular frequency of a simple Einstein model, respectively. If the recoil energy E_R introduced by the emission or absorption of a γ-ray is smaller than $h\nu_E$, the energy difference between two neighboring quantized energy levels, there will be no phonons excited in the lattice. Thus the recoil energy of single-phonon processes can be estimated by introducing a recoil-free fraction f, and the recoil energy can be estimated as: $E_R = (1-f)\hbar\omega_E$ [58].

The Debye model is more suitable than the Einstein model in describing the energy distribution of a solid at low temperatures. It is convenient to define a Debye temperature θ_D for the description of vibrational states of the solid: $h\nu_D = k_B\theta_D$, where the energy of an oscillator can be described by phonons with a Debye frequency ν_D. The recoil-free fraction in the Debye model can be evaluated as:

$$f = exp\left(-\frac{3E_R}{2k_B\theta_D}\right); T \ll \theta_D, \tag{69}$$

$$f = exp\left(-\frac{6E_RT}{2k_B\theta_D^2}\right); T > \theta_D, \tag{70}$$

where the f is also known as Debye-Waller factor [58].

The uncertainty in time of the γ-ray emission and absorption processes can be best described by Heisenberg's uncertainty principle:

$$\Delta E \cdot \Delta t \geq \hbar. \tag{71}$$

The energy distribution of the transition has the Lorentzian or Breit-Wigner form [59]. The energy uncertainty of the ground state is zero if its lifetime is infinite. Based on the uncertainty principle, the mean lifetime τ of the excited state governs the width of the energy uncertainty: $\Gamma\tau = \hbar$, where Γ is the full width at the half maximum of the transition spectral line. The intensity as a function of transition energy can be written as [59]:

$$I(E) \sim \frac{\Gamma/2\pi}{(E-E_0)^2+(\Gamma/2)^2}, \tag{72}$$

where E_0 is the energy of the ground state.

1.3.3 Hyperfine interactions

As discussed in the previous sections, the resolution of the Mössbauer spectrum is mainly limited by the natural line width governed by the uncertainty principle, and it makes the studies of electron- and spin-density distributions possible. There are three main hyperfine interactions corresponding to the nuclear moments determining the nuclear levels [60]: the isomer shift (electric monopole interaction), the nuclear Zeeman effect (magnetic dipole interaction), and the quadrupole splitting (electric quadrupole interaction) [60].

1.3.3.1 Isomer shift

The isomer shift arises from the electric monopole interaction of the nuclear-charge distribution over a non-zero volume of the nucleus in the exited and ground states and the electron charge density due to the s-electrons within the nucleus. This Coulomb interaction

varies the nuclear energy levels of the source and the absorber and results in a shift δ which can be estimated as [60]:

$$\delta = C\frac{\delta R}{R}(|\psi_A(0)|^2 - |\psi_S(0)|^2)\,, \tag{73}$$

where C is a constant, R is the radius of the nucleus, δR is the radius difference between the excited states and the ground states of the nuceus, and the term in the parenthesis gives the estimated electron density difference at the nucleus between absorber and source isotopes.

The Mössbauer spectrum is related to both source spectrum and the absorber spectrum by Doppler motion, and gives a relative result. In order to determine the actual isomer shift, either the source spectrum or the absorber spectrum has to be fixed in advance. One effective solution is to use a standard reference. In most cases, the reference is a standard absorber.

1.3.3.2 Nuclear Zeeman effect

The interaction between a static magnetic field and the nuclear magnetic dipole can result in a splitting of the nuclear states. Consider that the spin of the nuclear state of the nuclear magnetic dipole is I without the presence of the external magnetic field and that the magnetic moment of such a dipole is μ, the spin will split into ($2I$+1) sublevels with the eigenvalues [61]:

$$E_m = -\frac{\mu H m_I}{I} = -g_N\beta_N H m_I, \tag{74}$$

where m_I is the magnetic quantum number with the values I, I-1, ...-I, g_N is the nuclear Landé splitting factor, and β_N is the nuclear Bohr magneton.

The direction of the external magnetic field can change the nuclear Zeeman pattern. Assuming the angle between the direction of the applied magnetic field and the γ-ray

propagation direction is θ_m, the angular dependence of the hyperfine interaction of Fe^{57} can be seen in Table 5, Figure 25 and Figure 26.

Table 5. The angular dependence of the allowed transitions in a pure nuclear Zeeman pattern of Fe^{57}, where θ_m indicates the angle between the direction of the magnetic field at the nucleus and the propagation direction of the γ-ray [62].

Transition	Δm	Angular dependence
$\pm 3/2 \rightarrow \pm 1/2$	± 1	$\frac{3}{4}(1+\cos^2\theta_m)$
$\pm 1/2 \rightarrow \pm 1/2$	0	$\sin^2\theta_m$
$\mp 1/2 \rightarrow \pm 1/2$	∓ 1	$\frac{1}{4}(1+\cos^2\theta_m)$

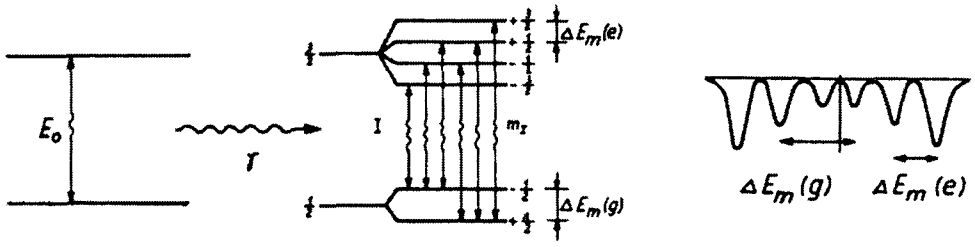

Figure 25. The energy level transitions and the absorption pattern of a pure nuclear Zeeman effect of ^{57}Fe [63].

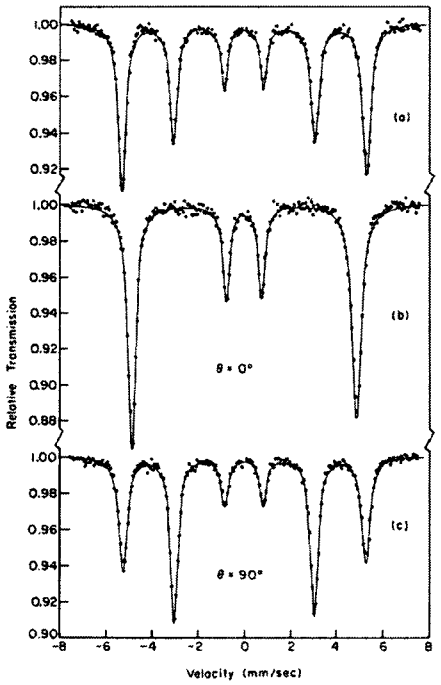

Figure 26. The Mössbauer transmission spectra of α-Fe at room temperature: a) H_{exl}=0, b) H_{exl}=50kOe, $\theta_m = 0°$, and c) H_{exl}=3.5kOe, $\theta_m = 90°$ [64].

The magnetic hyperfine interaction is of advantage to study the magnetic properties of materials, especially for those samples whose lattice sites exhibit their own hyperfine pattern. The influence of impurities in specific environments to the concerned isotopes can be investigated.

1.3.3.3 Quadrupole splitting

If the nuclear charge distribution deviates from a spherical symmetry, the electric quadrupole moment eQ is nonzero and the electric quadrupole interaction will occur with the presence of a nonzero EFG (electric field gradient). The electric quadrupole moment can be expressed by a tensor:

$$Q_{ij} = \int \rho_n(r)\,(x_i x_j - \delta_{ij} r^2) d\tau, \tag{75}$$

where ρ_n is the nuclear charge, x_i and x_j are Cartesian coordinates of r, and δ_{ij} is the Kronecker symbol [65]. The cylindrical symmetry of the electric quadrupole moment can be described with x_i and x_j, which are the coordinates in the principle axes system, and z, which is chosen as the preferred orientation. The sign of the electric quadrupole moment Q indicates the shape of the nucleus: positive for an elongated nuclear and negative for a flattened one. If the nuclear state spin quantum number I>1/2 (otherwise, the shape of the nuclear charge distribution is spherical).

The EFG caused by the electric charge distribution at nucleus is given by:

$$EFG = \vec{\nabla}\vec{\mathrm{E}} = -\vec{\nabla}\vec{\nabla}\mathrm{V} = \begin{bmatrix} \mathrm{V_{xx}} & \mathrm{V_{xy}} & \mathrm{V_{xz}} \\ \mathrm{V_{yx}} & \mathrm{V_{yy}} & \mathrm{V_{yz}} \\ \mathrm{V_{zx}} & \mathrm{V_{zy}} & \mathrm{V_{zz}} \end{bmatrix}, \tag{76}$$

If the symmetry of the electric quadrupole moment assumed above holds, only five components of the tensor are non-zero. By making $|V_{zz}| \geq |V_{xx}| \geq |V_{yy}|$, the EFG can be determined by two independent parameters: V_{zz} and η, where $\eta = \frac{V_{xx} - V_{yy}}{V_{zz}}$ is the symmetry parameter, and its value range is $0 \leq \eta \leq 1$. The physical origins of the EFG are: the lattice contribution which are caused by the charges on distant ions surrounding the Mössbauer atom in a non-cubic symmetry and the valence electron contribution which is due to the anisotropic electron distribution in the valence shell of the Mössbauer atom [66].

Working out the first-order perturbation matrix, one finds that the eigenvalues $\mathrm{E_Q}$ of the quadrupole splitting can be expressed as:

$$E_Q = \frac{eQV_{zz}}{4I(2I-1)}[3m_I^2 - I(I+1)](1+\eta^2/3)^2, \tag{77}$$

where m_I=I, I-1, …, -I is the nuclear magnetic spin quantum number [66].

The schematic Mössbauer spectrum and energy level diagram with allowed transition of Fe^{57} of the pure electric quadrupole splitting can be found in Figure 27.

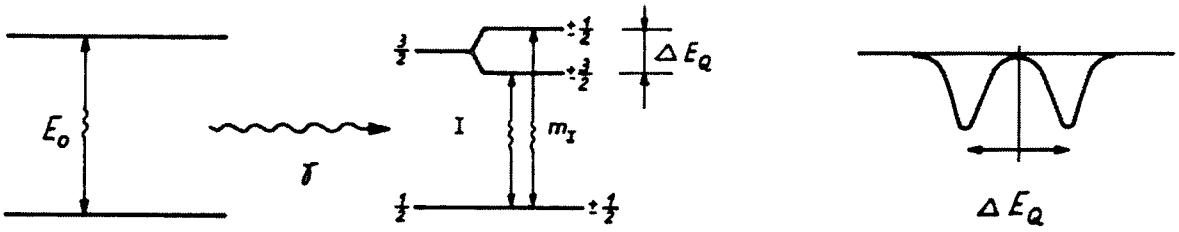

Figure 27. The pure quadrupole splitting in ^{57}Fe with I=3/2 in the excited state and I=1/2 in the ground state [63].

1.3.3.4 Combined hyperfine interaction Mössbauer spectrum

All three types of hyperfine interactions might occur in combination. The Fe^{57} Mössbauer spectra which contain the combine hyperfine interactions are given in Figure 28.

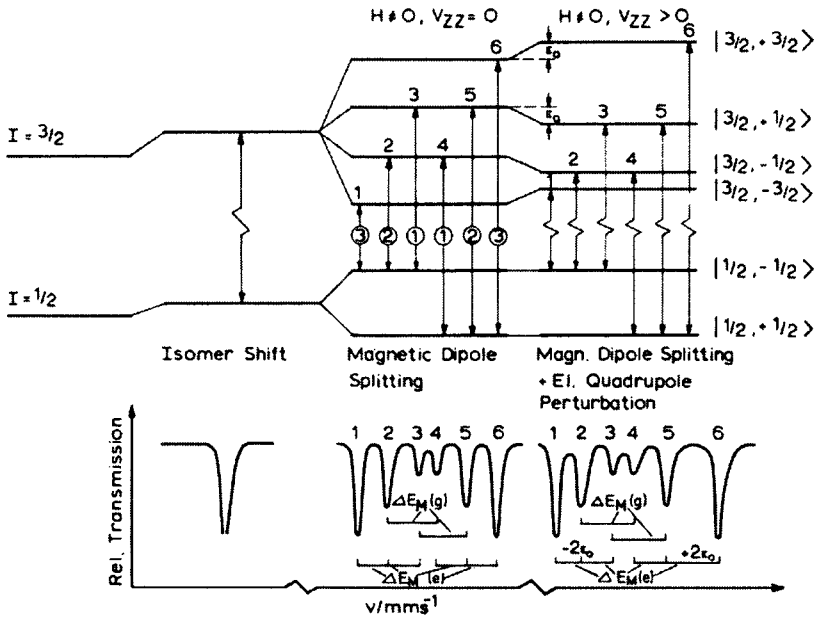

Figure 28. The combined ^{57}Fe Mössbauer spectra in a small applied magnetic field [66].

It is hard to distinguish different hyperfine interactions solely based on the raw Mössbauer spectra. However, one can retrieve the useful information by comparing the raw spectra with the well known standard spectra.

1.4 Electrical resistivity of disordered alloys

1.4.1 Classic and/or semi-classic approaches

The first successful classic or semi-classic approach in interpreting the electric resistivity is Ziman theory in the weak scattering limit. The assumptions made in this model fail to explain the high resistivity caused by strong scattering in the electrically disordered alloys. These assumptions are that: the mean free path of the electrons is longer than the average atomic distance, the transition probability is estimated by the Born approximation, multiple scattering is ignored, and the scattering processes are treated as elastic.

The Mott relation tried to explain the relative high resistivity found in amorphous alloys and quasicrystalline alloys by classifying the mobile electrons into two groups, s-electrons and d-electrons. The s-electrons possess higher mobility and act as the main electric carriers due to the fact that their energy levels are higher than the Fermi level. On the contrary, the d-electrons are confined to the local atom sites and their vacancies might trap the s-electrons, so that the number of electric carriers is reduced.

The theories that contain the classic concepts present fairly good agreement with the experimental results at high temperatures. However, at low temperatures, one has to take the quantum interference effects into account. The most widely accepted quantum models are: weak localization and enhanced electron-electron interaction.

1.4.2 Quantum approaches

1.4.2.1 Weak localization and spin-orbit scattering

The motions of the conduction electrons in the electrically disordered alloys can be described as waves where interference is possible. The result of the interference depends on the phase difference between the interfering waves.

Consider the phase change of a single wave. If a wave with wavelength λ moves a distance dq along its direction of propagation, its phase change is $2\pi dq/\lambda$. The wave number of such wave is $k = 2\pi/\lambda$. Therefore, the phase change can be re-written as kdq. Furthermore, it is convenient to use the momentum of the electron to express the phase change. From the de Broglie relation $\vec{p} = \hbar\vec{k}$, one can write the phase change as $\vec{p} \cdot d\vec{q}/\hbar$ in vector form.

If a quantum particle travels between two points, there are many possible paths between these two points. Since the phase difference is very sensitive to the length difference of the path, most phase changes tend to cancel each other. Only for those paths with an infinitesimal length difference, will the wavefunctions be in phase and reinforce each other.

When the magnetic field is applied, the electrons which execute an arbitrary closed path experience a phase change $\int \vec{B} d\vec{S}$, where $\vec{B}$ is the magnetic field and $d\vec{S}$ is an element of area and the integral is over any surface bounded by the closed path.

In 1959, Aharonov and Bohm claimed that if a charged particle encircled a region of magnetic field, it would suffer a change of phase in proportion to the magnetic flux enclosed by the path even though the particle never itself entered the magnetic field [67]. This effect is called the Aharonov-Bohm effect. It was verified by D.Yu. Sharvin and Yu.V. Sharvin in 1981 [67]. A

magnetic field is placed and confined inside a thin-walled cylinder made of lithium metal. Its direction is parallel to the axis of the cylinder. Then the resistance is measured between the two ends of the cylinder at low temperatures. The experimental diagram is shown in Figure 29. The resistance oscillates with a period of $\hbar/2e$ when the magnetic flux increases. The resistance *vs.* magnetic field curve is shown in Figure 30 [67].

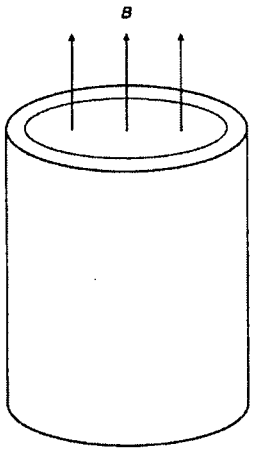

Figure 29. Thin-walled cylinder with magnetic flux confined within the inner wall [67].

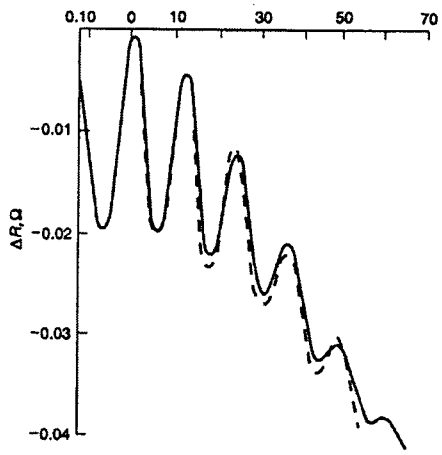

Figure 30. Change in resistance of thin-walled cylinder vs magnetic field showing its periodic variation with the flux [67].

The scattering processes are only elastic at low temperatures maintaining phase coherence. When the electrons execute closed loops without inelastic scattering, they interfere with each other. Figure 31 illustrates two different paths, clockwise and anticlockwise, of the electron trajectories.

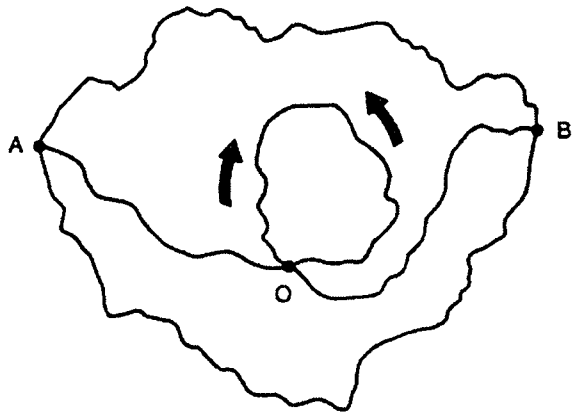

Figure 31. Possible electron paths including a closed path in which an electron returns to its starting point. In the closed path there are two paths of equal length corresponding to the two senses in which the path can be traversed. There are indicated by the arrows [67].

In order to calculate the weak localization effects, one has to calculate the probability of an electron leaving and returning to the original point in an enclosed path. The expression of the probability can be written as [67]

$$P = |\psi_1|^2 + |\psi_2|^2 + \psi_1^* \psi_2 + \psi_1 \psi_2^*, \tag{78}$$

where ψ_1 is the wavefunction of the anticlockwise path and ψ_2 is the wavefunction of the clockwise path. The first two terms are just classical probabilities, whereas the last two are not. Generally, the phase differences between ψ_1 and ψ_2 are random. The effect of the interference

terms average to zero when summed over all possible paths. In this case, the value of P is the same as the classical probability. In the case that the two paths are of identical length and experience identical scattering events, although encountered in the reversed sequence, ψ_1 and ψ_2 are completely in phase. Thus all four terms on the right-hand side of equation (78) have the same value. Compared the classical result, the value of P is doubled.

The applied magnetic field inside the cylinder introduces a phase change $e\Delta\phi/\hbar$ of the wavefunction for each electron that executes the closed loop, where $\Delta\phi$ is the change in magnetic flux. Consider the two electrons execute the loop in the opposite sense. The phase difference between the two wavefunctions of the electrons is $2e\Delta\phi/\hbar$ and varies periodically as the magnetic field increases. When the two electrons are completely out of phase, the coherence of the interference between them is destroyed. Thus the enhanced resistivity due to quantum interference also vanishes. In this case, the resistivity just takes the value predicted by the classical theories. The enhanced resistivity reaches its maximum value when the two electrons are in phase. The increased part of the resistivity proves the quantum interference effects predicted by Aharonov and Bohm.

The effect discussed above is called "weak localization". As mentioned above, the enhanced scattering due to weak localization only happens at low temperatures when inelastic scattering is ignored. When the temperature increases, more and more phonons are excited and the inelastic scattering becomes more and more dominant. Since the inelastic scattering tends to destroy the coherence of the wavefunction of some of the electrons that are participating in the enhanced scattering, the quantum interference enhanced resistivity also reduces. If the temperature keeps going up, the resistivity will increases with the number of thermally excited phonons after it

reaches a minimum value. Thus the resistivity minimum is formed. This explains why the TCR of amorphous alloys is negative at low temperatures and the resistivity is relatively high.

The electrons are randomly scattered in an alloy. The probability that an electron returns to its starting point can be calculated based on classical diffusion theory. In a three-dimensional disordered system, an initial state of an electron is defined as being located at the origin at $t = 0$. At time $t >> \tau$, where τ is the elastic scattering time, the electron diffuses into a volume $V_D \approx (Dt)^{3/2}$, where D is the diffusion constant. Assuming that an electron with a wavelength λ travels at a speed v_F, it sweeps out a tube of $\lambda_F^2 v_F dt$ in a time interval dt. The probability that an electron returns to its starting point is then [67]

$$p(t)dt \approx \lambda_F^2 v_F dt/(4\pi Dt)^{3/2}. \tag{79}$$

The coherence of the electron wavefunction will be destroyed beyond the inelastic scattering time τ_{ie}. In order to find the total probability that the electron returns to its original point, one has to integrate equation (79) from the mean free time τ of the elastic scattering to τ_{ie} [67]

$$\int_{\tau}^{\tau_{ie}} p(t)dt \approx \lambda_F^2 v_F[(\tau)^{-1/2} - (\tau_{ie})^{-1/2}]/(4\pi D)^{3/2}. \tag{80}$$

The Einstein relation is

$$\sigma = e^2 DN(E_F), \tag{81}$$

where $N(E_F)$ is the electron density of states at the Fermi level. Combining equation (80) and (81), one has the expression

$$\frac{\Delta D}{D} = \frac{\Delta\sigma}{\sigma} = -\frac{\Delta\rho}{\rho} = -\lambda_F^2 v_F[(\tau)^{-1/2} - (\tau_{ie})^{-1/2}]/(4\pi D)^{3/2}. \tag{82}$$

Using the relation $D = v_F l/3$ and $\lambda_F = 2\pi/k_F$, equation (82) can be written as [67]

by the inelastic scattering time.

So far, the elastic and inelastic scattering contributions were taken into account. If the system contains heavy elements, spin-orbit scattering has to be incorporated. The two electrons that propagate in opposite directions around the closed loop may have the same or opposite spin directions. If the two partial waves have the same spin directions, the probability that the two electrons recombine after counter-propagation is enhanced above the classical value. If the spin directions are opposite, the recombination of the two partial waves will reduce the classical probability.

Each electron in a pair has two possible opposite spin directions. Therefore, the two electrons can form four independent spin functions. The four states can be expressed as (↑↑), (↑↓), (↓↑), and (↓↓). The first three form the triplet combination, for which the total spin is $j = 1$. Their projections in the magnetic field direction are $m = +1, 0, -1$. The last term forms the singlet combination with $j = 0$ and $m = 0$. If the two partial waves have the opposite spin directions, there is only the singlet state. There are three such states where the two partial waves have the same spin directions. One assumes that there is no spin-orbit coupling involved in the scattering. The wavefunction is ψ_{00} for the singlet state and ψ_{11}, ψ_{10}, ψ_{0-1} for the triplet states. The interference term is given as [67]

$$I = (1/2)\{|\psi_{11}|^2 + |\psi_{10}{}^2| + |\psi_{1-1}|^2 - |\psi_{00}|^2\}. \tag{84}$$

When there are no spin-orbit effects, the absolute values of the four terms are the same. The interference term is equal to the classical value. If the strength of the spin-orbit interaction is very large, the triplet electron waves are out of phase. The interference among the electron waves is destroyed. Therefore the sum of the first three terms in equation (84) is zero. The singlet term will not be influenced since the angle between the spin and the velocity is the same at the corresponding scattering event for both waves. Then the total contribution from this effect is negative.

The strength of the spin-orbit interaction can be associated with the spin-orbit scattering time τ_{so}. The change of conductivity can be written as [67]

$$\Delta\sigma/\sigma \cong -\int_{\tau}^{\tau_{ie}} [\lambda^2 v_F dt / Dt^{3/2}]\{(3/2)\exp(-t/\tau_{so}) - 1/2\}. \tag{85}$$

When τ_{so} is long compared to τ_{ie}, as discussed above, the exponential part is unity throughout the integration. Then the effect of spin-orbit does not show up. If τ_{so} is short compared to τ_{ie}, the triplet terms decay exponentially. Only the contribution from the singlet term survives. The contribution of the quantum interference term is then negative.

The upper limit of τ_{so} is simply the inelastic scattering time. Beyond the limit, the inelastic scattering will destroy the coherence of the electrons. In this case, equation (85) will have the same form as equation (83). In the limit of $\tau_{so} << \tau_{ie}$, the whole integral in equation (86) results in a simple expression

$$\frac{\Delta\sigma}{\sigma} = \frac{1}{2} C(1 - \sqrt{\frac{\tau}{\tau_{ie}}}) / (k_F l)^2. \tag{86}$$

It can be seen from equation (86) that the strong spin-orbit interaction can change the sign of the weak localization contribution from positive to negative. Because the inelastic scattering time is temperature dependent, its value is getting smaller when the temperature increases. Thus the weak localization contribution to conductivity may also change from absolute zero to high temperatures.

The inelastic scattering time reflects the temperature dependence of conductivity of amorphous alloys. There are two major sources of the inelastic scattering, one is the electron-phonon processes, and the other one is electron-electron processes. Then the inelastic scattering time is given [67]

$$\frac{1}{\tau_{ie}} = \frac{1}{\tau_{e-e}} + \frac{1}{\tau_{e-p}}, \tag{87}$$

where $\tau_{e\text{-}e}$ is the electron-electron scattering time and $\tau_{e\text{-}e}$ is the electron-phonon scattering time. The electron-electron scattering time is given by [68]

$$\frac{1}{\tau_{e-e}} = \frac{\pi}{8}\frac{E^2}{E_F\hbar}[1 + \frac{4\sqrt{3}}{\pi}(\frac{1}{k_F l})^{3/2}(\frac{E_F}{E})^{1/2}], \tag{88}$$

where E is the energy of the electron which is of the order of k_BT. Equation (88) shows that when disorder is weak (k_Fl is large), $\tau_{e\text{-}e}$ varies as T^2, and for strong disorder (k_Fl is small), $\tau_{e\text{-}e}$ varies as $T^{3/2}$. The inelastic scattering time for electron-phonon processes can be evaluated as [69- 71]

$$\frac{1}{\tau_{e-p}} \propto T^2, \quad \text{for } T >> \frac{\hbar v_s}{l k_B} \tag{89}$$

$$\frac{1}{\tau_{e-p}} \propto T^4, \quad \text{for } T << \frac{\hbar v_s}{l k_B} \tag{90}$$

where v_s is the sound velocity.

The spin-orbit scattering tends to randomize the electron spin directions. When the conduction electron penetrates inside the core of an ion, there is an electrostatic coupling between its spin and its angular momentum. This coupling increases sharply with the nuclear charge. Thus the spin-orbit scattering is associated with heavy elements. The spin-orbit scattering time τ_{so} is believed to be temperature independent [72]. The overall electrical conductivity expression for the WL effects can be written as [67]

$$\Delta\sigma(T) = \frac{e^2}{2\pi^2\hbar}\frac{1}{\sqrt{D\tau_{so}}}\left(3\sqrt{1+\frac{\tau_{so}}{\tau_{io}}} - \sqrt{\frac{\tau_{so}}{\tau_{io}}} - 3\right). \tag{91}$$

Here τ_{io} can be used to calculate the inelastic scattering time $\tau_{ie} = \tau_{io}T^{-p}$. The constant 3 in equation (91) is usually added to keep $\Delta\sigma(T) = 0$ at $T = 0$.

The weak localization theory shows that the interference between incident and scattered waves in a closed loop can be important. The short mean free path of the conduction electrons is neglected in classical theories. This model proposes a reasonable explanation for the negative TCR at low temperatures and comparably high resistivity. The spin-orbit scattering is an additive effect on this quantum correction associated with heavy elements. The weak localization effect is believed to persist from low temperatures to room temperature.

1.4.2.2 Enhanced electron-electron interaction effect

Apart from the weak localization effect, another quantum effect arises from the interaction between one electron and another. This interaction effect is called the enhanced electron-electron interaction effect.

Equation $k'-k = \pm q$ holds for crystalline alloys. The plane wavefunctions are used to describe the motion of the electrons. In a disordered system, there is an uncertainty in k due to

scattering. The uncertainty is of order $1/l$, where l is the relevant mean free path. The quantum effects emerge when q, the scattering vector, is small. Under the condition $ql < 1$, a smaller mean free path is involved, for which classical theories fail. The enhanced electron-electron interaction effect will show up in the limit of a short mean free path. Since the mean free path of the electron in a disordered system is short, multiple scattering processes are unavoidable. The classical diffusion model can be used to describe this effect at large distances and time intervals. Diffusion motion also changes the strength of the interaction between electrons.

In order to calculate the contribution to the resistivity due to this effect, one can take the following steps. First, one has to find out the interaction forces between electrons. Second, perturbation theory can be used to calculate the interaction energy, which contains Hartree and exchange terms. Third, one should find out the contribution of each term.

Since the total negative charges of the electrons in an alloy equal the total positive charges of the ions, the medium is electrically neutral overall. According to Coulomb's law, the force between electrons is repulsive. When two electrons are a few inter-atomic spacing apart, the electrostatic force between them due to Coulomb interaction is very small. Together with the repulsive force between the electrons, the imperfect screening makes the electron-ion pseudopotential so weak that perturbation theory can be used in calculations. The pseudopotential can be written in terms of its Fourier transform. Using the Thomas-Fermi screening approximation, the pseudopotential takes the form [67]

$$V(q) = -\left[Ze^2 / \varepsilon_0 q^2 \right]\left[q^2 /(q^2 + \alpha^2)\right], \tag{92}$$

where Ze is the ionic charge, q is the scattering vector, and $\alpha^2 = N(E_0)Ze^2/\varepsilon_0$, where $N(E_0)$ is the density of states. In the limit of $q = 0$, $V(q) = -1/N(E_0)$. In this case, the charge of an ion is

perfectly screened. The pseudopotential is then independent of the ion. Figure 32 shows the potential in terms of Fourier transform. From the discussion above, the pseudopotential has negative value when $q \rightarrow 0$. This remarkable result shows that the force between electrons is attractive. The conductivity is enhanced due to this effect. This can be explained as follow. For Fermi electrons, $q = 2k_F sin\theta$. In the limit of $q \rightarrow 0$, the corresponding waves pass through the scattering centre without being deflected [67].

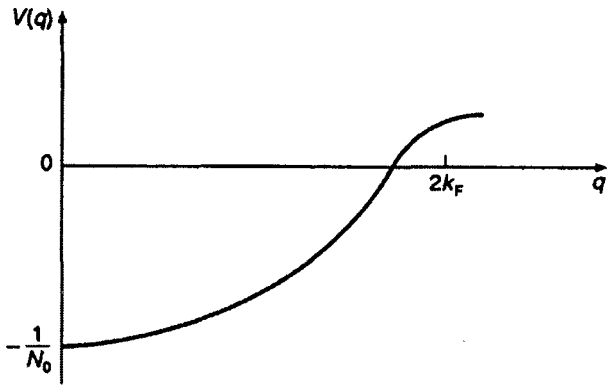

Figure 32. The main features of the Fourier transform of the pseudopotential (schematic).

The contribution of electron-electron interaction contains two sources. One is the diffusion channel and the other is the Cooper channel. The diffusion channel is a result of a direct interaction between an electron and a hole close to the Fermi level. The Cooper channel contribution describes the interaction between electrons and phonons. Each of the two contributions contains two terms: one is the Hartree term and the other is the exchange term. The Hartree term is the classical description of the interaction between electrons and the exchange term shows the quantum correction [67].

First order perturbation theory is used to quantize the interaction energy. Two electrons are defined: one is in a state of energy E at $\vec{r}$ and the other is in a state of energy E' at $\vec{r}'$. The spin states of the two electrons are taken into account. The spatial part of the wavefunction of a parallel spin pair of electrons can be written as [67]

$$\psi(\uparrow\uparrow) = \psi_E(\vec{r})\psi_{E'}(\vec{r}') - \psi_{E'}(\vec{r})\psi_E(\vec{r}'). \tag{93}$$

The spatial part of the wavefunction of an anti-parallel spin pair of electrons is zero due to Pauli Exclusion Principle. Using the first order perturbation theory, the interaction energy can be written as

$$E_{\text{int}}(\uparrow\uparrow) = (1/2)\iint[\psi^*(\uparrow\uparrow)V(\vec{r}-\vec{r}',t)\psi(\uparrow\uparrow)]d^3\vec{r}d^3\vec{r}', \tag{94}$$

where $d^3\vec{r}$ and $d^3\vec{r}'$ are the volume elements and $V(\vec{r}-\vec{r}',t)$ is the interaction energy. The integration is throughout the volume of the material. Substituting equation (93) into equation (94), one has two terms. The first one is called the Hartree term and is given as [67]

$$\iint\psi_E(\vec{r})\psi_E^*(\vec{r})V(\vec{r}-\vec{r}',t)\psi_{E'}(\vec{r}')\psi_{E'}^*(\vec{r}')d^3\vec{r}d^3\vec{r}'. \tag{95}$$

The second term is called exchange term and is expanded as

$$-\iint\psi_E(\vec{r}')\psi_{E'}^*(\vec{r}')V(\vec{r}-\vec{r}',t)\psi_E^*(\vec{r})\psi_{E'}(\vec{r})d^3\vec{r}d^3\vec{r}'. \tag{96}$$

The Hartree term can be interpreted as the classical interaction, whereas the exchange term is not. The exchange term, which is due to the quantum effect, arises from making the total wavefunction of the electron pairs antisymmetric.

For the diffusion channel, the exchange term makes important contributions to the density of states due to the strong energy dependence. By doing some simplifications, the change in density of states is given as [67]

$$\Delta N(\varepsilon) \propto N(0)V(0)\varepsilon^{1/2}/(\hbar D)^{3/2}. \tag{97}$$

It is clear from equation (96) that the density of states varies as $\varepsilon^{1/2}$. Using the Einstein relation (equation (81)) and the relation $\varepsilon = k_B T$, one can see that the conductivity varies as $T^{1/2}$. Figure 33 shows the density of states at the Fermi level due to the exchange contribution.

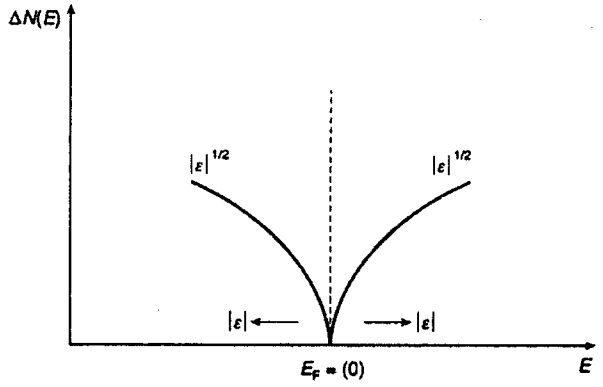

Figure 33. Minimum in the density of states at the Fermi level due to the interaction effect.

The Hartree terms in the diffusion channel show that the interference between electron-hole pairs can increase the mean free path of the electrons. The interference can be destroyed by the thermal incoherence and causes the conductivity to fall as $T^{1/2}$.

In the Cooper channel, the phonon mediated attraction between electrons alters the density of states. The sign of the contribution of this effect depends on the net interaction between electrons.

Similar to the weak localization, this diffusion process is destroyed by thermal incoherence rather than thermal inelastic scattering. The thermal coherence time τ_T can be evaluated as [73]

$$\tau_T \approx \hbar/(k_B T). \tag{98}$$

Combining all the effects, the total conductivity due to electron-electron interaction effects is given by [67]

$$\Delta\sigma(T) = 0.915\frac{e^2}{4\pi^2\hbar}\left(\frac{4}{3}-\frac{3}{2}\widetilde{F}_\sigma\right)\sqrt{\frac{k_BT}{\hbar D}}, \tag{99}$$

where the Coulomb interaction parameter $\tilde{F}_\sigma$ is [67]

$$\widetilde{F}_\sigma = -\frac{32}{3F}\left[1+\frac{3F}{4}-\left(1+\frac{F}{2}\right)^{3/2}\right]. \tag{100}$$

This parameter must be used in calculating the conductivity since the interaction between electron pairs is altered by the diffusive motion of the screening electrons [67].

The influence of spin-orbit coupling does not appear in the literature. The qualitative explanation is that the spin-orbit scattering destroys the phase relationship between electron pairs. The electrons in a pair execute the closed loop in the same sense but possess opposite spin direction. Only the Hartree term is altered by spin-orbit scattering. In the absence of spin-orbit scattering, both contributions vary as $T^{1/2}$ although with opposite sign.

1.4.2.3 The full expression of quantum interference effects

Combining equations (91) and (99), the overall electrical conductivity expression due to WL and EEI effects can be written as

$$\sigma = A0 + A1(3\sqrt{1+A2\times T^{A3}} - \sqrt{A2\times T^{A3}} - 3) + A4\sqrt{T}\,. \tag{101}$$

Here

$$A0 = \sigma(0), \tag{102}$$

$$A1 = \frac{e^2}{2\pi^2\hbar}\sqrt{\frac{1}{D\tau_{so}}}, \tag{103}$$

$$A2 = \frac{\tau_{so}}{4\tau_{io}}, \tag{104}$$

$$A3 = p, \tag{105}$$

$$A4 = \frac{e^2}{4\pi^2\hbar}\frac{1.3}{\sqrt{2}}\left(\frac{4}{3} - \frac{3}{2}\tilde{F}_\sigma\right)\sqrt{\frac{k_B}{\hbar}}\sqrt{\frac{1}{D}}, \tag{106}$$

where D is the diffusion constant, and τ_{so} is the elastic spin-orbit scattering relaxation time. The first term in equation (101) is the residual conductivity. The second term is due to the WL effects which contain spin-orbit scattering effect as well. The third term is due to the EEI contribution. Here the magnetic contribution is not included.

Chapter 2 Experimental details

2.1 Introduction

The experimental work carried out in this study consisted of two major steps: sample preparation and measurement of physical properties measurements. They are described in the following sections.

The first section describes sample preparation. In this section, the instruments (including customized and newly-constructed experimental setups) and sample-making techniques are described, followed by corresponding methodologies and other technical details. Based on the experimental results obtained, the improvements in sample preparation will be discussed.

The second section describes the measuring techniques and the instruments used in this study, i.e., the PANalytical® x-ray power diffractometer, a QD (Quantum Design®) MPMS® (Magnetic Property Measurement System) magnetometer, a Mössbauer spectrometer, and home-made resistivity measurement system. The analysis of the results is discussed at the end.

2.2 Sample preparation

One of the key factors in sample synthesis is temperature. The desired crystal structure can be formed for a given sample at certain temperatures and under certain conditions. One basic sample synthesis method is to make an ingot consisting of the right stoichiometric concentration of individual elements. This method is adequate for some samples, whereas other samples might require further treatment. For example, the Cu_2InGd sample was prepared in an arc furnace and cooled naturally to room temperature without further treatment [74], such as annealing. Each

element used to produce a given sample has a different melting temperature. It is important to ensure that the temperature in the heating zone of the furnace exceeds the highest melting point of the elements. At this temperature, all the elements will melt and mix to form an ingot.

2.2.1 Instrumentations

Different types of heat treatment instruments are used depending on the sample preparation requirements. In this section, the following instruments are described: arc-furnace, electric furnace, programmable electric furnace, induction furnace, levitation setup, and sample weighing instrument. The typical temperature range of the electric furnace is from room temperature to a maximum temperature of around 1700 °C. The best temperature accuracy can be achieved by using a thermocouple as the temperature sensor. Induction furnaces can reach temperatures above 3000 °C. The induction furnace can induce current in the thermocouple and cause inaccurate temperature reading, therefore the less accurate infrared pyrometer is chosen as the temperature sensor in the induction furnace to accomplish the negative-feedback temperature control. The temperature generated by an arc furnace can be as high as 3500 °C. The main use of an arc furnace is to melt samples and produce ingots. Therefore the precise temperature control is less important. A manually controlled pedal is used to regulate the feeding current to adjust the plasma temperature.

2.2.1.1 Arc furnace

Argon and helium are the noble gases usually used in the arc furnace because they seldom react with most of the known materials at room and high temperatures. The temperature of the plasma in the arc furnace can easily exceed 3500 °C (6332 °F) [75], which is higher than the melting temperature of tungsten (3410 °C) [76], the element with the highest melting point.

Normally, the melting point of the compound is lower than the highest melting point of the pure elements. Therefore, the arc-melting method is widely used for ingot making.

Another application of an arc furnace is to seal the metallic crucibles made of molybdenum, tantalum, and tungsten. The materials most often used to produce crucibles are alumina, silica, glassy carbon, molybdenum, tantalum, and tungsten [77]. These materials are relatively stable at high temperatures. It is important to verify that the crucible material does not react with any of the elements before making the sample. For example, a glassy carbon crucible reacts with silicon at high temperatures [78], therefore, it is not suitable for making samples containing silicon [78]. The crucibles used in this study are made of tantalum due to the fact that it can be easily formed into the desired shape using a regular lathe and milling machine and it can be easily melted to seal the sample in an argon gas environment with an arc furnace. The disadvantages of using tantalum are: it is sticky when machining, it reacts with oxygen at temperatures higher than 600 °C, and it becomes soft at temperatures higher than 1500 °C [76]. Howerver, tantalum is still the best crucible material available for use in this study.

The arc furnace used in this study was purchased from Centorr associates INC. Figure 34 shows the schematic structure of this furnace. It consists of upper and lower water-cooled sections separated by a transparent quartz observation tube. The quartz tube also serves as an insulator between the upper (negative polarity) section, and the lower (positive polarity) section. Electric power and water are fed to each of these sections by water-cooled power cables. A copper rod with a wooden handle crosses the top section via an insulator swivel ball which allows angular as well as vertical movement. A tungsten pin is attached to the end of the copper rod as the electrode. The bottom section contains a tapered opening which accepts different

copper hearths. Ports connected to the chamber are provided for inert gas inlet, outlet, and a rotary pump.

By opening the valve to the rotary pump, the air in the chamber can be evacuated. The high-purity argon gas is then filled into the chamber with a pressure higher than one atmosphere. By carefully adjusting the outlet valve, a steady argon gas flow can be formed in the chamber. The outgoing argon gas goes through a water bath to prevent external air from flowing back to the chamber. It is very important to keep the pressure inside the chamber higher than the ambient pressure. During the melting process, the pressure might be reduced. This is due to the fact that the arc flame might melt the elements with high vapor pressure first, such as indium, causing a higher pressure at this moment. Once the high vapor pressure element reacts with other element(s) to form a compound with much lower vapor pressure, the overall pressure in the chamber drops drastically. If the total pressure is lower than one atmosphere, water can be sucked into the chamber through the water bath port.

Once the elements are in place, the inert gas environment is ready, and the desired power is set, one can create an arc by touching the two tungsten pins on the copper rod and hearth. A titanium ball placed in the dent on the copper hearth is used to make uniform arc flame and remove any possible gas impurities from the furnace cavity. It is advisable to move the stinger around and over the elements in order to get a uniform and homogeneous melt. By repeating this procedures four to five times, excellent homogeneity of the ingot can be obtained.

Although arc melting is proven to be a clean and efficient sample making technique, there are still some problems. First, it is inevitable to lose a certain amount of the sample during the process, typically one to two percent. As mentioned above, when high-vapor-pressure

elements are melted, a small amount of these elements might escape from the sample as a vapor and deposit on the inner surface of the chamber. Second, the elements might react with the copper hearth during melting since the temperature inside the chamber could be as high as 3000 °C.

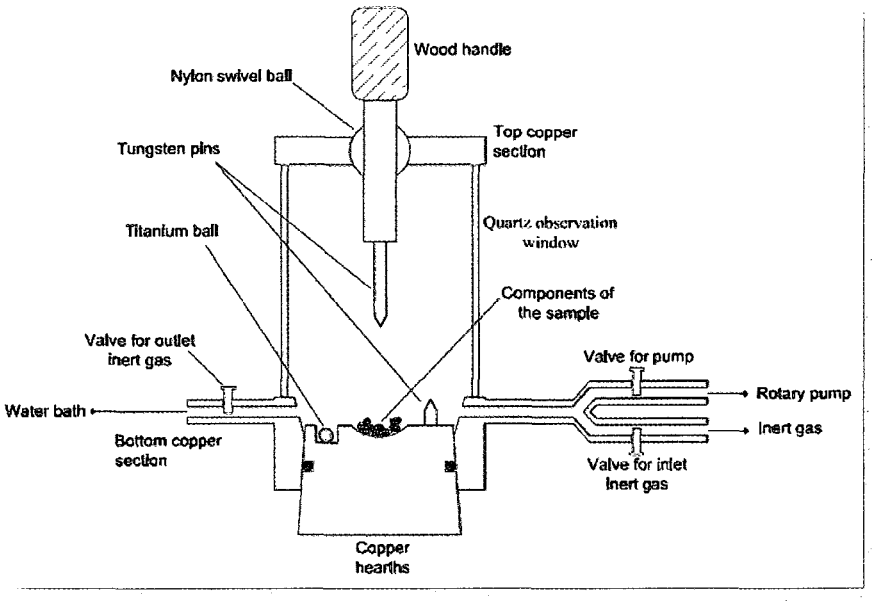

Figure 34. Schematic drawing of an arc furnace.

An improved sample making technique is proposed in this study. By sealing the elements in a tantalum crucible filled with argon gas, the sample loss can be reduced. Since it is physically and chemically stable at high temperatures, tantalum is suitable in making crucibles. Figure 35 shows a schematic drawing and the real image of a tantalum crucible.

Figure 35. The schematic drawing (left) and the picture (right) of a tantalum crucible.

The crucible consists of three parts: a tube, a plate-like bottom, and a cup-like lid. Arc furnace is used to join and seal the three parts. A modified water-cooled copper hearth used in this study is shown in Figure 36 (right). A removable copper block is used to clamp the tantalum tube with four stainless steel socket cap screws to ensure ideal thermal and electrical contact between the tantalum parts and the copper hearth.

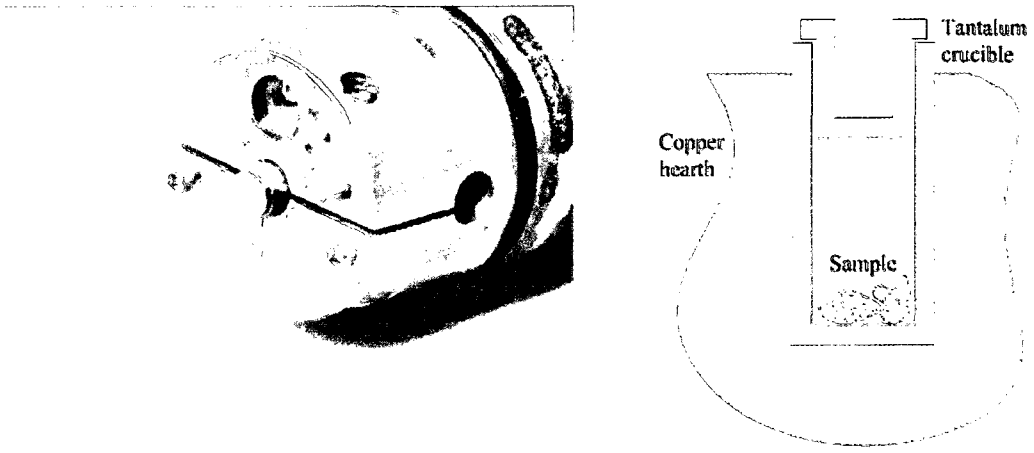

Figure 36. The modified copper hearth for sealing a tantalum crucible.

It takes two steps to make a sealed tantalum crucible. The first step is to seal the bottom of the Ta tube with the Ta plate. The detailed mounting method is shown in Figure 36 (left). The second step is to seal the sample in the tantalum crucible. The tantalum cup with elements in it is clamped by the copper hearth, as shown in Figure 36 (right). The bottom position of the lid is crucial. It should be kept below the surface level of the copper hearth as a radiation shield. Since the hearth is water cooled and made of copper, the heat generated during the sealing process can be easily taken away from the wall of the tantalum tube and the bottom of the lid without heating the elements in the crucible. The mechanical fitting between the lid and the tube leaves a gap in between. Therefore the air inside the tantalum crucible can be evacuated during the purging process and argon gas can be filled into the crucible during the inert gas flow setup procedure.

Compared to the direct arc melting method, the sealed tantalum crucible technique eliminates the sample loss completely. In addition, tantalum is more stable than copper at high temperatures, the sample can be heat treated in a cleaner environment.

Since tantalum reacts with oxygen at temperatures higher than 600 °C, the tantalum crucible cannot be heated in the air directly. One can create an inert gas or vacuum environment for the tantalum crucible. This increases the sample making cost and complexity dramatically. The simplest solution is to seal the tantalum crucible into an evacuated or an inert-gas filled quartz capsule. This method requires special skills, and is time consuming. Another alternative is to build an air sealed furnace. It is easy to maintain and operate once it is set up despite the relatively high initial cost and complexity.

2.2.1.2 Electric furnace

The most widely used instrument in sample making in solid state research is the electric furnace. The temperature range in a heating zone of an electric furnace can span from room temperature to around 1800 °C.

The techniques used to construct an electric furnace are mature and reliable. The temperature control mechanism in the electric furnace is the same as that in a house stove. The heating element is an electric resistor. The temperature can be controlled by varying the input electric power. A sensor is attached to the heater and sends the temperature readout to the controller. Scientific furnaces are specially engineered to meet higher precision and higher temperatures than in a house stove, and therefore more stringent environmental demands in laboratories. The heating elements most often used are nickel-chromium[79], MoSi2 [80]), and platinum alloys, for temperature ranges from room temperature to 1150 °C, 1800 °C, and 2500 °C, respectively. There are mainly two types of temperature sensors: a thermocouple and an infrared pyrometer. The complexity and functionality of high-temperature controller have changed rapidly in the past two decades. Modern temperature transmitters can provide sophisticated control, feedback and processing capabilities with full featured micro processors in them.

The fundamental setup of an electric laboratory furnace normally consists of a nickel-chromium filament, a K-type thermocouple and on-off relay with set point input. The advantages of such system are: low cost, high repeatability, good coverage of the temperature range of interest and ease of construction. The drawbacks are: the heating zone is open to the air, the body is bulky, its position is fixed, the temperature response is slow, the temperature reading accuracy is low and it is not programmable.

As indicated in the last section, an inert gas or vacuum environment is required for a tantalum crucible at high temperatures. The only solution without requiring a sophisticated instrument is to seal the Ta crucible into a larger quartz capsule. Figure 37 shows a picture of the two-layer structure of such a sample capsule.

Figure 37 The two layer structure of a sample capsule.

The two-layer structure of the sample capsule does provide the protection for the Ta crucible from being oxidized. It also brings more problems. In some cases, the sample should be rapidly quenched to room temperature from the annealing temperature in order to freeze the desired crystal structure formed at the annealing temperature. During the quenching process, the sample might experience complex phase changes if the quenching speed is not fast enough. Tantalum is a metallic element with good heat conductivity [76], whereas quartz, vacuum, and inert gases are good heat insulators which can slow down the quenching speed. The solution to this problem will be discussed in the next section.

2.2.1.3 Programmable Electric furnace

2.2.1.3.1 Introduction

An air sealed programmable furnace was designed and constructed in this study to solve the problems encountered in traditional electric furnaces. It has many advantages: A programmable precision temperature control system for faster and more accurate temperature control, inert gas or vacuum environment for heat treatment to avoid the oxidation of the elements with air and the reaction of the elements with water, a pressure regulation system to adjust the total amount of exchange gas in the furnace body, a furnace body position system to mix the elements uniformly and separate liquid and solid parts at the annealing temperature for a self-flux method of growing single crystals [81], a quick release structure to release the tantalum crucible directly from the heating zone of the furnace into cold water for rapid quenching, a dual helix heating filament structure to reduce the induced magnetic field in the furnace and the signal noise from the thermocouple, an observation window to provide the most direct visual information during the heating process and to be used to calibrate the infrared pyrometer, a hardware and software low-pass filter for temperature readings and position readings which can improve the SNR (signal-to-noise-ratio) by a factor of 20, and a water-cooled furnace body to reduce the hazards to the operator.

The main structure of the furnace contains four parts: furnace body, supporting structure, electric circuits, and control program.

2.2.1.3.2 The hardware structure

The 3D drawing of the furnace body and two aluminum end blocks are shown in Figure 38. The center piece of the body is made from a single aluminum block with a central through

hole and water circuits at the four corners. On the front side of this block, a slit serves as the observation window. Two end aluminum blocks are attached to the center piece by socket cap stainless steel screws with high-temperature silicone O-rings in between to form an air-sealed chamber and an enclosed water cooling loop. Being a good heat conductor, a water-cooled aluminum furnace body can efficiently take the heat away from the heating zone. The inner surface of the central cavity is polished to reduce energy loss through radiation from the heating filament.

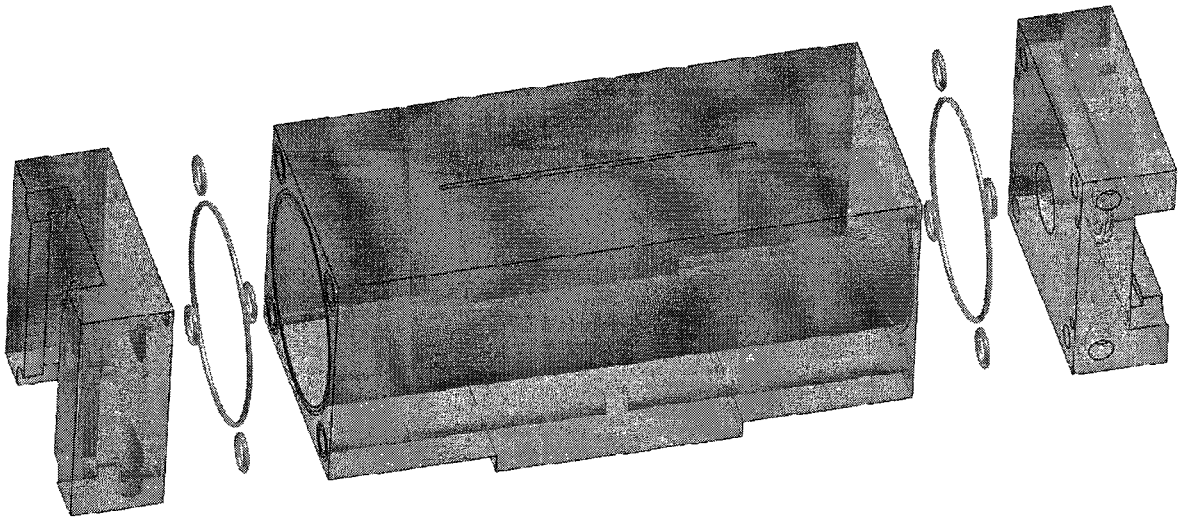

Figure 38. The furnace body and the end blocks of the electric programmable furnace.

The heating filament is supported by a ceramic tube with a dual helix groove on its outer surface. The filament wire can be held in position by the groove at all temperatures. The physical dimension of the groove determines the temperature distribution of the heating zone. The material used to make the filament holder is machinable ceramic 960 from Cotronics Corp. This

material can withstand at temperatures up to 1800°C. Its only weakness is that the maximum temperature change rate is 5 C°/min. Above this rate, a thermal shock effect can cause the ceramic tube to crack. The nickel-chromium heating wire is wound on the ceramic tube and held by two stainless steel sleeves (Figure 39), which in turn are clamped in between the two aluminum end blocks inside the furnace body. The heat conductivity of stainless steel is between that of ceramic and aluminum making it a good choice to buffer the large thermal expansion and temperature gradient between the hot ceramic tube and the water-cooled aluminum end blocks.

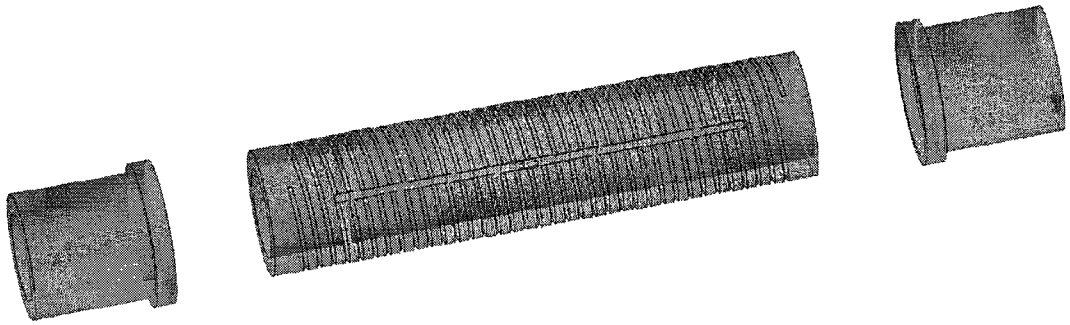

Figure 39. The high-temperature structure of the electric furnace that consists of a ceramic tube with the dual helix groove on its outer surface and two stainless steel sleeves.

A K-type thermocouple is attached to the wall of ceramic tube in the center of the heating zone. The heater and thermocouple wires are routed outside the furnace via four sealed high-temperature electrical feedthrough, as shown in Figure 40.

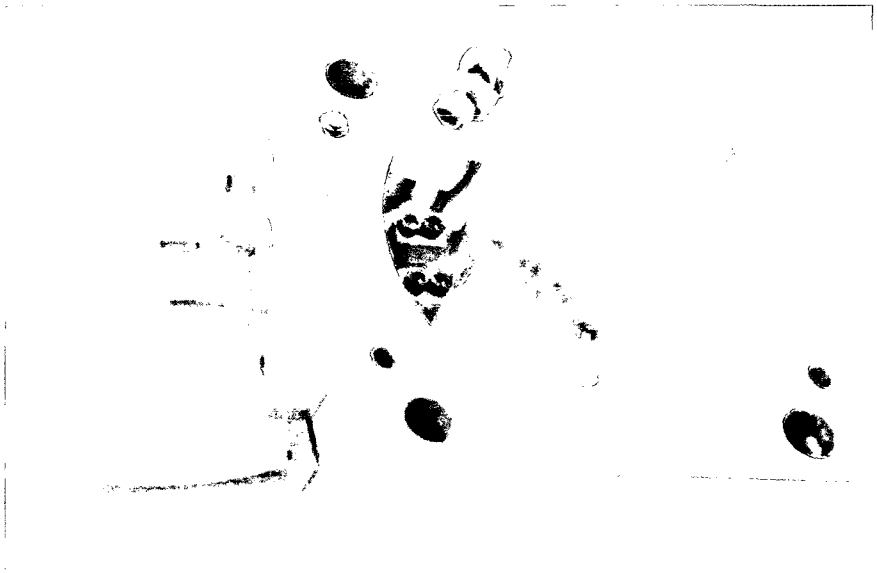

Figure 40. The detailed electric connections of the electric programmable furnace.

The sample quick-release structure is shown in Figure 41. Two inserts are attached to the aluminum end blocks with high-temperature silicone O-rings in between.

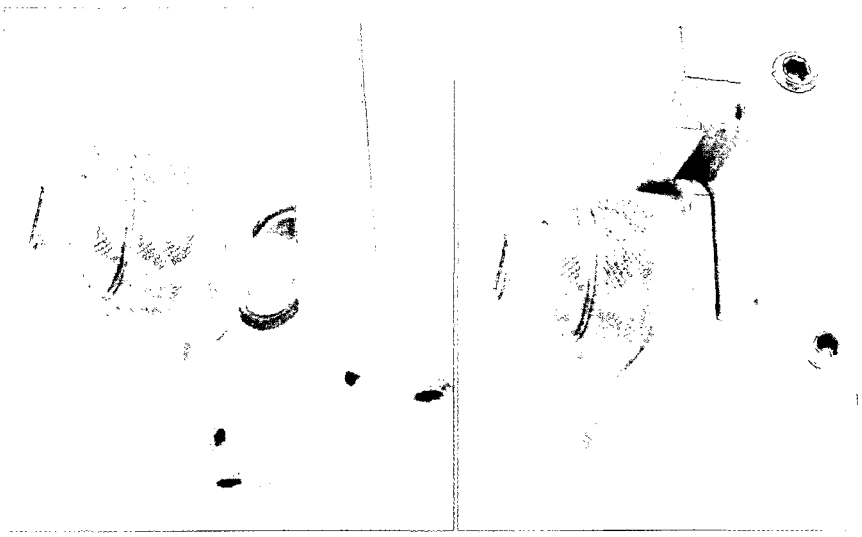

Figure 41. The sample quick-release structure of the electric programmable furnace.

The ends of the inserts are two shaped ceramic blocks. They are connected to the metal parts of the quick-release structure by two ceramic rods. The Ta crucible is positioned by these two ceramic blocks in the center of the heating zone (Figure 42).

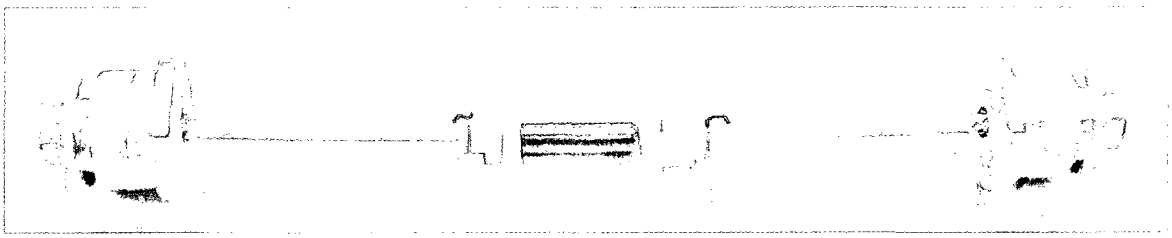

Figure 42. The tantalum crucible and the positioning structure of the electric programmable furnace.

The furnace body is attached to the supporting frame through an O-ring sealed rotatable structure. The gas pass on the stationary frame has three openings. One is connected to a pressure sensor. The other two are connected to the rotary pump and inert gas tank through two separate solenoid valves, respectively. A set of gears is installed between the furnace body and the supporting frame. A geared motor and a potentiometer are connected to the transmission gear set serving as the furnace body position servo system. The details of the transmission system are shown in Figure 43.

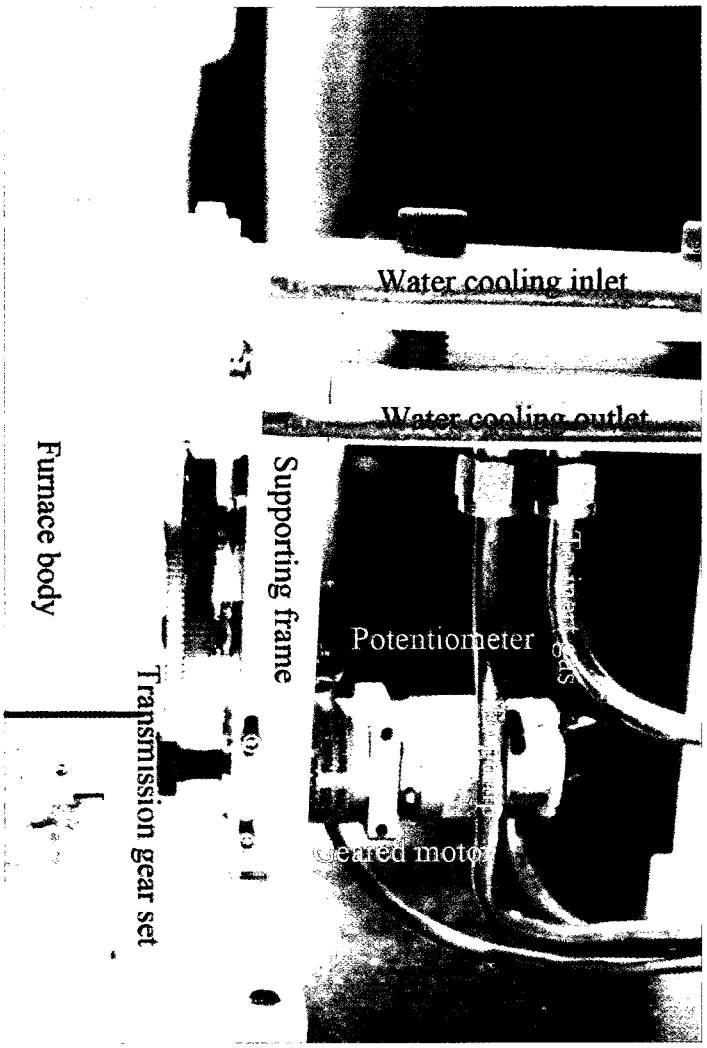

Figure 43. The transmission gear structure of the electric programmable furnace.

The position of the furnace body can be programmed. A periodic movement of the furnace body, typically with a frequency between 0.1 Hz to 1 Hz, can mix the different elements inside a tantalum crucible during the melting process. The maximum rotation angle of the furnace body is 240 °, which makes it possible to turn the tantalum crucible upside down to separate the liquid and the solid when a self-flux method of growing single crystals is used [81]. The modified tantalum crucible structure for such an application is shown in Figure 44.

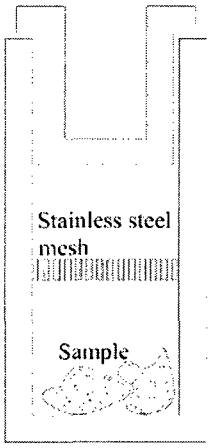

Figure 44. The schematic structure of the modified tantalum crucible for growing single crystals by a self-flux method.

The electronic system consists of power units, signal conditioning circuits, and DAQ (Data AcQuisition) card from NI (National Instrument Inc.). The DAQ card used in this study is PCI 6229. It contains 16 bit analog input and output ports and 32 multi-purpose digital I/Os [82]. Signal conditioning circuits are required between the DAQ card and the power units and sensors. Based on the mechanical structure of the furnace and the desired functions, the following tasks are accomplished with the signal conditioning unit: acquiring the temperature readings from the thermocouple, acquiring the position information of the furnace body, acquiring the pressure reading from the pressure sensor, sending the control signals to the DC power supply to drive the heater, sending the control signals to the geared motor to position the furnace body, and sending the control signals to the solenoid valves to control the pressure in the furnace body.

The signals directly read from a K-type thermocouple are measured in mV. Equation (107) and Table 5 give the relation between the electrical readouts and the measured temperatures.

$$T = d_0 + d_1 \times V + d_2 \times V^2 + d_3 \times V^3 + d_4 \times V^4 + d_5 \times V^5 + d_6 \times V^6 + d_7 \times V^7 + d_8 \times V^8 + d_9 \times V^9, \quad (107)$$

where T is the calculated temperature in °C, V is the voltage signal measured from the K-type thermocouple [83].

Table 6 Coefficients for equation (99) in different temperature ranges [83].

Temperature range / Coefficients	-200 to 0 °C	0 to 500 °C	500 to 1,372 °C
E range (mV)	-5.891 to 0.000	0.000 to 20.644	20.644 to 54.886
d_0	0.0000000E+00	0.0000000E+00	-1.3180580E+02
d_1	2.5173462E+01	2.5083550E+01	4.8302220E+01
d_2	-1.1662878E+00	7.8601060E-02	-1.6460310E+00
d_3	-1.0833638E+00	-2.5031310E-01	5.4647310E-02
d_4	-8.9773540E-01	8.3152700E-02	-9.6507150E-04
d_5	-3.7342377E-01	-1.2280340E-02	8.8021930E-06
d_6	-8.6632643E-02	9.8040360E-04	-3.1108100E-08
d_7	-1.0450598E-02	-4.4130300E-05	0.0000000E+00
d_8	-5.1920577E-04	1.0577340E-06	0.0000000E+00
d_9	0.0000000E+00	-1.0527550E-08	0.0000000E+00

The analog input range of the DAQ card is from -10 to 10 V. In order to make use of the maximum resolution of the DAQ card in the interested temperature range (from room

temperature to 1150 °C), a high-linearity and low-noise amplifier is adopted. The AD595 IC (integrated circuit) from Analog Devices Inc. is a monolithic amplifier with cold junction compensation and it is pre-trimmed for K-type thermocouples. It is recommended to calibrate the thermocouple with an ice-water mixture to achieve precise measurements for a regular thermocouple. The built-in ice point compensation circuits and self-contained Celsius calibration function in an AD595 help to avoid the cumbersome setup without sacrificing performance. The non-linear relationship between the measured temperature and the voltage readout from equation (99) could add huge work load to the conversion. Another benefit of using this IC is that it removes this nonlinear relationship and is laser wafer trimmed to achieve a calibration accuracy of 1 °C [84]. This matches the rated accuracy of a K-type thermocouple [84]. The major errors of a thermocouple usually arise from the thermocouple wire gauge and the uniformity of the constituents in the wire. The temperature reading error increases with temperature due to the increased diffusion mobility of the material impurities [84]. This is equivalent to adding a random noise to a slow changing DC signal. Further corrections can be made electrically in hardware and mathematically in software. The AD637 IC from Analog Devices is a complete, high-accuracy, monolithic RMS-to-DC converter that computes the true RMS value of any complex signal. A crest factor compensation scheme in the AD637 can improve the SNR by a factor of 10 with less than 1% additional error [85]. The amplitude adjustment circuits in AD637 can bring the maximum output from an AD595 from 11.495 V to a level slightly lower than 10 V in order to match the input range of the DAQ card. Figure 45 shows the schematic circuit.

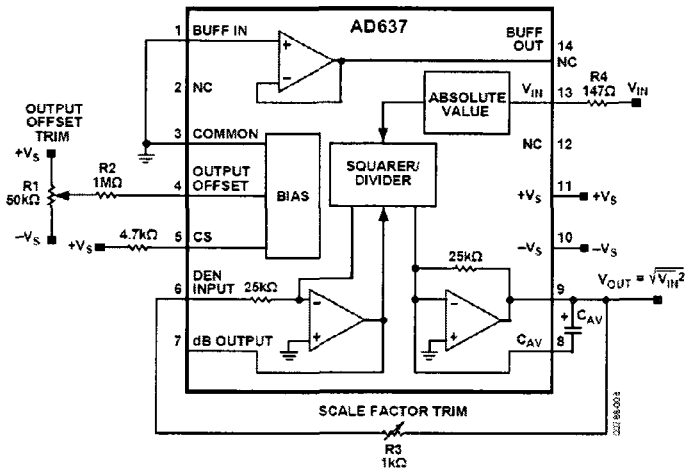

Figure 45. The schematic layout of the AD637, the RMS to DC converter [86].

The position sensor of the furnace body is simply a potentiometer that is driven by the geared motor. The gear connections are arranged in a cascade mode that can be seen in Figure 43. The moving probe of the potentiometer reflects the actual position of the furnace body. One fixed terminal of the potentiometer is connected to ground via a fixed resistor. The other fixed terminal is connected to a high-precision voltage reference via another fixed resistor. Therefore, the voltage range of the moving probe is confined between ground level and the reference voltage with a margin to both limits. The schematic circuit is shown in Figure 46.

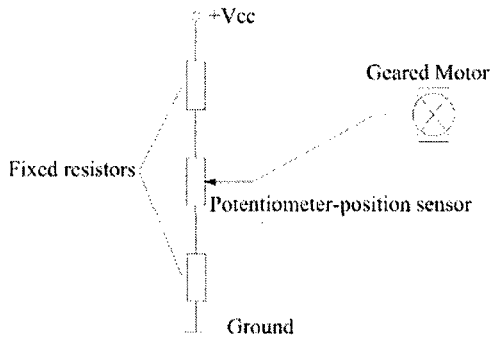

Figure 46. The furnace body position sensing circuit for the electric programmable furnace.

Extra care was taken to reduce the noise signal for this circuit. External noise mainly comes from the environmental electro-magnetic interferences, with the 50-60Hz power line noise being the strongest. A common-mode noise reduction transformer and a hardware low-pass filter can efficiently remove it. High-quality electronic components and a well-designed printed circuit board are used to reduce the inherent noise of the components and reduce the external interferences. The power supply of this circuit makes use of high-precision and super low-noise voltage reference IC, ADR445, from Analog Devices Inc. [86]. Further noise reduction can be achieved with software, which will be discussed in the software section below.

The pressure sensor used in constructing the furnace is 40PC015G2A from Honeywell Inc. It is a monolithic amplified pressure transducer. The effective range of this sensor is from 0 to 15 psi (pound per square inch) (1 atm = 14.695949 psi). This sensor is laser trimmed to ensure maximum of 0.20% non-linearity over the entire range of the output signal from 0.45 to 4.5 V. The output can be connected directly to the analog-in port on the DAQ card. This circuit uses the same noise reduction techniques as the position sensor: a common mode rejection transformer, the low-pass filter, and a high-precision low-noise voltage reference IC. Similarly, software noise reduction can also be used.

Conventional electric furnaces take the AC power directly from the outlet and apply to the heating filament through a controlled relay. Due to the large instantaneous power variation, the physical size of the heating zone is designed to be large to eliminate temperature variation. Furthermore, the on/off temperature control requires even larger heat capacity for the heating zone to keep the sample temperature stable. The advantages of such a system are low cost and a

large effective heating volume. However, when high precision, low noise, and fast temperature response are required, a better solution is required.

Most of modern high-output DC power supplies work in switching mode. The working frequency of such a PSU (Power Supply Unit) can vary from a few hundred Hz to a few hundred kHz, which is much higher than 50-60 Hz for traditional PSU. A higher working frequency helps to improve the transformer power conversion efficiencyand allows sue of a transformer with a mere compact size and a lighter weight. The power loss of such systems mainly comes from the on/off operation. Due to the delay of the current response of the switching components, the rising and falling edges of the on/off operation are not ideal for step functions but a finite step response with a slope. The area under the slopes is proportional to the power loss. A PWM (pulse width modulation) method is used to control and stabilize the output in switching mode PSU designs. The ratio of the on-duration and the off-duration in one period of the control signal, the so-called duty cycle, determines the output power. By varying the ratio, one can stabilize the output by using voltage or current as the feedback signal, depending on the application. The output from the secondary coil in the transformer can be smoothed by a passive low-pass filter consisting of resistor(s), capacitor(s), and inductor(s), or by an active regulator (IC). The frequency of the ripple in the output is the same as that of the PWM (pulse width modulation) signal. The amplitude of the ripple is mainly determined by the parameters of the low pass filter, the duty cycle, and the load.

In comparison with traditional temperature control systems, the programmable switching mode PSU can provide more continuous and precise average power to the heater. The noise introduced to the sensors from this kind of power supply can be easily removed by the same techniques used for the position sensor and the pressure sensor. With this design, it is possible to

make the heating zone smaller to achieve higher temperature precision and more prompt temperature response. The PSU used in this study can provide 2000 W DC output and is controlled by a 0-5 V DC signal. Because of its high input impedance, this PSU can be driven by the analog output signal from the DAQ card directly.

The required operations for positioning the furnace body are on/off control, direction control, and speed control. A DC motor is used to drive the furnace body due to its small size, high torque, and ease of operation as compared with a stepping motor. The most widely used DC motor driving circuit is an "H" bridge. Its working mechanism is illustrated in Figure 47.

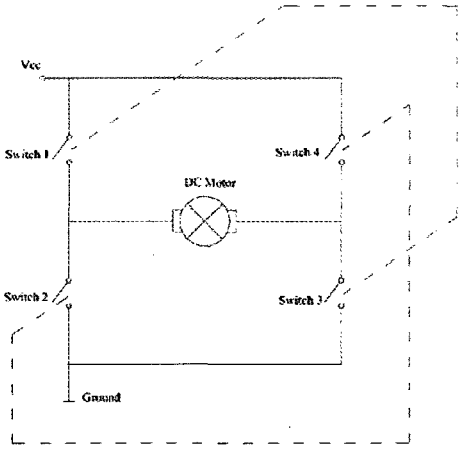

Figure 47. The schematic drawing of the "H" bridge circuit.

When switches 1 and 3 are on and switches 2 and 4 are off, the current going through the DC motor is from left to right. When switches 2 and 4 are on and switches 1 and 3 are off, the current going through the motor is reversed. Thus, the motor rotation direction control can be achieved by this circuit with a single end power supply. The PWM can be used for speed control.

Therefore, two digital output channels from the DAQ card are sufficient for the required operations. The switches in Fig.47 are MOSFETs in real circuits.

The pressure control is simply an on/off control. Two solid-state relays are connected between the solenoid valves and the AC outlets. The control signals are directly sent to the solid state relays from the two digital outputs on the DAQ card.

The main program consists of two functional blocks: a control and a user interface. They were developed on the Labview platform: the IDE (Integrated Development Environment) from National Instrument. The following aspects of the control function are discussed here: software noise reduction, temperature control mechanism, position control method, the pressure control and overall control considerations.

2.2.1.3.3 The Software design

2.2.1.3.3.1 Software noise reduction

The temperature, pressure, and position signals from different sensors in this system are mainly slowly varying DC signals with white noise on top of them. The aim of the noise reduction is to extract the slowly varied DC signal from the raw signal. Three mathematical methods to reduce the noise are used in this study.

The first one is a RMS to DC converter. The noise reduction mechanism of this method is the same as that of the hardware solution discussed in the thermocouple section. The sub VI (virtual instrument) provided in the Labview platform can be directly used between the raw signal and the negative-feedback control program.

The second one is a low-pass filter which is also provided as a sub VI in the Labview program. The performance of this function block is shown in Figure 48. The left chart shows the signal taken directly from the sensor with the noise amplitude around ±3 V where the sampling rate is 10000 points per second. The right chart is the signal output from Labview low-pass filter sub VI with a significantly reduced noise amplitude ±0.08 V. The low-pass filter is a 7^{th} order IIR type filter based on a Bessel topology [87]. The low-pass filter cutoff frequency is set at 7.5 Hz, which is far below the noise frequency from the power line at 60 Hz, but the noise level of the output signal increases drastically when the cutoff frequencies of the low pass filter increases.

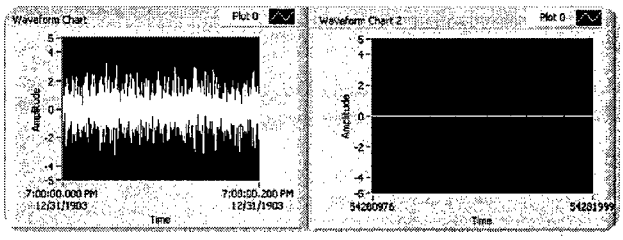

Figure 48. The comparison of the signals before and after the low-pass filter.

The third type is an arithmetic average. The noise reduction is not as good as in the second type. However, it provides effective odd point removal mainly caused by temporary device failure.

2.2.1.3.3.2 Temperature Control

The most widely used control mechanism in industry and scientific research is "PID" (Proportional, Integral, and Derivative) control. The control is based on equation (108):

$$V_o = P(e + I\int e \cdot dt + D\frac{de}{dt}), \tag{108}$$

where V_0 is the heater output, $e = Setp\ Value - Actual\ temperature$. The "I" function tends to reduce the noise by calculating the sum of the differences over time, while the "D" control tends to magnify the noise on the output which prevents the system from reaching stability.

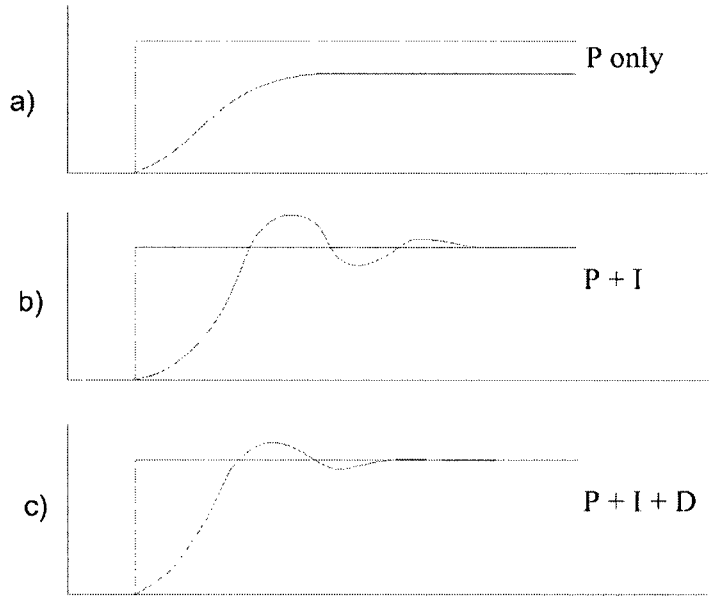

Figure 49. The step responses of the P, PI, and PID temperature controls.

The "P", "PI" and "PID" temperature control responses are shown in Figure 49. As shown in Figure 49 (a) for "P" control, there is a constant difference between the actual value and the set value. Figure 49 (b) shows the response of "PI" control where the actual value eventually approaches the set value, although it takes longer time. The combined "PID" control which is shown in Figure 49 (c) theoretically provides the best step response. However, the sample temperature with full "PID" control jumps around the set value with an amplitude of around 8 °C. Since the acquired temperature readings are discrete numbers, the derivative of the temperature

at a specific time is a positive or negative number with a fixed minimum value, which is much larger than the smallest increment in response of the actuator [88].

Overall, the "PI" control gives the most accurate temperature regulation, around ±0.045 °C over the entire temperature range in comparison to other combinations.

2.2.1.3.3.3 Position Control

Control of the furnace body position is realized from the Labview platform via a DAQ card. The Labview program calculates the direction and amplitude of the control signal based on the target and the measured position of the furnace body using the "P" control described in a previous section. A 500 Hz PWM control signal is generated by the Labview program and the internal counter on the DAQ card. The duty cycle of the PWM signal varies from 1 to 100%, which corresponds to slow and fast angular motion of the furnace body.

2.2.1.3.3.4 Pressure Control

The pressure regulation is based on on/off operations of two solenoid valves connected to the rotary vacuum pump and the inert gas tank, respectively. A latch mechanism is used to prevent the valves from switching on and off continuously by setting different thresholds for the on and off operations. For example, the valve for inert gas is turned on when the difference between the target pressure and the actual pressure is greater than 10 Torrs, and is turned off when the difference is lower than 0.5 Torrs.

Due to the limitation of physical properties of the ceramic tube, the temperature change rate cannot exceed 5 °C/min. This has been taken care of in the temperature ramp generation program. However, due to the constraints of time and resources, the protection functions such as water failure and sample loading sensing are not implemented.

This concludes the introduction to the design of the electric programmable furnace. This furnace meets all the requirements stated at the beginning of the section and has been used to produce the samples investigated in this study.

2.2.1.4 Induction furnace

As an alternative solution to the arc melting method, induction melting gives a cleaner melting environment without losing sample mass. With this method, the heat is generated by inducing currents in the metallic crucible body or the sample chunks directly. Since no mechanical movement or arc plasma is involved, the heating process is more stable and gives less chance to introduce impurities. A double-layer quartz tube with water flow in between is used to hold the sample (Figure 50). The water inlet is located at the bottom of the outer quartz tube. The water outlet is located on the top end of the outer quartz tube. The bottom of the inner tube is located at the center position of the outer tube to hold the crucible. The induction coil is located around the sample level outside the quartz structure. The top opening of the inner tube is used to load the sample and set up the required vacuum or inert-gas environment.

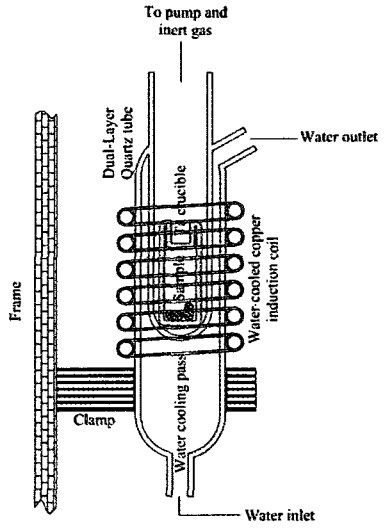

Figure 50. The schematic sample mount of an induction furnace.

The crucible materials that can be used in an induction furnace include tantalum, alumina, silica, and glassy carbon. When a metallic crucible is used, its body can act as the heating element due to the induction heating effect. A relatively high heat conductivity of the metallic material helps to make the temperature distribution of the crucible uniform. However, if the crucible material is non-metallic, such as glassy carbon, alumina, or silica, the samples must be metallic themselves to be heated and melted by the induction furnace. If the sample contains insulators and/or semiconductors, the resulting sample might be inhomogeneous.

The RF (Radio Frequency) generator of the induction furnace is from Ameritherm Inc., model Hotshot 5. It consists of a RF PSU and a remote station to which the induction coil is connected. The entire system is water cooled. The maximum output power of this system can reach 2 kW [89]. The LCD of the front panel on the PSU unit reflects the real-time working status, including output power, current, and frequency. The RF generator can automatically adjust the working frequency based on the parameters of the induction coil, load, and power range to achieve the best power coupling between the internal circuits and the induction coil. An analog control is provided on the rear panel of the PSU. With a properly calibrated infrared pyrometer, a programmable negative-feedback temperature control system can be formed.

2.2.1.4.1 Rapid quenching attachment

Rapid quenching is required to produce amorphous and some quasicrystalline alloys. This can be achieved by ejecting the melted sample rapidly onto a fast spinning copper wheel to form a ribbon. The typical thickness of the ribbon is around 15 μm. The mass of the copper wheel must be large enough for its temperature to be considered constant during the quenching process. Since copper possesses excellent thermal conductivity, the heat applied to its surface from the

melted sample can be quickly taken away. With this technique, a temperature drop of about 10^6 C°/s can be achieved.

In order to prevent the molten sample from reacting with the air during the quenching process, a sealed inert gas environment is required. A motorized copper wheel is placed inside a sealed aluminum box. A vacuum pump connector and an inert-gas connector are provided on the aluminum box. The sample ingot is placed in a separate quartz tube with a small hole on the bottom. The quartz tube opening is connected to a pressure triggering setup. A specially designed water-cooled copper coil is placed on top of the copper wheel through an airtight electric feedthrough on the aluminum box and connected to the remote station. The end of the quartz tube is placed in the center of the coil. After the aluminum box is purged and filled with inert gas, the RF generator sends power to the induction coil. Once the ingot is melted, the pressure trigger is used to eject the molten sample onto the rapid spinning copper wheel, forming a ribbon. A picture of the rapid quenching setup is shown in Figure 51.

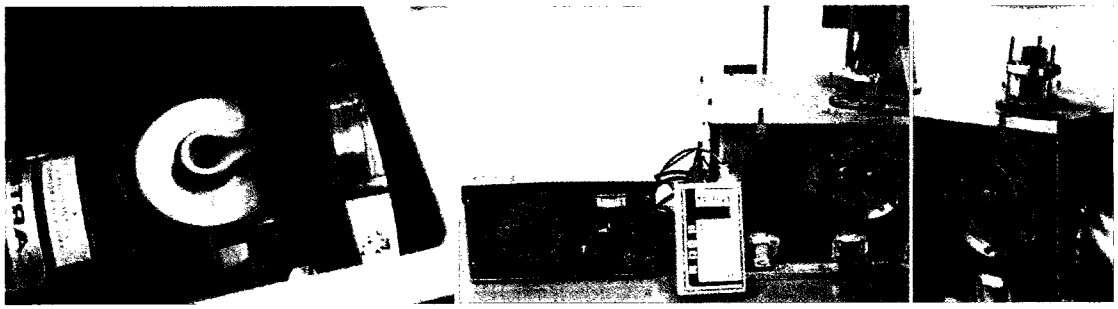

Figure 51. The rapid quenching setup for the RF generator.

2.2.1.5 Levitation melting

From Lenz's law, the magnetic field generated by the induced current tends to weaken the changing flux of the source field. This mechanism can be used for levitation melting, a

method that uses a specifically shaped coil to cause the sample to float while being heated. Figure 52 shows such a RF levitation coil.

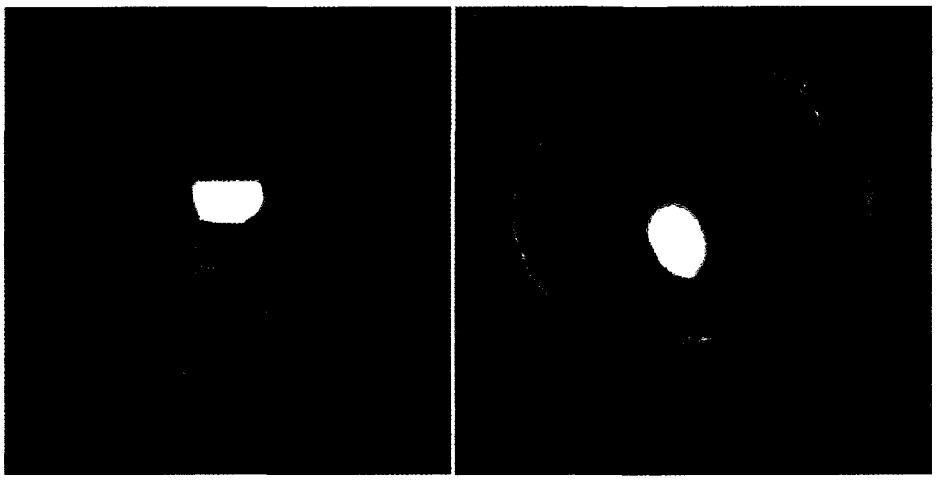

Figure 52. The levitation melting.

The diameter of the coil in Figure 52 expands gradually upwards. At the top, there is one reversed winding. The corn-shaped coil forms a magnetic field gradient along the vertical direction. The interaction between the induced magnetic field inside the sample and the magnetic field produced by the induction coil generates a levitation force. By adjusting the frequency and the power applied to the coil, the levitation force can cancel out the gravity of the sample and make the sample suspend in the coil. The reversed winding generates an opposite magnetic field that forms a trap to stabilize the sample. It can be seen in Figure 52 that the sample is lifted in the air without touching any surface. Levitation melting can be realized in air, inert-gas, or a vacuum environment. This is considered the cleanest sample melting solution. However, there are some drawbacks that prevent this method from being widely used: non-metallic samples cannot be levitated with this method; different elements have different conductivity which can result in different levitation level in the coil unless a uniformly conductive ingot is used; the initial

levitation is hard to achieve due to the relative small 3D space, gas turbulence, and temperature dependent conductivity of the sample; it is difficult to retrieve the sample from levitated melting state without introducing impurities; and sample loss is unavoidable for low vapor pressure samples.

2.2.1.6 Electronic balance

Keeping a precise starting stoichiometric composition is extremely important in making high-quality, single-phase samples. An AB54-S, a high-resolution electronic balance from Monobloc with 0.1 mg minimum increment is used to weigh the elements in this study.

2.2.2 Methodology

2.2.2.1 Sample weighing

The sample weighing accuracy directly affects the final sample quality. One should avoid using elements in powder or mesh forms as this inevitably leads to the loss of small amount of sample during transportation. Elements prepared in chunk and block forms can easily be handled and transported without mass loss.

2.2.2.2 Sample sealing

Most of the samples require inert gas or vacuum environment for heat treatment. If using the traditional electric furnace, the two layer quartz-tantalum capsule structure is required, as shown in Figure 37. The sealed tantalum layer provides a stable chemical and physical environment at high temperatures for the individual elements and prevents them from escaping. The quartz layer provides the protection for the tantalum crucible from being oxidized at high temperatures. However, the quartz capsule layer is not needed when the programmable electric

furnace is used. The sealed furnace body can provide the oxygen free environment by repeating the purging and inert-gas refilling processes a few times.

2.2.2.3 Sample melting

The goal of sample melting is to make a uniform ingot. Ideally, all elements are melted and mixed uniformly at a temperature higher than the melting points of all elements and cooled to room temperature to form an ingot.

The arc furnace is preferred in ingot making due to the ease of use and the highest temperature it can reach. First, the precisely prepared stoichiometric elements are melted into an ingot and naturally cooled to room temperature in the arc furnace. Second, the ingot is cut into smaller pieces and re-melted into one piece. One can ensure the homogeneity of the ingot by repeating the second step four to five times. Each time, the purging and inert gas refilling processes have to be repeated a few times to make sure there is no oxygen left in the arc furnace chamber.

The advantages of using an induction furnace to make the ingot are: it can provide a cleaner and more stable environment for the melting process in comparison with the arc furnace. Sample loss can be avoided when the sealed tantalum crucible is used to hold the sample. The temperature control in an induction furnace is more precise than the arc furnace. The induction furnace can provide a vacuum environment for the sample during the melting process whereas the arc furnace can only provide an argon or helium gas environment. However, it is difficult to take the ingot out of the crucible in an induction furnace. A cone-shaped crucible can help to remove the ingot completely. Sample loss is also avoided by using crucibles made by non-sticky materials (such as glassy carbon). However, sample loss is unavoidable when multiple re-melting

processes are involved. Moving the double-layer quartz tube up and down through the induction coil during the melting process can help to increase the homogeneity of the ingot.

Having similar advantages and disadvantages to the induction furnace, the electric programmable furnace can provide more precise temperature control. Its furnace body movement can also be programmed. Therefore, different elements can be mixed in a more predictable and reliable way in the melting process.

2.2.2.4 Sample annealing

Sample annealing is used to form the desired crystal structure at a specific temperature and keep this crystal structure when the sample is cooled to room temperature. The annealing temperature is close to the crystallization temperature of the target alloy. The annealing time can vary from the time it takes the sample to be cooled naturally to room temperature in an arc furnace to a few months.

The simplest annealing process is to cool the sample naturally to room temperature from the melting state in an arc furnace.

An induction furnace can provide a cleaner environment when a tantalum capsule is used to hold the sample. The sealed tantalum capsule can avoid the sample loss during the annealing process. Normally, an infrared pyrometer is paired up with an induction furnace to achieve the negative-feedback temperature control and obtain the temperature of the sample. Therefore, the temperature of the sample can be programmed. However, the sample can only be cooled to room temperature naturally in the double-layer quartz structure at the end of the annealing process. When rapid quenching is required to prevent the sample going through the intermediate phase(s) during the cooling process, one has to look for other solutions.

A more precise sample temperature reading and temperature control can be obtained from a programmable electric furnace. As discussed in the programmable electric furnace section, a K-type thermocouple is used with a programmable DC PSU to form a negative-feedback temperature control loop. A temperature precision of ±1 °C can be achieved in the range of 25-1100 °C. The sample temperature can be controlled as long as the temperature changing rate is less than 5 C°/min. The quick-release structure shown in Figure 41 and Figure 42 can quickly release the tantalum capsule into cold water in less than one second at the end of the annealing process. Since tantalum is a good heat conductor, the sample temperature can be dropped fast enough to room temperature to prevent the sample from going through undesired phase change(s).

2.2.2.5 Sample storage

Some samples are active in air or water. Traditionally, they are kept in a special oil to avoid degradation over time. To remove the oil from the samples can introduce impurities and mass loss. A cleaner and safer way to store the samples is to put the samples in a sealed desiccator filled with argon gas.

2.3 Measuring techniques

2.3.1 Introduction

The x-ray powder diffraction, magnetic, Mössbauer, and electrical resistivity measurements are used to investigate the physical properties of the novel alloys in this study. Each of the experimental setups and the relevant techniques will be discussed in the following sections.

2.3.2 X-ray powder diffractometer

The x-ray powder diffraction measurement is used to investigate the crystal structure of the sample. The wavelength of the x-ray used in a diffractometer is comparable or smaller than the distance between the neighboring atoms in a solid. Therefore, the x-ray diffraction pattern can reveal the detailed crystal structure of the sample. The x-ray powder diffractometer used in this study is from PANalytical research group.

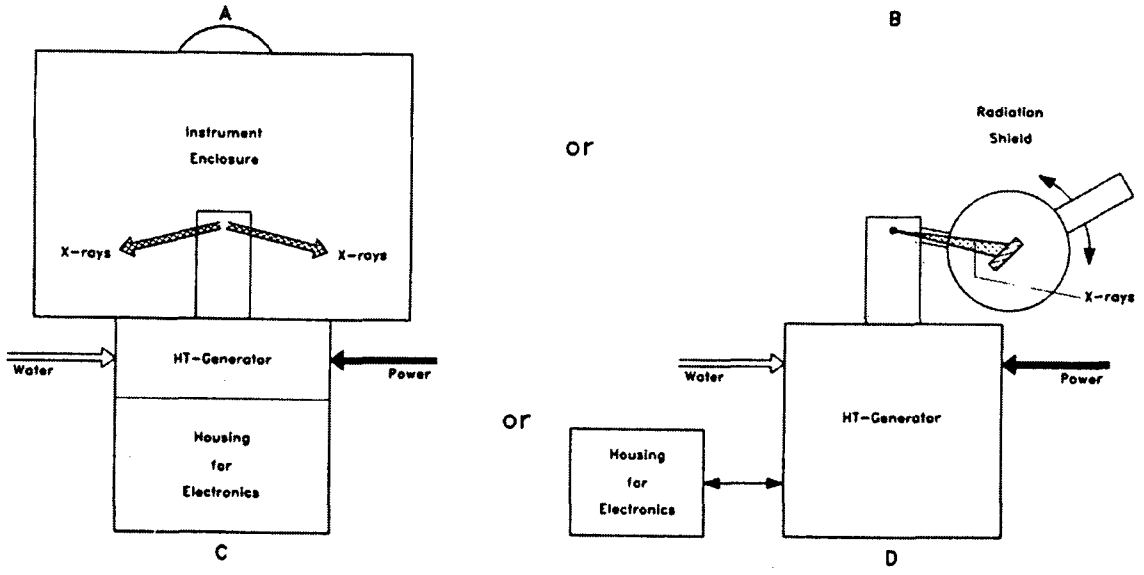

Figure 53. The schematic drawing of the x-ray diffractometer [90].

The structure of this diffractometer is shown schematically in Figure 53. The goniometer resides in an x-ray shielded hood. The HT generator is placed in a metal cabinet beneath the hood. The x-ray tube assembly provides the radiation source for two goniometers simultaneously, one on the left side and the other on the right side. D in Figure 53 shows the schematic arrangement of the right goniometer. The solid state x-ray detector electronics is located in the

cabinet beneath the HT-generator. The cooling water, control cables, and electric power are fed into the unit through the rear panel. The x-ray powder diffraction spectrum can be measured at different temperatures with proper attachments: high-temperature and low-temperature cameras. The following components of the x-ray powder diffractometer are described below: x-ray tube, goniometer, sample stage, variable slits, high temperature camera, low temperature camera, and user interface.

The x-ray is generated by bombarding a copper anode with high energy electrons. The electrons are generated by the tungsten filament and accelerated towards the copper anode across a high potential of 45 kV. The current in the x-ray tube is set at 40 mA in normal operation. Due to the low conversion efficiency (normally less than 1%) from electrons to x-ray, the copper target has to be water-cooled to prevent it from being damaged by the heat generated during the conversion. The anode is precisely shaped to give accurate foci for the outgoing x-rays. The kinetic energy of the x-ray is equal to the difference between the incident electron energy and the binding energy of the excited electron. Due to Auger effects, Compton scattering, and the complex atomic energy levels in copper, the spectrum of the generated x-ray contains many lines, $K\alpha_1$- $K\alpha_6$ [91]. By applying a proper filter, only a bichromatic radiation with $K\alpha_1$ and $K\alpha_2$ lines passes through and acts as the x-ray source. The wavelengths of the two lines are 1.540598 Å and 1.544426 Å, respectively. The schematic structure of the x-ray tube is shown in Figure 54.

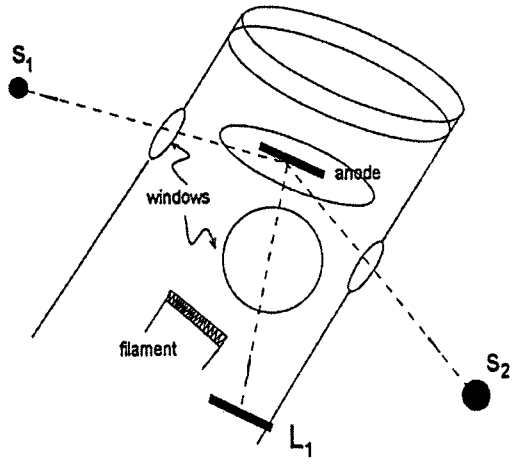

Figure 54. The schematic structure of the x-ray tube [92].

where L(s) indicate line foci and S(s) indicate spot foci. As seen from Figure 54, multiple x-ray beams can be generated by one tube with different directions and shapes.

The Bragg-Brentano diffractometer

The PANalytical x-ray diffractometer used in this study employs a vertical θ:2θ configuration. The geometry of such a goniometer is shown in Figure 55. The angle between an incident beam and the sample plane is defined as θ, and the angle of the incident and the diffracted beams is 2θ. The relative movements between the incident x-ray beam, the sample stage, and the x-ray detector are realized by a high precision and no-backlash mechanical system. The outgoing beam from the x-ray tube is focused at "F" (Figure 55). The beam goes through a divergent slit "DS" and reaches the specimen plate. The diffracted x-ray enters the detector through a receiving slit "RS". "SS1" and "SS2" are two sets of collimators which confine the width of the x-ray beam. The opening of the divergence slit is controlled by the program and varies with the 2θ value so that the irradiated sample area remains constant during the

measurement. The resulted spectrum can be converted between the ADS (Automatic Divergence Slit) and the FDS (Fixed Divergence Slit) mode with the Xpert Plus Highscore program. The ADS mode provides better statistics in high 2θ range compared to the FDS mode.

In order to satisfy the parafocusing condition, the distance between "F" and the center of "S" should be equal to the distance between the center of "S" and "RS". The dotted arc indicates the focus pass in Figure 55, where r_f is the radius of the dotted arc, and its length is the so-called sample shaft length. There are two goniometers in the diffractometer. The sample shaft length of the left goniometer is 230 mm and of the right goniometer is 173 mm. From the geometry shown in Figure 55, one can tell that the longer sample shaft gives higher angular resolution. Therefore, the left goniometer can reveal more details than the right one. The sample shaft angular accuracy of both goniometers is ±10 μrad, and the reproducibility is ±5 μrad.

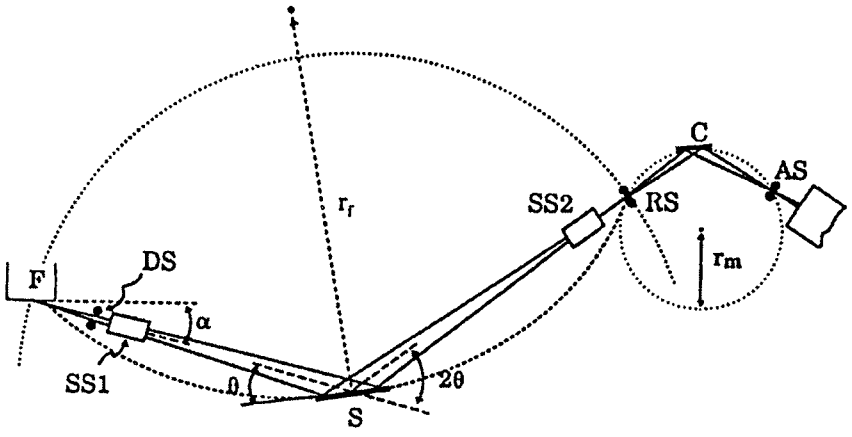

Figure 55. The geometric arrangement of the Bragg-Brentano diffractometer [93].

The most widely used x-ray detectors are scintillation counters, sealed gas proportional counters, and solid state (semiconductor) counters. The detailed structure of the detector (the

structure inside the dotted circle with a radius r_m) might differ from the one shown in Figure 55. The sealed gas proportional counter and the Kevex® solid state counter are installed on the left and right goniometer, respectively. The solid state counter is more sensitive to x-ray than the sealed gas proportional counter. Therefore, it takes less measuring time to obtain the same statistics.

The sample stage of the right goniometer is rotatable. The pulverized sample should be randomly distributed on the sample plane. The spin function of the sample stage can make the sample particles more randomly distributed. The spinning speed is fixed at 1 rev/s. The sample holder, which is placed on the sample stage, consists of a stainless steel rim, an aluminum plate, an elastic press (beneath the aluminum plate), and a precisely cut single crystal silicon wafer. The whole assembly is shown in Figure 56. One can apply a few drops of methanol or ethanol to the pulverized sample on the silicon wafer and gently shake the sample holder to make the sample powder spread uniformly on the wafer. When the liquid evaporates, the dried sample powder sticks to the silicon wafer even if the sample holder is tilted at 90°. The center of the surface of the silicon wafer is precisely aligned to the axis of the sample stage "S" in Figure 55.

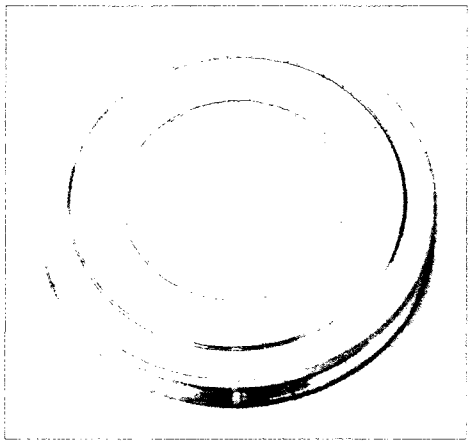

Figure 56. The x-ray powder diffraction sample holder.

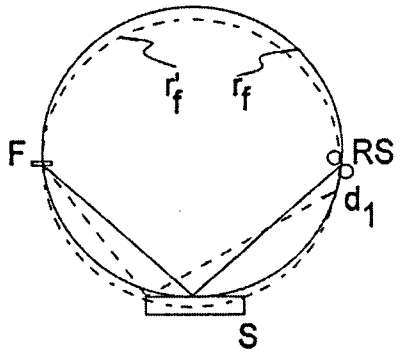

Figure 57. The illustration of the deviation caused by the sample thickness [94].

The sample thickness plays an important role in obtaining a precise x-ray spectrum. As can be seen from Figure 57, the illuminated sample area (marked with S) is actually a small portion of a cylinder rather than a perfect flat plane. The deviation of the sample surface from the ideal position (solid line) can result in wrong counts-2θ relationship of the measurement. The error caused by the sample thickness can be calculated as [95]:

$$\Delta 2\theta = -\frac{\alpha^2 cot\theta}{343.8}, \tag{109}$$

where α is the angular aperture of the divergence slit in degrees, and θ is expressed in radians.

The sample thickness error and the goniometer misalignment can be corrected by mixing the sample with a standard reference, such as germanium or silicon. The peak positions from the standard reference can be indexed with high accuracy. The difference between the experimental and the theoretical 2θ peak positions of the reference can be fitted with a fourth order polynomial, and furthermore the polynomial can be used to correct the sample spectrum.

2.3.3 Mössbauer spectrometer

There are three Mössbauer spectrometers used in this research: a room temperature to high temperature Mössbauer spectrometer; 2 K to room temperature Mössbauer spectrometer, and a 2 K to room temperature Mössbauer spectrometer with a 9 T super-conducting magnet. A basic Mössbauer spectrometer consists of a radiation source, a loud-speaker type transducer, an absorber, and a γ-ray detector. In this section, the general description of each element will be given, followed by the specifics of each type of a Mössbauer system.

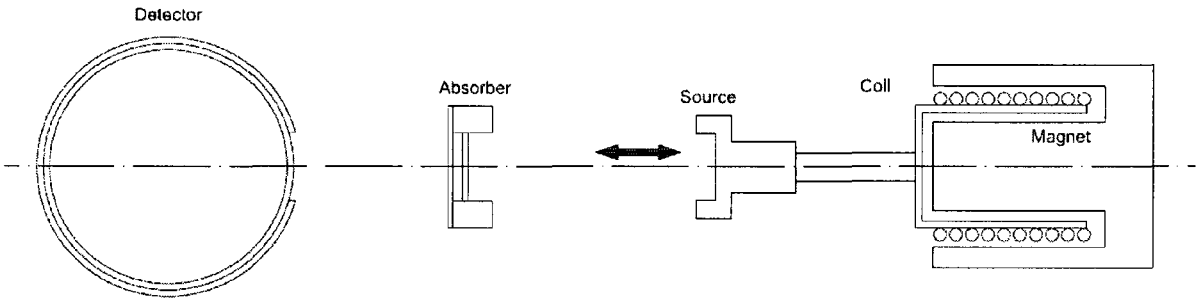

Figure 58. A schematic layout of a Mössbauer spectrometer.

The schematic layout of a Mössbauer spectrometer is shown in Figure 58. The detector, absorber, source, and sample transducer (the magnet and coil combination) are aligned along the same axis.

The useful radiation source is the resonant γ-ray from an excited to ground state in a recoil-free fashion of specific isotope. The non-resonant γ-ray from the same transitions, the radiation from all other transitions, and the secondary radiation produced in the matrix (mainly x-ray) contribute to the background. To a great extent, the decay effect and the nuclear

parameters determine the usefulness of an isotope [96]. Normally, the source is made by implanting the excited nuclei into a solid matrix.

The transducer is a close-loop (computer-controlled negative-feedback system) mechanical movement generator for the source or the absorber. Almost all modern Mössbauer spectrometers use a loud-speaker system as the transducer. The schematic structure of the loudspeaker transducer is shown in Figure 58. The source is attached to the pickup coil which moves in a homogeneous magnetic field that is generated by a rigidly fixed permanent magnet. The difference between the reference signal and the induced pickup signal is amplified and sent to the negative-feedback system to minimize the deviations. The error can be reduced to as low as 0.01% depending on the reference voltage waveform.

There are three types of γ-ray detector, the scintillation detector, the proportional counter, and the lithium-drifted germanium and silicon detectors. The scintillation detector converts the incoming photons or particles to a measurable electronic signal. The detector normally contains two parts, one is the scintillator, and the other is the photomultiplier.

A multichannel analyzer which contains 512 or 1024 channels is used to store the detected counts. The velocity from $-V_{max}$ to $+V_{max}$ is divided into 512 or 1024 increments with the same spacing (dv) which corresponds to the channels in the multichannel analyzer. The synchronization of the channel number with the velocity increment is performed by advancing the address of the memory one by one triggered by an external clock. The start impulse coincides with the beginning of the waveform and enables the multichannel analyzer to start with channel 1, the followed impulse corresponds channel 2 and so on, until the last channel in multichannel analyzer with the typical dwell time 50 to 100 μsec per channel. The unfolded Mössbauer

spectrum is obtained by accumulating the counts in each channel from each period from the beginning of the measurement to the end.

The layouts are the same for the three Mössbauer systems in this research. The differences among them are the peripheral setups.

The room-temperature to high-temperature Mössbauer systems contain an air sealed absorber chamber which can provide the vacuum or inert gas environment for the absorber. This is essential when measurement is performed at high temperatures to prevent the sample from being oxidized. A programmable negative-feedback temperature control unit is used to regulate the absorber temperature.

The 9 Tesla Mössbauer system with a 9 T super-conducting magnet features the SuperVaritemp system from Janis®. The absorber and source cooling is provided by the heated helium vapor to prevent the heat loads coming down from the top section of the cryostat. The liquid helium is fed to the sample chamber by a needle valve which can be adjusted by a knob on top of the flange. The sample chamber pressure can be regulated by a proportional valve and a vacuum pump combination. With the heater and the vaporizer located at the bottom of the sample chamber, the temperature of the source and the absorber can be stabilized to ±0.1 K around the set value. The sample chamber is isolated by a vacuum jacket which prevents the escaping warm gas from interacting with the main helium reservoir. The opening to the Mössbauer detector is a Mylar window vertically installed at the bottom of the cryostat. The source is attached to the loud-speaker transducer residing on the top of the sample insert outside the cryostat. Its velocity is measured by a Michelson Interferometer above the loud-speaker

transducer to get precise velocity information of the source. The schematic drawing of the head of the sample insert is shown in Figure 59.

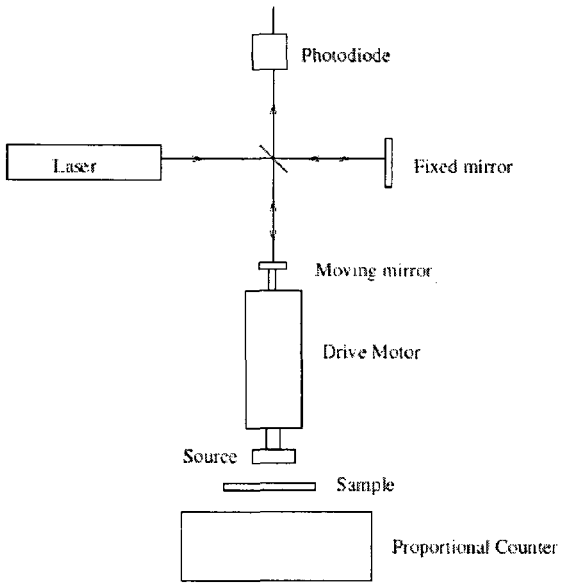

Figure 59. The schematic Michelson interferometer in the head of a sample insert used in the 9 T Mössbauer system.

2.3.4 Magnetometer

The magnetometer is a device that measures the time, the temperature, and the field dependent magnetic moments of a sample. The simplest magnetometer (zero-order pickup coil) is made of a single turn coil that is connected to a current meter. The induced current will be displayed on the current meter when the sample rapidly sweeps through the coil along its normal axis in a magnetic field. The maximum value of the induced current is proportional to the magnetic moment of the sample under that magnetic field. The resolution and sensitivity of such magnetometer is mainly limited by the sample mass, moving speed, coil size, magnetic field strength, and the magnetic susceptibility of the sample. To achieve higher sensitivity, one can

use the commercially available VSM (Vibrating Sample Magnetometer) and SQUID (Superconducting QUantum Interference Device) magnetometers.

With VSM, the sample is attached to the end of a shaft that is connected to a loud-speaker transducer which introduces the sinusoidal movement to the sample in a static magnetic field. The induced signal from the pickup coil reveals the AC magnetic moment of the sample. The VSM used in this study was from Lakeshore® with maximum magnetic field 1 T. The sample is placed in a Janis cryostat. Its temperature can be set from 2 K to room temperature. However, in the small signal range, the background noise is relatively large for this system.

More precise magnetic measurements can be done by using a DC MPMS system from QD with SQUID technology. Instead of measuring the induced current, the SQUID measures the absolute magnetic flux that goes through the pickup coils. A DC SQUID consists of a superconducting loop that has two Josephson junctions. The maximum superconducting current that flows through the device can be periodically modulated by the magnetic flux entering the loop with a period that is equal to the flux quantum.

In the MPMS system, the second derivative pickup coils are exploited to achieve higher SNR levels. The working mechanism is shown in Figure 60. The vertical pickup coils consist of four circular coaxial loops with equal areas. The two central coils are wound in the opposite direction from the top and bottom ones. The second derivative pickup coils make the magnetometer insensitive to uniform and linearly varying longitudinal fields [97] in comparison to the zero and first order pickup coils.

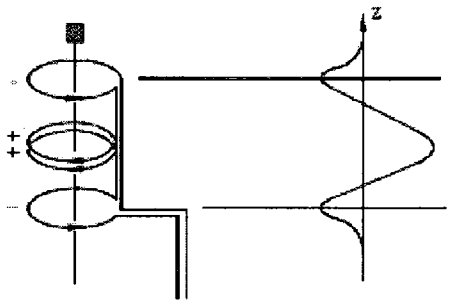

Figure 60. The second order pickup coils of a magnetometer and the measured signal [98].

The sample is moved from below the bottom coil to above the top coil by a motorized sample transducer. The measured signal is shown in Figure 60 (right) and fitted to:

$$f(Z) = X(1) + X(2)\cdot Z + X(3)\cdot\{2[R^2 + (Z + X(4))^2]^{-\frac{3}{2}} - [R^2 + (\Lambda + (Z + X(4)))^2]^{-\frac{3}{2}} - [R^2 + (-\Lambda + (Z + X(4)))^2]^{-3/2}\}, \quad (110)$$

where *f(Z)* is the raw voltage as a function of the sample position, Λ is the longitudinal coil separation with a value 1.519 cm, $X(1)$ is a constant offset voltage, $X(2)$ is the linear electronic drift parameter, $X(4)$ is the shift of the sample along the axis of the magnet, and $X(3)$ is the amplitude, from which the magnetic moment can be calculated as:

$$Magnetic\ moment\ (EMU) = \frac{X(3)\times longitudinal\ \ regression\ \ factor}{SQUID\ cal.factor\times sensitivity\ \ factor\times correction\ \ factor}. \quad (111)$$

The longitudinal regression factor and the SQUID calibration factor are device dependent values. They can be found in the MultiVu® software [99]. The sensitivity factor is determined by the sample scan range and the gain settings. The correction factor is a constant with a value 0.9125. The measured raw curve does not have the ideal pattern shown in Figure 60 (right) for small

signals, i.e., there might be coarse ripples, spikes, and linear background added to the basic pattern. The fitting function can extract the valid signal from the raw data without losing accuracy.

Figure 61 shows the detailed structure of the pickup coils and the superconducting magnet in the MPMS. The transverse pickup coils shown in the figure are not installed in the magnetometer used in this study. They are used to investigate the magnetic properties along different orientations for single-grain samples with the optional sample rotation attachment.

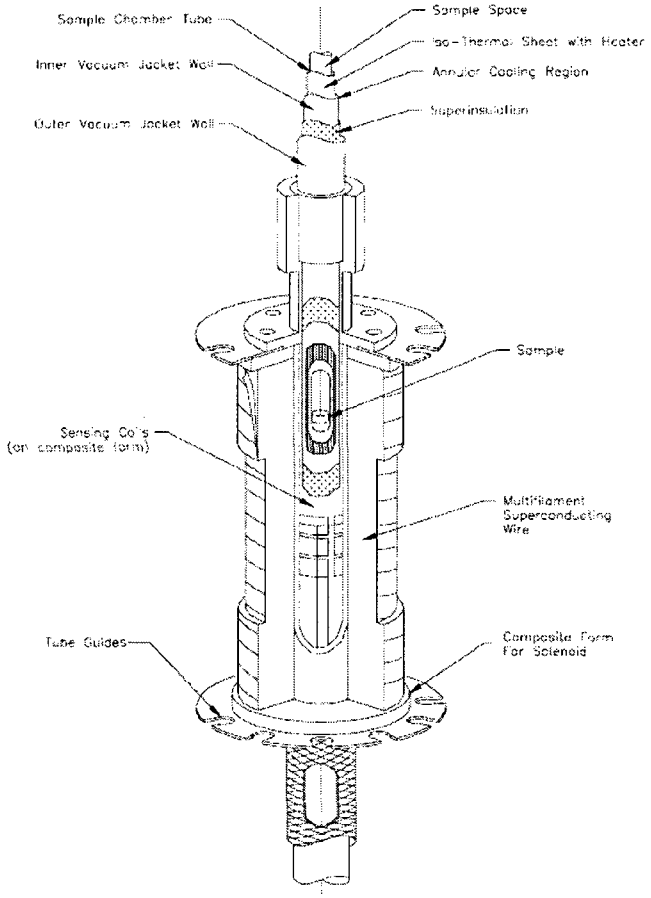

Figure 61. The detailed structure of the pickup coils and the superconducting magnet in the MPMS system [100].

The sample holder is made of non-magnetic material and mechanically attached to the sample transducer located on the top of the cryostat via a stainless steel and Be-Cu jointed stick. The recommended (by QD) sample holder material is a transparent straw [100]. This material is low cost and easy to obtain with small background signal (Figure 62 top). However, it is difficult to mount the pulverized sample on the straw and the straw can be deformed during the measurement. The deformation of the straw can make the sample deviate from the vertical axis of the cryostat and result in a larger near-field approximation error [97]. The straw is made of transparent plastic which can degrade with time. If the straw breaks, the sample might fall into the sample chamber and result in permanent damage of the magnetometer. The best sample holder material for a magnetometer is known to be high-purity quartz [101]. The temperature dependent magnetic susceptibility of quartz is mostly flat from 2 K to room temperature with a magnitude of the order of 10^{-7} EMU/(g·Oe). Other materials, such as silicon, also possess the desired magnetic properties, while other characteristics (price and machineability) might not make them the best candidates. The recommended sample container from QD is a medical capsule. It is low cost and easy to obtain in different sizes. However, when the set temperature is lower than 4.2 K, the vacuum pump is used to reduce the pressure in the sample chamber. The pressure difference between the sample chamber and the space inside the medical capsule can cause sample loss and pollution in the sample space. To solve the above problems, a customized sample holder and container set is proposed in this study, as shown in Figure 62.

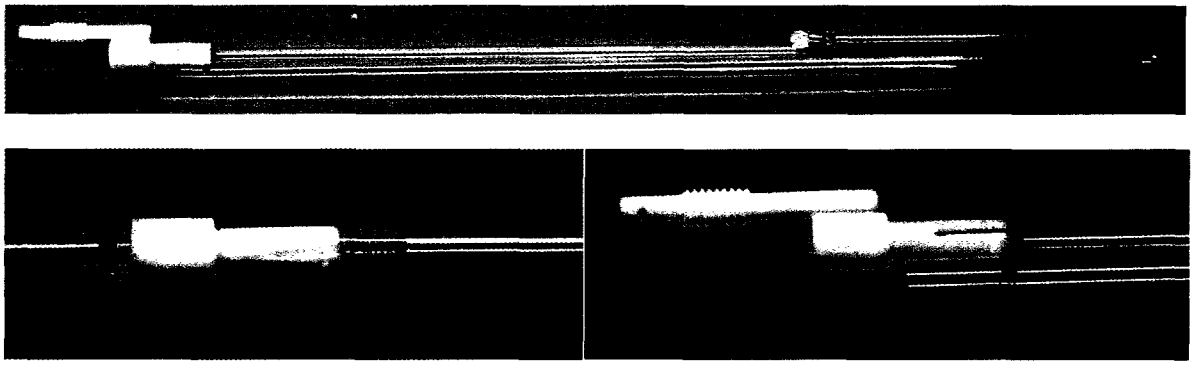

Figure 62. The pictures of the sample holder and container set.

As can be seen in Figure 62, the sample mount system consists of three pieces of high-purity NMR quartz tubes, two pieces of teflon attachments, one sample container, and a Cu-Be spring. The sample container is clamped by two small NMR quartz tubes inside the bigger one. The end of the bigger quartz tube shrinks inward to prevent the inner pieces from sliding out. The teflon pieces are used to make the joint between the quartz tubes and the metal rod. The Cu-Be spring can compensate for possible thermal expansion from different parts of the sample holder in the entire temperature range and holds the sample container in a specific position. The ends of the quartz tubes are open to the sample chamber which allows the helium vapor to hit the sample container directly to reduce the temperature gradient along the vertical direction in the sample holder position.

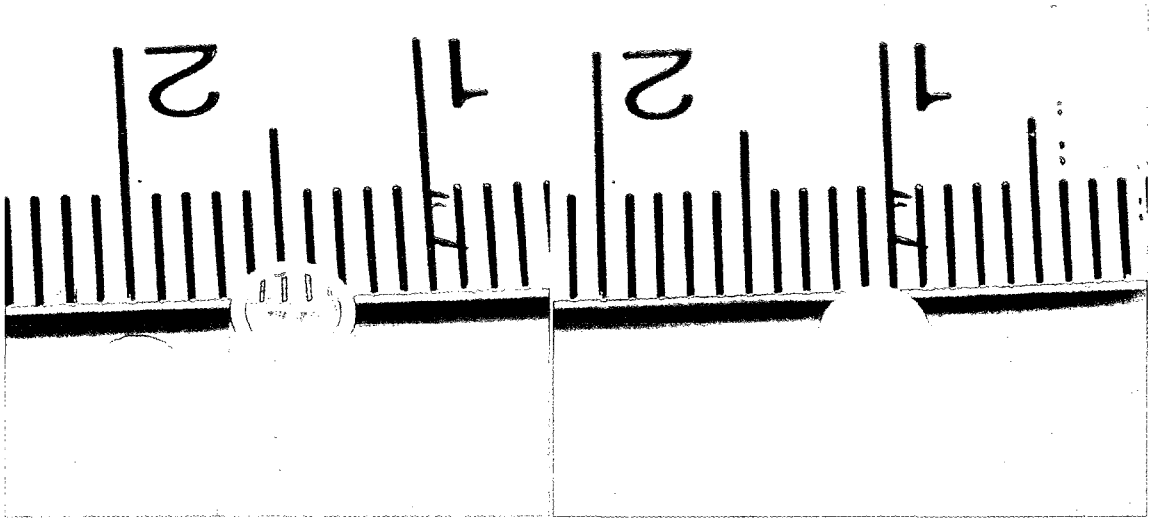

Figure 63. The pictures of the sample containers. The container on the left hand side is made of high-purity quartz, and the one on the right hand side is made of cast acrylic.

The ideal sample container material should be the same as that of the sample holder. The sample container on the left hand side in Figure 63 is made of quartz. The background signal of this kind of sample container is negligibly small and beyond the measurable range of the magnetometer. It is ideal for small signal samples that are in chunk or block forms. The container shown on the right hand side in Figure 63 is made of cast acrylic. It can be precisely machined to give an air-tight fitting between the cup and the lid. No sample leak occurs with this sample container even at temperatures below 2 K. The wall thickness of such a container is as small as 0.2 mm. Although cast acrylic is a poor heat conductor, it keeps the sample temperature the same as that of the helium vapor. The background signal from this sample container can be easily removed by the QD Multivu software.

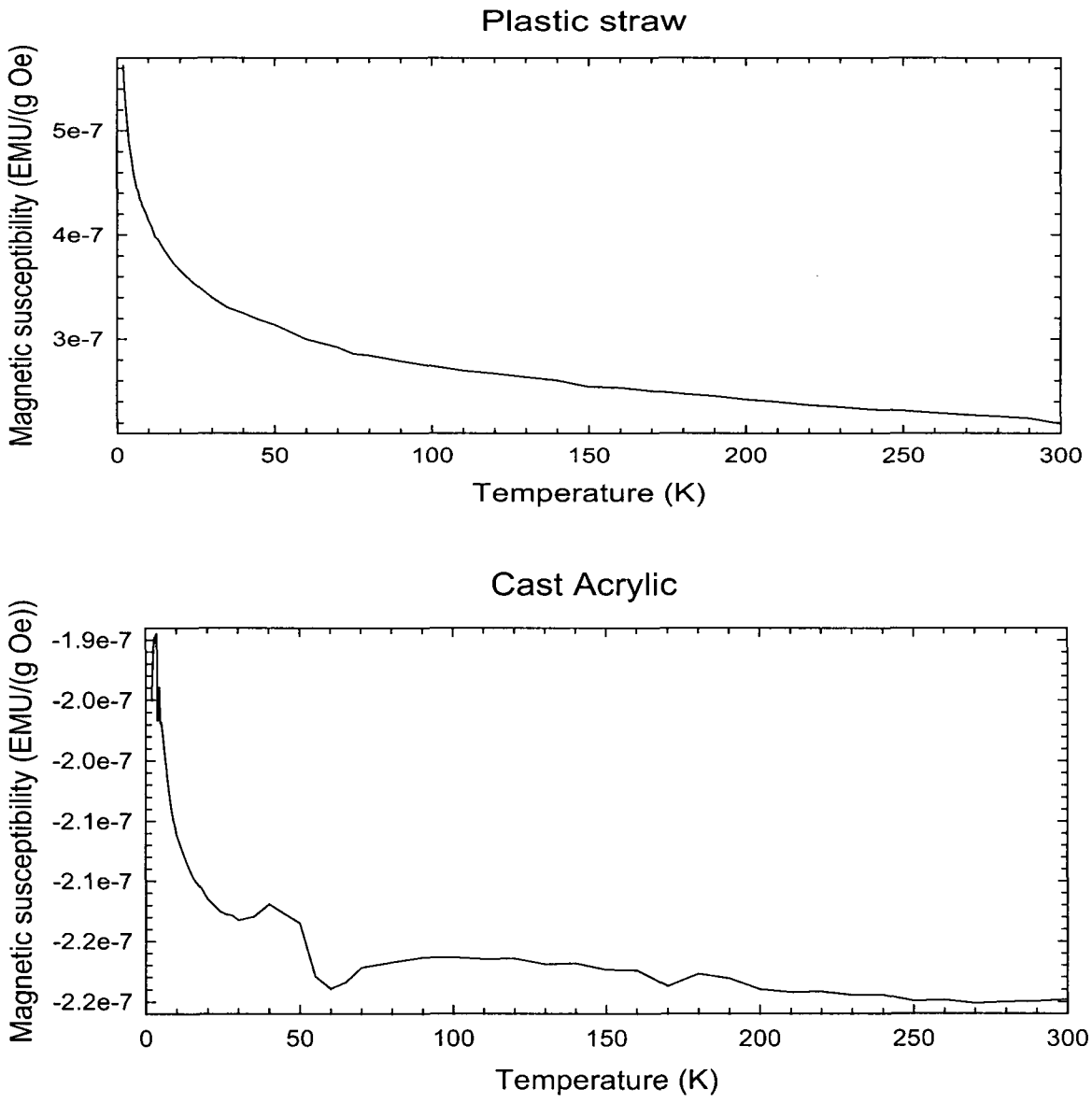

Figure 64. The temperature dependent magnetic susceptibilities of a transparent straw and a cast acrylic cylinder.

Figure 64 The magnetic susceptibility of a transparent straw and cast acrylic

Figure 64 presents the measured magnetic susceptibility curves of the transparent plastic straw and the cast acrylic as sample container materials in the temperature range of 2-300 K. It is clear

that the transparent plastic straw is weak paramagnetic and the cast acrylic is weak diamagnetic in the temperature range of above. However, the absolute susceptibility value of a cast acrylic is three times smaller than that of the transparent straw. It makes the cast acrylic a better sample container material than the transparent plastic straw.

2.3.5 Electrical resistivity measurement

The samples to be measured range from insulators to superconductors and their physical dimensions are normally small, typically 5-10 mm in length, 2-5 mm in width, and 1-2 mm in thickness. To measure the electric resistivity, the four-wire method is used to provide high accuracy results. The four-wire method is shown schematically in Figure 65.

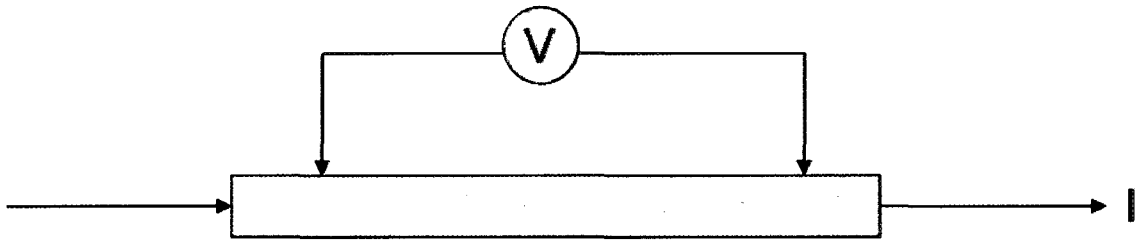

Figure 65. The four-wire method for measuring the electric resistivity of a sample.

The blue bar in Figure 65 indicates the sample to be measured. The current source is attached to the two ends of the sample. A high input impedance voltmeter is connected to the points inside the current source connections, as shown above. The resistance to be measured is typically 10^6 times smaller than the input impedance of a voltmeter. A seven and half digit precision scientific multimeter with input impedance above 10M Ω is used. The sample is pushed against an electrically insulated surface which possesses a larger thermal mass (the capacity of a body to store heat) by the spring-load electric probes. The temperature of the surface is well controlled.

With this structure, one can ensure that the temperature acquired from the sensor is the same as the real temperature of the sample. The EMF effect in low-level measurements can be further reduced by reversing the current direction and calculating the mathematical average of the two absolute voltage readings [102]. The electrical resistivity can be calculated with the measured resistance value and the geometric dimension of the sample.

Traditionally, silver paste or silver epoxy is used to attach the electrical terminals to the sample. The major drawback of this method is that the connections can break due to thermal expansion in the temperature range of 2-300 K. The mechanical spring-loaded electrical contact method is proven to be a more reliable solution. As can be seen in Figure 66, two types of mechanical sample holders were used to measure the electrical resistance in the temperature range of 2-300 K. The springs are made of Be-Cu, whose elastic coefficient is more or less constant in the temperature range of 2-300 K. This unique property makes this material the best for providing a constant pressure on the sample surface for the contacts for cryogenic applications.

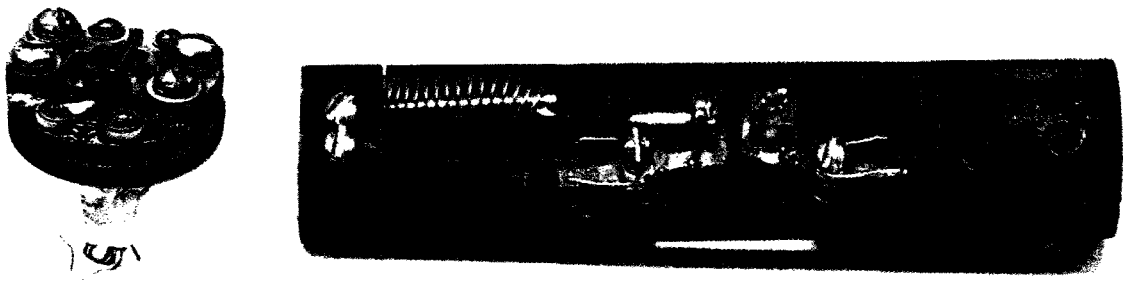

Figure 66. The sample holders for electric resistivity measurements.

The sample holder is attached to the end of an insert rod which is placed in the cryostat. The temperature of the sample is controlled by the combination of the heater installed on the sample holder and the cryostat.

References for Chapter 1 and 2

[1] V. K. Pecharsky and P.Y. Zavalij, *Fundamentals of Powder Diffraction and Structural Characterization of Materials* (Springer, New York, 2005), p. 6.

[2] V. K. Pecharsky and P.Y. Zavalij, *Fundamentals of Powder Diffraction and Structural Characterization of Materials* (Springer, New York, 2005), p. 32.

[3] http://escher.epfl.ch/eCrystallography/3.html

[4] V. K. Pecharsky and P.Y. Zavalij, *Fundamentals of Powder Diffraction and Structural Characterization of Materials* (Springer, New York, 2005), p. 16.

[5] Th. Hahn and A. Vos, in *International Tables for Crystallography*, edited by T. Hahn (Kluwer Academic, Dordrecht, 1989), Vol. **A**, p. 10.

[6] http://en.wikipedia.org/wiki/Crystal_system

[7] V. K. Pecharsky and P.Y. Zavalij, *Fundamentals of Powder Diffraction and Structural Characterization of Materials* (Springer, New York, 2005), p. 38.

[8] http://www.uwgb.edu/DutchS/symmetry/millerdx.htm

[9] V. K. Pecharsky and P.Y. Zavalij, *Fundamentals of Powder Diffraction and Structural Characterization of Materials* (Springer, New York, 2005), p. 51.

[10] V. K. Pecharsky and P.Y. Zavalij, *Fundamentals of Powder Diffraction and Structural Characterization of Materials* (Springer, New York, 2005), p. 72.

[11] V. K. Pecharsky and P.Y. Zavalij, *Fundamentals of Powder Diffraction and Structural Characterization of Materials* (Springer, New York, 2005), p. 65.

[12] W. Steurer, in *Physical Metallurgy*, edited by R. W. Cahn and P. Haasen (Elsevier Science, Amsterdam, 1996), Vol. **1**, p. 374.

[13] W. Steurer, in *Physical Metallurgy*, edited by R. W. Cahn and P. Haasen (Elsevier Science, Amsterdam, 1996), Vol. **1**, p. 377.

[14] W. Steurer, in *Physical Metallurgy*, edited by R. W. Cahn and P. Haasen (Elsevier Science, Amsterdam, 1996), Vol. **1**, p. 378.

[15] http://www.nature.com/nmat/journal/v6/n1/abs/nmat1799.html

[16] V. K. Pecharsky and P.Y. Zavalij, *Fundamentals of Powder Diffraction and Structural Characterization of Materials* (Springer, New York, 2005), p. 148.

[17] V. K. Pecharsky and P.Y. Zavalij, *Fundamentals of Powder Diffraction and Structural Characterization of Materials* (Springer, New York, 2005), p. 151.

[18] V. K. Pecharsky and P.Y. Zavalij, *Fundamentals of Powder Diffraction and Structural Characterization of Materials* (Springer, New York, 2005), p. 155.

[19] A. D. Krawitz, *Introduction to Diffraction in Materials Science and Engineering* (John Wiley & Sons, New York, 2001), p. 106.

[20] L. Liang, R. Rinaldi, and H. Schober, *Neutron Applications in Earth, Energy and Environmental Sciences* (Springer, New York, 2009), p. 15.

[21] D. L. Bish and J. E. Post, *Modern Powder Diffraction* (Reviews in Mineralogy, Washington, D. C., 1989), Vol. **20**, p. 333.

[22] D. L. Bish and J. E. Post, *Modern Powder Diffraction* (Reviews in Mineralogy, Washington, D. C., 1989), Vol. **20**, p. 335.

[23] G. L. Squires, *Thermal Neutron Scattering* (Cambridge University Press, London, 1978), p. 6.

[24] G. L. Squires, *Thermal Neutron Scattering* (Cambridge University Press, London, 1978), p. 14.

[25] G. Shirane, S. M. Shapiro, and J. M. Tranquada, Neutron Scattering with a Triple-Axis Spectrometer (Cambridge University Press, Cambridge, 2002).

[26] L. B. McCusker, R. B. Von Dreele, D. E. Cox, D. Louër and P. Scardi, J. Appl. Crystallogr. **32**, 36 (1999).

[27] V. K. Pecharsky and P.Y. Zavalij, *Fundamentals of Powder Diffraction and Structural Characterization of Materials* (Springer, New York, 2005), p. 174.

[28] K. H. J. Buschow and F. R. de Boer, *Physics of Magnetism and Magnetic Materials* (Kluwer Academic, New York, 2003), p. 24.

[29] A. H. Morrish, *The Physical Principles of Magnetism* (John Wiley & Sons, New York, 1965), p. 38.

[30] A. H. Morrish, *The Physical Principles of Magnetism* (John Wiley & Sons, New York, 1965), p. 46.

[31] A. P. Guimarães and I. S. Oliveira, *Magnetism and Magnetic Resonance in Solids* (John Wiley & Sons, New York, 1998), p. 33.

[32] A. P. Guimarães and I. S. Oliveira, *Magnetism and Magnetic Resonance in Solids* (John Wiley & Sons, New York, 1998), p. 45.

[33] A. H. Morrish, *The Physical Principles of Magnetism* (John Wiley & Sons, New York, 1965), p. 72.

[34] K. H. J. Buschow and F. R. de Boer, *Physics of Magnetism and Magnetic Materials* (Kluwer Academic, New York, 2003), p. 22.

[35] P. Mohn, in *Magnetism in the Solid State*, edited by M. Cardona, P. Fulde, K. von Klitzing, and H. J. Queisser (Springer, Berlin, 2006), p. 71.

[36] K. H. J. Buschow and F. R. de Boer, *Physics of Magnetism and Magnetic Materials* (Kluwer Academic, New York, 2003), p. 20.

[37] A. H. Morrish, *The Physical Principles of Magnetism* (John Wiley & Sons, New York, 1965), p. 261.

[38] K. H. J. Buschow and F. R. de Boer, *Physics of Magnetism and Magnetic Materials* (Kluwer Academic, New York, 2003), p. 21.

[39] A. H. Morrish, *The Physical Principles of Magnetism* (John Wiley & Sons, New York, 1965), p. 268.

[40] A. H. Morrish, *The Physical Principles of Magnetism* (John Wiley & Sons, New York, 1965), p. 263.

[41] A. H. Morrish, *The Physical Principles of Magnetism* (John Wiley & Sons, New York, 1965), p. 269.

[42] A. Arrott, Phys. Rev. **108**, 6 (1957).

[43] A. Arrott and J. E. Noakes, Phys. Rev. Lett. **19**, 14 (1967).

[44] K. H. J. Buschow and F. R. de Boer, *Physics of Magnetism and Magnetic Materials* (Kluwer Academic, New York, 2003), p. 26.

[45] K. H. J. Buschow and F. R. de Boer, *Physics of Magnetism and Magnetic Materials* (Kluwer Academic, New York, 2003), p. 34.

[46] H. Maletta and W. Zinn, in *Handbook on the Physics and Chemistry of Rare Earths* (Elsevier Science, Amsterdam, 1989), Vol. **12**, p. 215.

[47] H. Maletta and W. Zinn, in *Handbook on the Physics and Chemistry of Rare Earths* (Elsevier Science, Amsterdam, 1989), Vol. **12**, p. 230.

[48] H. Nishimori, in *Statistical Physics of Spin Glasses and Information Processing*, edited by J. Birman, S. F. Edwards, R. Friend, C. H. Llewellyn-Smith, M. Rees, D. Sherrington, and G. Veneziano (Oxford University Press, Oxford, 2001), p. 13.

[49] H. Maletta and W. Zinn, in *Handbook on the Physics and Chemistry of Rare Earths* (Elsevier Science, Amsterdam, 1989), Vol. **12**, p. 231.

[50] H. Nishimori, in *Statistical Physics of Spin Glasses and Information Processing*, edited by J. Birman, S. F. Edwards, R. Friend, C. H. Llewellyn-Smith, M. Rees, D. Sherrington, and G. Veneziano (Oxford University Press, Oxford, 2001), p. 14.

[51] H. Maletta and W. Zinn, in *Handbook on the Physics and Chemistry of Rare Earths* (Elsevier Science, Amsterdam, 1989), Vol. **12**, p. 232.

[52] H. Maletta and W. Zinn, in *Handbook on the Physics and Chemistry of Rare Earths* (Elsevier Science, Amsterdam, 1989), Vol. **12**, p. 234.

[53] H. Maletta and W. Zinn, in *Handbook on the Physics and Chemistry of Rare Earths* (Elsevier Science, Amsterdam, 1989), Vol. **12**, p. 243.

[54] H. Maletta and W. Zinn, in *Handbook on the Physics and Chemistry of Rare Earths* (Elsevier Science, Amsterdam, 1989), Vol. **12**, p. 249.

[55] P. Gütlich, R. Link, and A. Trautwein, *Mössbauer Spectroscopy andTransition Metal Chemistry* (Springer-Verlag, Berlin, 1978), p. 1.

[56] U. Gonser, *Mössbauer Spectroscopy* (Springer-Verlag, New York, 1975), p. 6.

[57] U. Gonser, *Mössbauer Spectroscopy* (Springer-Verlag, New York, 1975), p. 12.

[58] U. Gonser, *Mössbauer Spectroscopy* (Springer-Verlag, New York, 1975), p. 14.

[59] P. Gütlich, R. Link, and A. Trautwein, *Mössbauer Spectroscopy andTransition Metal Chemistry* (Springer-Verlag, Berlin, 1978), p. 4.

[60] U. Gonser, *Mössbauer Spectroscopy* (Springer-Verlag, New York, 1975), p. 22.

[61] U. Gonser, *Mössbauer Spectroscopy* (Springer-Verlag, New York, 1975), p. 24.

[62] U. Gonser, *Mössbauer Spectroscopy* (Springer-Verlag, New York, 1975), p. 26.

[63] U. Gonser, *Mössbauer Spectroscopy* (Springer-Verlag, New York, 1975), p. 17.

[64] U. Gonser, *Mössbauer Spectroscopy* (Springer-Verlag, New York, 1975), p. 25.

[65] P. Gütlich, R. Link, and A. Trautwein, *Mössbauer Spectroscopy andTransition Metal Chemistry* (Springer-Verlag, Berlin, 1978), p. 21.

[66] P. Gütlich, R. Link, and A. Trautwein, *Mössbauer Spectroscopy andTransition Metal Chemistry* (Springer-Verlag, Berlin, 1978), p. 22.

[67] J.S. Dugdale, *The Electrical Properties of Disordered Metals* (Cambridge University Press, New York, 1995).

[68] A. Schmid, Z. Physik **271**, 251 (1974).

[69] A. Schmid, Z. Physik **259**, 421 (1973).

[70] B. Keck and A. Schmid, J. Low. Temp. Phys. **24**, 611 (1976).

[71] S. Chakravarty and A. Schmid, Phys. Rep. **140**, 193 (1986).

[72] N.F. Mott, *Metal-Insulator Transitions* (Taylor & Francis, London, 1990).

[73] http://newton.ex.ac.uk/teaching/th/phy2208/lect19.pdf

[74] P. Wang and Z. M. Stadnik, J. Phys.: Condens. Matter **19**, 346235 (2007).

[75] http://www.centorr.com/lab/5bj.htm

[76] A. Berthault, L. Arles, and J. Matricon, Int. J. Thermophys. **7**, 1 (1986).

[77] J. D. Corbett and A. Simon, Inorg. Synth. **22**, 15 (1983).

[78] http://www.2spi.com/catalog/mounts/vitreous.html

[79] A. B. John, J. Neurosci. Meth. **135**, 89 (2004).

[80] http://www.sentrotech.com/technical.php

[81] P. C. Canfield and Z. Fisk, Philos. Mag. B **65**, 1117 (1991).

[82] http://sine.ni.com/nips/cds/print/p/lang/en/nid/14136

[83] http://srdata.nist.gov/its90/download/type_k.tab

[84] http://www.analog.com/static/imported-files/data_sheets/AD594_595.pdf

[85] http://www.analog.com/static/imported-files/data_sheets/AD637.pdf

[86] http://www.analog.com/static/imported-files/data_sheets/ADR440_441_443_444_445.pdf

[87] http://zone.ni.com/reference/en-XX/help/371361A-01/lvwave/averaged_dc_rms/

[88] http://www.eolss.net/ebooks/Sample%20Chapters/C18/E6-43-03-03.pdf

[89] http://www.ameritherm.com/PDFs/411-0050-00.pdf

[90] *X'pert System User's Guide, second edition* (1992).

[91] R. Jenkins and R. L. Snyder R L, *Introduction to X-ray Powder Diffractometry* (John Wiley & Sons, New York, 1996), p. 1.

[92] R. Jenkins and R. L. Snyder R L, *Introduction to X-ray Powder Diffractometry* (John Wiley & Sons, New York, 1996), p. 112.

[93] R. Jenkins and R. L. Snyder R L, *Introduction to X-ray Powder Diffractometry* (John Wiley & Sons, New York, 1996), p. 183.

[94] R. Jenkins and R. L. Snyder R L, *Introduction to X-ray Powder Diffractometry* (John Wiley & Sons, New York, 1996), p. 192.

[95] R. Jenkins and R. L. Snyder R L, *Introduction to X-ray Powder Diffractometry* (John Wiley & Sons, New York, 1996), p. 193.

[96] U. Gonser, *Mössbauer Spectroscopy* (Springer-Verlag, New York, 1975), p. 36.

[97] J. Vrba, A. A. Fife, and M. B. Burbank, Can. J. Phys. **60**, 1060 (1981).

[98] *MPMS MultiVu Application User's Manual* 1014-110C 3-10.

[99] *Quantum Design MPMS Application Note* 1014-213 (2002).

[100] *MPMS MultiVu Application User's Manual* 1014-110C.

[101] L. H. Lewis and M. B. Konrad, Rev. Sci. Instrum. **67**, 10 (1996).

[102] *Low Level Measurements*, edited by J. Yeager and M. A Hrusch-Tupta (Keithley, Cleveland, 1996).

Chapter 3 Magnetic properties and ^{155}Gd Mössbauer spectroscopy of the rare-earth Heusler compound Cu_2GdIn

P. Wang and Z.M. Stadnik.

J. Phys.: Condens. Matter, **19**, 346235 (2007).

IOP PUBLISHING JOURNAL OF PHYSICS: CONDENSED MATTER

J. Phys.: Condens. Matter **19** (2007) 346235 (10pp) doi:10.1088/0953-8984/19/34/346235

Magnetic properties and ^{155}Gd Mössbauer spectroscopy of the rare-earth Heusler compound Cu_2GdIn

Pu Wang and Zbigniew M Stadnik[1]

Department of Physics, University of Ottawa, Ottawa, ON, K1N 6N5, Canada

E-mail: stadnik@uottawa.ca

Received 28 May 2007, in final form 10 July 2007
Published 31 July 2007
Online at stacks.iop.org/JPhysCM/19/346235

Abstract

The results of x-ray diffraction, magnetic susceptibility, and ^{155}Gd Mössbauer spectroscopy studies of the rare-earth Heusler compound Cu_2GdIn are reported. The studied compound has the $L2_1$ crystal structure with the lattice constant of 0.666 43(3) nm. Cu_2GdIn is an antiferromagnet with the Néel temperature T_N = 9.6(1) K. The temperature dependence of the magnetic susceptibility above T_N follows the Curie–Weiss law with the effective magnetic moment of 7.98(4) μ_B per Gd atom and the paramagnetic Curie temperature of −41.2(9) K. The Debye temperature of Cu_2GdIn is 229(5) K. The temperature dependence of the hyperfine magnetic field follows a $J = 7/2$ Brillouin function. It is shown that the total contribution to the hyperfine magnetic field at ^{155}Gd nuclei in Gd-containing Heusler compounds resulting from the conduction electron polarization is +9.8(2.5) T.

(Some figures in this article are in colour only in the electronic version)

1. Introduction

Heusler compounds are ternary intermetallic compounds having the general composition X_2YZ. In the traditional Heusler compounds, X and Y stand for d-electron transition metals and Z denotes an sp-electron element [1]. These compounds possess the characteristic $L2_1$ crystal structure (space group $Fm\bar{3}m$, No 225) with the unit cell consisting of four interpenetrating face-centred cubic sub-lattices. They have been extensively investigated for their magnetic properties [1]. The majority of these traditional Heusler compounds are ferromagnets and some of them order antiferromagnetically [1].

[1] Author to whom any correspondence should be addressed.

0953-8984/07/346235+10$30.00

There is a small number of Heusler compounds in which Y is a rare earth element, R. These include the most intensively studied system Pd_2RSn (R = Tb–Lu) [2–18], Pd_2RIn (R = La, Gd, Ho, Yb, Lu) [19–23], Pd_2RPb (R = Gd–Lu) [24], Pd_2RSb (R = Gd–Er) [25, 26], Pd_2RBi (R = Dy–Er) [25, 26], Au_2RIn (R = La–Nd, Er–Yb) [27, 28], Ag_2RIn (R = La–Nd, Sm, Gd–Yb) [29–33], and Cu_2RIn (R = La–Nd, Sm, Gd–Er, Lu) [34–41]. In contrast to the traditional Heusler compounds, the majority of rare-earth Heusler compounds are antiferromagnets [3, 5, 7–9, 13, 15, 24, 25, 30–33, 35, 36, 38–41].

In this paper we report on an investigation of magnetism of the Heusler compound Cu_2GdIn through measurements of magnetic susceptibility and ^{155}Gd Mössbauer spectroscopy.

2. Experimental procedure

An ingot of nominal composition Cu_2GdIn was prepared by melting constituent elements in an induction furnace on a water-cooled Cu boat under an Ar atmosphere. Purities of the starting elements were 99.999%, 99.999%, and 99.998% for Cu, In, and Gd, respectively. The melting was repeated four times, in each case after turning the ingot over. The total weight loss after the melting was 1.1%.

X-ray diffraction measurement was performed at 298 K in Bragg–Brentano geometry on the PANanalytical X'Pert scanning diffractometer using Cu Kα radiation. The Kβ line was eliminated by using a Kevex PSi2 Peltier-cooled solid-state Si detector. In order to avoid the deviation from intensity linearity of the solid-state Si detector, its parameters and the parameters of the diffractometer were chosen in such a way as to limit the count rate from the most intense Bragg peaks to less than 9000 counts s^{-1} [42].

The magnetic susceptibility was measured with a Quantum Design superconducting quantum interference device magnetometer at various fields in the temperature range 4.5–295 K.

The ^{155}Gd MS measurements in the temperature range 1.5–20.0 K were conducted using a standard Mössbauer spectrometer operating in a sine mode and a source of $^{155}Eu(SmPd_3)$. The source was kept at the same temperature as that of the absorber. The spectrometer was calibrated with a Michelson interferometer [43], and the spectra were folded. The Mössbauer absorber was made of pulverized material pressed into a pellet which was then put into an Al disk container of thickness 0.008 mm to ensure a uniform temperature over the whole sample. The surface density of the Mössbauer absorber of the studied compound was 352 mg cm^{-2}. The 86.5 keV γ-rays were detected with a 2.5 cm NaI(Tl) scintillation detector covered with a 0.6 mm Pb plate to cut off the 105.3 keV γ-rays emitted from the source.

The Mössbauer spectra were analyzed by means of a least-squares fitting procedure which entailed calculations of the positions and relative intensities of the absorption lines by numerical diagonalization of the full hyperfine interaction Hamiltonian. The interference ξ factor for the E1 transition of 86.5 keV in ^{155}Gd was fixed to the value of 0.0520, which was derived from the fit of the ^{155}Gd Mössbauer spectrum of $GdFe_2$ at 4.2 K (data not shown here). The resonance line shape of the Mössbauer spectra was described by a transmission integral formula [44, 45]. In addition to the hyperfine parameters, only the absorber Debye–Waller factor f_a and the absorber linewidth Γ_a were fitted as independent parameters. The source linewidth $\Gamma_s = 0.334$ mm s^{-1} and the background-corrected Debye–Waller factor of the source f_s^* [44, 45], which were derived from the fit of the ^{151}Gd Mössbauer spectrum of $GdFe_2$ at 4.2 K, were used. The $^{155}Eu(SmPd_3)$ source at 1.5 K emits a broadened emission line; from the fit of the ^{151}Gd Mössbauer spectrum of $GdFe_2$ at 1.5 K we found that $\Gamma_s = 0.708$ mm s^{-1}.

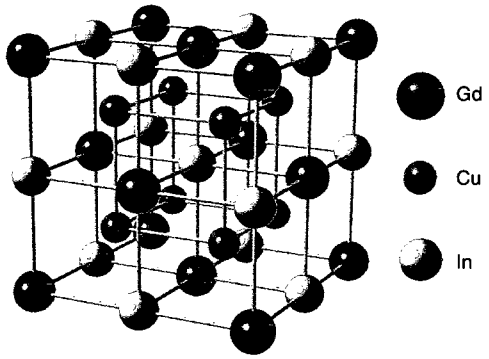

Figure 1. Heusler $L2_1$ crystal structure of Cu_2GdIn.

Table 1. Crystallographic data for Cu_2GdIn.

Atom	Site	Point symmetry	x	y	z	Occupancy
Gd	4a	$m\bar{3}m$	0	0	0	1.0
In	4b	$m\bar{3}m$	$\frac{1}{2}$	$\frac{1}{2}$	$\frac{1}{2}$	1.0
Cu	8c	$\bar{4}3m$	$\frac{1}{4}$	$\frac{1}{4}$	$\frac{1}{4}$	1.0

3. Results and discussion

3.1. Structural characterization

The compound Cu_2GdIn forms in the $L2_1$ crystal structure with the space group $Fm\bar{3}m$ (No 225). Figure 1 shows the crystal structure of Cu_2GdIn, and the crystallographic data for the Gd, In, and Cu sites are given in table 1.

The x-ray powder diffraction pattern of Cu_2GdIn is shown in figure 2. A Rietveld refinement of the x-ray powder diffraction data was performed, yielding the lattice constant $a = 0.666\,43(3)$ nm. The studied sample contains a trace of Cu_4GdIn second phase in the amount of 3.7(5) wt% as determined from the Rietveld refinement of the x-ray powder diffraction pattern (figure 2). The studied Heusler compound Cu_2GdIn could be thus slightly off stoichiometry.

3.2. Magnetic susceptibility

The temperature dependence of the magnetic susceptibility χ of Cu_2GdIn measured in an applied magnetic field of 0.5 T between 4.5 and 295 K is shown in figure 3(a). The $\chi(T)$ curve exhibits a sharp peak at 9.6(1) K (inset in figure 3(a)). This indicates that Cu_2GdIn is an antiferromagnet with the Néel temperature $T_N = 9.6(1)$ K.

The $\chi(T)$ data above 100 K could be fitted to a modified Curie–Weiss law

$$\chi = \chi_0 + \frac{C}{T - \theta_p}, \tag{1}$$

where χ_0 is the temperature independent magnetic susceptibility, C is the Curie constant, and θ_p is the paramagnetic Curie temperature. The Curie constant can be expressed as $C = \frac{N\mu_{eff}^2}{3k}$, where N is the concentration of magnetic atoms per unit mass and μ_{eff} is the effective magnetic moment. Figure 3(b) shows the inverse magnetic susceptibility corrected for the contribution

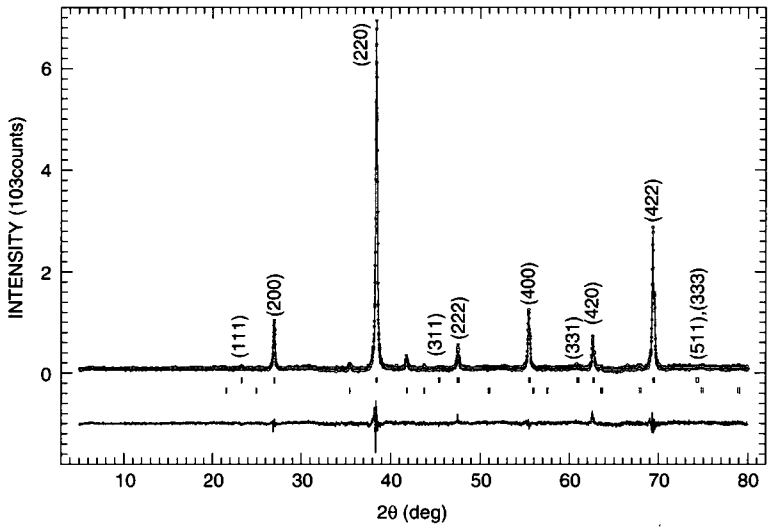

Figure 2. The x-ray powder diffraction spectrum of Cu_2GdIn at 298 K. The experimental data are denoted by open circles, while the line through the data represents the results of the Rietveld refinement. The upper set of vertical bars represents the Bragg peak positions corresponding to the principal Cu_2GdIn phase, while the lower set refers to the positions of the minor impurity Cu_4GdIn phase. The lower curve is the difference curve between the experimental data and the calculated curve.

χ_0, $(\chi - \chi_0)^{-1}$ versus temperature; the validity of the Curie–Weiss law is evident. The values of χ_0, C, and θ_p obtained from the fit are, respectively, 5.50(17) $\times$ 10^{-6} emu g^{-1}, 19.94(20) $\times$ 10^{-3} emu K g^{-1}, and $-41.2(9)$ K. This value of C corresponds to μ_{eff} of 7.98(4) μ_B per Gd atom.

For a free Gd^{3+} ion (electronic ground state $^8S_{7/2}$), the theoretical value of $\mu_{eff}^{th} = g\mu_B\sqrt{J(J+1)}$ is 7.94 μ_B [46]. The fact that the experimental value $\mu_{eff} = 7.98(4)$ μ_B is very close to the theoretical value of 7.94 μ_B confirms that the magnetic moment is localized on the Gd^{3+} ions and that, as expected, Cu and In atoms carry no magnetic moment. The negative value of θ_p indicates the predominantly antiferromagnetic interaction between the Gd^{3+} spins.

3.3. Mössbauer spectroscopy

Figure 4 displays ^{151}Gd Mössbauer spectra of Cu_2GdIn measured at temperatures above the Néel temperature. The Gd^{3+} ions are located in the Heusler structure at the site with the point symmetry $m\bar{3}m$ (table 1). This ensures a zero electric field gradient at the Gd^{3+} site and hence zero electric quadrupole splitting. The spectra in figure 4 exhibit thus no electric quadrupole interaction and are fitted with a single line. The parameters derived from the fits are given in table 2.

The values of the isomer shift (relative to the $^{155}Eu(SmPd_3)$ source) δ of $\sim$0.42 mm s^{-1} are characteristic for Gd atoms being in a trivalent state [47]. In terms of the Debye approximation of the lattice vibrations, the absorber Debye–Waller factor f_a is expressed [48, 49] by the Debye temperature, Θ_D, as

$$f_a(T) = \exp\left\{-\frac{3}{4}\frac{E_\gamma^2}{Mc^2k\Theta_D}\left[1 + \left(\frac{T}{\Theta_D}\right)^2 \int_0^{\Theta_D/T} \frac{x\,dx}{e^x - 1}\right]\right\}, \qquad (2)$$

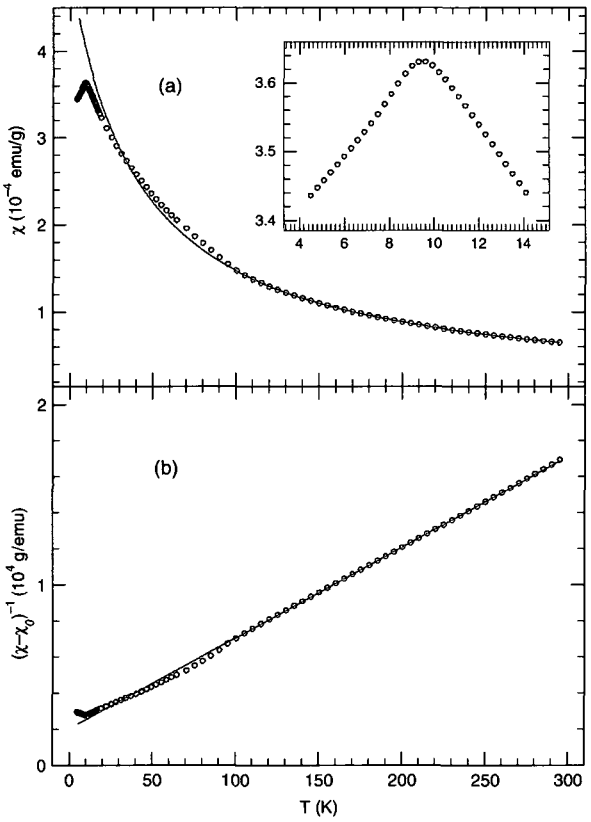

Figure 3. (a) The temperature dependence of the magnetic susceptibility of Cu_2GdIn, measured in an external magnetic field of 0.5 T. The solid line is the fit to equation (1) in the temperature range 100–295 K. The temperature dependence of the magnetic susceptibility in the low-temperature range is presented in the inset. (b) The inverse magnetic susceptibility corrected for the contribution χ_0, $(\chi - \chi_0)^{-1}$ versus temperature T of Cu_2GdIn. The solid line is the fit to equation (1) in the temperature range 100–295 K.

Table 2. Hyperfine interaction parameters derived from the fits to the ^{151}Gd Mössbauer spectra of Cu_2GdIn at various temperatures.

T (K)	δ (mm s^{-1})	Γ_a (mm s^{-1})	H_{hf} (T)	f_a (%)	χ^2
20.0	0.405(3)	0.408(10)		12.6(3)	1.00
12.6	0.415(4)	0.425(12)		13.3(3)	1.01
10.2	0.422(4)	0.460(13)		13.7(4)	1.13
9.1	0.406(3)	0.460(12)	6.62(32)	13.7(3)	0.91
8.1	0.421(4)	0.461(11)	12.51(22)	13.8(3)	1.01
7.0	0.405(4)	0.461(10)	16.37(20)	12.8(4)	1.03
5.9	0.414(3)	0.461(12)	18.51(15)	13.8(3)	1.15
4.9	0.407(4)	0.460(13)	20.56(16)	13.8(4)	1.20
1.5	0.414(5)	0.462(14)	22.72(27)	13.9(4)	1.17

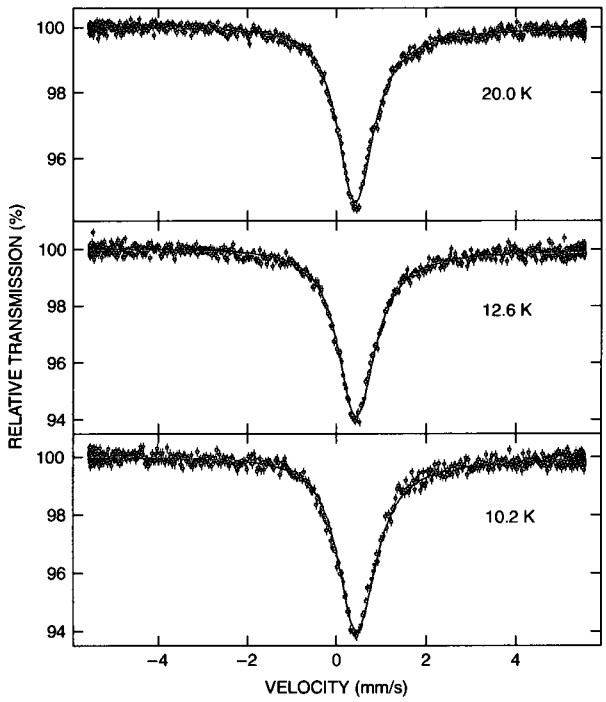

Figure 4. ^{155}Gd Mössbauer spectra of Cu_2GdIn at various temperatures above the Néel temperature. Solid lines are fits, as described in the text. The zero-velocity scale is relative to the source.

where E_γ is the energy of the Mössbauer transition, M is the mass of the Mössbauer nucleus, c is the speed of light, and k is the Boltzmann constant. The analysis of the values of f_a given in table 2 via equation (2) yields $\Theta_D = 229(5)$ K. This value compares well with $\Theta_D = 183$ K for an isostructural Heusler compound Cu_2LaIn [50].

^{151}Gd Mössbauer spectra of Cu_2GdIn measured at temperatures below the Néel temperature are shown in figure 5. They exhibit the presence of a magnetic dipole hyperfine interaction. It is not visually obvious that the ^{151}Gd Mössbauer spectrum at 9.1 K results from a non-zero magnetic dipole hyperfine interaction, i.e., that the non-zero hyperfine magnetic field, H_{hf}, sets in. The 9.1 K spectrum looks like a single-line spectrum, similar to those shown in figure 4. The fit of this spectrum with a single line yields $\Gamma_a = 0.539(9)$ mm s^{-1} and $\chi^2 = 0.99$. A substantial increase of Γ_a from 0.460(13) mm s^{-1} for the 8.0 K spectrum (table 2) to 0.539(9) mm s^{-1} for the 9.1 K spectrum proves that indeed the observed broadening results from the non-zero H_{hf} being established in the 9.1 K spectrum. In addition, the value of $\chi^2 = 0.91$ obtained for the fit of the 9.1 K spectrum with a Zeeman pattern (table 2) is smaller than the value of 0.99 obtained for a single-line fit. The parameters derived from the fits of the spectra in figure 5 with a non-zero magnetic dipole hyperfine interaction are given in table 2.

Figure 6 shows the temperature dependence of the hyperfine magnetic field determined from the fits of the spectra in figure 5. The hyperfine magnetic field is generally proportional to the magnetic moment of Gd atoms. Its temperature dependence will reflect the latter and follows a Brillouin function [46]. The temperature dependence of $H_{hf}(T)$ can thus be

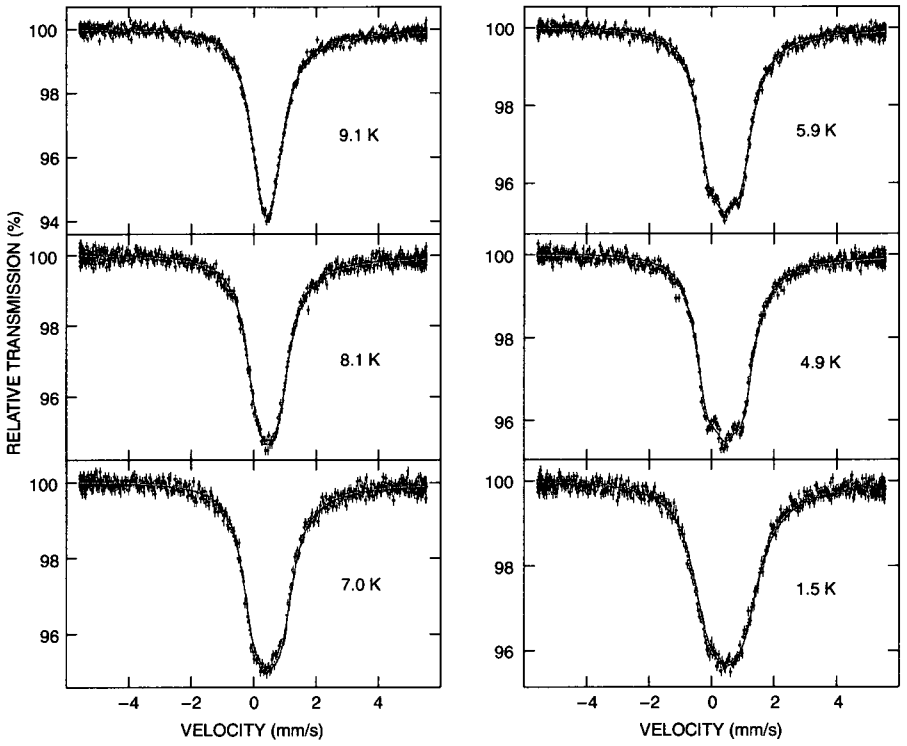

Figure 5. ^{155}Gd Mössbauer spectra of Cu_2GdIn at various temperatures below the Néel temperature. Solid lines are fits, as described in the text. The zero-velocity scale is relative to the source.

expressed as

$$H_{hf}(T) = H_{hf}(0)B_J(x), \tag{3}$$

where $H_{hf}(0)$ is the saturation hyperfine magnetic field, $B_J(x)$ is the Brillouin function defined as

$$B_J(x) = \frac{2J+1}{2J}\coth\left(\frac{2J+1}{2J}x\right) - \frac{1}{2J}\coth\left(\frac{x}{2J}\right) \tag{4}$$

and

$$x = \frac{3J}{J+1}\frac{H_{hf}(T)}{H_{hf}(0)}\frac{T_N}{T}. \tag{5}$$

A least-squares fit of the $H_{hf}(T)$ data to equation (3) with $J = 7/2$ yields $H_{hf}(0) = 23.68(25)$ T and $T_N = 9.5(1)$ K. The value of T_N determined from the fit is in excellent agreement with the value determined from the susceptibility measurement.

The hyperfine magnetic field at the ^{155}Gd nuclei in Cu_2GdIn can be expressed as the sum of three terms

$$H_{hf} = H_{cp} + H_s + H_{tr}. \tag{6}$$

The core polarization field, H_{cp}, is due to the exchange interaction between the local Gd 4f electrons and the core electrons. Its value, $-34.0(2.0)$ T [51–53], is assumed to be independent

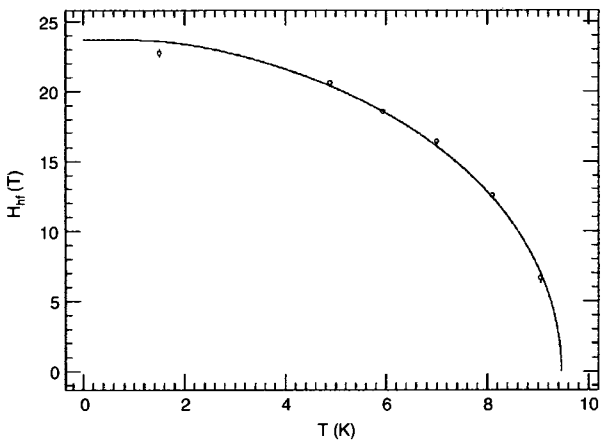

Figure 6. The temperature dependence of the hyperfine magnetic field of Cu_2GdIn. The solid line is the fit to a $J = 7/2$ Brillouin function (equation (3)), as explained in the text.

of the Gd environment in solids. The negative sign arises from the fact that H_{cp} is antiparallel to the parent Gd 4f magnetic moment. The self-polarization term, H_s, results from the conduction electron polarization by the spin of the parent Gd atom and is usually parallel to the Gd magnetic moment. The transferred field, H_{tr}, is due to the conduction electron polarization by the surrounding Gd spins. For collinear magnetic structure, it is parallel to the Gd magnetic moment. In the absence of an externally applied magnetic field, one cannot determine the sign of the measured H_{hf}. However, in many Gd compounds the sign of H_{hf} was demonstrated to be negative [54–57]. Assuming thus that $H_{hf}(0) = -23.68(25)$ T allows one by using equation (6) to determine the total contribution from the conduction electron polarization $H_s + H_{tr}$ to be $+10.32(2.25)$ T.

The magnitude of the hyperfine magnetic field at the ^{155}Gd nuclei in an isostructural Heusler compound Ag_2GdIn at 4.2 K is 24.8(8) T [58]. By using the same analysis as above, one finds that in Ag_2GdIn the total contribution from the conduction electron polarization is $+9.2(2.8)$ T. One can thus conclude that the total contribution to the hyperfine magnetic field at the ^{155}Gd nuclei from the conduction electron polarization in Gd-containing Heusler compounds is $+9.8(2.5)$ T.

4. Conclusions

A rare-earth Heusler compound Cu_2GdIn has been studied with x-ray diffraction, magnetic susceptibility, and ^{155}Gd Mössbauer spectroscopy. This compound has the $L2_1$ crystal structure with the lattice constant of 6.6643(3) Å. Gd magnetic moments order antiferromagnetically with the Néel temperature $T_N = 9.6(1)$ K. The temperature dependence of the magnetic susceptibility above T_N follows the Curie–Weiss law with the effective magnetic moment of 7.98(4) μ_B per Gd atom and the paramagnetic Curie temperature of $-41.2(9)$ K. The Debye temperature of Cu_2GdIn is 229(5) K. The temperature dependence of the hyperfine magnetic field at the ^{155}Gd nuclei follows a $J = 7/2$ Brillouin function and the saturation hyperfine magnetic field is $-23.68(25)$ T. It is shown that total contribution to the hyperfine magnetic field at ^{155}Gd nuclei in Gd-containing Heusler compounds resulting from the conduction electron polarization is $+9.8(2.5)$ T.

Acknowledgment

This work was supported by the Natural Sciences and Engineering Research Council of Canada.

References

[1] Webster P J and Ziebeck K R A 1988 *Magnetic Alloy and Compounds of d-Elements with Main Group Elements* (*Landolt-Börnstein New Series* Group III, vol 19c) ed H P J Wijn (Berlin: Springer) p 75
Ziebeck K R A and Neuman K-U 2001 *Magnetic Properties of Metals* (*Landolt-Börnstein New Series* Group III, vol 32) ed H P J Wijn (Berlin: Springer) p 64
[2] Johnson M J and Shelton R N 1984 *Solid State Commun.* **52** 839
[3] Malik S K, Umarji A M and Shenoy G K 1985 *Phys. Rev.* B **31** 6971
[4] Kierstead H A, Dunlap B D, Malik S K, Umarji A M and Shenoy G K 1985 *Phys. Rev.* B **32** 135
[5] Umarji A M, Malik S K and Shenoy G K 1985 *Solid State Commun.* **53** 1029
[6] Shelton R N, Hausermann-Berg L S, Johnson M J, Klavins P and Yang H D 1986 *Phys. Rev.* B **34** 199
[7] Malik S K, Umarji A M and Shenoy G K 1986 *Phys. Rev.* B **34** 3144
[8] Stanley H B, Lynn J W, Shelton R N and Klavins P 1987 *J. Appl. Phys.* **61** 3371
[9] Donaberger R L and Stager C V 1987 *J. Less-Common Met.* **127** 93
[10] Li W-H, Lynn J W, Stanley H B, Udovic T J, Shelton R N and Klavins P 1989 *Phys. Rev.* B **39** 4199
[11] Crangle J, Neumann K-U, Smith J G and Ziebeck K R A 1995 *J. Magn. Magn. Mater.* **140–144** 919
[12] Babateen M, Neumann K-U and Ziebeck K R A 1995 *J. Magn. Magn. Mater.* **140–144** 921
[13] Parsons M J, Crangle J, Dennis B, Neumann K-U and Ziebeck K R A 1996 *Czech. J. Phys.* **46** (Suppl. S4) 2059
[14] Aoki Y, Sato H R, Matsuda T D, Sugawara H and Sato H 1998 *J. Magn. Magn. Mater.* **177–181** 559
[15] Dönni A, Fischer P, Fauth F, Convert P, Aoki Y, Sugawara H and Sato H 1999 *Physica* B **259–261** 705
[16] Aoki Y, Sato H R, Sugawara H and Sato H 2000 *Physica* C **333** 187
[17] Amato A, Roessli B, Fischer P, Bernhoeft N, Stunault A, Baines C, Dönni A and Sugawara H 2003 *Physica* B **326** 369
[18] Giudicelli P, Roessli B, Stunault A, Ollivier J, Amato A, Sugawara H and Bernhoeft N 2004 *J. Magn. Magn. Mater.* **272–276** e141
[19] Neumann K-U, Crangle J, Giles R T, Visser D, Zayer N K and Ziebeck K R A 1992 *Solid State Commun.* **84** 577
[20] Babateen M, Crangle J, Fauth F, Furrer A, Neumann K-U and Ziebeck K R A 1995 *Physica* B **213/214** 300
[21] Parsons M J, Crangle J, Dennis B, Neumann K-U and Ziebeck K R A 1996 *Czech. J. Phys.* **46** (Suppl. S4) 2057
[22] Parsons M J, Crangle J, Neumann K-U and Ziebeck K R A 1998 *J. Magn. Magn. Mater.* **184** 184
[23] Taylor J W, Capellmann H, Neumann K-U and Ziebeck K R A 2000 *Eur. Phys. J.* B **16** 233
[24] Seaman C L, Dilley N R, de Andrade M C, Herrmann J, Maple M B and Fisk Z 1996 *Phys. Rev.* B **53** 2651
[25] Gofryk K, Kaczorowski D, Plackowski T, Leithe-Jasper A and Grin Yu 2005 *Phys. Rev.* B **72** 094409
[26] Kaczorowski D, Gofryk K, Plackowski T, Leithe-Jasper A and Grin Yu 2005 *J. Magn. Magn. Mater.* **290/291** 573
[27] Wernick J H, Hull G W, Geballe T H, Bernardini J E and Waszczak J V 1983 *Mater. Lett.* **2** 90
[28] Kurisu M, Fuse A, Nobata T and Nakamoto G 2000 *Physica* B **281/282** 147
[29] Lal H B and Methfessel S 1981 *J. Magn. Magn. Mater.* **23** 283
[30] Galera R M, Pierre J and Pannetier J 1982 *J. Phys. F: Met. Phys.* **12** 993
[31] Galera R M, Pierre J, Siaud E and Murani A P 1984 *J. Less-Common Met.* **97** 151
[32] Lahiouel R, Pierre J, Siaud E and Murani A P 1987 *J. Magn. Magn. Mater.* **63/64** 104
[33] Lahiouel R, Pierre J, Siaud E, Galera R M, Besnus M J, Kappler J P and Murani A P 1987 *Z. Phys.* B **67** 185
[34] Ōnuki Y, Yamazaki T, Kobori A, Omi T, Komatsubara T, Takayanagi S, Kato H and Wada N 1987 *J. Phys. Soc. Japan* **56** 4251
[35] Takagi S, Kimura T, Sato N, Satoh T and Kasuya T 1988 *J. Phys. Soc. Japan* **57** 1562
[36] Nakamura N, Kitaoka Y, Asayama K, Ōnuki Y and Komatsubara T 1988 *J. Phys. Soc. Japan* **57** 2276
[37] Sato K, Mizushima T, Kondo K, Ishikawa Y, Mori K and Umehara I 1991 *J. Appl. Phys.* **69** 4645
[38] Felner I 1985 *Solid State Commun.* **56** 315
[39] Neumann K-U, Crangle J, Visser D, Zayer N K and Ziebeck K R A 1993 *Phys. Lett.* A **177** 99
[40] Rotter M, Loewenhaupt M, Doerr M, Lindbaum A, Sassik H, Ziebeck K and Beuneu B 2003 *Phys. Rev.* B **68** 144418
[41] Rotter M, Doerr M, Loewenhaupt M, Lindbaum A, Ziebeck K and Beuneu B 2004 *Physica* B **350** e63
[42] Bish D L and Chipera S J 1989 *Powder Diffr.* **4** 137
[43] Otterloo B F, Stadnik Z M and Swolfs A E M 1983 *Rev. Sci. Instrum.* **54** 1575
[44] Margulies S and Ehrman J R 1961 *Nucl. Instrum. Methods* **12** 131

[45] Shenoy G K, Friedt J M, Maletta H and Ruby S L 1974 *Mössbauer Effect Methodology* vol 10 , ed I J Gruverman, C W Seidel and D K Dieterly (New York: Plenum) p 277
[46] Blundell S 2001 *Magnetism in Condensed Matter* (Oxford: Oxford University Press)
[47] Bauminger E R, Kalvius G M and Nowik I 1978 *Mössbauer Isomer Shifts* ed G K Shenoy and F E Wagner (Amsterdam: North-Holland) p 661
[48] Greenwood N N and Gibb T C 1971 *Mössbauer Spectroscopy* (London: Chapman and Hall)
[49] Gütlich P, Link R and Trautwein A 1978 *Mössbauer Spectroscopy and Transition Metal Chemistry* (Berlin: Springer)
[50] Sato K, Ishikawa Y and Mori K 1992 *J. Magn. Magn. Mater.* **104–107** 1435
[51] Gegenwarth R E, Budnick J I, Skalski S and Wernick J H 1967 *Phys. Rev. Lett.* **18** 9
[52] Hüfner S and Wernick J H 1968 *Phys. Rev.* **173** 448
[53] Khoï L D 1969 *Phys. Lett.* A **28** 671
[54] Jeandey C, Oddou J L, Boucher B, Tourbot R and Czjzek G 1967 *J. Magn. Magn. Mater.* **89** 335
[55] Ruebenbauer K, Fink J, Schmidt H, Czjzek G and Tomala K 1977 *Phys. Status Solidi* b **84** 611
[56] Sanchez J P, Tomala K and Szytula A 1991 *Solid State Commun.* **78** 419
[57] Malaman B, Venturini G, Welter R, Sanchez J P, Vulliet P and Ressouche E 1999 *J. Magn. Magn. Mater.* **202** 519
[58] De Vries J W C, Thiel R C and Buschow K H J 1985 *J. Less-Common Met.* **111** 313

Chapter 4 Magnetic properties and ^{61}Ni Mössbauer spectroscopy of the ternary phospide CrNiP

Z.M. Stadnik, P. Wang, N. Jansen, D. Walcher, P. Gütlich, and T. Kanomata.

J. Phys.: Condens. Matter, **20**, 285227 (2008).

IOP PUBLISHING JOURNAL OF PHYSICS: CONDENSED MATTER

J. Phys.: Condens. Matter **20** (2008) 285227 (7pp) doi:10.1088/0953-8984/20/28/285227

Magnetic properties and ^{61}Ni Mössbauer spectroscopy of the ternary phosphide CrNiP

Z M Stadnik[1,4], P Wang[1], N Jansen[2], D Walcher[2], P Gütlich[2] and T Kanomata[3]

[1] Department of Physics, University of Ottawa, Ottawa, ON, K1N 6N5, Canada
[2] Institut für Anorganische Chemie und Analytische Chemie, Johannes Gutenberg Universität, 55099 Mainz, Germany
[3] Faculty of Engineering, Tohoku Gakuin University, Tagajo, Miyagi 985-8537, Japan

E-mail: stadnik@uottawa.ca

Received 11 April 2008, in final form 30 May 2008
Published 24 June 2008
Online at stacks.iop.org/JPhysCM/20/285227

Abstract

The results of x-ray diffraction, dc magnetization, and ^{61}Ni Mössbauer spectroscopy studies of the ternary phosphide CrNiP are reported. This compound crystallizes in the orthorhombic Co_2P-type structure (space group *Pnma*) with the lattice parameters $a = 5.7965(1)$ Å, $b = 3.5337(1)$ Å, and $c = 6.8123(2)$ Å. NiCrP is a ferromagnet with Curie temperature $T_C = 135.1(1)$ K. The ferromagnetic-to-paramagnetic transition is characterized by the critical exponents $\beta = 0.355(22)$, $\gamma = 1.241(18)$, and $\delta = 4.585(20)$. Their values are close to those of a 3D Heisenberg ferromagnet. The temperature dependence of the magnetic susceptibility above T_C follows the modified Curie–Weiss law with a paramagnetic Curie temperature of 142.9(6) K and effective magnetic moment per transition-metal atom of 1.70(2) μ_B. The magnetic moment per formula unit at 4.2 K is found to be 0.816(13) μ_B. The hyperfine magnetic field at ^{61}Ni nuclei at 4.2 K of 32.3(1.3) kOe implies that the Ni atoms carry a magnetic moment of 0.14(8) μ_B, and that the moment carried by the Cr atoms is 0.68(9) μ_B. The Debye temperature of NiCrP is 261(3) K.

(Some figures in this article are in colour only in the electronic version)

1. Introduction

The crystallographic and magnetic properties of the ternary transition-metal phosphides $(T_{1-x}T'_x)_2P$ (T, T′ = transition metal) have been the subject of numerous investigations [1]. These ternary compounds crystallize in two different crystal structure types: the orthorhombic Co_2P-type structure and the hexagonal Fe_2P-type structure. These two structure types have a common sub-cell where there are two kinds of transition-metal sites: the tetrahedral site surrounded by four P atoms and the pyramidal site surrounded by five P atoms. The phosphides $(T_{1-x}T'_x)_2P$ show almost all possible types of magnetic ordering: ferromagnetism, antiferromagnetism, canted antiferromagnetism, and paramagnetism. The ternary phosphides containing Ni, $(Fe_{1-x}Ni_x)_2P$ [2–9] and $(Cr_{1-x}Ni_x)_2P$ [10, 11], are ferromagnets. It has been argued both qualitatively [3] and theoretically [4, 7, 12, 13] that Ni atoms in these phosphides carry a negligible magnetic moment, i.e., that the magnetic moment is carried solely by Fe or Cr atoms.

The ternary phosphide CrNiP is an itinerant ferromagnet with the Curie temperature, T_C, of 140–146 K and the magnetic moment per formula unit, μ_{FU}, of 0.83–0.85 μ_B [10, 11, 14]. It has been argued theoretically on the basis of a narrow *d*-band model [12] that Ni atoms in CrNiP carry no magnetic moment and that all the moment is carried by Cr atoms. On the other hand, electronic band structure calculations predict [13] that in the phosphide CrNiP, Ni atoms carry a non-zero magnetic moment of 0.06 μ_B and Cr atoms carry a magnetic moment of 0.97 μ_B.

[4] Author to whom any correspondence should be addressed.

The above controversy concerning the Ni magnetic moment in CrNiP can be resolved by using experimental techniques which probe this moment directly, such as the rarely used ^{61}Ni nuclear magnetic resonance (NMR) or ^{61}Ni Mössbauer effect (ME). If there exists a magnetic moment on the Ni atoms in CrNiP, the hyperfine magnetic field at ^{61}Ni nuclei determined from ^{61}Ni NMR or ^{61}Ni ME spectra must have a non-zero value. In this paper, we report on structural, magnetic, and ^{61}Ni ME studies of the ternary phosphide CrNiP.

2. Experimental procedure

A polycrystalline sample of CrNiP was prepared from powders of Cr, Ni, and P with purities of 99.99%, 99.99%, and 99.999%, respectively. The powders were mixed in the desired proportion, sealed in an evacuated silica tube and annealed at 873 K for 2 days and then quenched. The reaction product was next subjected to a vacuum heat treatment at 1073 K for 2 days and then quenched. Finally, the ingot was pulverized, mixed well and heated again in vacuum at 1173 K for 7 days and then quenched.

X-ray diffraction measurements were performed at 298 K in the Bragg–Brentano geometry on the PANanalytical X'Pert scanning diffractometer using Cu Kα radiation. The Kβ line was eliminated by using a Kevex PSi2 Peltier-cooled solid-state Si detector. In order to avoid the deviation from intensity linearity of the solid-state Si detector, its parameters and the parameters of the diffractometer were chosen in such a way as to limit the count rate from the most intense Bragg peaks to less than 9000 counts s^{-1} [15].

The magnetic measurements were carried out with a Quantum Design superconducting quantum interference device magnetometer at various fields in the temperature range 5.0–300 K.

The ^{61}Ni ME measurements were conducted using a standard Mössbauer spectrometer operating in sine mode, using the 67.4 keV transition in ^{61}Ni [16, 17]. Both the source and the absorber were in direct contact with liquid helium in a cryostat. The spectrometer was calibrated with a 6.35 μm-thick α-Fe foil [18], and the spectra were folded. The single line sources of ^{61}Co (half life = 99 min) in ^{62}Ni$_{0.85}$Cr$_{0.15}$ (^{62}Ni enriched to 97.7%) were activated in the MAinz MIcrotron (MAMI) using the nuclear reaction ^{62}Ni(γ, p)^{61}Co, with bremsstrahlung including the giant resonance region of 20–25 MeV necessary for this nuclear reaction to occur. A pneumatic tube approximately 50 m long was used to transport small platelets (4 × 4 mm^2) of ^{62}Ni$_{0.85}$Cr$_{0.15}$ to the activation position. Immediately after an activation of about 2 h, the radioactive source material was pneumatically ejected and transported into a cryostat in which the Mössbauer absorber was already cooled to 4.2 K. Three sources had to be used to obtain a Mössbauer spectrum of sufficient signal-to-noise ratio. The Mössbauer absorber was made of pulverized material pressed into a Teflon sample holder. The surface density of the Mössbauer absorber of the CrNiP alloy was 719 mg cm^{-2}. The 67.4 keV γ-rays were detected with a 2.0 mm NaI(Tl) scintillation detector.

The measured ^{61}Ni Mössbauer spectrum was analyzed by means of a least-squares fitting procedure which entailed calculations of the positions and relative intensities of the absorption lines by numerical diagonalization of the full hyperfine interaction Hamiltonian. In the principal axis system of the electric field gradient (EFG) tensor, the Hamiltonian can be written as [16, 17]

$$\hat{H} = g\mu_N H_{hf}\left[\hat{I}_z\cos\theta + \frac{1}{2}\left(\hat{I}_+ e^{-i\phi} + \hat{I}_- e^{i\phi}\right)\sin\theta\right] + \frac{eQV_{zz}}{4I(2I-1)}\left[3\hat{I}_z^2 - I(I+1) + \frac{\eta}{2}\left(\hat{I}_+^2 + \hat{I}_-^2\right)\right], \quad (1)$$

where g is a nuclear g-factor of a nuclear state, μ_N is the nuclear Bohr magneton, H_{hf} is the hyperfine magnetic field at a nuclear site, e is the proton charge, Q is the quadrupole moment of a nuclear state, I is the nuclear spin, V_{zz} is the z component of the EFG tensor, η is the asymmetry parameter defined as $\eta = |(V_{xx} - V_{yy})/V_{zz}|$ (if the principal axes are chosen such that $|V_{xx}| < |V_{yy}| < |V_{zz}|$, then $0 \leqslant \eta \leqslant 1$), θ is the angle between the direction of H_{hf} and the V_{zz}-axis, ϕ is the angle between the V_{xx}-axis and the projection of H_{hf} onto the xy plane, and the $\hat{I}_z$, $\hat{I}_+$, and $\hat{I}_-$ operators have their usual meaning. During the fitting procedure, the g factors and the quadrupole moments for ^{61}Ni ($I_g = 3/2$, $I_{ex} = 5/2$) were constrained to $g_{ex} = 0.1905$ and $g_g = -0.499\,87$, and $Q_{ex} = -0.196b$ and $Q_g = 0.162b$, respectively [19].

The resonance line shape of the Mössbauer spectra was described by a transmission integral formula [20, 21]. In addition to the hyperfine parameters, only the absorber Debye–Waller factor f_a and the absorber linewidth Γ_a were fitted as independent parameters. The source linewidth $\Gamma_s = 0.440$ mm s^{-1} and the background-corrected Debye–Waller factor of the source $f_s^* = 0.11$ [22], were used in the fit.

3. Results and discussion

3.1. Structural characterization

The ternary phosphide CrNiP forms in the Co_2P-type crystal structure with the space group *Pnma* (No. 62). Three different 4*c* positions (x, $\frac{1}{4}$, z) are occupied by Cr, Ni, and P, respectively, which correspond to four formula units of CrNiP per unit cell. The crystal structure of CrNiP is shown in figure 1. The Cr atoms are pyramidally coordinated by five P atoms and the Ni atoms are tetrahedrally coordinated by four P atoms.

The x-ray powder diffraction pattern of the sample studied is shown in figure 2. A Rietveld refinement of the x-ray powder diffraction data was performed yielding the lattice parameters $a = 5.7965(1)$ Å, $b = 3.5337(1)$ Å, and $c = 6.8123(2)$ Å. The obtained atomic positions for the Cr, Ni, and P sites are listed in table 1 and the interatomic distances are listed in table 2. The sample studied contains traces of second phases of CrNiP (space group $P\bar{6}2m$ [23]) in the amount of 9.7(3) wt% and of Cr_2O_3 (space group $R\bar{3}c$) in the amount of 1.8(2) wt%, as determined from the Rietveld refinement of the x-ray powder diffraction pattern (figure 2).

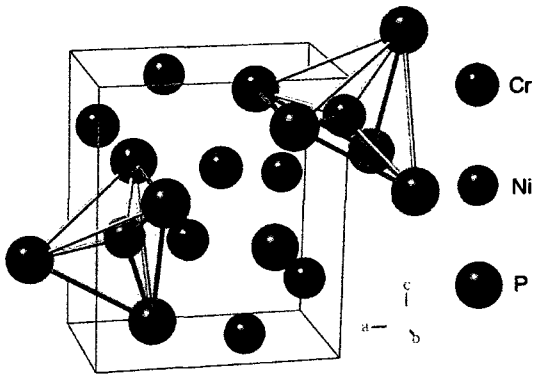

Figure 1. Crystal structure of CrNiP. The pyramidal and tetrahedral coordinations of the Cr and Ni atoms are indicated.

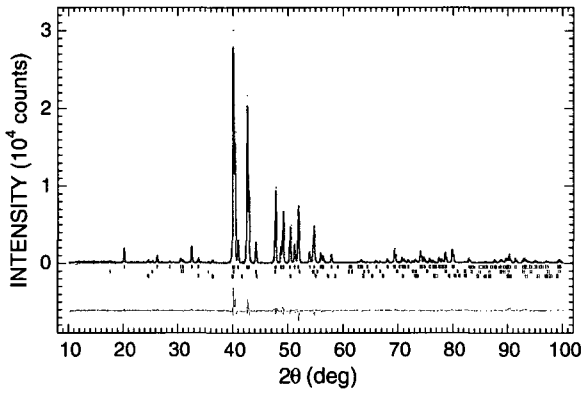

Figure 2. The x-ray powder diffraction spectrum of CrNiP at 298 K. The experimental data are denoted by open circles, while the line through the circles represents the results of the Rietveld refinement. The upper set of vertical bars represents the Bragg peak positions corresponding to the principal CrNiP phase, while the lower two sets refer to the positions of the minor impurity phases of CrNiP (space group $P\bar{6}2m$ [23]) and Cr_2O_3 (space group $R\bar{3}c$). The lower curve shows the difference between the experimental data and the calculated curve.

Table 1. Atomic positions for the orthorhombic phosphate CrNiP obtained through Rietveld analysis.

Atom	Site	Point symmetry	x	y	z	Occupancy
Cr	4c	m	0.0271(3)	$\frac{1}{4}$	0.1673(2)	1.0
Ni	4c	m	0.1423(2)	$\frac{1}{4}$	0.5642(2)	1.0
P	4c	m	0.7608(5)	$\frac{1}{4}$	0.6274(3)	1.0

3.2. Magnetic properties

The temperature dependence of the magnetization M of CrNiP measured in an applied magnetic field of 15 kOe between 5.0 and 300 K is shown in figure 3. This phosphide is obviously a ferromagnet. For a mean-field ferromagnet, $M^2 \propto T_C - T$ near T_C [24]. From a linear fit of M^2 versus T (inset in figure 3), T_C was estimated to be 152.7(1.2) K.

The temperature dependence of the inverse magnetic susceptibility χ of CrNiP is shown in figure 4. In the

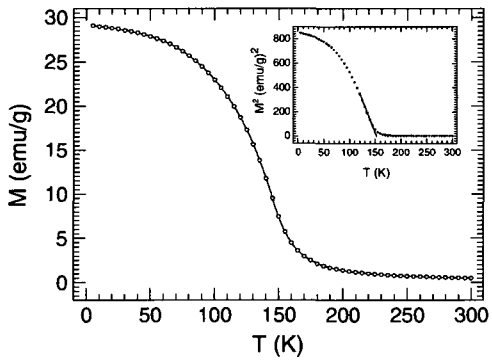

Figure 3. The temperature dependence of the magnetization of CrNiP, measured in an external magnetic field of 15 kOe. The solid line is a guide for the eye. The inset shows the temperature dependence of the square of the magnetization and the solid line is a linear fit of the data around T_C.

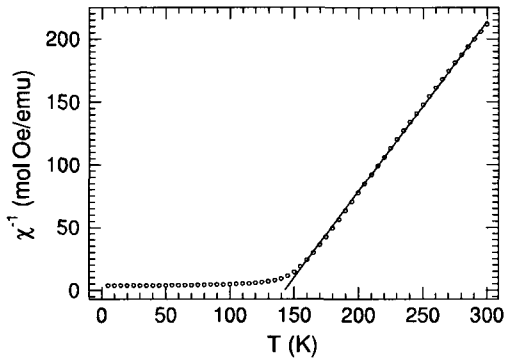

Figure 4. The temperature dependence of the inverse magnetic susceptibility of CrNiP, measured in an external magnetic field of 15 kOe. The solid line is the fit to equation (2) in the temperature range 150–300 K.

Table 2. Interatomic distances (in Å) for the orthorhombic phosphate CrNiP.

Cr		Ni		P	
1P	2.424(3)	1P	2.210(3)	1Ni	2.210(3)
2P	2.446(2)	1P	2.253(3)	1Ni	2.253(3)
2P	2.566(2)	2P	2.267(2)	2Ni	2.267(2)
2Ni	2.700(2)	2Ni	2.571(1)	1Cr	2.424(3)
2Ni	2.726(1)	2Cr	2.700(2)	2Cr	2.446(2)
1Ni	2.730(2)	2Cr	2.726(1)	2Cr	2.566(2)
1Ni	2.785(2)	1Cr	2.730(2)	2P	3.344(4)
2Cr	2.901(1)	1Cr	2.785(2)	1Cr	3.493(3)
2Cr	3.109(2)				
1P	3.493(3)				

paramagnetic region the $\chi(T)$ data could be fitted to a modified Curie–Weiss law

$$\chi = \chi_0 + \frac{C}{T - \theta_p}, \tag{2}$$

where χ_0 is the temperature independent magnetic susceptibility, C is the Curie constant, and θ_p is the paramagnetic

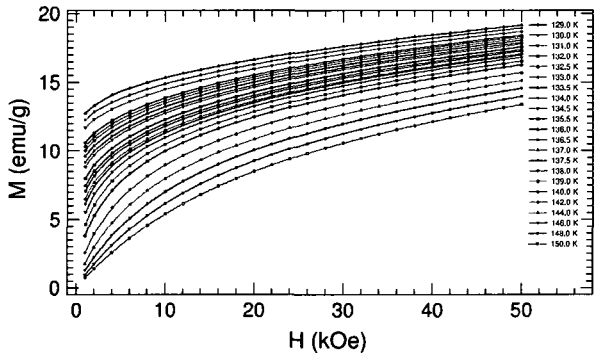

Figure 5. The magnetization isotherms versus the magnetic field at temperatures between 129 and 150 K. The solid lines are guides for the eye.

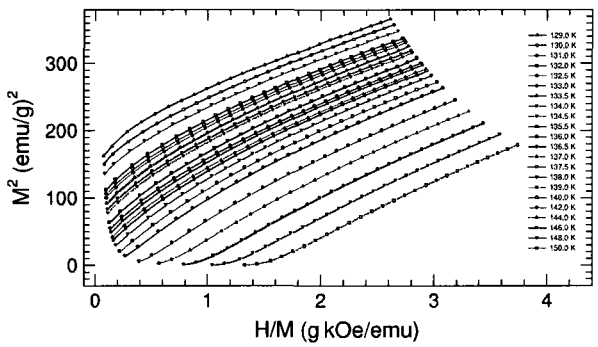

Figure 6. The Arrott plot for CrNiP. The solid lines are guides for the eye.

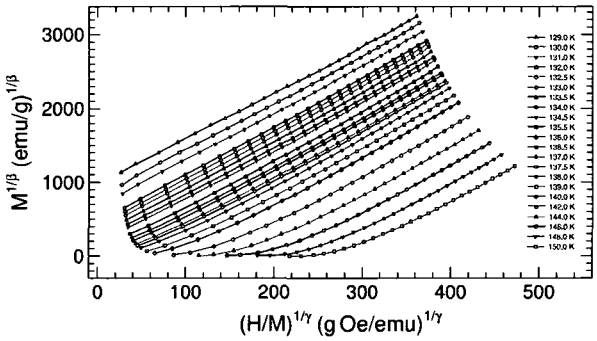

Figure 7. The modified Arrott plot for CrNiP with $\beta = 0.365$ and $\gamma = 1.336$. The solid lines are guides for the eye.

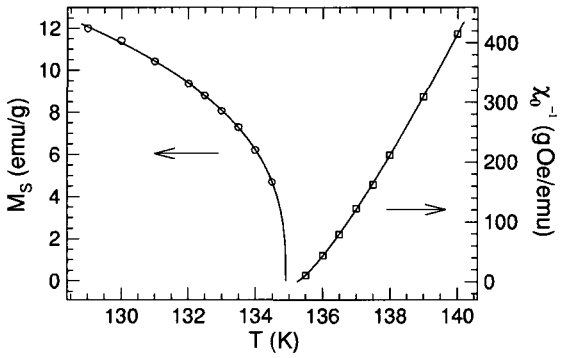

Figure 8. The temperature dependence of the spontaneous magnetization and the inverse initial susceptibility. The solid lines are fits of the experimental data to equations (3) and (4).

Curie temperature. The Curie constant can be expressed as $C = \frac{N\mu_{\text{eff}}^2}{3k}$, where N is the concentration of magnetic atoms per unit mass, k is the Boltzmann constant, and μ_{eff} is the effective magnetic moment. The values of χ_0, C, and θ_p obtained from the fit are 7.67(97) $\times$ 10^{-5} emu Oe^{-1} mol^{-1}, 0.723(13) emu Oe^{-1} K mol^{-1}, and 142.9(6) K, respectively. This value of C corresponds to μ_{eff} of 1.70(2) μ_{B} per transition-metal atom. The positive paramagnetic Curie temperature is consistent with the ferromagnetic ordering, and the value of θ_p is close to T_{C}.

Figure 5 shows a series of magnetization isotherms measured in the vicinity of T_{C}, estimated above. The usual procedure for extracting the spontaneous magnetization $M_{\text{S}}(T) = \lim_{H\to 0} M$, the inverse initial susceptibility $\chi_0^{-1} = \lim_{H\to 0}(H/M)$, and T_{C} from the $M(H)$ isotherms is to make use of the Arrott plot [25], M^2 versus H/M. According to mean-field theory, near T_{C} this plot should consist of a series of parallel lines for different temperatures, with the line at $T = T_{\text{C}}$ passing through the origin, and the $M_{\text{S}}(T)$ and $\chi_0^{-1}(T)$ are determined from the intercept values on the ordinate ($T \leqslant T_{\text{C}}$) and abscissa ($T \geqslant T_{\text{C}}$), respectively. However, in the present case the curves in the Arrott plot (figure 6) are nonlinear and concave. This shows that CrNiP is not a mean-field ferromagnet. Therefore, we analyzed the $M(H)$ data using a modified Arrott plot [26], in which $M^{1/\beta}$ is plotted versus $(M/H)^{1/\gamma}$, where β and γ are critical exponents defined through the relations [27]

$$M_{\text{S}}(T) = M_0(-\varepsilon)^{\beta}, \qquad \varepsilon < 0 \tag{3}$$

$$\chi_0^{-1}(T) = (h_0/M_0)\varepsilon^{\gamma}, \qquad \varepsilon > 0, \tag{4}$$

where $\varepsilon = (T - T_{\text{C}})/T_{\text{C}}$, and M_0 and h_0/M_0 are the critical amplitudes. At T_{C}, a critical exponent δ relates M and H by [27]

$$M = DH^{1/\delta}, \qquad \varepsilon = 0, \tag{5}$$

where D is a critical amplitude. Different values of β and γ were taken as trial values and it was found that the values of $\beta = 0.365$ and $\gamma = 1.336$, which are similar to those of the three-dimensional (3D) magnet [28], resulted in nearly straight lines for sufficiently high fields (figure 7). Using the modified Arrott plot (figure 7), a linear extrapolation of the straight lines of the isotherms from fields above 2.0 kOe to $(M/H)^{1/\gamma} = 0$ and $M^{1/\beta} = 0$ yields intercepts on the $M^{1/\beta}$ and $(M/H)^{1/\gamma}$ axes, respectively, from which the values of $M_{\text{S}}(T)$ and $\chi_0^{-1}(T)$ are computed. These values as a function of temperature are plotted in figure 8. The fits of the $M_{\text{S}}(T)$ and $\chi_0^{-1}(T)$ data (figure 8) to equations (3) and (4) respectively give $\beta = 0.355(22)$, $T_{\text{C}} = 134.91(3)$ K and $\gamma = 1.241(18)$, $T_{\text{C}} = 135.24(3)$ K. The value of T_{C} for CrNiP is then taken

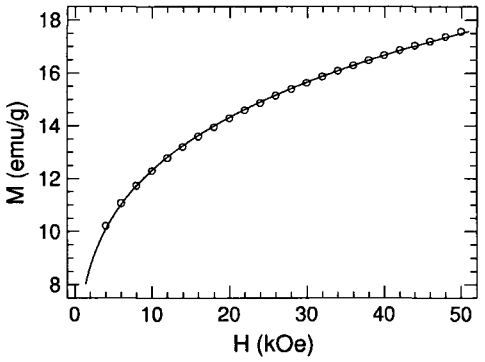

Figure 9. The magnetization isotherm versus the magnetic field at 135.5 K. The solid line is the fit to equation (5).

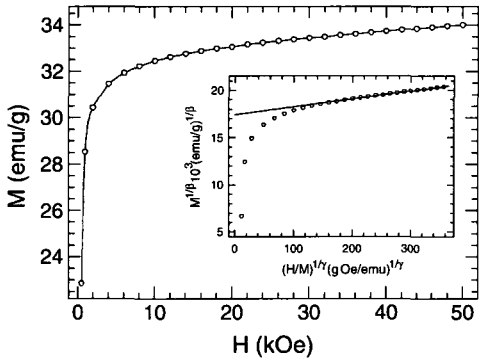

Figure 10. The magnetization isotherm versus the magnetic field at 4.2 K. The solid line is a guide for the eye. The inset shows the modified Arrott plot with $\beta = 0.355$ and $\gamma = 1.241$. The solid line is a linear fit to the high-field data.

as 135.1(1) K. The critical exponents obtained in this way are close to those of the short-range 3D Heisenberg model predictions ($\beta = 0.3689(3)$, $\gamma = 1.3960(9)$) [28].

To obtain the value of δ, we plot M versus H for the closest measured isotherm, 135.5 K, to $T_C = 135.1(1)$ K in figure 9. The fit of this isotherm to equation (5) (figure 9) gives $\delta = 4.585(20)$. This value is close to the value of $\delta = 4.783(3)$ expected [28] for a 3D Heisenberg ferromagnet.

The critical exponents β, γ, and δ should fulfill the Widom exponent relation [29] $\gamma - \beta(\delta - 1) = 0$. The determined values of β, γ, and δ satisfy this relation well ($-0.103(108)$), within experimental error.

The magnetic field dependence of the magnetization measured at 4.2 K is shown in figure 10. The magnetization does not saturate, even in a field of 50 kOe. The saturation magnetization at 4.2 K was obtained from a modified Arrott plot (inset in figure 10) by a linear extrapolation of the high-field data to $(M/H)^{1/\gamma} = 0$. This yielded $M_S = 32.17(53)$ emu g^{-1}, which corresponds to the magnetic moment per formula unit $\mu_{FU} = 0.816(13)\ \mu_B$, or to the magnetic moment per transition metal (TM) (assuming that P atoms carry no magnetic moment) $\mu_{TM} = 0.408(7)\ \mu_B$.

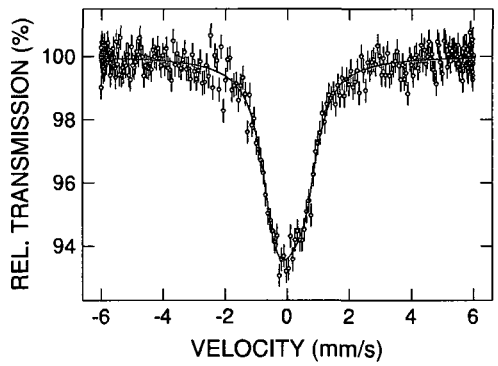

Figure 11. The ^{61}Ni Mössbauer spectrum of CrNiP measured at 4.2 K. The solid line is a fit, as described in the text. The zero-velocity origin is relative to the source.

3.3. Mössbauer spectroscopy

Figure 11 shows a ^{61}Ni Mössbauer spectrum of CrNiP measured at 4.2 K. The Ni atoms are located in the crystal structure at the site with the point symmetry m (table 1). This ensures a non-zero electric field gradient at the Ni site and hence a possible non-zero electric quadrupole splitting. The spectrum in figure 11 clearly exhibits the presence of a poorly resolved hyperfine magnetic interaction. It was fitted with the transmission integral by diagonalization of the hyperfine Hamiltonian (equation (1)). The following values of the hyperfine parameters were inferred from the fit: $\Gamma_a = 0.399(8)$ mm s^{-1}, the isomer shift (relative to the ^{61}Co(Ni$_{0.85}$Cr$_{0.15}$) source) $\delta = 0.017(15)$ mm s^{-1}, $V_{zz} = -0.137(81) \times 10^{22}$ V m^{-2}, $f_a = 6.9(2)\%$ and $H_{hf} = 32.3(1.3)$ kOe.

The value of Γ_a is only slightly larger than the natural linewidth $\Gamma_{nat} = 0.385$ mm s^{-1} [19], as expected. Similarly to what has been found for other metallic systems [17, 30], the values of δ and V_{zz} are essentially equal to zero. In terms of the Debye approximation for the lattice vibrations, the absorber Debye–Waller factor f_a is expressed [16, 17] by the Debye temperature, Θ_D, as

$$f_a(T) = \exp\left\{-\frac{3}{4}\frac{E_\gamma^2}{Mc^2k\Theta_D} \times \left[1 + \left(\frac{T}{\Theta_D}\right)^2 \int_0^{\Theta_D/T} \frac{x\,dx}{e^x - 1}\right]\right\}, \quad (6)$$

where E_γ is the energy of the Mössbauer transition, M is the mass of the Mössbauer nucleus, c is the speed of light, and k is the Boltzmann constant. The value of f_a obtained from the fit via equation (6) yields $\Theta_D = 261(3)$ K.

A non-zero value of H_{hf} implies a non-zero value of the nickel magnetic moment μ_{Ni} in CrNiP. There is no firmly established relationship between the measured H_{hf} and μ_{Ni}. There are two major contributions to H_{hf} at the nuclei of TM elements in metallic alloys [16, 17]: the core contribution, due to the polarization of core s electrons and the polarization of the conduction electrons by the 3d electrons (i.e., by the on-site magnetic moment), and the conduction

electron contribution, due to the polarization of the conduction electrons by the surrounding magnetic moments. The first contribution is proportional to the local magnetic moment μ_l, whereas the second contribution is assumed to be proportional to the average moment per magnetic atom μ_{TM} Thus, a phenomenological relation is used [31]

$$H_{hf} = a\mu_l + b\mu_{TM}, \tag{7}$$

where a and b are assumed to be constant for a given alloy system. This relation enables one to estimate the value of μ_l from the measured values of H_{hf} and μ_{TM}, provided that the values of a and b are known from an earlier calibration. Due to the scarcity of data on the values of H_{hf} at ^{61}Ni nuclei in Ni-containing alloys, the values of a and b are known only for a few alloy series [32–36]. From an earlier calibration for the ternary pnictide CrNiAs for which the Ni magnetic moment is known from the neutron diffraction study, we found that $a = 63(5)$ kOe/μ_B and $b = 57(5)$ kOe/μ_B [37]. Using the value of μ_{TM} determined above and the measured value of H_{hf}, one obtains $\mu_{Ni} = 0.14(8)$ μ_B from equation (7). It is thus concluded that the Ni atoms in the CrNiP ferromagnet do carry a magnetic moment. This finding is at variance with the theoretical prediction of $\mu_{Ni} = 0$ in CrNiP [12] and in agreement with the prediction based on the electronic structure calculations of the non-zero μ_{Ni} in CrNiP [13]. Since the Ni and Cr magnetic moments are coupled ferromagnetically in CrNiP, the values of $\mu_{Ni} = 0.14(8)$ μ_B and $\mu_{FU} = 0.816(13)$ μ_B imply that the Cr atoms carry a magnetic moment of 0.68(9) μ_B.

4. Conclusions

The ternary phosphide CrNiP has been studied by means of x-ray diffraction, magnetization measurements, and ^{61}Ni Mössbauer spectroscopy. The studied compound has the orthorhombic Co_2P-type structure (space group *Pnma*) with the lattice parameters $a = 5.7965(1)$ Å, $b = 3.5337(1)$ Å, and $c = 6.8123(2)$ Å. The Curie temperature T_C is found to be 135.1(1) K and three critical exponents are determined $\beta = 0.355(22)$, $\gamma = 1.241(18)$, and $\delta = 4.585(20)$. The values of these critical exponents are close to those of a 3D Heisenberg ferromagnet. The temperature dependence of the magnetic susceptibility above T_C follows the modified Curie–Weiss law with the paramagnetic Curie temperature of 142.9(6) K and the effective magnetic moment per transition-metal atom of 1.70(2) μ_B. The magnetic moment per formula unit at 4.2 K is found to be 0.816(13) μ_B. The hyperfine magnetic field of 32.3(1.3) kOe at ^{61}Ni nuclei at 4.2 K implies that the Ni atoms carry a magnetic moment of 0.14(8) μ_B, and that the moment carried by the Cr atoms is 0.68(9) μ_B. The Debye temperature of CrNiP is 261(3) K.

Acknowledgment

This work was supported by the Natural Sciences and Engineering Research Council of Canada.

References

[1] Beckman O and Lundgren L 1991 *Handbook of Magnetic Materials* vol 6, ed K H J Buschow (Amsterdam: Elsevier) p 181
[2] Fruchart R, Roger A and Senateur J P 1969 *J. Appl. Phys.* **40** 1250
[3] Fuji H, Hōkabe T, Fujiwara H and Okamoto T 1978 *J. Phys. Soc. Japan* **44** 96
[4] Kaprzyk S, Nizioł S, Tobola J, Zach R, Bacmann M, Fruchart D and Wolfers P 1997 *Acta Phys. Pol.* A **91** 475
[5] Kumar S, Paranjpe S K, Srivastava B K and Krishnamurthy A 1999 *Phys. Status Solidi* a **175** 693
[6] Średniawa B, Duraj R, Pacyna A, Bombik A, Zach R, Bacmann M, Fruchart D, Nizioł S, Fornal P and Stanek J 2000 *Acta Phys. Pol.* A **97** 921
[7] Zach R, Tobola J, Średniawa B, Kaprzyk S, Casado C, Bacmann M and Fruchart D 2004 *J. Alloys Compounds* **383** 322
[8] Fruchart D, Allab F, Balli M, Gignoux D, Hlil E K, Koumina A, Skryabina N, Tobola J, Wolfers P and Zach R 2005 *Physica* A **358** 123
[9] Balli M, Fruchart D, Gignoux D, Tobola J, Hlil E K, Wolfers P and Zach R 2007 *J. Magn. Magn. Mater.* **316** 358
[10] Iwata N, Matsushima T, Fujii H and Okamoto T 1981 *J. Phys. Soc. Japan* **50** 729
[11] Kanomata T, Endo H, Yamauchi H, Yamaguchi Y, Yoshida H, Kaneko T, Aruga Katori H and Goto T 1997 *Physica* B **237/238** 517
[12] Goodenough J B 1973 *J. Solid State Chem.* **7** 428
[13] Ishida S, Takiguchi T, Fujii S and Asano S 1996 *Physica* B **217** 87
[14] Nylund M A, Roger A, Sénateur J P and Fruchart R 1972 *J. Solid State Chem.* **4** 115
[15] Bish D L and Chipera S J 1989 *Powder Diffr.* **4** 137
[16] Greenwood N N and Gibb T C 1971 *Mössbauer Spectroscopy* (London: Chapman and Hall)
[17] Gütlich P, Link R and Trautwein A 1978 *Mössbauer Spectroscopy and Transition Metal Chemistry* (Berlin: Springer)
[18] Cali J P (ed) *Certificate of Calibration, Iron Foil Mössbauer Standard,* NBS (US) Circular No. 1541 (Washington, DC: US Government Printing Office)
[19] Stevens J G 1981 *CRC Handbook of Spectroscopy* vol 3, ed J W Robinson (Boca Raton, FL: CRC Press) p 403
[20] Margulies S and Ehrman J R 1961 *Nucl. Instrum. Methods* **12** 131
[21] Shenoy G K, Friedt J M, Maletta H and Ruby S L 1974 *Mössbauer Effect Methodology* vol 10, ed I J Gruverman, C W Seidel and D K Dieterly (New York: Plenum) p 277
[22] Rummel H 1982 ^{61}Ni-Mössbauer-Untersuchungen der Magnetischen Hyperfeinfelder in Nickelspinellen *PhD Thesis* Johannes Gutenberg-Universität, Mainz
[23] Orishchin S V and Kuz'ma Yu B 1984 *Inorg. Mater.* **20** 360
[24] Zijlstra H 1967 *Experimental Methods in Magnetism* vol 2 (Amsterdam: North-Holland)
[25] Arrott A 1957 *Phys. Rev.* **108** 1394
[26] Arrott A and Noakes J E 1967 *Phys. Rev. Lett.* **19** 786
[27] Stanley H E 1971 *Introduction to Phase Transitions and Critical Phenomena* (New York: Oxford University Press)
[28] Campostrini M, Hasenbusch M, Pelissetto A, Rossi P and Vicari E 2002 *Phys. Rev.* B **65** 144520
[29] Widom B 1964 *J. Chem. Phys.* **41** 1633
Widom B 1965 *J. Chem. Phys.* **43** 3898
[30] Tomala K, Czjzek G, Fink J and Schmidt H 1977 *Solid State Commun.* **24** 857

[31] Johnson C E, Ridout M S and Cranshaw T E 1963 *Proc. Phys. Soc.* **81** 1079
Collins M F and Wheeler D A 1963 *Proc. Phys. Soc.* **82** 633
Panissod P, Durand J and Budnick J I 1982 *Nucl. Instrum. Methods* **199** 99
Panissod P 1985 *Hyperfine Interact.* **124–126** 607
[32] Erich U 1969 *Z. Phys.* **227** 25
Ebert H, Winter H, Gyorffy B L, Johnson D D and Pinski F J 1988 *J. Phys. F: Met. Phys.* **18** 719
[33] Stadnik Z M, Griesbach P, Dehe G, Gütlich P and Maniawski F 1987 *J. Magn. Magn. Mater.* **70** 436
[34] Tansil J E, Obenshain F E and Czjzek G 1972 *Phys. Rev.* B **6** 2796
[35] Streever R L and Uriano G A 1966 *Phys. Rev.* **149** 295
[36] Stadnik Z M, Griesbach P, Dehe G, Gütlich P, Stroink G and Miyazaki T 1987 *Phys. Rev.* B **35** 8740
[37] Stadnik Z M, Wang P, Jansen N, Walcher D, Gütlich P and Kanomata T 2008 unpublished results

Chapter 5 Magnetization and ^{61}Ni Mössbauer effect study of the ternary arsenide CrNiAs

Z.M. Stadnik, P. Wang, N. Jansen, D. Walcher, P. Gütlich, and T. Kanomata.

J. Phys.: Condens. Matter, **20**, 325230 (2008).

IOP PUBLISHING JOURNAL OF PHYSICS: CONDENSED MATTER

J. Phys.: Condens. Matter **20** (2008) 325230 (7pp) doi:10.1088/0953-8984/20/32/325230

Magnetization and ^{61}Ni Mössbauer effect study of the ternary arsenide CrNiAs

Z M Stadnik[1,4], P Wang[1], N Jansen[2], D Walcher[2], P Gütlich[2] and T Kanomata[3]

[1] Department of Physics, University of Ottawa, Ottawa, ON, K1N 6N5, Canada
[2] Institut für Anorganische Chemie und Analytische Chemie, Johannes Gutenberg Universität, 55099 Mainz, Germany
[3] Faculty of Engineering Tohoku Gakuin University, Tagajo, Miyagi 985-8537, Japan

E-mail: stadnik@uottawa.ca

Received 1 May 2008
Published 18 July 2008
Online at stacks.iop.org/JPhysCM/20/325230

Abstract

The results of x-ray diffraction, dc magnetization, and ^{61}Ni Mössbauer spectroscopy studies of the ternary arsenide CrNiAs are reported. This compound crystallizes in the orthorhombic Fe_2P-type structure (space group $P\bar{6}2m$) with the lattice parameters $a = 6.1128(2)$ Å and $c = 3.6585(1)$ Å. CrNiAs is a mean-field ferromagnet with Curie temperature $T_C = 171.9(1)$ K and the critical exponents $\beta = 0.514(18)$, $\gamma = 1.010(16)$, and $\delta = 2.922(10)$. The temperature dependence of the magnetic susceptibility above T_C follows the modified Curie–Weiss law with a paramagnetic Curie temperature of 176.0(3) K and effective magnetic moment per transition metal atom of 2.42(1) μ_B. The magnetic moment per formula unit at 4.2 K is found to be 1.114(33) μ_B. The hyperfine magnetic field at ^{61}Ni nuclei at 4.2 K of 41.5(1.0) kOe implies that the Ni atoms carry a magnetic moment of 0.15(3) μ_B, and that the moment carried by the Cr atoms is 0.95(6) μ_B. The Debye temperature of CrNiAs is 221(1) K.

(Some figures in this article are in colour only in the electronic version)

1. Introduction

The ternary transition-metal arsenides $(T_{1-x}T'_x)_2As$ (T, T' = transition metal) have been investigated intensively with respect to their crystal structures and greatly varying physical properties [1–26]. These compounds crystallize either in the hexagonal Fe_2P-type structure or in the orthorhombic Co_2P-type structure. Common to these two structure types is a sub-cell where there are two kinds of transition-metal sites: the tetrahedral site surrounded by four As atoms and the pyramidal site surrounded by five As atoms. The arsenides $(T_{1-x}T'_x)_2As$ show almost all possible types of magnetic ordering: ferromagnetism, antiferromagnetism, ferrimagnetism, and spin glass. The ternary arsenides containing Ni, $(Cr_{1-x}Ni_x)_2As$ [10], are ferromagnetic for $0.45 < x \leqslant 0.7$ and antiferromagnetic for $0.4 < x \leqslant 0.45$.

The ternary arsenide CrNiAs is a ferromagnet with the Curie temperature, T_C, reported to be in the range of 182–195 K [1, 6, 10, 12, 22, 25] and the magnetic moment per formula unit, μ_{FU}, reported to be in the range of 1.10–1.19 μ_B [6, 10, 12, 22]. It has been argued [22] that Ni atoms in CrNiAs, similarly to the case for the ferromagnetic ternary phosphides $(Cr_{1-x}Ni_x)_2P$ [27], carry no magnetic moment and that all the moment is carried by Cr atoms. On the other hand, electronic band structure calculations by Ishida *et al* [23] predict that $\mu_{Cr} = 1.19$ μ_B and $\mu_{Ni} = 0.11$ μ_B and those by Toboła *et al* [24] conclude that $\mu_{Cr} = 1.23$ μ_B and $\mu_{Ni} = 0.12$ μ_B. Early neutron diffraction measurements of CrNiAs at 77 K suggested [12] that the Cr and Ni magnetic moments, μ_{Cr} and μ_{Ni}, are coupled ferrimagnetically with $\mu_{Cr} = 0.55(15)$ μ_B and $\mu_{Ni} = -0.65(15)$ μ_B. It was concluded from recent neutron diffraction measurements [25] that $\mu_{Cr} = 1.25(5)$ μ_B and $\mu_{Ni} = 0.15(3)$ μ_B.

The above controversy concerning the Ni magnetic moment in CrNiAs can be resolved by using experimental techniques which probe this moment directly, such as rarely used ^{61}Ni nuclear magnetic resonance (NMR) or ^{61}Ni Mössbauer effect (ME). If there exists a magnetic moment on the Ni atoms in CrNiAs, the hyperfine magnetic field at ^{61}Ni

[4] Author to whom any correspondence should be addressed.

nuclei determined from ^{61}Ni NMR or ^{61}Ni ME spectra must have a non-zero value. In this paper, we report on structural, magnetic, and ^{61}Ni ME studies of the ternary arsenide CrNiAs.

2. Experimental procedure

A polycrystalline sample of CrNiAs was prepared from powders of Cr, Ni, and As with purities of 99.99%, 99.99%, and 99.999%, respectively. The powders were mixed in the desired proportion, sealed in an evacuated silica tube and annealed at 873 K for 2 days and then quenched. The reaction product was next subjected to a vacuum heat treatment at 1073 K for 2 days and then quenched. Finally, the ingot was pulverized, mixed well and heated again in vacuum at 1173 K for 7 days and then quenched.

X-ray diffraction measurements were performed at 298 K in Bragg–Brentano geometry on the PANanalytical X'Pert scanning diffractometer using Cu Kα radiation. The Kβ line was eliminated by using a Kevex PSi2 Peltier-cooled solid-state Si detector. In order to avoid the deviation from intensity linearity of the solid-state Si detector, its parameters and the parameters of the diffractometer were chosen in such a way as to limit the count rate from the most intense Bragg peaks to less than 9000 counts s^{-1} [28].

The magnetic measurements were carried out with a Quantum Design superconducting quantum interference device magnetometer at various fields in the temperature range 5.0–300 K.

The ^{61}Ni ME measurements were conducted using a standard Mössbauer spectrometer operating in sine mode, using the 67.4 keV transition in ^{61}Ni [29, 30]. Both the source and the absorber were in direct contact with liquid helium in a cryostat. The spectrometer was calibrated with a 6.35 μm-thick α-Fe foil [31], and the spectra were folded. The single line sources of ^{61}Co (half life = 99 min) in $^{62}Ni_{0.85}Cr_{0.15}$ (^{62}Ni enriched to 97.7%) were activated in the MAinz MIcrotron (MAMI) using the nuclear reaction ^{62}Ni (γ, p) ^{61}Co, with bremsstrahlung including the giant resonance region of 20–25 MeV necessary for this nuclear reaction to occur. A pneumatic tube approximately 50 m long was used to transport small platelets (4 × 4 mm^2) of $^{62}Ni_{0.85}Cr_{0.15}$ to the activation position. Immediately after activation of about 2 h, the radioactive source material was pneumatically ejected and transported into a cryostat in which the Mössbauer absorber was already cooled to 4.2 K. Three sources had to be used to obtain a Mössbauer spectrum of sufficient signal-to-noise ratio. The Mössbauer absorber was made of pulverized material pressed into a teflon sample holder. The surface density of the Mössbauer absorber of the CrNiAs alloy was 839 mg cm^{-2}. The 67.4 keV γ-rays were detected with a 2.0 mm NaI(Tl) scintillation detector.

The measured ^{61}Ni Mössbauer spectrum was analyzed by means of a least-squares fitting procedure which entailed calculations of the positions and relative intensities of the absorption lines by numerical diagonalization of the full hyperfine interaction Hamiltonian. In the principal axis system of the electric field gradient (EFG) tensor, the Hamiltonian can be written as [29, 30]

$$\hat{H} = g\mu_N H_{hf}\left[\hat{I}_z\cos\theta + \tfrac{1}{2}\left(\hat{I}_+ e^{-i\varphi} + \hat{I}_- e^{i\varphi}\right)\sin\theta\right] + \frac{eQV_{zz}}{4I(2I-1)}\left[3\hat{I}_z^2 - I(I+1) + \frac{\eta}{2}\left(\hat{I}_+^2 + \hat{I}_-^2\right)\right], \quad (1)$$

where g is the nuclear g-factor of a nuclear state, μ_N is the nuclear Bohr magneton, H_{hf} is the hyperfine magnetic field at a nuclear site, e is the proton charge, Q is the quadrupole moment of a nuclear state, I is the nuclear spin, V_{zz} is the z component of the EFG tensor, η is the asymmetry parameter defined as $\eta = |(V_{xx} - V_{yy})/V_{zz}|$ (if the principal axes are chosen such that $|V_{xx}| < |V_{yy}| < |V_{zz}|$, then $0 \leqslant \eta \leqslant 1$), θ is the angle between the direction of H_{hf} and the V_{zz}-axis, φ is the angle between the V_{xx}-axis and the projection of H_{hf} onto the xy plane, and the $\hat{I}_z$, $\hat{I}_+$, and $\hat{I}_-$ operators have their usual meaning. During the fitting procedure, the g factors and the quadrupole moments for ^{61}Ni ($I_g = 3/2$, $I_{ex} = 5/2$) were constrained to $g_{ex} = 0.1905$ and $g_g = -0.499\,87$, and $Q_{ex} = -0.196$ b and $Q_g = 0.162$ b, respectively [32].

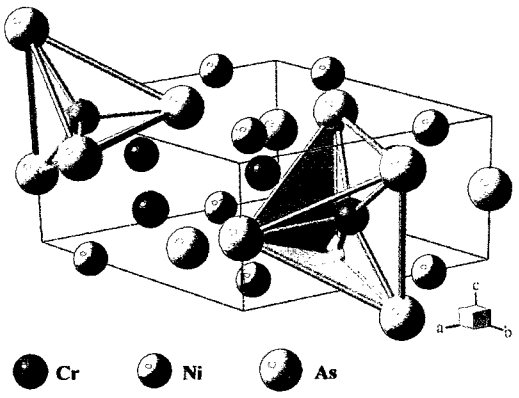

Figure 1. Crystal structure of CrNiAs. The pyramidal and tetrahedral coordinations of the Cr and Ni atoms are indicated.

The resonance line shape of the Mössbauer spectra was described by a transmission integral formula [33, 34]. In addition to the hyperfine parameters, only the absorber Debye–Waller factor f_a and the absorber linewidth Γ_a were fitted as independent parameters. The source linewidth Γ_s = 0.440 mm s^{-1} and the background-corrected Debye–Waller factor of the source $f_s^* = 0.11$ [35], were used in the fit.

3. Results and discussion

3.1. Structural characterization

The ternary arsenide CrNiAs crystallizes in the Fe_2P-type crystal structure with the space group $P\bar{6}2m$ (No. 189). In this structure type, the Cr and Ni atoms occupy, respectively, the 3g and 3f sites, whereas the As atoms occupy both the 1b and 2c sites. The unit cell contains four formula units of CrNiAs. The crystal structure of CrNiAs is shown in figure 1. The local surroundings of the Cr atoms are square pyramids of five As atoms, whereas the Ni atoms are located in tetrahedra of four As atoms.

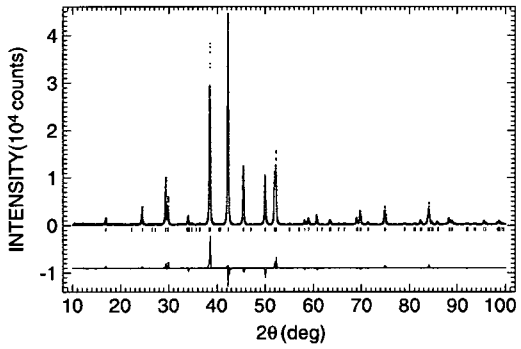

Figure 2. X-ray powder diffraction spectrum of CrNiAs at 298 K. The experimental data are denoted by open circles, while the line through the circles represents the results of the Rietveld refinement. The vertical bars represent the Bragg peak positions corresponding to the CrNiAs phase. The lower solid line represents the difference curve between experimental and calculated spectra.

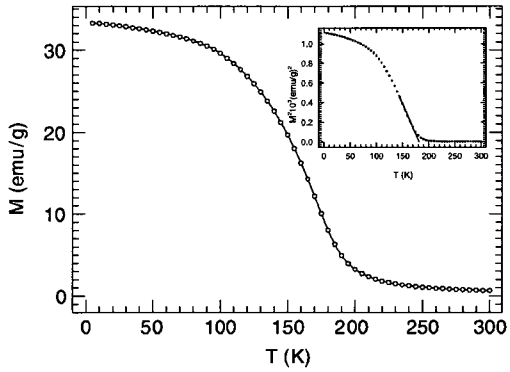

Figure 3. Temperature dependence of the magnetization of CrNiAs, measured in an external magnetic field of 10 kOe. The solid line is a guide for the eye. The inset shows the temperature dependence of the square of the magnetization and the solid line is a linear fit of the data around T_C.

Table 1. Atomic positions for the hexagonal arsenide CrNiAs obtained through Rietveld analysis.

Atom	Site	Point symmetry	x	y	z	Occupancy
Cr	3g	$m2m$	0.5729(3)	0	$\frac{1}{2}$	1.0
Ni	3f	$m2m$	0.2515(2)	0	0	1.0
As1	1b	$\bar{6}2m$	0	0	$\frac{1}{2}$	1.0
As2	2c	$\bar{6}$..	$\frac{1}{3}$	$\frac{2}{3}$	0	1.0

The x-ray powder diffraction pattern of the sample studied is shown in figure 2. A Rietveld refinement of the x-ray powder diffraction data was performed yielding the lattice parameters $a = 6.1128(1)$ Å and $c = 3.6585(1)$ Å. The obtained atomic positions for the Cr and Ni sites are listed in table 1 and the interatomic distances are listed in table 2. The sample studied is single phase.

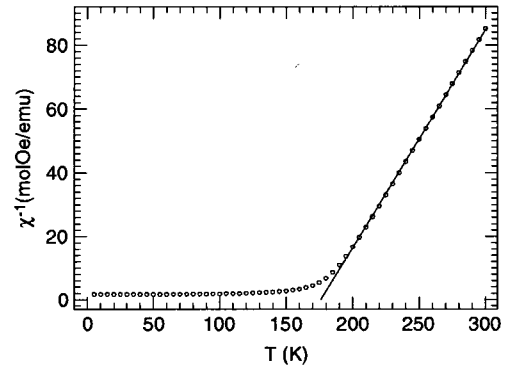

Figure 4. Temperature dependence of the inverse magnetic susceptibility of CrNiAs, measured in an external magnetic field of 10 kOe. The solid line is the fit to equation (2) in the temperature range 195–300 K.

3.2. Magnetic properties

The temperature dependence of the magnetization M of CrNiAs measured in an applied magnetic field of 10 kOe between 5.0 and 300 K is shown in figure 3. This arsenide is obviously a ferromagnet. For a mean-field ferromagnet, $M^2 \propto T_C - T$ near T_C [36]. From a linear fit of M^2 versus T (inset in figure 3), T_C was estimated to be 181.4(1.5) K.

The temperature dependence of the inverse magnetic susceptibility χ of CrNiAs is shown in figure 4. In the paramagnetic region the $\chi(T)$ data could be fitted to a modified Curie–Weiss law

$$\chi = \chi_0 + \frac{C}{T - \theta_p}, \qquad (2)$$

where χ_0 is the temperature independent magnetic susceptibility, C is the Curie constant, and θ_p is the paramagnetic Curie temperature. The Curie constant can be expressed as $C = \frac{N\mu_{eff}^2}{3k}$, where N is the concentration of magnetic atoms per unit mass, k is the Boltzmann constant, and μ_{eff} is the effective magnetic moment. The values of χ_0, C, and θ_p obtained from the fit are 1.57(2.34) × 10^{-7} emu Oe^{-1} mol^{-1}, 1.461(6) emu Oe^{-1} K mol^{-1}, and 176.0(3) K, respectively. This value of C corresponds to μ_{eff} of 2.42(1) μ_B per transition-metal atom. The positive paramagnetic Curie temperature is consistent with the ferromagnetic ordering, and the value of θ_p is close to T_C.

Figure 5 shows a series of magnetization isotherms measured in the vicinity of T_C, estimated above. The usual procedure for extracting the spontaneous magnetization $M_S(T) = \lim_{H\to 0} M$, the inverse initial susceptibility $\chi_0^{-1} = \lim_{H\to 0}(H/M)$, and T_C from the $M(H)$ isotherms is to make use of the Arrott plot [37], M^2 versus H/M. According to mean-field theory, near T_C this plot should consist of a series of parallel lines for different temperatures, with the line at $T = T_C$ passing through the origin and $M_S(T)$ and $\chi_0^{-1}(T)$ are determined from the intercept values on the ordinate ($T \leqslant T_C$) and abscissa ($T \geqslant T_C$), respectively. Figure 6 shows the Arrott plot for CrNiAs. It consists of approximately parallel lines for fields larger than 6.0 kOe. The critical isotherm crossing the origin is found at 171.5(4) K.

Table 2. Interatomic distances (in Å) for the hexagonal arsenide CrNiAs.

Cr	4As	2.580(1)	Ni	2As	2.328(1)	As1	6Ni	2.389(1)	As2	3Ni	2.328(1)
	1As	2.611(1)		2As	2.389(1)		3Cr	2.611(1)		6Cr	2.580(1)
	2Ni	2.684(1)		2Ni	2.663(1)						
	4Ni	2.918(1)		2Cr	2.684(1)						
	4Cr	3.152(1)		4Cr	2.918(1)						

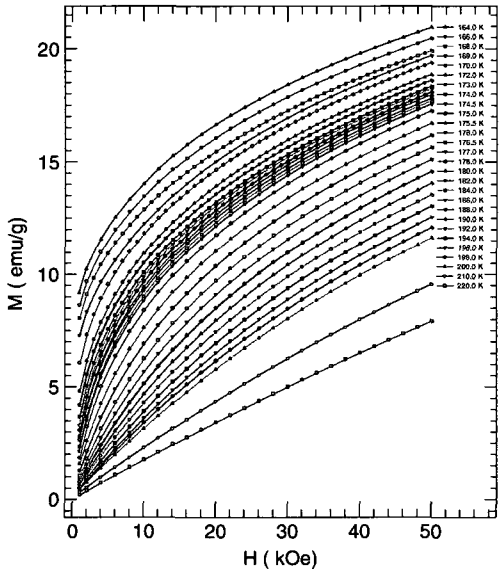

Figure 5. Magnetization isotherms versus magnetic field at temperatures between 164 and 220 K. The solid lines are guides for the eye.

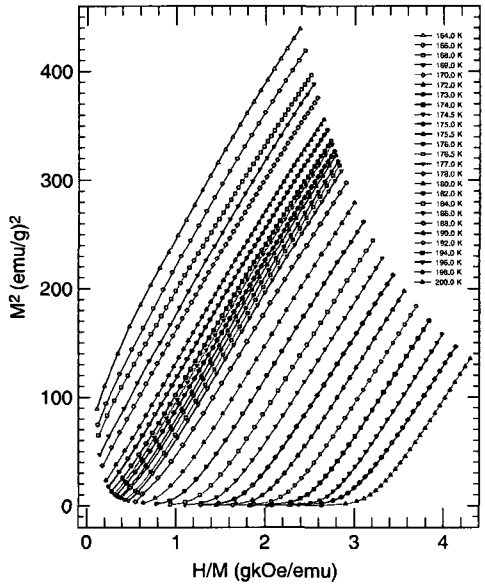

Figure 6. The Arrott plot for CrNiAs. The solid lines are guides for the eye.

According to the static scaling law equation, the second-order phase transition around T_C is governed by a set of critical exponents β, γ, and δ through the relations [38]

$$M_S(T) = M_0(-\varepsilon)^{\beta}, \qquad \varepsilon < 0 \tag{3}$$

$$\chi_0^{-1}(T) = (h_0/M_0)\varepsilon^{\gamma}, \qquad \varepsilon > 0, \tag{4}$$

where $\varepsilon = (T - T_C)/T_C$, and M_0 and h_0/M_0 are the critical amplitudes. At T_C, a critical exponent δ relates M and H by [38]

$$M = DH^{1/\delta}, \qquad \varepsilon = 0, \tag{5}$$

where D is a critical amplitude. Using the Arrott plot (figure 6), a linear extrapolation of the straight lines of the isotherms from fields above 6.0 kOe to $(M/H) = 0$ and $M = 0$ yields intercepts on the M and (M/H) axes, respectively, from which the values of $M_S(T)$ and $\chi_0^{-1}(T)$ are computed. These values as a function of temperature are plotted in figure 7. The fits of the $M_S(T)$ and $\chi_0^{-1}(T)$ data (figure 7) to equations (3) and (4) respectively give $\beta = 0.514(18)$, $T_C = 171.99(14)$ K and $\gamma = 1.010(16)$, $T_C = 171.83(6)$ K. The value of T_C for CrNiAs is then taken as 171.9(1) K. The critical exponents obtained in this way are very close to those predicted by the mean-field theory ($\beta = 0.5$ and $\gamma = 1.0$).

To obtain the value of δ, M is plotted versus H at 172.0 K in figure 8, the measured temperature closest to $T_C = 171.9(1)$ K. The fit of this isotherm to equation (5) (figure 8) gives $\delta = 2.922(10)$. This value is close to the value of $\delta = 3.0$ predicted by mean-field theory.

The critical exponents β, γ, and δ should fulfill the Widom exponent relation [39] $\gamma - \beta(\delta - 1) = 0$. The determined values of β, γ, and δ satisfy this relation well (0.022(56)), within experimental error.

The magnetic field dependence of the magnetization measured at 4.2 K is shown in figure 9. The magnetization does not saturate, even in a field of 50 kOe. The saturation magnetization at 4.2 K was obtained from the Arrott plot (inset in figure 9) by a linear extrapolation of the high-field data to $(M/H) = 0$. This yielded $M_S = 33.52(1.01)$ emu g^{-1}, which corresponds to the magnetic moment per formula unit $\mu_{FU} = 1.114(33)\ \mu_B$, or to the magnetic moment per transition metal (TM) atom (assuming that As atoms carry no magnetic moment) $\mu_{TM} = 0.557(17)\ \mu_B$.

3.3. Mössbauer spectroscopy

Figure 10 shows a ^{61}Ni Mössbauer spectrum of CrNiAs measured at 4.2 K. The Ni atoms are located in the crystal structure at a site with point symmetry *m*2*m* (table 1). This ensures a non-zero electric field gradient at the Ni site and hence a possible non-zero electric quadrupole splitting. The spectrum in figure 10 clearly exhibits the presence of a poorly resolved hyperfine magnetic interaction. It was

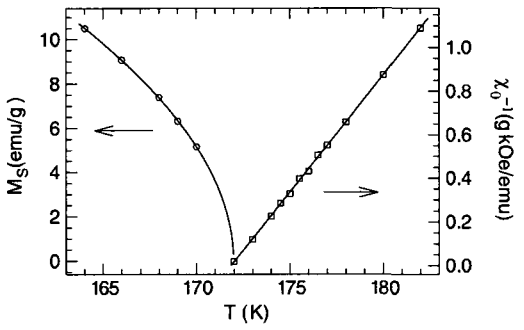

Figure 7. Temperature dependence of the spontaneous magnetization and the inverse initial susceptibility. The solid lines are fits of the experimental data to equations (3) and (4).

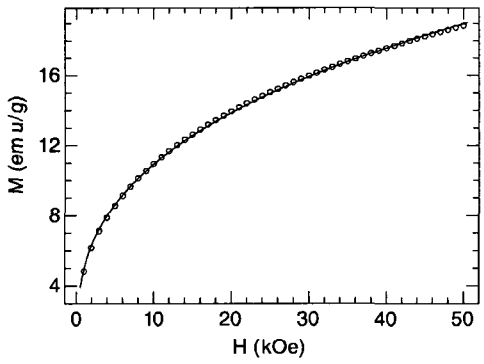

Figure 8. Magnetization isotherm versus magnetic field at 172.0 K. The solid line is the fit to equation (5).

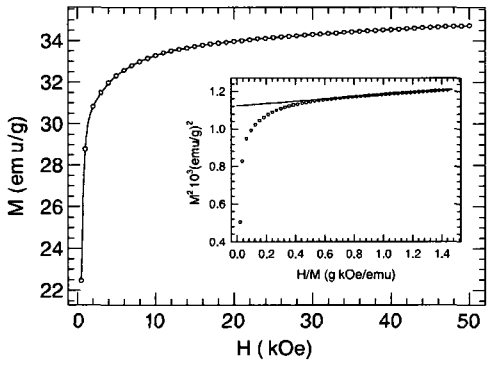

Figure 9. Magnetization isotherm versus magnetic field at 4.2 K. The solid line is a guide for the eye. The inset shows the Arrott plot. The solid line is a linear fit to the high-field data.

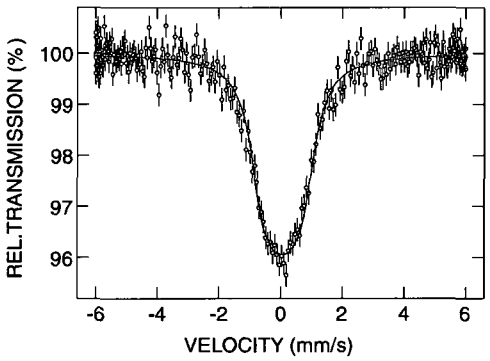

Figure 10. The ^{61}Ni Mössbauer spectrum of CrNiAs measured at 4.2 K. The solid line is a fit, as described in the text. The zero-velocity origin is relative to the source.

fitted with the transmission integral by diagonalization of the hyperfine Hamiltonian (equation (1)). The following values of the hyperfine parameters were inferred from the fit: $\Gamma_a = 0.395(9)$ mm s^{-1}, the isomer shift (relative to the ^{61}Co ($Ni_{0.85}Cr_{0.15}$) source) $\delta = 0.042(13)$ mm s^{-1}, $V_{zz} = -0.012(44) \times 10^{22}$ V m^{-2}, $f_a = 4.3(1)\%$, and $H_{hf} = 41.5(1.0)$ kOe.

The value of Γ_a is only slightly larger than the natural linewidth $\Gamma_{nat} = 0.385$ mm s^{-1} [32], as expected. Similarly to what has been found for other metallic systems [30, 40], the values of δ and V_{zz} are essentially equal to zero. In terms of the Debye approximation for the lattice vibrations, the absorber Debye–Waller factor f_a is expressed [29, 30] by the Debye temperature, Θ_D, as

$$f_a(T) = \exp\left\{-\frac{3}{4}\frac{E_\gamma^2}{Mc^2k\Theta_D}\left[1+\left(\frac{T}{\Theta_D}\right)^2\int_0^{\Theta_D/T}\frac{x\,dx}{e^x-1}\right]\right\}, \quad (6)$$

where E_γ is the energy of the Mössbauer transition, M is the mass of the Mössbauer nucleus, c is the speed of light, and k is the Boltzmann constant. The value of f_a obtained from the fit via equation (6) yields $\Theta_D = 221(1)$ K.

A non-zero value of H_{hf} implies a non-zero value of the nickel magnetic moment μ_{Ni} in CrNiAs. There is no firmly established relationship between the measured H_{hf} and μ_{Ni}. There are two major contributions to H_{hf} at the nuclei of TM elements in metallic alloys [29, 30]: the core contribution, due to the polarization of core s electrons and the polarization of the conduction electrons by the 3d electrons (i.e., by the on-site magnetic moment), and the conduction electron contribution, due to the polarization of the conduction electrons by the surrounding magnetic moments. The first contribution is proportional to the local magnetic moment μ_l, whereas the second contribution is assumed to be proportional to the average moment per magnetic atom μ_{TM} Thus, a phenomenological relation is used [41]

$$H_{hf} = a\mu_l + b\mu_{TM}, \quad (7)$$

where a and b are assumed to be constant for a given alloy system. This relation enables one to estimate the value of μ_l from the measured values of H_{hf} and μ_{TM}, provided that the values of a and b are known from an earlier calibration. Due to the scarcity of data on the values of H_{hf} at ^{61}Ni nuclei in Ni-containing alloys, the values of a and b are known only for a few alloy series [42–46]. For the ternary pnictides Cr–Ni–X (X = metalloid), $a = 63$ kOe/μ_B and $b = 57$ kOe/μ_B [47]. Using the value of μ_{TM} determined above and the measured value of H_{hf}, one obtains $\mu_{Ni} = 0.15(3)$ μ_B

from equation (7). It is thus concluded that the Ni atoms in the CrNiAs ferromagnet do carry a magnetic moment. This finding is at variance with the theoretical prediction of $\mu_{Ni} = 0$ in CrNiAs [22, 27] and in agreement with the prediction based on the electronic structure calculations of the non-zero μ_{Ni} in CrNiAs [23, 24]. Since the Ni and Cr magnetic moments are coupled ferromagnetically in CrNiAs, the values of $\mu_{Ni} = 0.15(3)\ \mu_B$ and $\mu_{FU} = 1.114(33)\ \mu_B$ imply that the Cr atoms carry a magnetic moment of $0.95(6)\ \mu_B$.

4. Conclusions

The ternary arsenide CrNiAs has been studied by means of x-ray diffraction, magnetization measurements, and ^{61}Ni Mössbauer spectroscopy. The studied compound has the hexagonal Fe_2P-type structure (space group $P\bar{6}2m$) with the lattice parameters $a = 6.1128(1)$ Å and $c = 3.6585(1)$ Å. The Curie temperature T_C is found to be 171.9(1) K and three critical exponents are determined $\beta = 0.514(18)$, $\gamma = 1.010(16)$, and $\delta = 2.922(10)$. The values of these critical exponents are close to those of a mean-field ferromagnet. The temperature dependence of the magnetic susceptibility above T_C follows the modified Curie–Weiss law with a paramagnetic Curie temperature 176.0(3) K and an effective magnetic moment per transition metal atom $2.42(1)\ \mu_B$. The magnetic moment per formula unit at 4.2 K is found to be $1.114(33)\ \mu_B$. The hyperfine magnetic field of 41.5(1.0) kOe at ^{61}Ni nuclei at 4.2 K implies that the Ni atoms carry a magnetic moment of $0.15(3)\ \mu_B$, and that the moment carried by the Cr atoms is $0.95(6)\ \mu_B$. The Debye temperature of CrNiAs is 221(3) K.

Acknowledgment

This work was supported by the Natural Sciences and Engineering Research Council of Canada.

References

[1] Hollan A 1966 *Ann. Chim. Fr.* **1** 437
[2] Nylund A, Roger A, Senateur J P and Fruchart R 1971 *Monatsh. Chem.* **102** 1631
[3] Roy-Montreuil M, Deyris B, Michel A, Rouault A, L'Héritier P, Nylund A, Sénateur J P and Fruchart R 1971 *Mater. Res. Bull.* **7** 813
[4] Nylund A, Roger A, Sénateur J P and Fruchart R 1972 *J. Solid State Chem.* **4** 115
[5] Jognson V 1973 *Mater. Res. Bull.* **8** 1067
[6] Krumbügel-Nylund A, Sénateur J P, Boursier D and Fruchart R 1974 *C. R. Acad. Sci. Paris* C **278** 85
[7] Senateur J P, Rouault A, Fruchart R, Capponi J J and Perroux M 1976 *Mater. Res. Bull.* **11** 631
[8] Guérin R and Sergent M 1977 *Mater. Res. Bull.* **12** 381
[9] Sénateur J P, Fruchart D, Boursier D, Rouault A, Montreuil J R and Deyris B 1977 *J. Physique Coll.* **12** C7 61
[10] Iwata N, Matsushima T, Fujii H and Okamoto T 1980 *J. Phys. Soc. Japan* **49** 1318
[11] Fruchart R 1982 *Ann. Chim. Fr.* **7** 563
[12] Fruchart D, Fruchart R and Sénateur J P 1982 *Proc. VII Int. Conf. on Solid Comp. Trans. Elem. (Grenoble)* p IIIA1
[13] Backmann M and Fruchart D 1982 *Proc. VII Int. Conf. on Solid Comp. Trans. Elem. (Grenoble)* p IIIA2
[14] Chaudouët P, Montreuil J R, Senateur J P, Boursier D, Rouault A and Fruchart R 1982 *Proc. VII Int. Conf. on Solid Comp. Trans. Elem. (Grenoble)* p IIIA4
[15] Meisner G P, Ku H C and Barz H 1983 *Mater. Res. Bull.* **18** 983
[16] Chenevier B, Fruchart D, Backmann M, Senateur J P, Chaudouet P and Lundgren L 1984 *Phys. Status Solidi* a **84** 199
[17] Backmann M, Chenevier B, Fruchart D, Laborder O and Soubeyroux J L 1986 *J. Magn. Magn. Mater.* **54–57** 1541
[18] Bartolomé J, Garcia J, Floría L M, Falo F, Navarro R, Fruchart D, Backmann M and de Jongh L J 1986 *J. Magn. Magn. Mater.* **54–57** 1547
[19] Kanomata T, Shirakawa K, Yasui H and Kaneko T 1987 *J. Magn. Magn. Mater.* **68** 286
[20] Chenevier B, Laborder O, Backmann M, Fruchart D, Fruchart R and Puertolas J A 1988 *J. Phys. F: Met. Phys.* **18** 1867
[21] Kanomata T, Kawashima T, Utsugi H, Goto T, Hasegawa H and Kaneko T 1991 *J. Appl. Phys.* **69** 4639
[22] Ohta S, Kaneko T, Yoshida H, Kanomata T and Yamauchi H 1995 *J. Magn. Magn. Mater.* **150** 157
[23] Ishida S, Takiguchi T, Fujii S and Asano S 1996 *Physica* B **217** 87
[24] Tobola J, Kaprzyk S, Fruchart D, Bacmann M, Wolfers P and Fruchart R 1997 *J. Alloys Compounds* **262/263** 65
[25] Bacmann M, Fruchart D, Koumina A and Wolfers P 2004 *Mater. Sci. Forum* **443/444** 379
[26] Fruchart D, Allab F, Balli M, Gignoux D, Hlil E K, Koumina A, Skryabina N, Tobola J, Wolfers P and Zach R 2005 *Physica* A **358** 123
[27] Goodenough J B 1973 *J. Solid State Chem.* **7** 428
[28] Bish D L and Chipera S J 1989 *Powder Diffract.* **4** 137
[29] Greenwood N N and Gibb T C 1971 *Mössbauer Spectroscopy* (London: Chapman and Hall)
[30] Gütlich P, Link R and Trautwein A 1978 *Mössbauer Spectroscopy and Transition Metal Chemistry* (Berlin: Springer)
[31] Cali J P (ed) 1971 *Certificate of Calibration, Iron Foil Mössbauer Standard* (Washington, DC: US Government Printing Office) NBS (US) Circular No. 1541
[32] Stevens J G 1981 *CRC Handbook of Spectroscopy* vol 3, ed J W Robinson (Boca Raton, FL: CRC Press) p 403
[33] Margulies S and Ehrman J R 1961 *Nucl. Instrum. Methods* **12** 131
[34] Shenoy G K, Friedt J M, Maletta H and Ruby S L 1974 *Mössbauer Effect Methodology* vol 10, ed I J Gruverman, C W Seidel and D K Dieterly (New York: Plenum) p 277
[35] Rummel H 1982 ^{61}Ni-Mössbauer-Untersuchungen der Magnetischen Hyperfeinfelder in Nickelspinellen *PhD Thesis* Johannes Gutenberg-Universität Mainz
[36] Zijlstra H 1967 *Experimental Methods in Magnetism* vol 2 (Amsterdam: North-Holland)
[37] Arrott A 1957 *Phys. Rev.* **108** 1394
[38] Stanley H E 1971 *Introduction to Phase Transitions and Critical Phenomena* (New York: Oxford University Press)
[39] Widom B 1964 *J. Chem. Phys.* **41** 1633
Widom B 1965 *J. Chem. Phys.* **43** 3898
[40] Tomala K, Czjzek G, Fink J and Schmidt H 1977 *Solid State Commun.* **24** 857
[41] Johnson C E, Ridout M S and Cranshaw T E 1963 *Proc. Phys. Soc.* **81** 1079
Collins M F and Wheeler D A 1963 *Proc. Phys. Soc.* **82** 633
Panissod P, Durand J and Budnick J I 1982 *Nucl. Instrum. Methods* **199** 99

Panissod P 1985 *Hyperfine Interact.* **124–126** 607
[42] Erich U 1969 *Z. Phys.* **227** 25
Ebert H, Winter H, Gyorffy B L, Johnson D D and Pinski F J 1988 *J. Phys. F: Met. Phys.* **18** 719
[43] Stadnik Z M, Griesbach P, Dehe G, Gütlich P and Maniawski F 1987 *J. Magn. Magn. Mater.* **70** 436
[44] Tansil J E, Obenshain F E and Czjzek G 1972 *Phys. Rev.* B **6** 2796
[45] Streever R L and Uriano G A 1966 *Phys. Rev.* **149** 295
[46] Stadnik Z M, Griesbach P, Dehe G, Gütlich P, Stroink G and Miyazaki T 1987 *Phys. Rev.* B **35** 8740
[47] Stadnik Z M, Wang P, Jansen N, Walcher D, Gütlich P and Kanomata T 2008 unpublished results

Chapter 6 Absence of charge fluctuations of europium in metallic single crystals of $EuCu_2Si_2$

Z.M. Stadnik, P. Wang, J. Żukrowski, and B.K. Cho.

Hyperfine Interact., **169**, 1295 (2006).

Hyperfine Interact (2006) 169:1295–1299
DOI 10.1007/s10751-006-9440-0

Absence of charge fluctuations of europium in metallic single crystals of $EuCu_2Si_2$

Z. M. Stadnik · P. Wang · J. Żukrowski · B. K. Cho

Published online: 16 November 2006

Abstract The ^{151}Eu Mössbauer effect study in the temperature range 2.2–299.5 K on pulverized single crystals of $EuCu_2Si_2$ synthesized from an indium flux is presented. In contrast to previous studies on polycrystalline samples in which valence fluctuations for Eu were reported, we find that the Eu atoms are divalent in the whole temperature range. Therefore, there are no charge fluctuations of Eu in $EuCu_2Si_2$.

Key words valence fluctuation · divalent Eu

1 Introduction

The ternary alloy $EuCu_2Si_2$ is one of the first europium-based alloys in which intermediate valence behaviour was observed [1]. It is also one of the most well studied [2–5]. Previous ^{151}Eu Mössbauer studies of $EuCu_2Si_2$ [1, 4, 5] found that the effective valence of Eu changes from ~2.6 at room temperature to ~2.8 at lowest temperature.

Recently, single crystals of $EuCu_2Si_2$ were synthesized from an In flux and studied again [6, 7]. Surprisingly, magnetic susceptibility, electron-spin-resonance, and specific heat results [6, 7] are consistent with Eu being in stable divalent state. Here, we present the preliminary ^{151}Eu Mössbauer spectroscopy results on the single crystals of $EuCu_2Si_2$. We demonstrate that Eu in $EuCu_2Si_2$ is in the divalent state in the temperature range 2–300 K.

Z. M. Stadnik (✉) · P. Wang
Department of Physics, University of Ottawa, Ottawa, ON K1N 6N5, Canada
e-mail: stadnik@uottawa.ca

J. Żukrowski
Solid State Physics Department, AGH University of Technology, 30-059 Cracow, Poland

B. K. Cho
Department of Materials Science and Engineering, Gwangju Institute of Science and Technology (GIST), Gwangju 500-712, South Korea

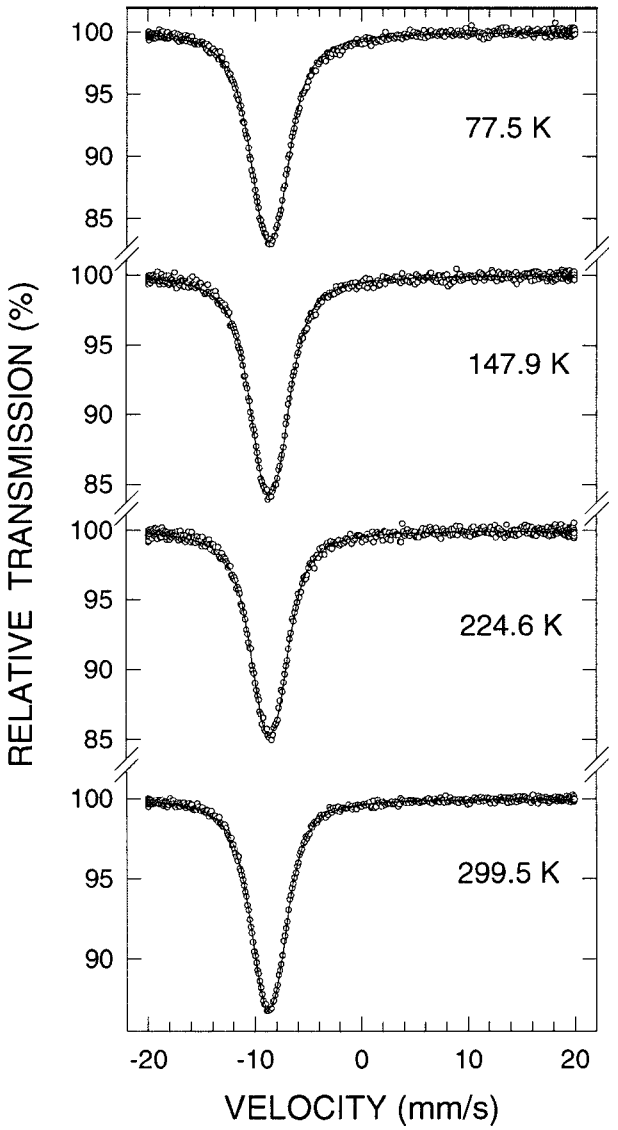

Figure 1 ^{151}Eu Mössbauer spectra of $EuCu_2Si_2$ at various temperatures above the magnetic ordering temperature. The zero of the velocity scale is relative to the $^{151}Sm(SmF_3)$ source at room temperature. The *solid line* is a least-squares fit, as described in the text.

2 Experimental procedure

Single crystals of $EuCu_2Si_2$ were synthesized from an In flux, as described in [7]. They were found to be single phase, crystallizing in the tetragonal $ThCr_2Si_2$ structure with lattice constants a=4.10 Å and c=9.93 Å [7].

^{151}Eu Mössbauer measurements were performed in the temperature range 2.2–299.5 K with a standard Mössbauer spectrometer operating in a sine mode using a 330 mCi $^{151}Sm(SmF_3)$ source kept at room temperature. The spectrometer was calibrated with a 6.35-μm α-Fe foil, and the spectra were folded. The Mössbauer absorber was prepared by mixing the

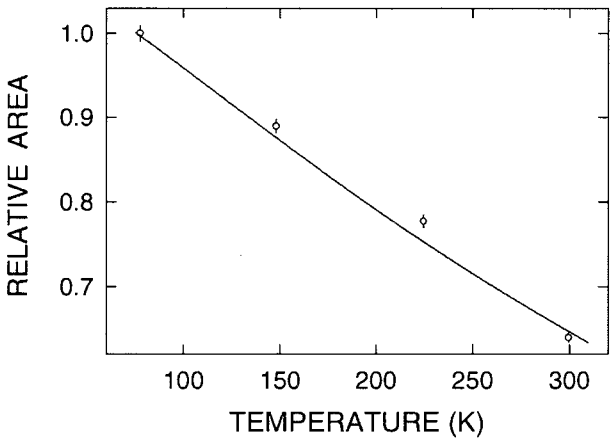

Figure 2 Temperature dependence of the normalized area under the resonance curve. The *solid line* is a least-squares fit based to the expression for the Lamb–Mössbauer factor within the Debye model of lattice vibrations.

pulverized crystals of $EuCu_2Si_2$ with powdered BN to ensure a uniform thickness of the absorber and the random orientation of sample particles. This mixture was then put into a plastic sample holder. The surface density of the Mössbauer absorber was 18.0 mg Eu/cm^2, which corresponds to the effective absorber thickness $8.1f_a$, where f_a is the absorber Lamb–Mössbauer factor.

3 Results and discussion

The Mössbauer spectra of $EuCu_2Si_2$ at selected temperatures above the antiferromagnetic ordering temperature T_N=8.5 K [8] are shown in Figure 1. In contrast to the Mössbauer spectra of a polycrystalline $EuCu_2Si_2$ [1, 4, 5], the spectra of the studied specimen consist of one line located at ~−8.65 mm/s. This shows that Eu is divalent and there are no signs of valence fluctuations in the temperature range 77.5–299.5 K.

The spectra in Figure 1 result from a pure electric quadrupole interaction. They were fitted with the transmission integral and the positions and relative intensities of absorption lines were calculated by numerical diagonalization of the hyperfine Hamiltonian [8]. The source $^{151}Sm(SmF_3)$ used is not a monochromatic source as ^{151}Sm nuclei are located in the SmF_3 matrix at the site of noncubic symmetry. By measuring the spectra of the cubic EuSe we determined [8] that the electric quadrupole coupling constant eQ_gV_{zz} in our source is −3.98(13) mm/s (Q_g=0.903 b [9]), which is very close to the value found in [10]. The precise shape of the source emission line was taken into account in the fits of the spectra in Figure 1.

The values of the electric quadrupole coupling constant eQ_gV_{zz} and the asymmetry paramer η obtained from the fits of the spectra in Figure 1 are temperature independent [8] and are, respectively, 6.11(8) mm/s and η=1.0(1). The temperature dependence of the area under the resonance curve (Figure 2) derives from the temperature dependence of f_a. The fit of the relative area to the expression for f_a within the Debye theory of lattice vibration gives the Debye temperature Θ_D=236(4) K. This value is close to the value of 210 K found from the specific heat data for the polycrystalline $EuCu_2Si_2$ [2].

The Mössbauer spectra of $EuCu_2Si_2$ at selected temperatures below and around T_N are shown in Figure 3. It is evident that these spectra are the spin relaxation spectra, even at the

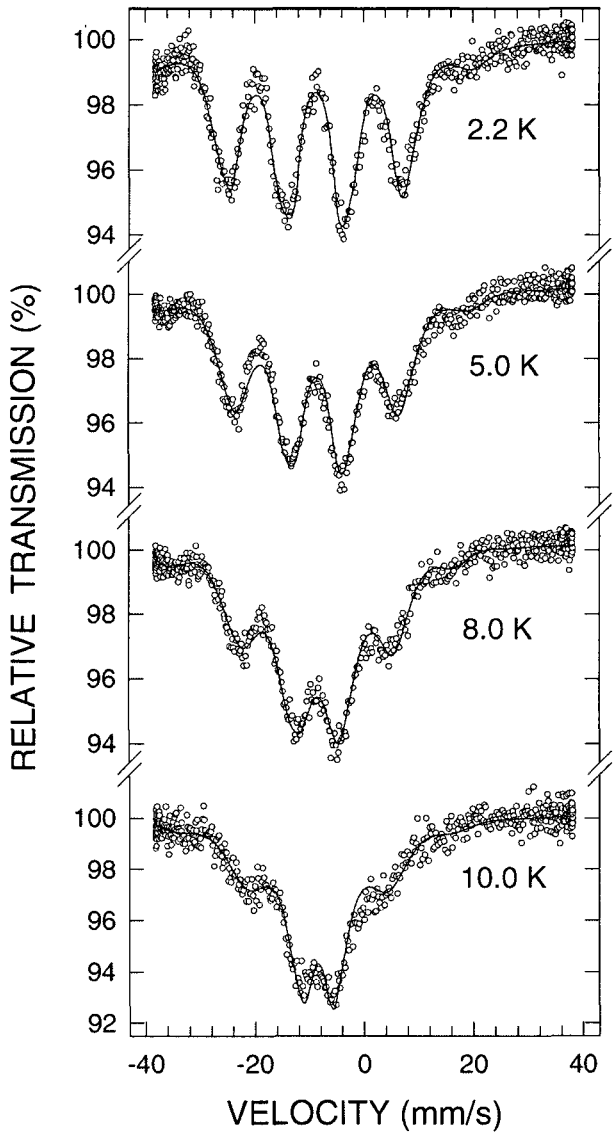

Figure 3 ^{151}Eu Mössbauer spectra of $EuCu_2Si_2$ at various temperatures below and around the magnetic ordering temperature. The zero of the velocity scale is relative to the ^{151}Sm (SmF_3) source at room temperature. The *solid line* is a least-squares fit, as described in the text.

lowest temperature of 2.2. K. They were fitted (Figure 3) using the line shape function given by Blume and Tjon [11]. The analysis of these relaxation spectra are discussed in detail elsewhere [8]. Here we notice that the isomer shift δ of these spectra is ~−8.68 mm/s. This demonstrates that the Eu atoms in the studied alloy are divalent.

The temperature dependence of δ of the spectra in Figures 1 and 3 is shown in Figure 4. It is evident that δ changes very little with temperature and its value proves that Eu in $EuCu_2Si_2$ is divalent in the temperature range 2.2–299.5 K. Consequently, there are no charge fluctuations of Eu in $EuCu_2Si_2$.

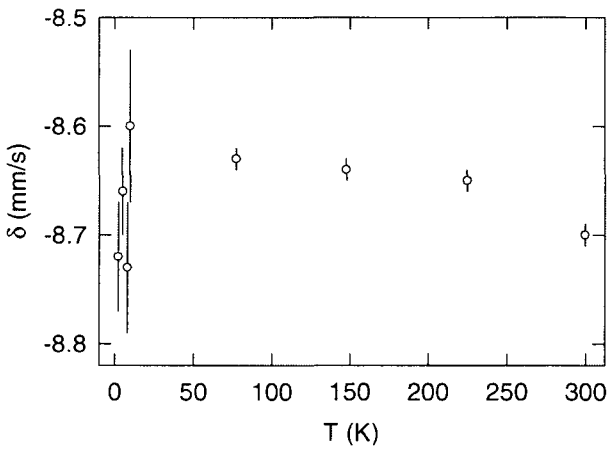

Figure 4 Temperature dependence of the ^{151}Eu isomer shift in $EuCu_2Si_2$.

4 Conclusions

The ^{151}Eu Mössbauer effect study in the temperature range 2.2–299.5 K on a ternary alloy $EuCu_2Si_2$ synthesized from an In flux has been presented. The values of the electric quadrupole coupling constant eQ_gV_{zz} and the asymmetry paramer η are, respectively, 6.11 (8) mm/s and η=1.0(1). The Debye temperature of the studied alloy is 236(4) K. The Eu atoms are in stable divalent state in the temperature range 2.2–299.5 K.

Acknowledgements This work was supported by the Natural Sciences and Engineering Research Council of Canada. The work at GIST was supported by ABRL program in Ewha Woman University funded by KRF, Korea.

References

1. Bauminger, E.R., Froindlich, D., Nowik, I., Ofer, S., Felner I., Mayer, I.: Phys. Rev. Lett. **30**, 1053 (1973)
2. Sales, B.C., Viswanathan, R.: J. Low Temp. Phys. **23**, 449 (1976)
3. Buschow, K.H.J., Campagna, M., Wertheim, G.K.: Solid State Commun. **24**, 253 (1977)
4. Röhler, J., Wohlleben, D., Kaindl G., Balster, H.: Phys. Rev. Lett. **49**, 65 (1982)
5. Abd-Elmeguid, M.M., Sauer, C., Zinn, W.: J. Phys. C **18**, 345 (1985)
6. Pagliuso, P.G., Sarrao, J.L., Thompson, J.D., Hundley, M.F., Sercheli, M.S., Urbano, R.R., Rettori, C., Fisk Z., Oseroff, S.B.: Phys. Rev., B **63**, 092406 (2001)
7. Rhyee, J.-S., Cho, B.K., Ri, H.C.: J. Appl. Phys. **93**, 8346 (2003)
8. Stadnik, Z.M., Wang, P., Żukrowski J., Cho, B.K. (to be published)
9. Tanaka, Y., Steffen, R.M., Shera, E.B., Reuter, W., Hoehn, M.V., Zumbro, J.D.: Phys. Rev. C **29**, 1830 (1984)
10. Nowik, I., Felner, I.: Hyperfine Interact. **28**, 959 (1986)
11. Blume, M., Tjon, J.A.: Phys. Rev. **165**, 446 (1968)

Chapter 7 Low-field negative magnetization and coercive-field magnetization reversal in transition metal chalogenides; Cr_2FeSe_4 magnetic structure from neutron diffraction

G. Lamarche, I. Bulyzhenkov, P. Wang, M. Quintero, and A.-M. Lamarche.

J. Phys. Chem. Solids, 69, 884 (2008).

Available online at www.sciencedirect.com
ScienceDirect
Journal of Physics and Chemistry of Solids 69 (2008) 884–890
JOURNAL OF PHYSICS AND CHEMISTRY OF SOLIDS
www.elsevier.com/locate/jpcs

Low-field negative magnetization and coercive-field magnetization reversal in transition metal chalcogenides; Cr_2FeSe_4 magnetic structure from neutron diffraction

G. Lamarche[a,*], I. Bulyzhenkov[a], P. Wang[a], M. Quintero[b], A.-M. Lamarche[a]

[a]*Department of Physics, Ottawa-Carleton Institute for Physics, University of Ottawa, 150 Louis-Pasteur, CP 450 Succ A, Ottawa, Canada K1N 6N5*
[b]*Departamento de Fisica, Facultad de Ciencias, Universidad de los Andes, Mérida, Venezuela*

Received 17 May 2007; received in revised form 28 September 2007; accepted 2 October 2007

Abstract

Low-field negative magnetization, of the order of -10^{-1} emu/g-Oe, from 4.2 K up to room temperature and higher (350 K), and coercive-field magnetization reversal are both present in $Cr_{(3-x)}Fe_xX_4$ for X = S, Se, Te and $x = 0$ to 3, and for Cr_5Te_8 and Cr_7Te_8. For Cr_2FeSe_4 the zero-field-cooled (ZFC) magnetization is negative for 5 Oe and below. To obtain a more detailed knowledge of the magnetic phases involved in the observed magnetization versus temperature $M(T)$ curves, we obtained and studied neutron diffraction (n.d.) scans on the compound Cr_2FeSe_4, taken at 14 temperatures from 4.2 to 300 K. For this same n.d. sample, the temperature for magnetization reversal of value -3×10^{-4} emu/g-Oe is 80 K in 40 Oe applied field, then the reversal disappears for 65 Oe applied field. The complex magnetic interactions responsible for this reversal are revealed in the hysteresis curves.

Keywords: A. Chalcogenides; D. Magnetic properties; D. Magnetic structure

1. Introduction

For over four decades, transition metal chalcogenides have attracted much attention ([1–3,13], and references therein), and they are now being studied for their interesting magnetic and thermoelectric properties in view of possible applications in technology [4–10]. These ternary and binary compounds, in three different crystallographic structures, have been found to give a surprisingly large negative magnetization in low applied fields, from 4.2 K to room temperature and above. The present paper describes this phenomenon and also shows the more common magnetization reversal at low temperatures for slightly higher applied fields. Negative magnetization has often been reported for the case where two opposing magnetic moments are not equal; however, it is shown from our magnetic neutron diffraction (n.d.) study that non-compensation is not the mechanism.

The majority of transition metal chalcogenides have the monoclinic NiAs defect structure with ordered vacancies and cation sites 2(*c*) and 4(*i*) each in octahedral coordination. To form the magnetic cell, the *a*- and *c*-axes are most often doubled, and for the compounds Cr_5X_8 and Cr_7X_8 the *b*-axis is also doubled to accommodate ordered vacancies. The spinel sulfide Cr_2FeS_4 is an exception, with the Cr in octahedral coordination, the Fe in tetrahedral coordination and no ordered vacancies. The other exception studied, and found to have low-field negative magnetization, is $Fe^{2+}Se_2$ with the orthorhombic marcasite structure, where $FeSe_6$ octahedra share edges and form chains of linked octahedra.

In the monoclinic defect structure, Bertaut et al. [1] defined four different antiferromagnetic (a.f.) orderings of the cation spins (named A, B, C, and D) in the magnetic cell. Chevreton and Andron [2] reported an a.f. refinement, type C, in their 4.2 K n.d. scan, while Adachi et al. [3] found a ferrimagnetic refinement of their 77 K n.d. scan.

*Corresponding author. Tel.: +1 613 562 5800x6792; fax: +1 613 562 5190.
E-mail address: glamarch@science.uottawa.ca (G. Lamarche).

0022-3697/$ - see front matter © 2007 Elsevier Ltd. All rights reserved.
doi:10.1016/j.jpcs.2007.10.012

No complete n.d. study from 4.2 to 300 K at appropriate neutron wavelength, permitting to separate antiferromagnetic and ferromagnetic Bragg peaks and also to define critical temperatures and other characteristics, has yet been reported. Recently, Snyder et al., [4] found magnetization reversal for Cr_2FeSe_4 between 45 and 80 K with $M/H = -4 \times 10^{-6}$ emu/g-Oe. In our $M(T)$ studies, we found reversal for fields 20, 40 and 60 Oe. The reversal at 80 K is shown later, for a field of 40 Oe with $M/H = -3 \times 10^{-4}$ emu/g-Oe at 4.2 K, and is attributed to a secondary coercive-field reversal, judging from negative inflections in the first and fourth quadrants of the $M(H)$ hysteresis curves.

In ac non-linear susceptibility studies of the spinel sulfide Cr_2FeS_4, Tsurkan et al. [6] found broad negative curves of value −0.0042 emu/g at 60 K, where we found, as that same temperature in our dc magnetic studies of Cr_2FeS_4, a broad dip (maximum negativity) in $M(T)$, and ferrimagnetic hysteresis of +0.0035 emu/g-Oe superposed on the negative magnetization of −0.234 emu/g-Oe in Earth's field. Ac magnetization studies of our Cr_2FeSe_4 samples by Junod [7] suggested our dc pattern but did not reveal any significant diamagnetism for Cr_2FeSe_4.

Magnetization reversal at low temperatures is common and easily identified from hysteresis runs, while very low-field negative magnetization is a new and intriguing phenomenon. Negative magnetization at various fields, and not due to reversal, has been reported and attributed to inhomogeneity of the sample, to surface phenomena and to competing magnetic interactions. Those magnetizations had different behavior to that observed in our homogeneous chalcogenides. Our magnetization experiments first discovered the low-field phenomenon in the selenides [8], and then in the sulfides and the tellurides, which have higher critical temperatures, up to 350 K [9]. The negative magnetization can be modeled from the Ginzburg–Landau (GL) theory by coupling two or more magnetic subsystems without referring to microscopic origins of their moments [10]. This theory predicts bistable states and controlled magnetic memory in systems with magnetic coupling. Therefore, detailed knowledge of magnetic structures might be very important for further search and specification of prospective materials with negative residual moments, with possibilities for spintronics. As a first step toward an understanding of the microscopic physics behind the negative magnetization, a magnetic n.d. study from 4.2 to 300 K was undertaken on a homogeneous sample of Cr_2FeSe_4.

The magnetic cell in Fig. 1(a) shows the cations forming chains (by t_{2g} orbitals) along the c-axis and rows of cations in triangular arrangement in the ab plane. The b-axis spin

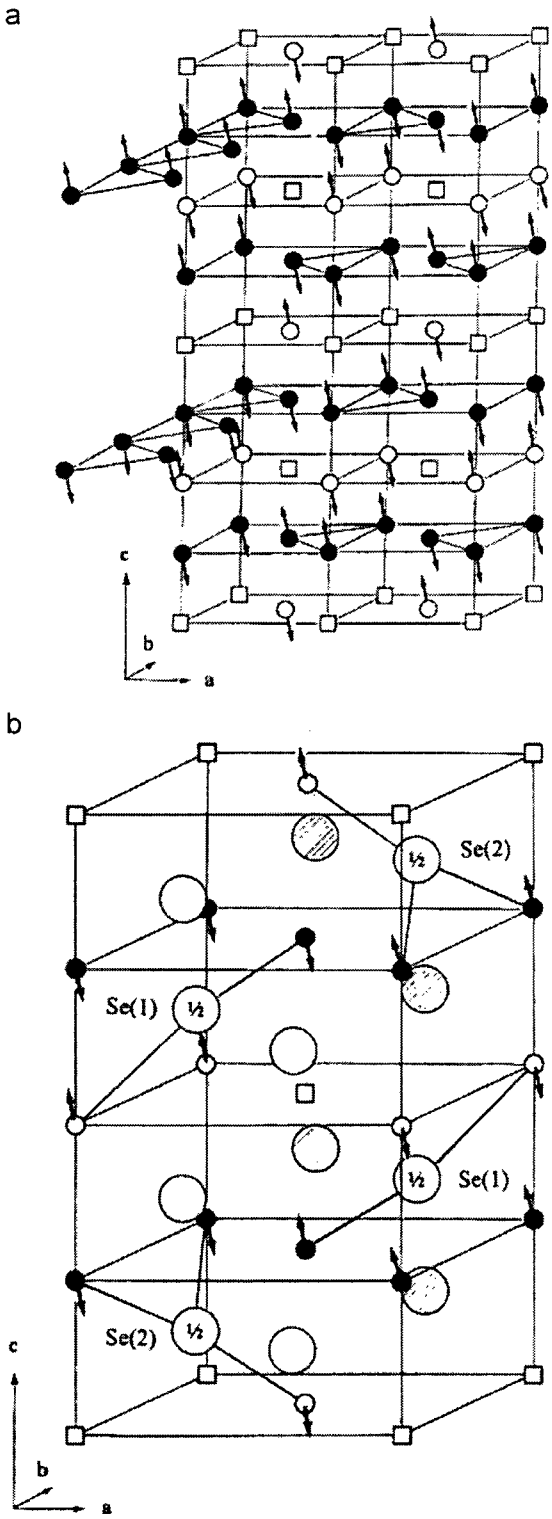

Fig. 1. (a) The magnetic cell for antiferromagnetic Cr_2FeSe_4 showing the chemical cell doubled on a- and c-axes: (○) Fe, (●) Cr, (□) vacancy. (b) One-quarter of the magnetic cell showing the Se anions on their 4(i) sites at $y = 0$ and $y = \frac{1}{2}$. Two of the anions at $y = \frac{1}{2}$ are shown each bonded to two Fe cations and one Cr cation at intermediate angle: (○) Fe, (●) Cr, (□) vacancy.

components are not illustrated. The chemical cell (Fig. 1(b)) shows the anions in 4(*i*) sites with the cations participating in interlayer cation–anion–cation bonding, where the strongly polarizable anions contribute 2p electrons to the empty Cr^{3+} e_g orbitals.

For crystals with low symmetry, antiferromagnetism is always accompanied by weak ferrimagnetism, as given by theoretical symmetry considerations. The value of our negative magnetization, attaining -2.3×10^{-1} emu/g-Oe in Earth's field, is at least 10^2 times the value of the weak ferrimagnetism found from our low-field hysteresis runs.

2. Magnetic measurements

Previous to our magnetic n.d. study, our compound in very fine platelets form was studied by a custom assembled SQUID magnetometer [11], where the sample is moved between two astatic coils. In this instrument, the applied magnetic field generated by a Cu wire solenoid is well defined and not ambiguous as in the case of a superconducting solenoid, where a remnant field has to first be destroyed at least at the sample position, leaving the possibility of generating unknown fields in regions outside that position through which the sample has to be exposed, as it is brought in, prior to zero-field-cooling (ZFC) measurements.

In Fig. 2(b), circles give the ZFC M/H as a function of temperature for a field of 1.65 Oe, and the solid line gives the magnetization per Oersted of a similar sample recorded continuously in a field of 1.5 Oe, as the temperature varied, with the sample stationary in the vertical position, adjusted at the center of one of the two astatic coils, to have the largest signal. We observe very similar behavior eliminating the possibility of a reversal of magnetization due to some inhomogeneous field when the sample is moved for measurements. The samples in Figs. 2–4 were all taken from the n.d. material described below.

$M(T)$ studies are shown in Fig. 2(a) at Earth's field (0.56 Oe) at 5 Oe and 40 Oe. The sample weight is 0.1308 g. FC and ZFC runs have the same pattern. The 40 Oe ZFC run shows the low-temperature magnetization reversal at 80 K. Later, in Fig. 4 (inset), we give the temperatures of reversal for applied fields of 20, 40 and 60 Oe from $M(T)$ studies.

A Lakeshore vibrating sample magnetometer (VSM) was used in hysteresis studies at various temperatures. Fig. 3 shows the low-field hysteresis for the n.d. sample for ± 3 Oe applied field at 95 K, and the hysteresis for ± 5 Oe at 10 K. For the 95 K hysteresis, the sample had previously been exposed to a field of 1000 Oe, while for the 10 K hysteresis the sample had not been exposed to a field greater than 0.56 Oe prior to measurements. In the second case, we saw, at all temperatures, similar loops shifted down to negative values 100 times stronger. The loops give $M/H = +9 \times 10^{-4}$ emu/g-Oe at 10 K, $+6 \times 10^{-4}$ emu/g-Oe at 95 K, and $+8 \times 10^{-4}$ emu/g-Oe at 150 K (± 3 Oe, not shown). Inflections in the curves are real and reproducible.

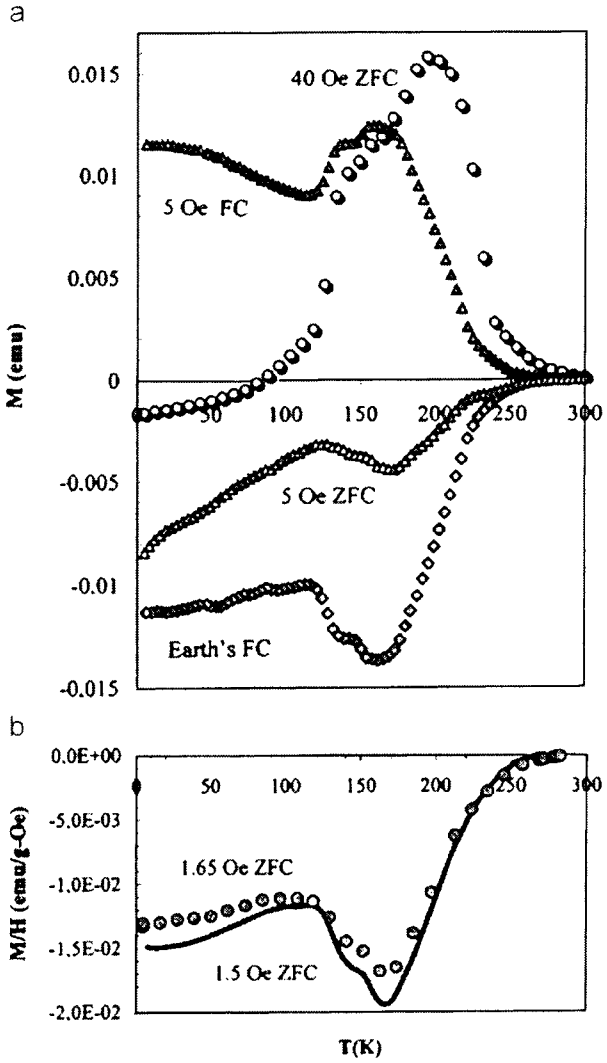

Fig. 2. (a) $M(T)$ curves for Earth's field, for at 5 Oe (ZFC and FC), and for 40 Oe (ZFC). (b) ZFC magnetization of Cr_2FeSe_4 measured by SQUID as the sample is moved in a magnetic field of 1.65 Oe (○) and ZFC magnetization in 1.5 Oe measured by SQUID with the sample stationary at optimum position.

Fig. 4 shows three hysteresis patterns for temperatures 5, 90, and 150 K, at higher fields, for ± 1000 Oe. The inflections that are evident at 90 K are also visible in the 150 K curve (shown) and the 200 K curve (not shown). At 190 K and above, we do not see any magnetic Bragg peaks from the n.d. study, only short-range order, while the hysteresis curve at 200 K is ferrimagnetic and the coercive field is narrower than for the 150 K hysteresis. The ferrimagnetism in high field at 90 K is 2.5×10^{-3} emu/g-Oe. For 5 K (shown), and also at 30 K, we found antiferromagnetism hysteresis with weak ferrimagnetism, $+1 \times 10^{-4}$ emu/g-Oe.

The inset in Fig. 4 shows the temperature of magnetization reversal for three applied fields. The hysteresis curve at

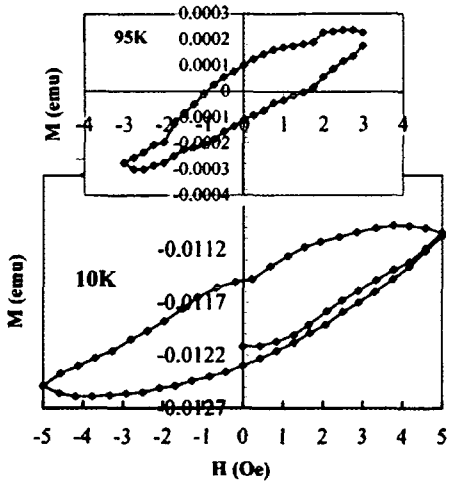

Fig. 3. Hysteresis patterns ±3 Oe at 150 K, and ±5 Oe at 10 K.

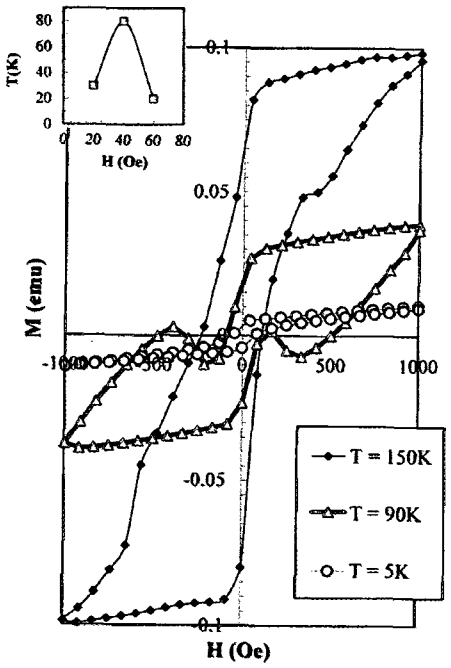

Fig. 4. Hysteresis patterns ±1000 Oe at 5, 90, and 150 K. The inset gives the low temperatures of magnetization reversal for three applied fields, 20, 40 and 60 Oe.

90 K with a negative inflection in positive field is typical of curves in those low temperatures. The M/H value of the negative inflection is -1.8×10^{-4} emu/g-Oe, while our value from the $M(T)$ curve for 40 Oe is -3×10^{-4} emu/g-Oe at 4.2 K.

3. Neutron diffraction

The six grams of Cr_2FeSe_4 for the n.d. experiment were prepared by solid solution in quartz tubes in batches of 1 to 2 g, heating to 1050 °C, annealing at 625 °C, and then quenching. Stoichiometry $Se_{4.12}$ is necessary to avoid cation excess. The platelet portions were selected and studied, and those having the same $M(T)$ curve were then intimately mixed to obtain the final homogeneous 6 g n.d. sample. Diffraction scans were obtained at the C2 spectrometer on the NRU reactor of Chalk River Laboratories, at 14 different temperatures from 4.2 to 300 K, in Earth's field, for neutron wavelength 2.3696 Å, for 2θ from 5° to 85°, and for 2θ from 35° to 115°.

The nuclear Rietveld profile refinement is given in Fig. 5(a) for the 280 K scan, the a.f. refinement for the 4.2 K scan in Fig. 5(b) and the nuclear and ferrimagnetic

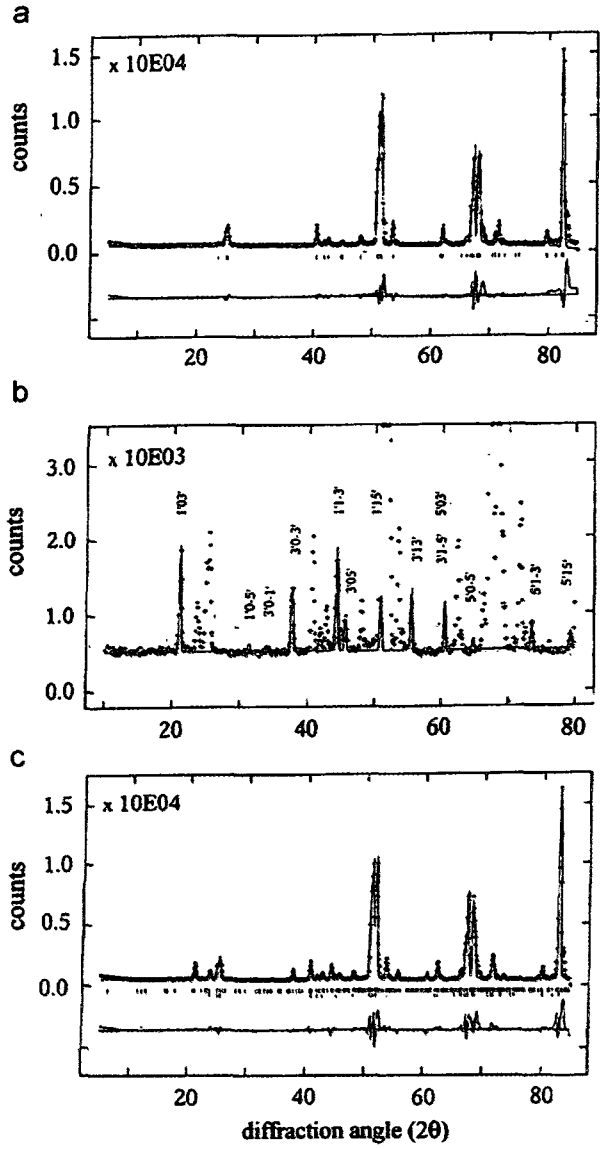

Fig. 5. Rietveld profile refinements for Cr_2FeSe_4 neutron diffraction scans with $\lambda = 2.3696$ Å: (a) nuclear solution at 280 K; (b) antiferromagnetic solution at 4.2 K; (c) ferrimagnetic and nuclear solutions at 4.2 K.

refinements for the 4.2 K scan in Fig. 5(c). Strong a.f. magnetic peaks are indexed. All 14 scans were refined to give the temperature variation of atom parameters and of magnetic peaks. The profile parameters are the default values $G(U)$, $G(V)$, $G(W)$ for the pseudovoigt profiles with small Lorentzians $L(U) = 2$ and $L(V) = 2$, to satisfy the profile tails. The magnetic solutions were refined on the n.d. scans by the Rietveld profile refinement (GSAS [12]) using four sets of Hartree–Fock coefficients in the magnetic form factors for Cr^{3+} and for Fe^{2+}.

In the Rietveld ferrimagnetic refinement, the (0 0 4′) peak is the only strong ferromagnetic peak, and only the Cr^{3+} spins are contributing. Fortunately, the nuclear peak (0 0 2) is very small. The Fe^{2+} spins contribute to the (1 0 $\bar{1}$)(2′ 0 $\bar{2}$′) and (1 0 1)(2′ 0 2′) peaks, and to a few other nuclear peaks ($l = 2n$). The temperature dependence of the integrated intensities (Gaussians) of strong a.f. peaks (1′ 0 3′), (1′ 1 $\bar{3}$′) and (3′ 0 $\bar{3}$′) and the ferromagnetic (0 0 4′) peak is given in Fig. 6(a), along with the thermal dependence of the tail of the (0 0 4′) peak.

The ferromagnetic peak (0 0 4′) at $2\theta = 23.4°$ has the characteristic Bragg rise and then a slower decrease identifying long-range order coexisting with short-range order. The long-range order was extracted for the intensity

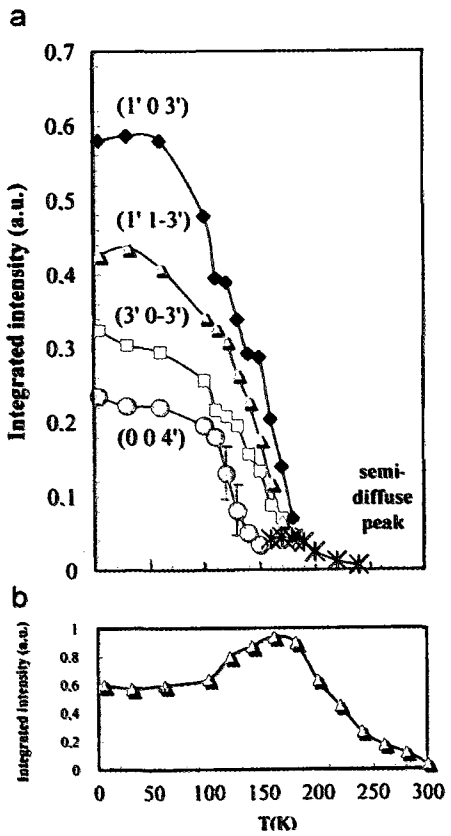

Fig. 6. (a) Integrated intensities of magnetic Bragg peaks, and of the semi-diffuse peak in the tail of (0 0 4′). (b) Integrated intensity of the diffuse peak at $2\theta = 24°$.

plot, using the peak width characteristic of the other magnetic peaks. The errors in the integration are within the size of the symbols used in the plot, while the error in the neutron counts is equal to $(\text{counts})^{1/2}$. The sample was studied with a low temperature DTA instrument developed in our laboratory. The leading edge of the DTA peak found on the cooling curve gives a transition at 185 K (±5).

The values of magnetic moment are $2.57(5)\,\mu_B$ on the 2(*c*) sites and $1.74(5)\,\mu_B$ on the 4(*i*) sites. The value of the magnetic moment on Cr^{3+} at 4.2 K is reduced to 55% from the theoretical spin-only value. For Fe^{2+} the reduction is 62% from the spin-orbital value, or 48% from the spin-only value. Fe^{2+} in octahedral sites has a strong orbital contribution to the magnetic moment. The absence of the magnetic peak (1′ 0 $\bar{1}$′) at $2\theta = 12.25°$ at all temperatures is a proof that the values of Cr^{3+} and Fe^{2+} magnetic moments are compensated.

In Fig. 1(a), *a*-axis components are exaggerated for visibility, the refined angles are 3.75° from the *c*-axis for Cr^{3+} and 3.43° for Fe^{2+}. The *b*-axis spin components are $M_y = |0.337(2)\ (M_{Cr})\,\mu_B|$ and $M_y = |0.441(4)\ (M_{Fe})\,\mu_B|$. Then $2|M_y(\text{Cr})| - |M_y(\text{Fe})|$ gives $M/H = 6 \times 10^{-4}$ emu/g-Oe. The value of M/H on the initial curve of the low-field hysteresis (Fig. 3) is 1.3×10^{-4} emu/g-Oe at 0.5 Oe and 2.3×10^{-4} emu/g-Oe at 1.0 Oe. The value found at three high-field hysteresis curves, 250, 500 and 1000 Oe, is 4×10^{-4} emu/g-Oe. The values found are valid provided the ferrimagnetic order is complete (all spins having *b*-axis components). However, there is some short-range order in the *a*–*b* planes and in the planes (1 0 $\bar{1}$) and (1 0 1) up to 300 K (Fig. 6(b)). The thermal dependence of the integration of the weak scattering (Lorentzian distribution) located under the first set of strong peaks for Cr_2FeSe_4 at $2\theta = 24°$ has a shape which is a positive parallel to the negative $M(T)$ curves obtained at low fields, as shown in Fig. 2(a) and (b). This could be incidental, but it shows that the ferrimagnetic solution could be more complicated than given by the refinement.

4. Nuclear structure

The strong nuclear peaks have shoulders that could not be satisfied by varying the profile parameters. Simulations with all published parameters for Fe compositions $1 < x < 3$ were not at all conclusive, and did not permit to identify the shoulders. The origin is probably stacking faults and twinning, both common in hcp structures. Our 2(*c*) and 4(*i*) cation site occupancies, 0.93 (Cr on 4(*i*)) and 0.88 (Fe on 2(*c*)), are in agreement with the 9% Fe^{3+} population found from the Mossbauer study of Goya and Sagredo [5].

Table 1 gives the 300 K lattice parameters and the atom positions in space group I2/m. The temperature variations of β and c/a are shown in Fig. 7. The ratio c/a is invariant from 4.2 to 120 K, after which the extreme distortion, $c/a = 1.879$, of the Se octahedra decreases only slightly. The temperature variation of angle β shows a cusp at

Table 1
$Cr_2Fe\square Se_4$ lattice parameters and atom positions in space group I2/m at 300 K

Atom	Site	x	y	z	Occupancy
□	2(*a*)	0	0	0	0
Fe	2(*c*)	0	0	0.5	0.88 Fe/0.12 Cr
Cr	4(*i*)	0.0299	0	0.2384	0.93 Cr/0.07 Fe
Se(1)	4(*i*)	0.3329	0	0.8643	1.0
Se(2)	4(*i*)	0.3302	0	0.3799	1.0

$a = 6.267(1)$ Å, $b = 3.606(1)$ Å, $c = 11.726(4)$ Å, $\beta = 91.03(1)°$, $c/a = 1.871$, density $= 5.945\,g/cm^3$, $U_{iso} = 0.03115$, preferred orientation (0 0 1) = 1.19, $R_p = 0.1268$.

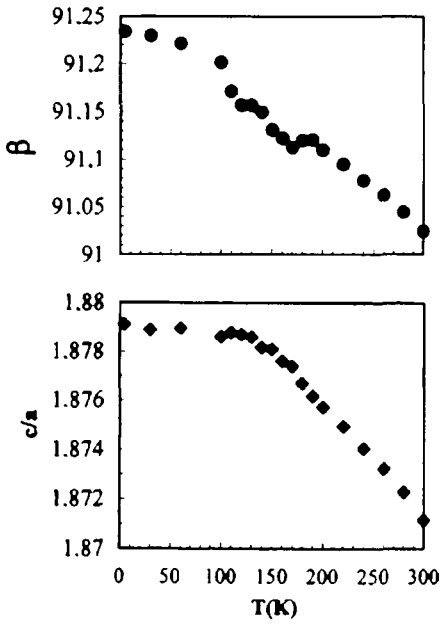

Fig. 7. Temperature variation of the cell parameters β and c/a.

180 K, the Néel temperature, and an inflection at 100–110 K. The diffraction scans were searched for possible impurities, elements, oxides and selenides, and none were found.

5. Discussion: magnetic structure

Cr^{3+} and Fe^{2+} are on 4(*i*) and 2(*c*) sites in octahedral coordination with hcp Se anions, Se(1) and Se(2), respectively. The cation chains Cr^{3+}–Fe^{2+}–Cr^{3+}–□–Cr^{3+}–Fe^{2+}–Cr^{3+}–□– along the *c*-axis have cation separation within the critical intercation separation R_c [14] for direct exchange through Se octahedra having a common face. These interactions are the strongest of the structure.

Covalence in the interlayer cation–anion–cation bonding is the main reason for the reduction of the magnetic form factors [15]. In Fig. 1(b), one-quarter of the magnetic cell is given to show the 4(*i*) sites of Se atoms. At $y = \frac{1}{2}$, the two Se situated between the cation vacancy positions are shown each bonded interlayer at an angle 126.6° to two Fe^{2+} and one Cr^{3+}, with a.f. interaction, while the two other Se at $y = \frac{1}{2}$ are involved in ferromagnetic bonding of one Fe^{2+} and two Cr^{3+}, with the same angle 126.6°.

The critical intermediate angle for antiferro- to ferro-interactions is between 125° and 150°. In our structure, there is another consideration related to the orbitals of the cations involved in the bonding. From theoretical considerations on cation–anion–cation bonding [16], when the cation has empty e_g orbitals (Cr^{3+}), the interaction is ferromagnetic, and when the cation has half-filled e_g orbitals (Fe^{2+}), the interaction is antiferromagnetic. In the case of exchange of cations, 9% for our sample of Cr_2FeSe_4, the interactions could be disturbed.

6. Conclusions

In hysteresis runs at 170–180 K and higher, we find ferrimagnetic patterns for the short-range order observed in our n.d. scans. The short-range magnetic ordering is along the *b*-axis, and this lattice moment could participate in magnetic coupling to the electronic subsystem. The negative magnetization observed cannot be related to the Fe cation alone, either on 2(*c*) sites or on 4(*i*) sites, because we have found negative magnetization in the compounds Cr_3X_4 (S, Se, Te), as well as in Cr_5Te_8, Cr_7Te_8, $Cr_{48}Te_{52}$, Cr_2TiTe_4, Ti_2CrTe_4, Ti_3Te_4, and V_3Te_4. In our $M(T)$ study of Cr_3Se_4, the very sharp a.f. peak at 80 K, which identifies the transition at 80 K from commensurate order below 80 K to incommensurate order above 80 K [17] is clearly superposed on a negative magnetization. The pattern of the weak ferrimagnetism of Cr_2FeSe_4 in the low-field negative magnetization is not so evident. For the negative magnetization at 4.2 K, the Earth's field value is -2.3×10^{-1} emu/g-Oe, and for 5 Oe, the value is -1.3×10^{-2} emu/g-Oe.

We conclude that our n.d. sample has antiferromagnetism with weak ferrimagnetism due to the two different distortions of the Cr^{3+} octahedra and of the Fe^{2+} octahedra. Previously reported $M(T)$ studies of Cr_2FeSe_4 did not include magnetization in fields below 50 Oe and gave $T_N = 208$–260 K [5,6,13], all in very high field. This low-field phenomenon is found only below about 5 Oe for the chalcogenides, except for the cases of semiconductor doping of the vacancies, which gave negative magnetization up to 40 Oe. The temperature range of the negative/positive behavior, extending to 60 K above room temperature, is already sufficiently high for spintronics applications.

Acknowledgments

We wish to acknowledge a past research grant from NSERC to one of the authors (G.L.). Discussions and exchange of data with F. Lamarche, A. Junod, R. Lortz, Z. Stadnik, and A. Geim were very productive, and very much appreciated. We give special recognition to

R. Hammond for assistance on the neutron diffraction studies at Chalk River Laboratories, and we give thanks for the valuable contributions from our summer student B. Chauvineau.

References

[1] E.F. Bertaut, G. Roult, R. Aléonard, R. Pauthenet, M. Chevreton, R. Jansen, J. Phys. 25 (1964) 582.
[2] M. Chevreton, B. Andron, C.R. Acad. Sci. Paris, B 264 (1967) 316.
[3] K. Adachi, K. Sato, K. Kojima, Research Reports, Faculty of Engineering, Nagoya University, 1970, p. 253.
[4] G.J. Snyder, T. Caillet, J.-P. Fleurial, Phys. Rev. B 62 (10) (2000) 185.
[5] G.F. Goya, V. Sagredo, Solid State Commun. 125 (2003) 247.
[6] V. Tsurkan, J. Hemberger, M. Klemm, S. Klimm, A. Loidl, S. Horn, R. Tidecks, J. Appl. Phys. 90 (2001) 4639.
[7] A. Junod, private communication.
[8] G. Lamarche, F. Lamarche, A.-M. Lamarche, Europhys. Lett. 53 (2001) 378.
[9] G. Lamarche, I. Bulyzhenkov, to be published.
[10] I. Bulyzhenkov, A.-M. Lamarche, G. Lamarche, Phys. Rev. B 72 (2005) 155203.
[11] G. Lamarche, Rev. Sci. Instrum. 60 (1989) 943.
[12] A. Larson, R. von Dreele, General Structure Analysis System, Los Alamos National Laboratory, Los Alamos, 1994.
[13] B.L. Morris, P. Russo, A. Wold, J. Phys. Chem. Solids 31 (1970) 635.
[14] J. Goodenough, Magnetism and the Chemical Bond, Wiley, New York, 1963 (Chapter I).
[15] J. Hubbard, W. Marshall, Proc. Phys. Soc. 86 (1965) 561.
[16] Yu. Izyumov, R. Oserov, Magnetic Neutron Diffraction, Plenum Press, New York, p. 76.
[17] D. Babot, M. Chevreton, J.L. Buevoz, R. Lagnier, B. Lambert-Andron, M. Wintenberger, Solid State Commun. 30 (1979) 253.

Chapter 8 Physical properties of icosahedral quasicrystal $Al_{60}Cr_{19.9}Fe_{0.1}Ge_{20}$

Z.M. Stadnik and P. Wang.

J. Phys.: Condens. Matter, **18**, 8363 (2006).

INSTITUTE OF PHYSICS PUBLISHING JOURNAL OF PHYSICS: CONDENSED MATTER

J. Phys.: Condens. Matter **18** (2006) 8383–8394 doi:10.1088/0953-8984/18/35/022

Physical properties of the icosahedral quasicrystal $Al_{60}Cr_{19.9}Fe_{0.1}Ge_{20}$

Zbigniew M Stadnik and Pu Wang

Department of Physics, University of Ottawa, Ottawa, ON, K1N 6N5, Canada

Received 20 June 2006, in final form 3 August 2006
Published 18 August 2006
Online at stacks.iop.org/JPhysCM/18/8383

Abstract

The results of x-ray diffraction, ^{57}Fe Mössbauer spectroscopy, magnetic susceptibility, and electrical conductivity studies of the metastable icosahedral alloy $Al_{60}Cr_{19.9}Fe_{0.1}Ge_{20}$ are reported. The observed broadening of the diffraction Bragg peaks reflects the presence of the topological/chemical disorder. The distribution of the electric quadrupole splitting derived from Mössbauer spectra indicates the existence of a multiplicity of Fe sites. The average quadrupole splitting decreases with temperature as $T^{3/2}$. The vibrations of the Fe atoms are well described by a Debye model, with the Debye temperature of 463(15) K. The temperature dependence of the magnetic susceptibility follows the Curie–Weiss law with the effective magnetic moment of 0.312(3) μ_B per Cr/Fe atom. The origin of the presence of the magnetic moment, and its absence in similar crystalline alloys, is discussed. The temperature dependence of the electrical conductivity can be successfully fitted with the use of theories of quantum interference effects, and values for spin–orbit and inelastic scattering times are extracted from the fits. The scattering process in the studied quasicrystal is dominated by inelastic electron–electron scattering.

(Some figures in this article are in colour only in the electronic version)

1. Introduction

Solids are traditionally divided into two categories: crystalline and amorphous. The dramatic discovery of an icosahedral (i) Al–Mn alloy by Shechtman *et al* [1] extended this dichotomous division by introducing the notion of quasicrystals (QCs). These are materials that possess a new type of long-range translational order, *quasiperiodicity*, and a noncrystallographic orientational order associated with the classically forbidden fivefold, eightfold, tenfold, and twelvefold symmetry axes [2].

Soon after the discovery of the first i QCs in the binary Al–TM (TM = transition metal) system, it was found that the addition of a metalloid (Me) improves their structural quality [3]. These ternary Al–TM–Me i alloys were mainly studied with respect to their formation and

0953-8984/06/358383+12$30.00

structural properties [4–6]. The only physical property investigated was the electrical resistivity, ρ. It was found that in the i alloys Al–Mn–Ge [4, 7], Al–Mn–Si [8, 9], and Al–Cr–Ge [4, 7], ρ exhibits a nonmetallic behaviour (i.e., $\partial\rho/\partial T$ is negative). For the Al–Cr–Si i alloys, contradictory findings were reported: Inoue *et al* [4] reported that ρ is of metallic type ($\partial\rho/\partial T$ is positive) whereas Kimura *et al* [7] found that ρ is of nonmetallic type. The unexpected increase of ρ with decreasing temperature was interpreted qualitatively in terms of the electron–electron interaction and weak localization effects [8, 9].

In this paper, we report on structural, Mössbauer spectroscopy (MS), magnetic, and transport studies of the i alloy $Al_{60}Cr_{19.9}Fe_{0.1}Ge_{20}$.

2. Experimental procedure

An ingot of composition $Al_{60}Cr_{19.9}Fe_{0.1}Ge_{20}$ was prepared by arc melting in an argon atmosphere a mixture of high-purity Al, Ge, Cr, and Fe enriched to 95% in an ^{57}Fe isotope. The ingot was melt spun in air by ejecting molten alloy at 1423(10) K through a 0.7 mm orifice in a quartz tube onto a surface of a copper wheel rotating with a tangential velocity of 71(1) m s^{-1}. The resulting ribbons were about 2 cm long and 2 mm wide.

X-ray diffraction (XRD) measurements were performed at 298 K in Bragg–Brentano geometry on the PANanalytical X'Pert scanning diffractometer using Cu Kα radiation. The Kβ line was eliminated by using a Kevex PSi2 Peltier-cooled solid-state Si detector. In order to avoid the deviation from intensity linearity of the solid-state Si detector, its parameters and the parameters of the diffractometer were chosen in such a way as to limit the count rate from the most intense Bragg peaks to less than 9000 counts s^{-1} [10]. To allow for the possible instrumental aberration and specimen displacement, corrections were made to the 2θ angles using a fourth-order polynomial calibration curve [11] obtained from the scan of the specimen mixed with 10 wt% of a Si standard [12].

The ^{57}Fe Mössbauer spectroscopy (MS) measurements in the temperature range 4.2–299.7 K were conducted using a standard Mössbauer spectrometer operating in a sine mode and a source of ^{57}Co(Rh) at room temperature. The spectrometer was calibrated with a 6.35 μm-thick α-Fe foil (with a surface density of 107 μg ^{57}Fe cm^{-2}) [13], and the spectra were folded. The full linewidth at half maximum of the inner pair of the α-Fe Zeeman pattern was 0.203(3) mm s^{-1} and this value can be regarded as the resolution of the Mössbauer spectrometer. The surface density of the Mössbauer absorber of the i $Al_{60}Cr_{19.9}Fe_{0.1}Ge_{20}$ alloy was 34 μg ^{57}Fe cm^{-2}. This absorber can therefore be regarded as being thin [14]. The electrical resistivity measurement was made with a standard dc four-probe method between 2.0 and 300 K. The magnetic susceptibility was measured with a Quantum Design superconducting quantum interference device magnetometer in a field of 1 kOe between 2.0 and 300 K.

3. Results and discussion

3.1. Structural characterization

The XRD pattern of the studied sample measured in the 2θ range 20°–100° (figure 1) shows the presence of 11 i Bragg peaks, the weaker of which were not observed earlier [4, 5] in the patterns obtained with a scintillation/proportional counter. This increased sensitivity for weak lines is due to the solid-state detector which has a higher counting efficiency (due to the elimination of a monochromator in the diffracted beam) and lower background count rate as compared to more conventional detectors used in combination with a diffracted-beam monochromator [10]. Two weak Bragg peaks due to an unidentified second phase are also

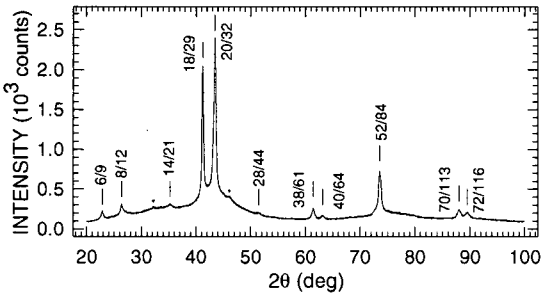

Figure 1. The XRD spectrum of an $Al_{60}Cr_{19.9}Fe_{0.1}Ge_{20}$ alloy at 298 K. The vertical lines labelled with indices N/M above all detected i Bragg peaks correspond to the positions calculated for the Cu Kα_1 radiation, as explained in the text. The position, full width at half maximum, and relative intensity of each detected i peak are given in table 1 together with the corresponding index. The symbol ▼ indicates the peak positions corresponding to an unidentified second phase.

Table 1. Positions in terms of $2\theta_1$ (in degrees) corresponding to Cu Kα_1 radiation and Q_{exp} (in $Å^{-1}$), full width at half maximum Γ_Q (in $Å^{-1}$), and relative intensity INT normalized to 100.0 of all detected icosahedral Bragg peaks. Q_{cal} (in $Å^{-1}$) is the calculated Q value by taking the position of the fourth line with the $I1$ index 18/29 as the reference line. $I1$ and $I2$ are the indices (N/M) and $(h/h', k/k', l/l')$ based on the indexing scheme of Cahn *et al* [17], whereas $I3$ and $I4$ are the indices corresponding, respectively, to the indexing schemes of Elser [18] and Bancel *et al* [19].

$2\theta_1$	Q_{exp}	Q_{cal}	Γ_Q	INT	$I1$	$I2$	$I3$	$I4$
22.813	1.613	1.615	0.032	5.7	6/9	011200	111000	110001
26.343	1.859	1.865	0.024	5.5	8/12	002200	111100	1110$\bar{1}$0
35.276	2.472	2.467	0.018	0.9	14/21	102300	211100	2100$\bar{1}$1
41.198	2.870	2.870	0.019	89.5	18/29	122300	211111	100000
43.415	3.017	3.018	0.028	100.0	20/32	002400	221001	110000
51.449	3.540	3.547	0.016	0.8	28/44	222400	311111	210001
61.389	4.164	4.164	0.039	6.7	38/61	233400	322101	111000
63.058	4.266	4.267	0.046	2.3	40/64	242400	322111	111100
73.529	4.882	4.882	0.024	24.9	52/84	004600	332002	101000
87.989	5.666	5.663	0.031	8.2	70/113	124700	432112	110010
89.411	5.738	5.740	0.044	3.7	72/116	244600	433101	200000

observed (figure 1). The positions of all the detected i Bragg peaks corresponding to Cu Kα_1 radiation (the value of its wavelength λ is 1.5405981 Å [15]) in terms of the angle $2\theta_1$ and the corresponding wavenumber $Q_{exp} = 4\pi \sin\theta_1/\lambda$, as well as their relative intensities and full widths at half maximum Γ_Q, were determined from the profile fitting using the procedure described by Schreiner and Jenkins [16]. These parameters corresponding to 11 detected i peaks, whose positions are indicated by vertical lines in figure 1, are presented in table 1. This table also contains the theoretical positions Q_{cal} which were calculated by taking the position of the second most intense i peak as the reference. Since there are several schemes employed to index the i peaks, we present in table 1 the indices that correspond to the most frequently used schemes [17–19].

There is a good agreement between the observed Q_{exp} and the theoretical Q_{cal} positions of the i Bragg peaks (figure 1 and table 1). The absence of Bragg peaks that correspond to half-integer indices confirm that the i $Al_{60}Cr_{19.9}Fe_{0.1}Ge_{20}$ QC has a simple icosahedral (SI) six-dimensional Bravais lattice characteristic for i alloys that cannot be produced as

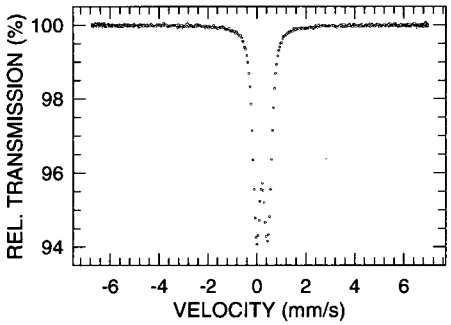

Figure 2. The ^{57}Fe Mössbauer spectrum of the icosahedral $Al_{60}Cr_{19.9}Fe_{0.1}Ge_{20}$ at 299.7 K. The zero-velocity scale is relative to α-Fe at room temperature.

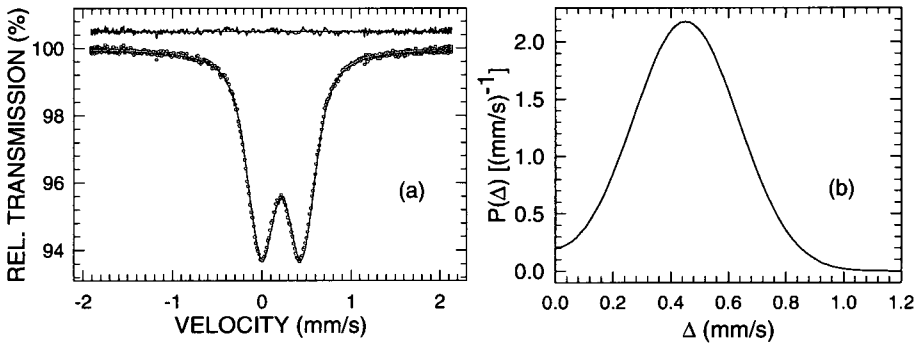

Figure 3. The ^{57}Fe Mössbauer spectrum (a) of the icosahedral $Al_{60}Cr_{19.9}Fe_{0.1}Ge_{20}$ at 297.4 K fitted (solid line) with the distribution $P(\Delta)$ shown in (b). The zero-velocity scale is relative to α-Fe at room temperature. The residuals are shown above the spectrum.

thermodynamically stable. The value of the six-dimensional hypercubic lattice constant calculated from the value Q_{exp} that corresponds to the (18, 29) i peak is 6.558(2) Å. The widths Γ_Q of the i peaks is significantly larger than the instrumental resolution (about 0.006 Å^{-1}) of the XRD spectrometer. This broadening, as well as the small shifts of Q_{exp} from their ideal positions Q_{cal}, indicates the presence of some structural disorder in the i $Al_{60}Cr_{19.9}Fe_{0.1}Ge_{20}$ QC.

A Mössbauer spectrum of the i $Al_{60}Cr_{19.9}Fe_{0.1}Ge_{20}$ QC (figure 2) measured in a wide velocity range shows a pattern due to the presence of only the electric quadrupole interaction; no patterns due to the presence of magnetically ordered Fe-containing second phases are detected.

3.2. Mössbauer spectroscopy

The Mössbauer spectrum of the i $Al_{60}Cr_{19.9}Fe_{0.1}Ge_{20}$ QC consists of a broadened doublet (figure 3(a)) which results from the distribution of the quadrupole splittings, $P(\Delta)$ [20]. A quadrupole splitting

$$\Delta = \tfrac{1}{2}eQ|V_{zz}|(1 + \tfrac{1}{3}\eta^2)^{1/2}, \tag{1}$$

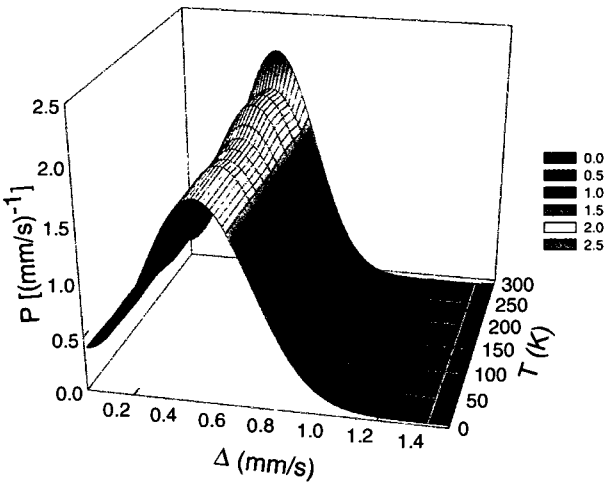

Figure 4. A 3D projection of the distributions $P(\Delta)$ for the icosahedral $Al_{60}Cr_{19.9}Fe_{0.1}Ge_{20}$.

where e is the proton charge and Q is the electric quadrupole moment of the ^{57}Fe nucleus. The asymmetry parameter $\eta = (V_{xx} - V_{yy})/V_{zz}$, $(0 \leqslant \eta \leqslant 1)$, where V_{yy}, V_{xx}, and V_{zz} are the eigenvalues of the electric field gradient (EFG) tensor in order of increasing magnitude [14]. The distribution $P(\Delta)$ is the consequence of the distributions of the EFG and of the asymmetry parameter. The Mössbauer spectrum in figure 3(a) was fitted with the constrained version [21] of the Hesse–Rübartsch method [22]. A slight asymmetry of the spectrum was accounted for by assuming a linear relation between the centre shift, δ, and the quadrupole splitting Δ of the elemental Lorentzian doublets of full width at half maximum Γ, $\delta = \delta_0 + a\Delta$, where δ_0 and a are fitted parameters [20]. The best fit of the Mössbauer spectrum of the i $Al_{60}Cr_{19.9}Fe_{0.1}Ge_{20}$ QC (figure 3(a)) could be obtained with the probability function $P(\Delta)$ shown in figure 3(b). The elemental doublet parameters obtained from the fit are $\Gamma = 0.216(7)$ mm s^{-1}, $\delta_0 = 0.212(2)$ mm s^{-1}, and $a = 8.66(1.22) \times 10^{-5}$. The average values of δ and Δ over the distribution $P(\Delta)$ are $\bar{\delta} = 0.212(2)$ mm s^{-1} and $\bar{\Delta} = 0.452(1)$ mm s^{-1}.

The presence of a wide distribution $P(\Delta)$ observed here (figure 3(b)) and in other i QCs [20] is direct evidence for the multiplicity of Fe sites. In other words, $P(\Delta)$ is a signature of an intrinsic topological disorder present in the i QC. The lack of *ab initio* calculations of the distribution of the EFG in i QCs inhibits a comparison of the experimentally determined $P(\Delta)$ with theory. Such calculations are very desirable since the experimentally determined shape of $P(\Delta)$ could be directly used to determine which of the proposed structural models of a given i QC is the most appropriate.

Distributions $P(\Delta)$ similar to that in figure 3(b) were determined from the fits of the Mössbauer spectra of the i $Al_{60}Cr_{19.9}Fe_{0.1}Ge_{20}$ QC measured at other temperatures (figure 4). One can note a small increase of $\bar{\Delta}$ with decreasing temperature. The temperature dependence of $\bar{\Delta}$ could be fitted (figure 5) to the empirical equation

$$\bar{\Delta}(T) = \bar{\Delta}(0)(1 - BT^{3/2}), \tag{2}$$

where $\bar{\Delta}(0)$ is the value of $\bar{\Delta}$ at 0 K and B is a constant. Such a $T^{3/2}$ temperature dependence has been observed in many metallic noncubic crystalline alloys [23], in some amorphous [24, 25] alloys, and recently in QCs [25, 26] over temperature ranges from a few

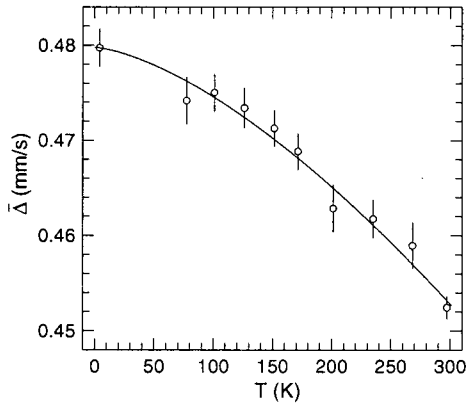

Figure 5. The temperature dependence of the average quadrupole splitting of the icosahedral $Al_{60}Cr_{19.9}Fe_{0.1}Ge_{20}$. The solid line is the fit to equation (2), as explained in the text.

K to the melting point. This seemingly universal $T^{3/2}$ dependence is not well understood. Its origin seems to be associated with a strong temperature dependence of mean-square lattice displacements and, to a lesser extent, with the temperature dependence of lattice expansion [27]. The values of $\bar{\Delta}(0)$, B determined from the fit for the i $Al_{60}Cr_{19.9}Fe_{0.1}Ge_{20}$ QC are 0.480(1) mm s^{-1}, 1.08(5) $\times$ 10^{-5} $K^{-3/2}$. The value of B is similar to that found for other metallic amorphous alloys and QCs [24–26].

The average centre shift at temperature T, $\bar{\delta}(T)$, determined from the fits of the spectra of the studied sample measured at different temperatures is given by

$$\bar{\delta}(T) = \delta_0 + \delta_{SOD}(T), \tag{3}$$

where δ_0 is the intrinsic isomer shift and $\delta_{SOD}(T)$ is the second-order Doppler (SOD) shift which depends on lattice vibrations of the Fe atoms [14]. In terms of the Debye approximation of the lattice vibrations, $\delta_{SOD}(T)$ is expressed [14] by the Debye temperature, Θ_D, as

$$\delta_{SOD}(T) = -\frac{9}{2}\frac{kT}{Mc}\left(\frac{T}{\Theta_D}\right)^3 \int_0^{\Theta_D/T} \frac{x^3\,dx}{e^x - 1}, \tag{4}$$

where M is the mass of the Mössbauer nucleus, k is the Boltzmann constant, and c is the speed of light. By fitting the experimental data $\bar{\delta}(T)$ (figure 6) to equation (3), the quantities δ_0 and Θ_D were found to be, respectively, 0.331(2) mm s^{-1} and 463(15) K. The value of Θ_D found here is comparable to the values of Θ_D found for other i QCs [25, 26].

3.3. Magnetic susceptibility

The magnetic susceptibility of the i $Al_{60}Cr_{19.9}Fe_{0.1}Ge_{20}$ QC measured in an applied magnetic field of 1 kOe between 2.0 and 300 K is shown in figure 7. Between 20 and 300 K, the $\chi(T)$ data can be well fitted to

$$\chi = \chi_0 + \frac{C}{T - \theta_p}, \tag{5}$$

where χ_0 is the temperature-independent magnetic susceptibility, C is the Curie constant, and θ_p is the paramagnetic Curie temperature. The Curie constant can be expressed as $C = \frac{N\mu_{eff}^2}{3k}$, where N is the concentration of magnetic atoms per unit mass and μ_{eff} is the

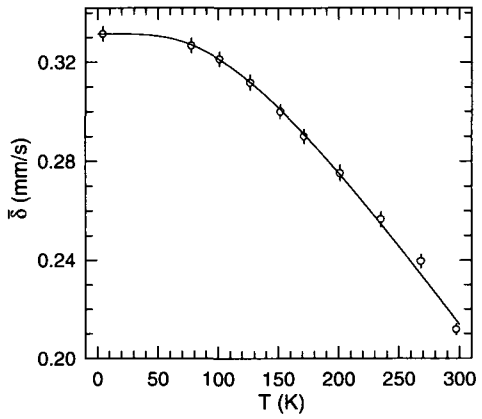

Figure 6. The temperature dependence of the average centre shift of the icosahedral $Al_{60}Cr_{19.9}Fe_{0.1}Ge_{20}$. The solid line is the fit to equation (3), as explained in the text.

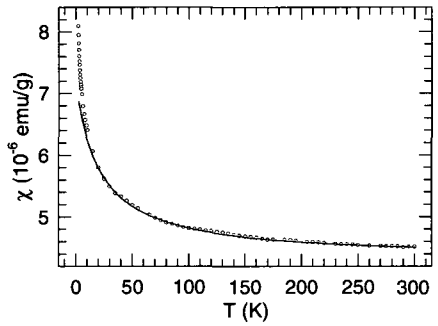

Figure 7. The temperature dependence of the magnetic susceptibility of the icosahedral $Al_{60}Cr_{19.9}Fe_{0.1}Ge_{20}$, measured in a field of kOe. The solid line is the fit to equation (5), as explained in the text.

effective magnetic moment. The values of χ_0, C, and θ_p obtained from the fit are, respectively, $4.33(1) \times 10^{-6}$ emu g^{-1}, $6.15(13) \times 10^{-5}$ emu K g^{-1}, and $-22.1(9)$ K. This value of C corresponds to μ_{eff} of 0.312(3) μ_B per TM atom. Magnetic susceptibility measurements on an i QC of a similar composition $Al_{65}Cr_{20}Ge_{15}$ [28] found $\theta_p = -10.9$ K and $\mu_{eff} = 0.45$ μ_B per Cr atom.

A deviation from the Curie–Weiss law below 20 K (figure 7) may be due to the presence of some magnetic impurity in the sample. The negative values of θ_p indicates the predominantly antiferromagnetic interaction between the TM atoms, which was also observed in other i Al–TM QCs [28, 29]. Magnetic susceptibility measurements in Al–Cr crystalline alloys showed that Cr atoms do not carry a magnetic moment [30]. No measurable magnetic moment on Cr atoms was found in the i $Al_{74}Cr_{20}Si_6$ QC [31]. A sizeable magnetic moment of 0.312(3) μ_B observed here confirms an earlier observation [28] that there is a local magnetic moment on Cr in the i Al–Cr–Ge QC.

The non-zero value of μ_{eff} on the Cr atoms in the i Al–Cr–Ge QCs, and its absence in Al–Cr crystalline alloys, raises the question of its origin. It is conceivable that the i symmetry induces

a large density of states at the Fermi level, $N(E_F)$, and hence leads via the Stoner criterion to the formation of the magnetic moment on the Cr atoms [32]. There are neither electronic structure calculations nor the experimental electronic structure studies for the i Al–Cr–Ge QC available to ascertain the possibility of the high $N(E_F)$. However, one can use the following qualitative argument to show that this value must be small. The formation and stability of the i QCs appears to be qualitatively explained in terms of the Hume-Rothery rules [3]. The i QCs seem to form for certain well defined values of the electron-per-atom ratio e/a [3]. At these critical ratios the Fermi sphere of radius k_F just touches a Brillouin zone plate, i.e., $2k_F = Q$. This corresponds to the opening of an energy gap at the Fermi surface, giving rise to a minimum of $N(E_F)$. Assuming the valence electron numbers of +3 for Al, +4 for Ge, −4.66 for Cr, and −2.66 for Fe [3], one can find that the value of e/a for the i $Al_{60}Cr_{19.9}Fe_{0.1}Ge_{20}$ QC is 1.670. The radius of the Fermi sphere is calculated from the equation $k_F = (3\pi^2 n_e)^{1/3}$, where n_e is the electron concentration. The electron concentration can be derived from the relation $n_e = \frac{(e/a)dN_A}{M}$, where d is the mass density of the alloy, M is its atomic weight, and N_A is the Avogadro number. With the value $e/a = 1.67$, one gets $2k_F = 2.880$ Å^{-1}. The latter compares well with the Q value of 2.870 Å^{-1} corresponding to the 18/29 i peak (table 1). It thus appears that i symmetry, similarly as is the case for the i Al–Mn QCs [33], is not responsible for the formation of a magnetic moment on the Cr atoms.

The most probable origin of the non-zero magnetic moment on the Cr atoms in the i $Al_{60}Cr_{19.9}Fe_{0.1}Ge_{20}$ QC is the presence of the topological disorder inherent to the i structure. This interpretation was first suggested in [34] in relation to the i Al–Mn QCs. It was later justified theoretically [35]. It is well known that magnetic interactions depend crucially upon interatomic distances. In alloys containing TM atoms it was shown using total-energy band calculations [36] that there is a system-dependent critical separation between the TM atoms below which they do not carry a magnetic moment; this moment appears for separations larger than the critical one. This general result then implies that the presence of topological disorder, which involves different TM–TM separations, in an alloy may be crucial for the formation of a magnetic moment. The presence of this disorder in the studied i $Al_{60}Cr_{19.9}Fe_{0.1}Ge_{20}$ QC is clearly manifested in the broadening of the i Bragg peaks and the appearance of the distribution $P(\Delta)$.

3.4. Electrical conductivity

The temperature dependence of ρ and of the electrical conductivity σ ($\sigma = 1/\rho$) for the i $Al_{60}Cr_{19.9}Fe_{0.1}Ge_{20}$ QC is shown in figure 8. The most salient feature of this dependence is a remarkably large value of ρ, as compared to that of amorphous and crystalline alloys of similar composition, and the negative $\partial\rho/\partial T$ over a large temperature range. At low temperatures, ρ increases with temperature from $\rho_{2\,K} = 1398.2$ $\mu\Omega$ cm and passes through a shallow maximum at 37.2 K where $\rho_{37.2\,K} = 1407.6$ $\mu\Omega$ cm; the total increase from 2 to 37.2 K, $(\rho_{37.2\,K} - \rho_{2\,K})/\rho_{37.2\,K} = 0.7\%$, is very small. Above this temperature, ρ decreases almost linearly with increasing temperature to $\rho_{300\,K} = 1345.5$ $\mu\Omega$ cm, thus by 4.4% of its maximum value.

The temperature dependence of σ in QCs was shown to be well described by the quantum interference effects (QIEs), i.e., the electron–electron interaction (EEI) and the weak localization (WL) effects [37]. The form of the temperature dependence of σ due to QIEs is

$$\sigma(T) = \sigma(0) + \Delta\sigma_{EEI}(T) + \Delta\sigma_{WL}(T), \tag{6}$$

where $\sigma(0)$ is the temperature-independent background conductivity, $\Delta\sigma_{EEI}$ is the EEI

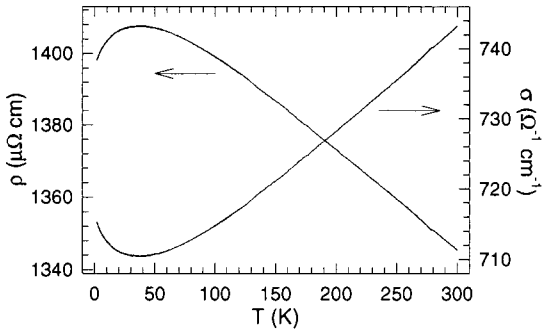

Figure 8. The temperature dependence of the electrical resistivity and conductivity of the icosahedral $Al_{60}Cr_{19.9}Fe_{0.1}Ge_{20}$.

contribution, and $\Delta\sigma_{WL}$ is the WL contribution. The EEI contribution [38] is written as

$$\Delta\sigma_{EEI}(T) = \frac{1.3}{\sqrt{2}}\frac{e^2}{4\pi^2\hbar}\left(\frac{4}{3} - \frac{3}{2}F_\sigma\right)\sqrt{\frac{kT}{\hbar D}}, \tag{7}$$

where F_σ is the Coulomb interaction parameter and D is the diffusion constant. The WL contribution [38] is in the form

$$\Delta\sigma_{WL}(T) = \frac{e^2}{2\pi^2\hbar\sqrt{D}}\left(3\sqrt{\frac{1}{\tau_{so}} + \frac{1}{4\tau_i}} - \sqrt{\frac{1}{4\tau_i}} - 3\sqrt{\frac{1}{\tau_{so}}}\right), \tag{8}$$

where τ_{so} is the spin–orbit scattering time and τ_i is the inelastic scattering time. The last term in equation (8) is added in order to get $\Delta\sigma_{WL} = 0$ at $T = 0$. Only τ_i in equation (8) is temperature dependent and is usually expressed by a simple power law $\tau_i = \tau_{i0}T^{-p}$, where τ_{i0} is a constant and the exponent p depends on the type of inelastic scattering mechanism. Combining equations (7) and (8), the final form of the expression for the conductivity due to QIE corrections is

$$\sigma(T) = \sigma(0) + a\sqrt{T} + b\left(3\sqrt{1 + cT^d} - \sqrt{cT^d} - 3\right), \tag{9}$$

where the fitted parameters $a = \frac{1.3}{\sqrt{2}}\frac{e^2}{4\pi^2\hbar}\left(\frac{4}{3} - \frac{3}{2}F_\sigma\right)\sqrt{\frac{k}{\hbar D}}$, $b = \frac{e^2}{2\pi^2\hbar\sqrt{D\tau_{so}}}$, $c = \frac{\tau_{so}}{4\tau_{i0}}$, and $d = p$.

The value of the diffusivity can be estimated using the Einstein equation for the Boltzmann conductivity $\sigma(0) = e^2N(E_F)D$. The value of $\sigma(0) = 717.3(1)\ \Omega^{-1}\ cm^{-1}$ was obtained from the extrapolation of the experimental $\sigma(T)$ data (figure 8) to 0 K. $N(E_F)$ was estimated from the electronic specific heat coefficient γ of 1.0 mJ ($mol^{-1}\ K^{-2}$) [39] via the relation $\gamma = \pi^2kN(E_F)/3$. This gave $D = 0.175\ cm^2\ s^{-1}$. The electrical conductivity of the i $Al_{60}Cr_{19.9}Fe_{0.1}Ge_{20}$ QC was fitted to equation (9) (figure 9), and from the values of a, b, c, and d one can extract values of F_σ, τ_{so}, τ_{i0}, and p (table 2). It is not obvious up to what maximum temperature, T_{max}, do QIEs contribute to $\sigma(T)$ [37]. It was demonstrated [40] that QIE corrections to $\sigma(T)$ in the i Al–Cu–Fe QCs extend up to $T_{max} = 300$ K. We first fitted the subsection of the $\sigma(T)$ data between 2 K and $T_{max} = 100$ K (figure 9(a)). A good fit was obtained with sensible values [37, 40, 41] for the F_σ, τ_{so}, τ_{i0}, and p parameters (table 2). It can be seen that the fitted curve continues to describe $\sigma(T)$ data well above 100 K up to about 200 K. Next we fitted the subsection of the $\sigma(T)$ data between 2 K and $T_{max} = 200$ K (figure 9(b)). A good fit for slightly different values of F_σ, τ_{so}, τ_{i0}, and p (table 2) is evident.

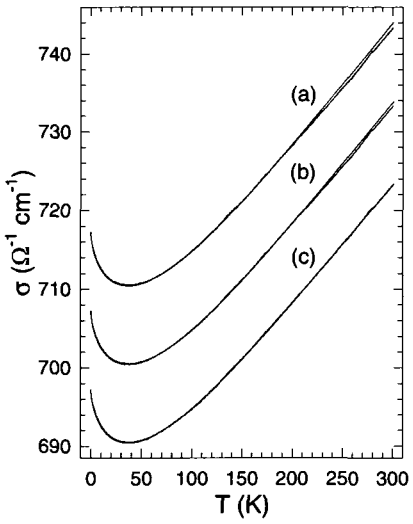

Figure 9. The electrical conductivity (red curve) fitted (solid line) to equation (9) between 2.0 K and (a) T_{max} = 100 K, (b) T_{max} = 200 K, and (c) T_{max} = 300 K, as explained in the text. The experimental and fitted curves in (b) and (c) are shifted by 10 and 20 Ω^{-1} cm^{-1}, respectively.

Table 2. EEI and WL parameters obtained from the fits of $\sigma(T)$ to equation (9) between 2.0 K and T_{max}.

T_{max} (K)	F_σ	τ_{so} (ps)	τ_{i0} (ps)	p
100	0.885(13)	0.521(86)	104(21)	1.27(1)
200	0.902(2)	0.659(23)	128(5)	1.29(4)
300	0.923(2)	0.895(25)	166(5)	1.31(4)

The fitted curve describes $\sigma(T)$ data well above 200 K up to about 220 K. Figure 9(c) shows the fit in the entire temperature range 2–300 K for the F_σ, τ_{so}, τ_{i0}, and p parameters given in table 2.

The Coulomb interaction parameter F_σ found here (table 2) is within the range 0.6–1.5 found for other i QCs [40, 41]. The value of τ_{so} of $\sim$1 ps is of the same order of magnitude as that found in other i QCs [40, 41]. At 300 K, τ_i is of the order 0.1 ps, which is consistent with the corresponding values found in i Al–Cu–Fe QCs [40, 41]. The p value of about 1.3 indicates that the scattering mechanism in the studied QC is dominated by inelastic electron–electron scattering [40]. It is concluded that QIE corrections to σ account well for the temperature dependence of $\sigma(T)$ up to room temperature.

4. Conclusions

A distribution of the electric quadrupole splitting in the studied quasicrystal reflects the presence of a structural disorder. The temperature dependence of the average quadrupole splitting follows the $T^{3/2}$ dependence. The vibrations of the Fe atoms are well described by a Debye model, with the Debye temperature of 463(15) K. The formation of the magnetic moment of 0.312(3) μ_B per Cr/Fe atom results from the topological disorder inherent to the

icosahedral structure. The temperature dependence of the electrical conductivity up to room temperature is well accounted for quantitatively by theories of quantum interference effects. The scattering process in the studied quasicrystal is dominated by inelastic electron–electron scattering.

Acknowledgment

This work was supported by the Natural Sciences and Engineering Research Council of Canada.

References

[1] Shechtman D, Blech I, Gratis D and Cahn J W 1984 *Phys. Rev. Lett.* **53** 1951
[2] Suck J-B, Schreiber M and Häussler P (ed) 2002 *Quasicrystals, An Introduction to Structure, Physical Properties, and Applications* (Berlin: Springer)
[3] Tsai A P 1999 *Physical Properties of Quasicrystals* ed Z M Stadnik (Berlin: Springer) p 5
[4] Inoue A, Kimura H M, Masumoto T, Tsai A P and Bizen Y 1987 *J. Mater. Sci. Lett.* **6** 771
[5] Inoue A, Kimura H M and Masumoto T 1987 *J. Mater. Sci.* **22** 1864
[6] Inoue A, Bizen Y and Masumoto T 1988 *Met. Trans.* A **19** 383
[7] Kimura H M, Inoue A, Bizen Y, Masumoto T and Chen H S 1988 *Mater. Sci. Eng.* **99** 449
[8] Kimura K, Yamane H, Hashimoto T and Takeuchi S 1987 *Mater. Sci. Forum* **22–24** 471
[9] Kimura K, Yamane H, Hashimoto T and Takeuchi S 1988 *Mater. Sci. Eng.* **99** 435
[10] Bish D L and Chipera S J 1989 *Powder Diffr.* **4** 137
[11] Wong-Ng W and Hubbard C R 1987 *Powder Diffr.* **2** 242
[12] 2000 *Standard Reference Material 640c, Silicon Powder Line Position and Line Shape Standard for X-ray Diffraction* Natl. Inst. Stand. Techn. (US)
[13] Cali J P (ed) 1971 *Certificate of Calibration, Iron Foil Mössbauer Standard,* NBS (US) Circular No. 1541 (Washington, DC: US Government Printing Office)
[14] Greenwood N N and Gibb T C 1971 *Mössbauer Spectroscopy* (London: Chapman and Hall)
Gütlich P, Link R and Trautwein A 1978 *Mössbauer Spectroscopy and Transition Metal Chemistry* (Berlin: Springer)
[15] Jenkins R and Schreiner W N 1989 *Powder Diffr.* **4** 74
[16] Schreiner W N and Jenkins R 1983 *Adv. X-ray Anal.* **26** 141
[17] Cahn J W, Shechtman D and Gratias D 1986 *J. Mater. Res.* **1** 13
[18] Elser V 1986 *Acta Crystallogr.* A **42** 36
[19] Bancel P A, Heiney P A, Stephens P W, Goldman A I and Horn P M 1985 *Phys. Rev. Lett.* **54** 2422
[20] Stadnik Z M 1996 *Mössbauer Spectroscopy Applied to Magnetism and Materials Science* vol 2, ed G J Long and F Grandjean (New York: Plenum) p 125
[21] Le Caër G and Dubois J M 1979 *J. Phys. E: Sci. Instrum.* **12** 1083
[22] Hesse J and Rübartsch A 1974 *J. Phys. E: Sci. Instrum.* **7** 526
[23] Kaufmann E N and Vianden R J 1979 *Rev. Mod. Phys.* **51** 161 and references therein
[24] Deppe P and Rosenberg M 1983 *Hyperfine Interact.* **15/16** 735
Kopcewicz M, Kopcewicz B and Gonser U 1987 *J. Magn. Magn. Mater.* **66** 79
Mao M, Ryan D H and Altounian Z 1994 *Hyperfine Interact.* **92** 2163
[25] Stadnik Z M, Saida J and Inoue A 2001 *Ferroelectrics* **250** 297
Stadnik Z M, Rapp Ö, Srinivas V, Saida J and Inoue A 2002 *J. Phys.: Condens. Matter* **14** 6883
[26] Stadnik Z M, Takeuchi T and Mizutani U 2000 *Mater. Sci. Eng.* A **294–296** 331
Brand R A, Voss J and Calvayrac Y 2000 *Mater. Sci. Eng.* A **294–296** 666
Stadnik Z M, Takeuchi T, Tanaka N and Mizutani U 2003 *J. Phys.: Condens. Matter* **15** 6365
Stadnik Z M and Zhang G 2006 *J. Phys.: Condens. Matter* **17** 6599
[27] Jena P 1976 *Phys. Rev. Lett.* **36** 418
Nishiyama K, Dimmling F, Kornrumph Th and Riegel D 1976 *Phys. Rev. Lett.* **37** 357
Christiansen J, Heubes P, Keitel R, Klinger W, Loeffler W, Sandner W and Witthuhn W 1976 *Z. Phys.* B **24** 177
[28] McHenry M E, Dunlap R A, Srinivas V, Bahadur D and O'Handley R C 1990 *Phys. Rev.* B **41** 6933
[29] Stadnik Z M, Stroink G, Ma H and Williams G 1989 *Phys. Rev.* B **39** 9797
[30] Taylor M A 1961 *Proc. Phys. Soc. London* **78** 1244
[31] McHenry M E, Srinivas V, Bahadur D, O'Handley R C, Lloyd D J and Dunlap R A 1989 *Phys. Rev.* B **39** 3611

[32] Stadnik Z M and Müller F 1995 *Phil. Mag.* B **71** 221 and references therein
[33] de Coulon V, Reuse F A and Khanna S N 1993 *Phys. Rev.* B **48** 814
Liu F, Khanna S N, Magaud L, Jena P, de Coulon V, Reuse F, Jaswal S S, He X-G and Cyrot-Lackmann F 1993 *Phys. Rev.* B **48** 1295
[34] Hauser J J, Chen H S, Espinosa G P and Waszczak J V 1986 *Phys. Rev.* B **34** 4674
Warren W W, Chen H-S and Espinosa G P 1986 *Phys. Rev.* B **34** 4902
[35] Bratkovsky A M, Smirnov A V, Nguyen Manh D and Pasturel A 1995 *Phys. Rev.* B **52** 3056
Smirnov A V and Bratkovsky A M 1996 *Phys. Rev.* B **53** 8515
[36] Moruzzi V L and Marcus P M 1992 *Phys. Rev.* B **45** 2934
Moruzzi V L and Marcus P M 1993 *Phys. Rev.* B **47** 7878
[37] Rapp Ö 1999 *Physical Properties of Quasicrystals* ed Z M Stadnik (Berlin: Springer) p 127
[38] Lee P A and Ramakrishnan T V 1985 *Rev. Mod. Phys.* **57** 287
Altshuler B L and Aronov A G 1985 *Electron–Electron Interaction in Disordered Conductors* ed A L Efros and M Pollak (New York: Elsevier) p 1
Dugdale J S 1995 *The Electrical Properties of Disordered Metals* (Cambridge: Cambridge University Press)
[39] Mizutani U 1993 *Mater. Sci. Eng.* B **19** 82
[40] Ahlgren M, Lindqvist P, Rodmar M and Rapp Ö 1997 *Phys. Rev.* B **55** 14847
Rodmar M, Ahlgren M and Rapp Ö 1995 *Proc. 5th Int. Conf. Quasicrystals* ed C Janot and R Mosseri (Singapore: World Scientific) p 518
[41] Chernikov M A, Bernasconi A, Belli C and Ott H R 1993 *Europhys. Lett.* **21** 767
Ahlgren M, Rodmar M, Klein Th and Rapp Ö 1995 *Phys. Rev.* B **51** 7287
Lindqvist P, Lanco P, Berger C, Jansen A G M and Cyrot-Lackmann F 1995 *Phys. Rev.* B **51** 4796

Chapter 9 Magnetic properties and ^{155}Gd Mössbauer spectroscopy of the icosahedral quasicrystal $Ag_{50}In_{36}Gd_{14}$

Z.M. Stadnik, K. Al-Qadi, and P. Wang.

J. Phys.: Condens. Matter, **18**, 8363 (2006).

IOP PUBLISHING JOURNAL OF PHYSICS: CONDENSED MATTER

J. Phys.: Condens. Matter **19** (2007) 326208 (11pp) doi:10.1088/0953-8984/19/32/326208

Magnetic properties and ^{155}Gd Mössbauer spectroscopy of the icosahedral quasicrystal $Ag_{50}In_{36}Gd_{14}$

Zbigniew M Stadnik[1], Khalid Al-Qadi and Pu Wang

Department of Physics, University of Ottawa, Ottawa, ON, K1N 6N5, Canada

E-mail: stadnik@uottawa.ca

Received 17 April 2007, in final form 8 June 2007
Published 16 July 2007
Online at stacks.iop.org/JPhysCM/19/326208

Abstract

The results of x-ray diffraction, magnetic susceptibility, and ^{155}Gd Mössbauer spectroscopy studies of the recently discovered icosahedral quasicrystal $Ag_{50}In_{36}Gd_{14}$ are reported. The studied quasicrystal has a simple six-dimensional Bravais lattice with the six-dimensional hypercubic lattice constant of 7.805(2) Å. The observed broadening of the diffraction Bragg peaks reflects the presence of the topological/chemical disorder. The temperature dependence of the magnetic susceptibility follows the Curie–Weiss law with an effective magnetic moment of 8.15(1) μ_B per Gd atom and the paramagnetic Curie temperature of −37.1(2) K. The studied quasicrystal is a spin glass with a freezing temperature of 4.25(5) K. The presence of a distribution of the electric quadrupole splitting in the Mössbauer spectra indicates the existence of a multiplicity of Gd sites. The values of the principal component of the electric field gradient tensor and the asymmetry parameter at these sites are, respectively, $-4.91(10) \times 10^{21}$ V cm^{-2} and $\eta = 1.00(20)$. The Debye temperature of $Ag_{50}In_{36}Gd_{14}$ is 199(2) K. The hyperfine magnetic field sets in at a temperature higher than the freezing temperature.

(Some figures in this article are in colour only in the electronic version)

1. Introduction

Solids are traditionally divided into two groups: crystalline and amorphous. The dramatic discovery of an icosahedral (i) Al–Mn alloy by Shechtman *et al* [1] extended this dichotomous division by introducing the notion of quasicrystals (QCs). These are materials that possess a new type of long-range translational order, *quasiperiodicity*, and a noncrystallographic orientational order associated with the classically forbidden fivefold, eightfold, tenfold, and

[1] Author to whom any correspondence should be addressed.

0953-8984/07/326208+11$30.00

twelvefold symmetry axes [2]. A main problem in condensed matter physics is determining whether quasiperiodicity leads to physical properties which are significantly different from those of crystalline and amorphous materials of the same/similar compositions.

One of the central questions in the physics of QCs is that of the possibility of the existence of long-range magnetic order in these alloys. Initial intuition suggests that quasiperiodicity necessarily leads to geometrical frustration and is therefore incompatible with long-range magnetic order. However, various theoretical models dealing with magnetism in QCs indicate the possibility of existence of long-range magnetic order in QCs. There are geometrical models [3] and physical models, such as the Ising model [4], the XY model [5], the Heisenberg model [6], and the Hubbard model [7].

On the experimental side, all known QCs are either diamagnets, paramagnets or spin glasses [8]. The recent claim [9] of the existence of long-range magnetic order in i R–Mg–Zn (R = rare earth) QCs was shown [10] to result from the presence of magnetic impurities in the studied samples. Recent extensive neutron diffraction studies [11] of i R–Mg–Zn and i R–Mg–Cd QCs, which are of very high structural quality and which can be produced in a single-grain form, revealed the presence of short-range spin correlations at low temperatures and the absence of long-range magnetic order; these QCs are spin glasses.

Recently, new metastable i QCs were discovered in the $Ag_{50}In_{36}R_{14}$ system [12]. These QCs are formed by replacing all of Cd in the binary i $YbCd_{5.7}$ QC [13] with Ag and In, and Yb with other R elements. It is thus expected that the crystal structure of the i $Ag_{50}In_{36}R_{14}$ QCs must be similar to that of the i $YbCd_{5.7}$ QC. Very recently, the crystal structure of the i $YbCd_{5.7}$ QC has been solved [14]. It is based on three building units (rhombic triacontahedra linked with acute and obtuse rhombohedra) arranged quasiperiodically with unique atomic decorations. One would expect that R atoms are located at the Yb sites (on the vertices of the icosahedron and inside the acute rhombohedron) and the Ag and In atoms are distributed among the Cd sites. The new i $Ag_{50}In_{36}R_{14}$ QCs are expected to posses well localized and sizeable 4f magnetic moments on the R elements and perhaps exhibit long-range magnetic order. In this paper, we report on structural, magnetic, and ^{155}Gd Mössbauer spectroscopy studies of the i alloy $Ag_{50}In_{36}Gd_{14}$.

2. Experimental procedure

An ingot of nominal composition $Ag_{50}In_{36}Gd_{14}$ was prepared by melting constituent elements in an induction furnace on water-cooled Cu boat under an Ar atmosphere. Purities of the starting elements were 99.999%, 99.999%, and 99.998% for Ag, In, and Gd, respectively. The melting was repeated four times, in each case after turning the ingot. The total weight loss after the melting was 1.5%. The ingot was then melt spun in an Ar atmosphere by ejecting molten alloy through a 0.7 mm orifice in a quartz tube onto a surface of a copper wheel rotating with a tangential velocity of 47 m s^{-1}. The resulting ribbons were about 1.0 cm long and 20 μm thick.

X-ray diffraction (XRD) measurements were performed at 298 K in Bragg–Brentano geometry on a PANanalytical X'Pert scanning diffractometer using Cu Kα radiation. The Kβ line was eliminated by using a Kevex PSi2 Peltier-cooled solid-state Si detector. To allow for the possible instrumental aberration and specimen displacement, corrections were made to the 2θ angles using a fourth-order polynomial calibration curve [15] obtained from the scan of the specimen mixed with 10 wt% of a Si standard [16].

The magnetic susceptibility was measured with a Quantum Design superconducting quantum interference device magnetometer at various fields in the temperature range 2.0–300 K.

The ^{155}Gd Mössbauer spectroscopy measurements in the temperature range 1.5–10.4 K were conducted using a standard Mössbauer spectrometer operating in a sine mode and a source of ^{155}Eu($SmPd_3$). The source was kept at the same temperature as that of the absorber. The spectrometer was calibrated with a Michelson interferometer [17], and the spectra were folded. The Mössbauer absorber was made of pulverized material pressed into a pellet which was then put into an Al disc container of thickness of 0.008 mm to ensure a uniform temperature over the whole sample. The surface density of the Mössbauer absorber of the i $Ag_{50}In_{36}Gd_{14}$ alloy was 304 mg cm^{-2}. The 86.5 keV γ-rays were detected with a 2.5 cm NaI(Tl) scintillation detector covered with a 0.6 mm Pb plate to cut off the 105.3 keV γ-rays emitted from the source.

The Mössbauer spectra were analysed by means of a least-squares fitting procedure which entailed calculations of the positions and relative intensities of the absorption lines by numerical diagonalization of the full hyperfine interaction Hamiltonian [18]. The following hyperfine parameters are obtained from the fits: the hyperfine magnetic field at a nuclear site, H_{hf}, the z-component of the electric field gradient (EFG) tensor, V_{zz}, the asymmetry parameter, η, defined as $\eta = |(V_{xx} - V_{yy})/V_{zz}|$ (if the principal axes are chosen such that $|V_{xx}| < |V_{yy}| < |V_{zz}|$, then $0 \leqslant \eta \leqslant 1$), the angle between the direction of H_{hf} and the V_{zz}-axis, θ, and the angle between the V_{xx}-axis and the projection of H_{hf} onto the xy-plane, ϕ. During the fitting procedure, the g-factor and the quadrupole moment ratios for ^{155}Gd ($I_g = 3/2$, $I_{ex} = 5/2$) were constrained to, respectively, $g_{ex}/g_g = 1.235$ and $Q_{ex}/Q_g = 0.087$ [19]. The interference ξ-factor for the E1 transition of 86.5 keV in ^{155}Gd was fixed to the value of 0.0520, which was derived from the fit of the ^{155}Gd Mössbauer spectrum of $GdFe_2$ at 4.2 K [20].

The resonance line shape of the Mössbauer spectra was described by a transmission integral formula [21]. In addition to the hyperfine parameters, only the absorber Debye–Waller factor f_a and the absorber linewidth Γ_a were fitted as independent parameters. The source linewidth $\Gamma_s = 0.334$ mm s^{-1} and the background-corrected Debye–Waller factor of the source f_s^* [22], which were derived from the fit of the ^{151}Gd Mössbauer spectrum of $GdFe_2$ at 4.2 K [20], were used. The ^{155}Eu($SmPd_3$) source at 1.5 K emits a broadened emission line; from the fit of the ^{151}Gd Mössbauer spectrum of $GdFe_2$ at 1.5 K we found that $\Gamma_s = 0.708$ mm s^{-1} [20].

3. Results and discussion

3.1. Structural characterization

The XRD pattern of the studied sample measured in the 2θ range 5°–100° (figure 1) shows the presence of 19 i Bragg peaks, the weaker of which were not observed earlier [12] in the patterns obtained with a scintillation/proportional counter. Four weak Bragg peaks due to an unidentified second phase are also observed (figure 1). The positions of all the detected i Bragg peaks corresponding to Cu Kα_1 radiation (the value of its wavelength λ is 1.540 5981 Å [22]) in terms of the angle $2\theta_i$ and the corresponding wavenumber $Q_{exp} = 4\pi \sin\theta_i/\lambda$, as well as their relative intensities and full widths at half maximum Γ_Q, were determined from the profile fitting using the procedure described by Schreiner and Jenkins [23]. These parameters corresponding to 19 detected i peaks, whose positions are indicated by vertical lines in figure 1, are presented in table 1. This table also contains the theoretical positions Q_{cal} which were calculated by taking the position of the second most intense i peak as the reference. Since there are several schemes employed to index the i peaks, we present in table 1 the indices that correspond to the most frequently used schemes [24–26].

There is a good agreement between the observed Q_{exp} and the theoretical Q_{cal} positions of the i Bragg peaks (figure 1 and table 1). The absence of Bragg peaks that correspond

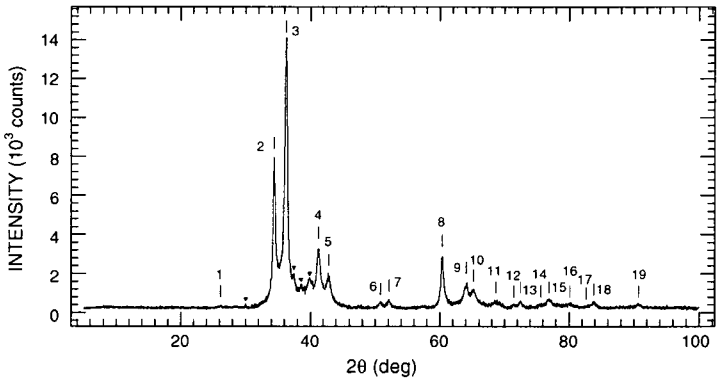

Figure 1. The XRD spectrum of an $Ag_{50}In_{36}Gd_{14}$ alloy at 298 K. The vertical lines labelled with integers above all detected i Bragg peaks correspond to the positions calculated for the Cu $K\alpha_1$ radiation, as explained in the text. The position, full width at half maximum, and relative intensity of each detected i peak are given in table 1 together with the corresponding index. The symbol ▼ indicates the peak positions corresponding to an unidentified second phase.

Table 1. Positions in terms of $2\theta_l$ (in deg) corresponding to Cu $K\alpha_1$ radiation and Q_{exp} (in $Å^{-1}$), full width at half maximum Γ_Q (in $Å^{-1}$), and relative intensity INT normalized to 100.0 of all detected icosahedral Bragg peaks, which are labelled with consecutive integers in column 1, as obtained from the fit [23]. The integers correspond to the vertical lines in figure 1. Q_{cal} (in $Å^{-1}$) is the calculated Q-value by taking the position of the second line with the $I1$ index 18/29 as the reference line. $I1$ and $I2$ are the indices (N/M) and $(h/h', k/k', l/l')$ based on the indexing scheme of Cahn *et al* [24], whereas $I3$ and $I4$ are the indices corresponding, respectively, to the indexing schemes of Elser [25] and Bancel *et al* [26].

Label	$2\theta_l$	Q_{exp}	Q_{cal}	Γ_Q	INT	$I1$	$I2$	$I3$	$I4$
1	26.146	1.845	1.842	0.025	0.5	12/16	022200	211000	$31\bar{1}\bar{1}1$
2	34.388	2.411	2.411	0.024	44.0	18/29	122300	211111	100000
3	36.229	2.536	2.535	0.027	100.0	20/32	002400	221001	110000
4	41.230	2.872	2.876	0.034	22.4	26/41	013400	222100	111101
5	42.832	2.978	2.980	0.037	11.3	28/44	222400	311111	210001
6	50.831	3.501	3.499	0.036	3.5	38/61	233400	322101	111000
7	52.104	3.582	3.585	0.039	4.4	40/64	242400	322111	111100
8	60.376	4.102	4.102	0.031	23.9	52/84	004600	332002	101000
9	64.008	4.323	4.321	0.040	13.3	58/93	233600	333101	210000
10	65.169	4.393	4.391	0.043	10.1	60/96	224600	422211	$210\bar{1}00$
11	68.637	4.599	4.596	0.069	6.9	66/105	104700	432002	$2111\bar{1}1$
12	71.426	4.761	4.758	0.034	1.7	70/113	124700	432112	110010
13	72.485	4.822	4.822	0.034	3.9	72/116	244600	433101	200000
14	75.698	5.005	5.009	0.052	2.7	78/125	344601	433201	211001
15	76.916	5.073	5.071	0.037	3.8	80/128	004800	442002	220000
16	80.149	5.251	5.249	0.085	3.5	86/137	364500	443101	310001
17	82.674	5.388	5.392	0.016	0.4	90/145	015800	522222	111110
18	83.815	5.448	5.448	0.041	4.1	92/148	115801	443102	211000
19	90.709	5.803	5.801	0.028	1.8	104/168	464600	533212	111010

to half-integer indices confirm that the i $Ag_{50}In_{36}Gd_{14}$ QC has a simple icosahedral (SI) six-dimensional Bravais lattice characteristic for i alloys that cannot be produced as

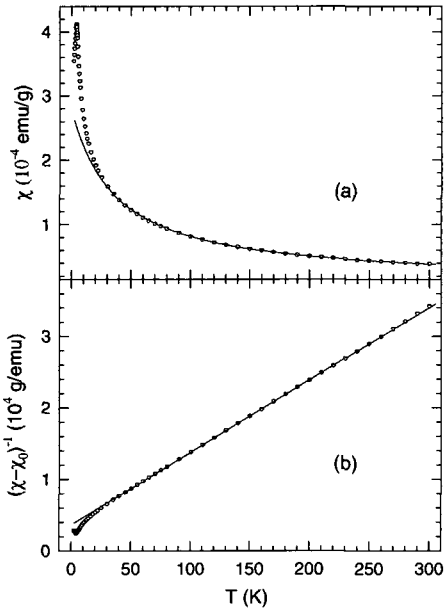

Figure 2. (a) The temperature dependence of the magnetic susceptibility of the icosahedral $Ag_{50}In_{36}Gd_{14}$, measured in an external magnetic field of 30 Oe. The solid line is the fit to equation (1) in the temperature range 50–300 K, as explained in the text. (b) The inverse magnetic susceptibility corrected for the contribution χ_0, $(\chi - \chi_0)^{-1}$ versus temperature T of the icosahedral $Ag_{50}In_{36}Gd_{14}$. The solid line is the fit to equation (1).

thermodynamically stable. The value of the six-dimensional hypercubic lattice constant calculated from the value Q_{exp} that corresponds to the (18, 29) i peak is 7.805(2) Å. The widths Γ_Q of the i peaks is significantly larger than the instrumental resolution (about 0.006 $Å^{-1}$) of the XRD spectrometer. This broadening, as well as the small shift of Q_{exp} from their ideal positions Q_{cal}, indicates the presence of some structural/chemical disorder in the i $Ag_{50}In_{36}Gd_{14}$ QC.

3.2. Magnetic susceptibility

The magnetic susceptibility χ of the i $Ag_{50}In_{36}Gd_{14}$ QC measured in an applied magnetic field of 30 Oe between 2.0 and 300 K is shown in figure 2(a). The sample was zero-field cooled to the lowest temperature and the measurement was performed while warming the sample up to 300 K. The $\chi(T)$ curve exhibits a definite peak at 4.20(5) K, indicating magnetic ordering. The $\chi(T)$ data above 50 K could be fitted to a modified Curie–Weiss law,

$$\chi = \chi_0 + \frac{C}{T - \theta_p}, \tag{1}$$

where χ_0 is the temperature-independent magnetic susceptibility, C is the Curie constant, and θ_p is the paramagnetic Curie temperature. The Curie constant can be expressed as $C = \frac{N\mu_{eff}^2}{3k}$, where N is the concentration of magnetic atoms per unit mass and μ_{eff} is the effective magnetic moment. Figure 2(b) shows the inverse magnetic susceptibility corrected for the contribution χ_0, $(\chi - \chi_0)^{-1}$ versus temperature; the validity of the Curie–Weiss law is evident. The values

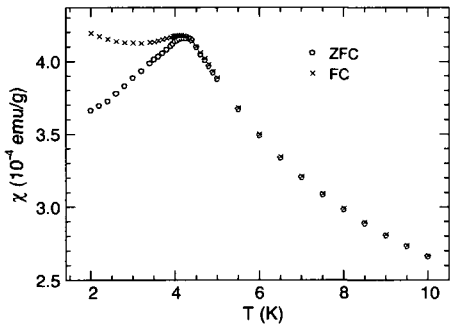

Figure 3. The temperature dependence of the zero-field-cooled (ZFC) and field-cooled (FC) magnetic susceptibility of the icosahedral $Ag_{50}In_{36}Gd_{14}$, measured in an external magnetic field of 30 Oe.

of χ_0, C, and θ_p obtained from the fit are, respectively, 8.57(10) $\times$ 10^{-6} emu g^{-1}, 9.91(3) $\times$ 10^{-3} emu K g^{-1}, and $-37.1(2)$ K. This value of C corresponds to μ_{eff} of 8.15(1) μ_B per Gd atom.

For a free Gd^{3+} ion (electronic ground state $^8S_{7/2}$), the theoretical value of $\mu_{eff}^{th} = g\mu_B\sqrt{J(J+1)}$ is 7.94 μ_B [27]. The fact that the experimental value $\mu_{eff} = 8.15(1)$ μ_B is very close to the theoretical value of 7.94 μ_B confirms that the magnetic moment is localized on the Gd^{3+} ions and that, as expected, Ag and In atoms carry no magnetic moment. The negative value of θ_p indicates the predominantly antiferromagnetic interaction between the Gd^{3+} spins.

To determine the nature of the magnetic transition at 4.20 K, we measured the temperature dependence of the zero-field-cooled (ZFC) and field-cooled (FC) magnetic susceptibility around 4.2 K in an applied magnetic field of 30 Oe (figure 3). The occurrence of a bifurcation between the ZFC and FC data at the freezing temperature $T_f = 4.25(5)$ K is evident. Above T_f both ZFC and FC data are identical. Such a behaviour of the ZFC and FC susceptibility data is characteristic of a spin glass [28]. The i $Ag_{50}In_{36}Gd_{14}$ QC is thus a spin glass with a freezing temperature $T_f = 4.25(5)$ K.

The occurrence of a spin-glass behaviour requires both randomness and frustration [28, 29]. The frustration parameter f, defined as $f = -\theta_p/T_f$ [30], is an empirical measure of frustration. Its value for the i $Ag_{50}In_{36}Gd_{14}$ QC is 8.7(1), which indicates that the studied QC belongs to a category of strongly geometrically frustrated magnets [30].

There are two other Gd-containing i alloys, $Zn_{50}Mg_{42}Gd_8$ with face-centred icosahedral (FCI) structure [31] and $Cd_{50}Mg_{40}Gd_{10}$ with SI structure [32], which are also spin glasses. The values of θ_p and T_f for these i alloys are, respectively, -38 K, 5.5 K and $-37.8(1.0)$ K, 4.3(1) K. These are very similar to the values of $-37.1(2)$ K, 4.25(5) K found here for the i $Ag_{50}In_{36}Gd_{14}$ QC with SI structure. It would thus appear that SI and FCI Gd-containing i alloys have very similar bulk magnetic properties.

All three known Gd-containing ternary i alloys, $Zn_{50}Mg_{42}Gd_8$ [31], $Cd_{50}Mg_{40}Gd_{10}$ [32], and $Ag_{50}In_{36}Gd_{14}$ studied here, exhibit no long-range magnetic order and are spin glasses. Is then the spin-glass state inherent to the quasicrystalline structure of these alloys or does it result from structural/chemical disorder present in them? $Zn_{50}Mg_{42}Gd_8$ and $Cd_{50}Mg_{40}Gd_{10}$ QCs are thermodynamically stable, whereas the $Ag_{50}In_{36}Gd_{14}$ QC is metastable. The fact that the spin-glass state occurs both in thermodynamically stable and metastable i QCs seems to exclude the structural disorder as the main reason for its occurrence. These three Gd-containing ternary i QCs possess some chemical disorder which may lead to the development of the

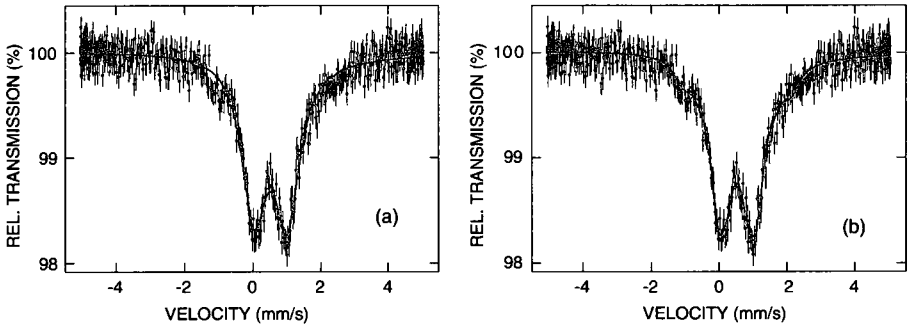

Figure 4. The ^{155}Gd Mössbauer spectrum of the icosahedral $Ag_{50}In_{36}Gd_{14}$ at 10.4 K fitted (solid line) with (a) one quadrupole pattern and (b) a distribution of quadrupole patterns. The zero-velocity scale is relative to the source.

spin-glass state. The fact that the thermodynamically stable binary i QC $YbCd_{5.7}$ with no chemical disorder is not a spin glass [33] seems to support this suggestion.

3.3. Mössbauer spectroscopy

Figure 4(a) shows a ^{151}Gd Mössbauer spectrum of the i $Ag_{50}In_{36}Gd_{14}$ QC at 10.4 K, i.e., well above T_f. This spectrum exhibits a substantial electric quadrupole hyperfine interaction. For ^{155}Gd nuclei, the quadrupole moment of the excited nuclear state with spin $I_{ex} = 5/2$, $Q_{ex} = 0.12$ b [19], is significantly smaller than that of the ground nuclear state with spin $I_g = 3/2$, $Q_g = 1.30$ b [34]. This causes the quadrupole splitting of the excited nuclear state, which is sensitive to the sign of V_{zz} and the magnitude of η, to be smaller than the natural linewidth $\Gamma_{nat} = 0.250$ mm s^{-1}. Consequently, only the absolute value of the effective quadrupole splitting parameter $\Delta_g^{eff} = eQ_g|V_{zz}|\sqrt{1+\eta^2/3}$ can be derived from a Mössbauer spectrum of a sample in the paramagnetic state [35]. The parameters derived from the fit ($\chi^2 = 1.10$) of the 10.6 K Mössbauer spectrum (figure 4(a)) are: the isomer shift (relative to the ^{155}Eu(SmPd$_3$) source) $\delta = 0.513(8)$ mm s^{-1}, $\Delta_g^{eff} = 2.030(27)$ mm s^{-1}, $f_a = 9.9(2)\%$, and $\Gamma_a = 0.508(23)$ mm s^{-1}. Although a relatively good fit was obtained, the value of Γ_a is unphysically large. This large value of Γ_a indicates the presence of a distribution of Δ_g^{eff}. In a QC, variations of the local coordination from site to site are expected to give rise to a distribution of the parameters V_{zz} and η [36]. The distribution of Δ_g^{eff} was simulated by fitting the 10.6 K Mössbauer spectrum with six component quadrupole patterns with Δ_g^{eff}-values extending from 0.0 to 1.5 mm s^{-1}; the absorber linewidth was fixed to the value of Γ_{nat} and the same values of δ and f_a were assumed for all components. The parameters deduced from the fit assuming a distribution of Δ_g^{eff} (figure 4(b)), δ, the average Δ_g^{eff}, $\bar{\Delta}_g^{eff}$, and f_a are given in table 2. The ^{151}Gd Mössbauer spectra of the i $Ag_{50}In_{36}Gd_{14}$ QC at 5.9 and 5.3 K (figure 5) display the presence of a distribution of Δ_g^{eff} and were fitted in the same way as the corresponding spectrum of the i $Ag_{50}In_{36}Gd_{14}$ QC at 10.6 K; the parameters derived from the fits are given in table 2.

The ^{151}Gd Mössbauer spectrum of the i $Ag_{50}In_{36}Gd_{14}$ QC at 4.4 K, i.e., slightly above T_f, clearly shows (figure 5) the presence of a combined electric quadrupole and magnetic dipole hyperfine interactions. It was analysed by assuming a distribution of the quadrupole splitting constant $\Delta_g = eQ_gV_{zz}$, and the same value of H_{hf} was used for all component patterns; the value of θ was fixed to 0.0° in the fit. The negative value of the average Δ_g, $\bar{\Delta}_g = eQ_g\bar{V}_{zz}$, obtained from the fit (table 2) clearly establishes that the V_{zz} component of the

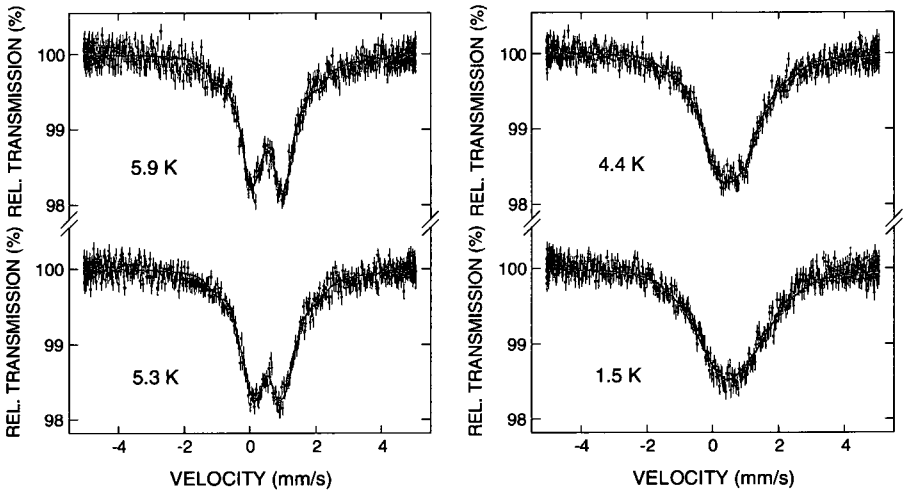

Figure 5. ^{155}Gd Mössbauer spectra of the icosahedral $Ag_{50}In_{36}Gd_{14}$ at various temperatures. Solid lines are fits, as described in the text. The zero-velocity scale is relative to the source.

Table 2. Hyperfine interaction parameters derived from the fits to the ^{151}Gd Mössbauer spectra of the icosahedral $Ag_{50}In_{36}Gd_{14}$ at various temperatures.

T (K)	δ (mm s^{-1})	$\tilde{\Delta}_g^{\text{eff}}$ or $\tilde{\Delta}_g$ (mm s^{-1})	η	H_{hf} (kOe)	f_a (%)	χ^2
10.4	0.511(7)	2.498(37)			9.9(1)	0.99
5.9	0.522(7)	2.541(51)			10.0(1)	1.06
5.3	0.512(8)	2.385(87)			10.0(1)	1.19
4.4	0.501(9)	−2.212(45)	1.00(20)	69.8(7.5)	10.1(2)	1.04
1.5	0.516(16)	−2.426(95)	0.84(24)	119.6(11.2)	10.5(2)	1.10

EFG tensor at the Gd sites in the i $Ag_{50}In_{36}Gd_{14}$ QC is negative. The complete set of the EFG tensor parameters at the Gd sites in the i $Ag_{50}In_{36}Gd_{14}$ QC determined experimentally here is: $\tilde{V}_{zz} = -4.91(10) \times 10^{21}$ V cm^{-2} and $\eta = 1.00(20)$. The ^{151}Gd Mössbauer spectrum of the i $Ag_{50}In_{36}Gd_{14}$ QC at 1.5 K (figure 5) was fitted in the same way as the corresponding spectrum at 4.4 K; the parameters derived from the fit are given in table 2.

The studied i $Ag_{50}In_{36}Gd_{14}$ QC is formed [12] by replacing all of Cd in the binary i $YbCd_{5.7}$ QC [13] with Ag and In, and Yb with Gd. It is thus expected that the crystal structure of the i $Ag_{50}In_{36}Gd_{14}$ QC must be similar to that of the i $YbCd_{5.7}$ QC. The crystal structure of the i $YbCd_{5.7}$ QC has been recently solved [14]. One would expect that Gd atoms are located at the Yb sites (on the vertices of the icosahedron and inside the acute rhombohedron) and that the Ag and In atoms are distributed among the Cd sites. Clearly, the existence of the multiplicity of Gd sites observed here is compatible with this structural model. The complete set of the EFG tensor parameters at the Gd sites in the i $Ag_{50}In_{36}Gd_{14}$ QC determined experimentally here could be compared with the corresponding parameters obtained from *ab initio* calculations of the EFGs for a possible structural model for the i $Ag_{50}In_{36}Gd_{14}$ QC, similarly as has been done for the i Al–Cu–Fe QC [37]. This could lead to the solution of the structure of the i $Ag_{50}In_{36}Gd_{14}$ QC.

In terms of the Debye approximation of the lattice vibrations, the absorber Debye–Waller factor f_a is expressed [18] by the Debye temperature, Θ_D, as

$$f_a(T) = \exp\left\{-\frac{3}{4}\frac{E_\gamma^2}{Mc^2k\Theta_D}\left[1+\left(\frac{T}{\Theta_D}\right)^2\int_0^{\Theta_D/T}\frac{x\,dx}{e^x-1}\right]\right\}, \quad (2)$$

where E_γ is the energy of the Mössbauer transition, M is the mass of the Mössbauer nucleus, c is the speed of light, and k is the Boltzmann constant. The analysis of the values of f_a given in table 2 via equation (2) yields $\Theta_D = 199(2)$ K. This is the lowest value among the known ternary i QCs. This value compares well with the anomalously low value of Θ_D (in the range 138–145 K) for the i $Yb_{5.7}Cd$ QC [33, 38].

The freezing temperature determined by the Mössbauer effect, T_f^m, is defined as a temperature at which the magnetic dipole hyperfine interaction sets in. The presence of the magnetic dipole hyperfine interaction in the Mössbauer spectrum of the i $Ag_{50}In_{36}Gd_{14}$ QC at 4.4 K, and its absence in the Mössbauer spectrum at 5.3 K, shows that T_f^m lies between 4.4 and 5.3 K. Clearly, T_f^m is larger than T_f. The systematically higher values of T_f^m than T_f have been observed for many spin-glass systems [28, 39]. The inequality $T_f^m > T_f$ results from a time window of an experimental technique used to determine the freezing temperature: as the time window decreases, the freezing temperature increases [28, 39].

4. Conclusions

A newly discovered icosahedral quasicrystal $Ag_{50}In_{36}Gd_{14}$ has been studied with x-ray diffraction, magnetic susceptibility, and ^{155}Gd Mössbauer spectroscopy. The studied quasicrystal has a simple six-dimensional Bravais lattice with the six-dimensional hypercubic lattice constant of 7.805(2) Å. The observed broadening of the diffraction Bragg peaks reflects the presence of the topological/chemical disorder. The temperature dependence of the magnetic susceptibility follows the Curie–Weiss law with the effective magnetic moment of 8.15(1) μ_B per Gd atom and the paramagnetic Curie temperature of −37.1(2) K. The studied quasicrystal is a spin glass with a freezing temperature of 4.25(5) K. The presence of the distribution of the electric quadrupole splitting in the Mössbauer spectra indicates the existence of a multiplicity of Gd sites. The values of the principal component of the electric field gradient tensor and the asymmetry parameter at these sites are, respectively, $-4.91(10) \times 10^{21}$ V cm^{-2} and $\eta = 1.00(20)$. The Debye temperature of the studied quasicrystal is 199(2) K. The hyperfine magnetic field sets in at a temperature higher than the freezing temperature.

Acknowledgments

This work was supported by the Natural Sciences and Engineering Research Council of Canada.

References

[1] Shechtman D, Blech I, Gratis D and Cahn J W 1984 *Phys. Rev. Lett.* **53** 1951
[2] Suck J-B, Schreiber M and Häussler P (ed) 2002 *Quasicrystals, an Introduction to Structure, Physical Properties, and Applications* (Berlin: Springer)
[3] Lifshitz R 1995 *Proc. 5th Int. Conf. Quasicrystals* ed C Janot and E Mosseri (Singapore: World Scientific) p 43
Lifshitz R 1998 *Phys. Rev. Lett.* **80** 2717
Lifshitz R 2000 *Mater. Sci. Eng.* A **294–296** 508
Lifshitz R and Mandel S E-D 2004 *Acta Crystallogr.* A **60** 167
[4] Godrèche C, Luck J M and Orland H 1986 *J. Stat. Phys.* **45** 777
Bhattacharjee S M, Ho J-S and Johnson J A Y 1987 *J. Phys. A: Math. Gen.* **20** 4439

Okabe Y and Niizeki K 1988 *J. Phys. Soc. Japan* **57** 16
Duneau M, Dunlop F, Jagannathan A and Oguey C 1991 *Mod. Phys.* B **5** 1895
Matsuo S, Ishimasa T and Nakano H 2000 *Mater. Sci. Eng.* A **294–296** 633
Matsuo S, Ishimasa T and Nakano H 2002 *J. Magn. Magn. Mater.* **246** 223
Matsuo S, Nakano H, Motomura S and Ishimasa T 2005 *J. Phys. Soc. Japan* **74** 1036
Matsuo S, Motomura S and Ishimasa T 2007 *Phil. Mag.* **87** 51
[5] Ledue D, Teillet J, Carnet J and Dujardin J 1993 *J. Non-Cryst. Solids* **153/154** 403
Reid R W, Bose K and Mitrovi B 1998 *J. Phys.: Condens. Matter* **10** 2303
Hermission J 2000 *J. Phys. A: Math. Gen.* **33** 57
[6] Wessel S, Jagannathan A and Hass S 2003 *Phys. Rev. Lett.* **90** 177205
Vedmedenko E Y, Oepen H P and Kirschner J 2003 *Phys. Rev. Lett.* **90** 137203
Jagannathan A 2004 *Phys. Rev. Lett.* **92** 047202
Vedmedenko E Y, Grimm U and Wiesendanger R 2004 *Phys. Rev. Lett.* **93** 076407
Jagannathan A 2005 *Phys. Rev.* B **71** 115101
Vedmedenko E Y 2004 *Ferroelectrics* **305** 129
Vedmedenko E Y, Grimm U and Wiesendanger R 2006 *Phil. Mag.* **86** 733
[7] Jagannathan A and Schultz H J 1997 *Phys. Rev.* B **55** 8045
Hida K 2001 *Phys. Rev. Lett.* **86** 1331
[8] Stadnik Z M, Stroink G, Ma H and Williams G 1989 *Phys. Rev.* B **39** 9797
Fukamichi K 1999 *Physical Properties of Quasicrystals* ed Z M Stadnik (Berlin: Springer) p 295
[9] Charrier B, Ouladdiaf B and Schmitt D 1997 *Phys. Rev. Lett.* **78** 4637
[10] Sato T J, Takakura H, Tsai A P and Shibata K 1998 *Phys. Rev. Lett.* **81** 2364
Noakes D R, Kalvius G M, Wäppling R, Stronach C E, White M F Jr, Saito H and Fukamichi K 1998 *Phys. Lett.* A **238** 197
Islam Z, Fisher I R, Zarestky J, Canfield P C, Stassis C and Goldman A I 1998 *Phys. Rev.* B **57** R11047
[11] Sato T J, Takakura H, Tsai A P, Shibata K, Ohoyama K and Andersen K H 2000 *Phys. Rev.* B **61** 476
Sato T J, Takakura H, Tsai A P, Ohoyama K, Shibata K and Andersen K H 2000 *Mater. Sci. Eng.* A **294–296** 481
Sato T J, Takakura H, Guo J, Tsai A P and Ohoyama K 2002 *J. Alloys Compounds* **342** 365
Sato T J 2005 *Acta Crystallogr.* A **61** 39
Sato T J, Takakura H, Tsai A P and Shibata K 2006 *Phys. Rev.* B **73** 054417
[12] Iwano S, Nishimoto H, Tamura R and Takeuchi S 2006 *Phil. Mag.* **86** 435
[13] Tsai A P, Guo J Q, Abe E, Takakura H and Sato T J 2000 *Nature* **408** 537
Guo J Q, Abe E and Tsai A P 2000 *Phys. Rev.* B **62** R14605
[14] Takakura H, Gómez C P, Yamamoto A, de Boissieu M and Tsai A P 2007 *Nat. Mater.* **6** 58
[15] Wong-Ng W and Hubbard C R 1987 *Powder Diffr.* **2** 242
[16] *Standard Reference Material 640c, Silicon Powder Line Position and Line Shape Standard for X-ray Diffraction* 2000 (US: Natl. Inst. Stand. Techn)
[17] Otterloo B F, Stadnik Z M and Swolfs A E M 1983 *Rev. Sci. Instrum.* **54** 1575
[18] Greenwood N N and Gibb T C 1971 *Mössbauer Spectroscopy* (London: Chapman and Hall)
Gütlich P, Link R and Trautwein A 1978 *Mössbauer Spectroscopy and Transition Metal Chemistry* (Berlin: Springer)
[19] Armon H, Bauminger E R and Ofer S 1973 *Phys. Lett.* B **43** 380
[20] Stadnik Z M and Żukrowski J 2005 unpublished results
[21] Margulies S and Ehrman J R 1961 *Nucl. Instrum. Methods* **12** 131
Shenoy G K, Friedt J M, Maletta H and Ruby S L 1974 *Mössbauer Effect Methodology* vol 10, ed I J Gruverman, C W Seidel and D K Dieterly (New York: Plenum) p 277
[22] Jenkins R and Schreiner W N 1989 *Powder Diffr.* **4** 74
[23] Schreiner W N and Jenkins R 1983 *Adv. X-ray Anal.* **26** 141
[24] Cahn J W, Shechtman D and Gratias D 1986 *J. Mater. Res.* **1** 13
[25] Elser V 1986 *Acta Crystallogr.* A **42** 36
[26] Bancel P A, Heiney P A, Stephens P W, Goldman A I and Horn P M 1985 *Phys. Rev. Lett.* **54** 2422
[27] Ashcroft N W and Mermin N D 1976 *Solid State Physics* (Philadelphia, PA: Saunders)
[28] Mydosh J A 1993 *Spin Glasses: an Experimental Introduction* (London: Taylor and Francis)
[29] Toulouse G 1977 *Commun. Phys.* **2** 116
Binder K and Young A P 1986 *Rev. Mod. Phys.* **58** 801
[30] Ramirez A P 2001 *Handbook of Magnetic Materials* vol 13, ed K H J Buschow (Amsterdam: Elsevier) p 423
[31] Hattori Y, Niikura A, Tsai A P, Inoue A, Masumoto T, Fukamichi K, Aruga-Katori H and Goto T 1995 *J. Phys.: Condens. Matter* **7** 2313

[32] Sebastian S E, Huie T, Fisher I R, Dennis K W and Kramer M J 2004 *Phil. Mag.* **84** 1029
[33] Dhar S K, Palenzona A, Manfrinetti P and Pattalwar S M 2002 *J. Phys.: Condens. Matter* **14** 517
[34] Tanaka Y, Laubacher D B, Steffen R M, Shera E B, Wohlfahrt H D and Hoehn M V 1982 *Phys. Lett.* B **108** 8
[35] Czjzek G 1993 *Mössbauer Spectroscopy Applied to Magnetism and Materials Science* vol 1, ed G J Long and F Grandjean (New York: Plenum) p 373
[36] Stadnik Z M 1996 *Mössbauer Spectroscopy Applied to Magnetism and Materials Science* vol 2, ed G J Long and F Grandjean (New York: Plenum) p 125
[37] Zijlstra E S, Kortus J, Krajčí M, Stadnik Z M and Bose S K 2004 *Phys. Rev.* B **69** 094206
[38] Tamura R, Murao Y, Takeuchi S, Tokiwa K, Watanabe T, Sato T J and Tsai A P 2001 *Japan. J. Appl. Phys.* **40** L912
Pope A L, Tritt T M, Gagnon R and Strom-Olsen J 2001 *Appl. Phys. Lett.* **79** 2345
Tamura R, Murao Y, Kishino S, Takeuchi S, Tokiwa K and Watanabe T 2004 *J. Mater. Sci. Eng.* A **375–377** 1002
Kramer M J, Lograsso T A and Sordelet D J 2005 *Phil. Mag. Lett.* **85** 151
[39] Murani A P 1977 *J. Magn. Magn. Mater.* **5** 95
Murani A P 1981 *J. Magn. Magn. Mater.* **22** 271
Wagner H G and Gonser U 1983 *J. Magn. Magn. Mater.* **31–34** 1343
Meyer C, Hartmann-Boutron F, Gros Y and Campbell I A 1985 *J. Magn. Magn. Mater.* **46** 254
Aruga H, Tokoro T and Ito A 1988 *J. Phys. Soc. Japan* **57** 261
Bogner J, Reissner M, Steiner W and Dubiel S M 1998 *J. Phys.: Condens. Matter* **10** 9849

Chapter 10 A structural, magnetic and Mössbauer spectral study of the icosahedral quasicrystal $Zn_{77}Fe_7Sc_{16}$

K. Al-Qadi, P. Wang, Z.M. Stadnik, and J. Przewoźnik.

Phys. Rev. B, submitted.

A structural, magnetic and Mössbauer spectral study of the icosahedral quasicrystal $Zn_{77}Fe_7Sc_{16}$

K. Al-Qadi,[1] P. Wang,[1] Z.M. Stadnik,[1,*] and J. Przewoźnik[2]

[1]*Department of Physics, University of Ottawa, Ottawa, Ontario K1N 6N5, Canada*

[2]*Solid State Physics Department, Faculty of Physics and Applied Computer Science, AGH University of Science and Technology, 30-059 Kraków, Poland*

(Dated: February 4, 2009)

Abstract

The structural, magnetic and Mössbauer spectral properties of the icosahedral quasicrystal $Zn_{77}Fe_7Sc_{16}$ are reported. The thermodynamically stable quasicrystal $Zn_{77}Fe_7Sc_{16}$ has a primitive six-dimensional Bravais lattice at room temperature with a six-dimensional hypercubic lattice constant of 7.087(1) Å. Based on dc magnetization measurements, no evidence is found for a transition to a ground state with long-range magnetic order in the temperature range between 2 and 300 K. The temperature dependence of the dc magnetic susceptibility follows a modified Curie-Weiss law with a paramagnetic Curie temperature of 10.6(2) K and an effective magnetic moment 3.55(1) μ_B per Fe atom. The dc zero-field-cooled and field-cooled susceptibility data indicate that the studied quasicrystal is a spin glass with freezing temperature $T_f = 7.75(2)$ K. This is further confirmed by observing ageing effects through the dc zero-field-cooled magnetization and the thermoremanent magnetization time decays, and by the analysis of the frequency dependence of T_f using the Vogel-Fulcher law, and the dynamic scaling behavior near T_f. However, the observed increase of the thermoremanent magnetization with the magnetic field in the low-field regime is incompatible with the ultrametrically organized phase space of a canonical spin glass. The nature of the spin-glass state of the icosahedral quasicrystal $Zn_{77}Fe_7Sc_{16}$ is therefore fundamentally different from that of a canonical spin glass. The bimodal distribution of the electric quadrupole splitting and of the hyperfine magnetic field derived from Mössbauer spectra indicates the existence of two classes of Fe sites. The average quadrupole splitting decreases with temperature as $T^{3/2}$. The hyperfine magnetic field sets in at a temperature of 9.87(5) K, which is significantly higher than T_f. The vibrations of the Fe atoms are well described by a Debye model, with the Debye temperature of 443(8) K.

PACS numbers: 61.44.Br, 75.50.Kj, 75.50.Lk, 76.80.+y

I. INTRODUCTION

Quasicrystals (QC's) are a new form of the solid state which differs from the other two known forms, crystalline and amorphous, by possessing a new type of long-range translational order, quasiperiodicity, and a noncrystallographic orientational order associated with the classically forbidden symmetry axes.[1] A central problem in condensed-matter physics is determining whether quasiperiodicity leads to physical properties which are significantly different from those of crystalline and amorphous materials of the same/similar compositions.

One of the main questions in the physics of QC's is that of the possibility of the existence of long-range magnetic order in these alloys. The initial intuition suggests that quasiperiodicity necessarily leads to geometrical frustration and is therefore incompatible with long-range magnetic order. However, various theoretical models dealing with magnetism in QCs indicate the possibility of the existence of long-range magnetic order in these alloys. These models are geometrical models[2] and the physical ones, such as the Ising model,[3] the XY model,[4] the Heisenberg model,[5] and the Hubbard model.[6]

On the experimental side, all known QC's are either diamagnets, paramagnets or spin glasses.[7] The recent claim[8] of the existence of long-range magnetic order in icosahedral (i) R-Mg-Zn (R = rare earth) QC's was shown[9] to result from the presence of magnetic impurities in the studied samples. Recent extensive neutron diffraction studies[10] of i-R-Mg-Zn and i-R-Mg-Cd QC's, which are of very high structural quality and which can be produced in single-grain form, revealed the presence of short-range spin correlations at low temperatures and the absence of long-range magnetic order; these QC's are spin glasses.

Recently, new thermodynamically stable i QC's were discovered in the Zn-TM-Sc (TM = transition metal) system.[11] These QC's are formed by replacing some of the Zn in the binary 1/1 approximant Zn_6Sc[12] with TM. As the 1/1 approximant Cd_6Yb of the thermodynamically stable binary i-$YbCd_{5.7}$ QC is isostructural with the Zn_6Sc, it is expected that the structure of the i-Zn-TM-Sc QC's must be similar to that of the i-$YbCd_{5.7}$ QC. The crystal structure of the i-$YbCd_{5.7}$ QC has been solved very recently.[13] It is based on three building units (rhombic triacontahedra linked with acute and obtuse rhombohedra) arranged quasiperiodically with unique atomic decorations. One would expect that Sc and TM atoms are distributed among the Yb sites (on the vertices of the icosahedron and inside the acute rhombohedron) and the Zn atoms are located at the Cd sites. The new i-Zn-TM-Sc QC's

could possibly possess sizeable $3d$ magnetic moments on the TM atoms[14] and perhaps exhibit long-range magnetic order. We report in this paper on structural, magnetic, and ^{57}Fe Mössbauer spectroscopy studies of the i alloy $Zn_{77}Fe_7Sc_{16}$.

II. EXPERIMENTAL METHODS

As starting elements, Zn shots (purity 99.999%), Fe foil (purity 99.99%) and Sc chunks (purity 99.9%) were used as received; Fe element was enriched to 95.4% in a ^{57}Fe isotope. Appropriate amounts of these elements corresponding to the composition $Zn_{77}Fe_7Sc_{16}$ were weighed ($\pm$0.1 mg) and weld-sealed under an argon atmosphere into a tantalum container. The container was in turn held within an evacuated SiO_2 jacket to avoid its air oxidation. The mixture was melted at 1000°C for 2 h, followed by annealing at 700°C for 120 h.

X-ray diffraction (XRD) measurements were performed at 298 K in Bragg-Brentano geometry on the PANanalytical X'Pert scanning diffractometer using Cu $K\alpha$ radiation. The $K\beta$ line was eliminated by using a Kevex PSi2 Peltier-cooled solid-state Si detector. In order to avoid deviation from intensity linearity of the solid-state Si detector, its parameters and the parameters of the diffractometer were chosen in such a way as to limit the count rate from the most intense Bragg peaks to less than 9000 counts/s.[15] To allow for possible instrumental aberration and specimen displacement, corrections were made to the 2θ angles using a fourth-order polynomial calibration curve[16] obtained from a scan of the specimen mixed with 10 wt % of a Si standard.[17]

The dc magnetic susceptibility was measured with a Quantum Design superconducting quantum interference device (SQUID) magnetometer at various magnetic fields in the temperature range 2.0–300 K. The ac magnetic susceptibility data were collected in a Quantum Design physical property measurement system between 2.0 and 30 K in a 1 Oe ac magnetic field and zero external magnetic field for frequencies varying from 20 Hz to 10 kHz.

The ^{57}Fe Mössbauer spectroscopy (MS) measurements in the temperature range 1.9–289.4 K were conducted using a standard Mössbauer spectrometer operating in sine mode and a ^{57}Co(Rh) source at room temperature. The spectrometer was calibrated with a 6.35-μm-thick α-Fe foil,[18] and the spectra were folded. The full linewidth at half maximum of the inner pair of the α-Fe Zeeman pattern was 0.210(2) mm/s and this value can be regarded as the resolution of the Mössbauer spectrometer. The Mössbauer absorber consisted of a

mixture of pulverized material and boron nitride, which were pressed into a pellet that was put into an Al disc container of thickness 0.008 mm to ensure a uniform temperature over the whole absorber. The surface densities of the Mössbauer absorbers of the i-$Zn_{77}Fe_7Sc_{16}$ QC were 1.10 and 1.21 mg $^{57}Fe/cm^2$ for measurements below and above 4.2 K, respectively.

III. RESULTS AND DISCUSSION

A. Structural characterization

The XRD pattern of the sample measured in the 2θ range 5–90° (Fig. 1) shows the presence of 39 i Bragg peaks. Bragg peaks of very small intensity due to an unidentified second phase are also observed (Fig. 1). The positions of all the detected i Bragg peaks corresponding to $K\alpha_1$ radiation (the value of its wavelength λ is 1.5405981 Å[19]) in terms of the angle $2\theta_1$ and the corresponding wave number $Q_{exp} = 4\pi \sin\theta_1/\lambda$, as well as their relative intensities and full widths at half maximum Γ_Q, were determined from the profile fitting using the procedure described by Schreiner and Jenkins.[20] These parameters, corresponding to 39 detected i peaks, whose positions are indicated by vertical lines in Fig. 1, are presented in Table I. This table also contains the theoretical positions Q_{cal} which were calculated by taking the position of the second most intense i peak as the reference. Since there are several schemes employed to index the i peaks, we present in Table I the indices that correspond to the most frequently used schemes.[21–23]

The form of indices of the observed i Bragg peaks (Table I) shows that the i-$Zn_{77}Fe_7Sc_{16}$ QC has a primitive six-dimensional Bravais lattice. There is good agreement between the observed Q_{exp} and theoretical Q_{cal} positions of the i Bragg peaks (Fig. 1 and Table I). The value of the six-dimensional hypercubic lattice constant calculated from the value Q_{exp} that corresponds to the (18,29) i peak is 7.087(1) Å. The width Γ_Q of most of the i peaks is very narrow: for example, $\Gamma_Q = 0.009$ $\mathring{A}^{-1}$ corresponding to the (52/84) i Bragg peak (Table I) is nearly equal to that of the (400) Bragg peak of the Si standard (0.008 $\mathring{A}^{-1}$) measured with the same x-ray diffractometer. This is indicative of a high degree of structural order of the studied QC.

B. Magnetic measurements

1. *dc magnetic susceptibility*

The magnetic susceptibility χ of the *i*-$Zn_{77}Fe_7Sc_{16}$ QC measured in an applied magnetic field of 50 Oe between 2.0 and 300 K is shown in Fig. 2(a). The sample was zero-field cooled (ZFC) to 2.0 K and the measurement was performed while warming the sample up to 300 K. The $\chi(T)$ curve exhibits a definite peak at 7.74(4) K indicating magnetic ordering. The $\chi(T)$ data above 40 K could be fitted to a modified Curie-Weiss law

$$\chi = \chi_0 + \frac{C}{T - \Theta_p}, \tag{1}$$

where χ_0 is the temperature-independent magnetic susceptibility, C is the Curie constant, and Θ_p is the paramagnetic Curie temperature. The Curie constant can be expressed as $C = \frac{N\mu_{eff}^2}{3k_B}$, where N is the concentration of magnetic atoms per unit mass, μ_{eff} is the effective magnetic moment, and k_B is the Boltzmann constant. Figure 2(b) shows the inverse magnetic susceptibility corrected for the contribution χ_0, $(\chi - \chi_0)^{-1}$ versus temperature; the validity of the modified Curie-Weiss law is evident. The values of χ_0, C, and Θ_p obtained from the fit are, respectively, $1.07(1) \times 10^{-5}$ emu/g, $1.80(1) \times 10^{-3}$ emu K/g, and 10.6(2) K. This value of C corresponds to μ_{eff} of 3.55(1) μ_B per Fe atom.

The positive value of Θ_p indicates the predominantly ferromagnetic interaction between the Fe atoms. The magnetic moment of 3.55 μ_B per Fe atom is the highest ever reported for a stable QC containing a TM element.[7,14] Recent electronic structure calculations[24] for a cubic approximant to the *i*-$Zn_{77}Fe_7Sc_{16}$ QC predict the magnetic moment per Fe atom in the range 1.2–2.4 μ_B.

To determine the nature of the magnetic transition at 7.74 K, we measured the temperature dependence of the ZFC and field-cooled (FC) magnetic susceptibility around 8.0 K in an applied magnetic field of 50 Oe (Fig. 3). The occurrence of a bifurcation between the ZFC and FC data at the freezing temperature $T_f = 7.75(2)$ K is evident. Above T_f both ZFC and FC data are identical. Such a behavior of the ZFC and FC susceptibility data is characteristic of a spin glass.[25] The *i*-$Zn_{77}Fe_7Sc_{16}$ QC is thus a spin glass with a freezing temperature $T_f = 7.75(2)$ K.

2. Relaxation effects in the dc magnetization

An ageing phenomenon, which was discovered by Lundgren *et al.*,[26] is an inherent characteristics of a spin-glass system. The measurement of ageing effects in spin glasses is carried out either via the ZFC magnetization decay measurement or the complementary thermoremanent magnetization (TRM) decay measurement.[25] The first involves cooling the sample in zero magnetic field from above T_f to the measuring temperature T_m below T_f, allowing the sample to stay at T_m a certain waiting time t_w, and then applying a small magnetic field and recording the change of magnetization with time. The second utilizes cooling the sample in a small magnetic field from above T_f to T_m below T_f, keeping the sample at T_m for time t_w, and then rapidly removing the magnetic field and recording the change of magnetization with time. The dependence of the magnetization decays on t_w is called ageing.

Figure 4 shows the ZFC magnetization decays at $T_m = 4.8$ K $= 0.62T_f$ and in 20 Oe for different waiting times. It is clear from the figure that the measured ZFC magnetization strongly depends on t_w: the longer the t_w, the slower the decay of the ZFC magnetization. The system becomes "stiffer" for larger waiting times. This confirms the existence of aging processes in the i-$Zn_{77}Fe_7Sc_{16}$ QC. The observed dependence of the ZFC magnetization on t_w is the same as that observed for canonical spin glasses.[25]

Among the various functional forms that have been proposed to describe the magnetization decay, one of the most successful in describing the data is a stretched exponential of the form

$$M(t) = M_0 - M_r \exp\left[-\left(\frac{t}{\tau_r}\right)^{1-n}\right], \tag{2}$$

where M_0 relates to an intrinsic ferromagnetic component, M_r is a glassy component, τ_r is the characteristic time constant, and n is the stretched exponential exponent.[27] The time constant τ_r and the exponent n are related to the relaxation rate of the spin glass. The data could be well fitted to Eq. (2) as evidenced by the solid lines in Fig. 4. The values of the fitted parameters are listed in Table II. To within experimental error, n and M_r are independent of t_w, whereas τ_r increases with t_w. The independence of n and M_r on t_w was observed for canonical spin glasses.[27,28]

The ageing phenomenon in the i-$Zn_{77}Fe_7Sc_{16}$ QC was also studied by the TRM decay measurements. Figure 5 shows the TRM decays for different waiting times at a cooling field of 50 Oe and at $T_m = 4.8$ K $= 0.62T_f$ and $T_m = 6.0$ K $= 0.77T_f$. The following observations

follow from the data (Fig. 5): (1) the TRM decreases substantially as T_f is approached; (2) the larger the t_w, the larger the TRM; (3) the time decay of the TRM slows down as t_w increases. These three dependencies are precisely the same as those observed for canonical spin glasses[27–30] and can be explained within the context of an ultrametric organization of the metastable states in a spin glass.[29,30]

The ultrametric topology of the metastable states was predicted by Parisi via replica-symmetry solution[31,32] of the Sherrington-Kirkpatrick infinite-range spin-glass model.[33] A pure state α of a spin glass is characterized by the thermal average magnetization at a site i, m_i^α. An overlap function between two states α and β is $q^{\alpha\beta} = N^{-1}\sum_{i=1}^{N} m_i^\alpha m_i^\beta$, where N is the total number of spins, which are assumed here to be of Ising type. The self-overlap $q^{\alpha\alpha}$ is the Edwards-Anderson order parameter[34] and it fulfills the relation $-q_{EA}(T) \leq q^{\alpha\beta} \leq q_{EA}(T)$. The number N_S of metastable states, or equivalently the number of relative minima of the free energy, is equal to the number of solutions to the Thouless-Anderson-Palmer equations.[35] Close to T_f, N_S increases exponentially with T as[36] $N_S = \exp\left[(8/81)\, N\, (1 - T/T_f)^6\right]$. As a result, the complexity of the free-energy landscape in configuration space increases dramatically with decreasing T. It was shown[32,37] that the structure of the organization of the metastable states obeys a property called ultrametricity: for any three states α, β, and γ , having mutual overlaps $q^{\alpha\beta}$, $q^{\alpha\gamma}$, and $q^{\beta\gamma}$, at least two of the overlaps are equal and the third is larger than or equal to the other two. This property can be represented as a hierarchical tree-like organization of the states[38] (Fig. 6). As the temperature is lowered from, say, T_1 to T_2 ($T_2 < T_1 < T_f$), a given metastable state α at T_1 gives "birth"to N_α new states at T_2.

The three dependencies of the TRM observed here for the studied i-$Zn_{77}Fe_7Sc_{16}$ QC and for canonical spin glasses can be explained[29,30] within the framework of the ultrametric organization of the metastable states (Fig. 6). When the spin system is cooled to T_m in the magnetic field H, it explores during the waiting time t_w different metastable states in the phase space by jumping over the energy barriers. Assuming that the jumps occur via a thermally activated process, the part of the phase space explored is characterized by the highest surmounted energy barrier Δ_{max} that depends on T_m and t_w and is given by $\Delta_{max}(T_m, t_w) = T_m \ln\left(\frac{t_w}{\tau}\right)$, where τ is a macroscopic attempt time. At the end of the waiting time t_w, the magnetic field is reduced from H to zero, and the TRM decay is measured. Here, two closely related processes take place. First, a new set of metastable states with

zero magnetization replaces the set of the metastable states with magnetization M_{FC} as the ground state. Second, this results in a "tilt"in the free-energy surface which rapidly empties those occupied states with M_{FC} with energy barriers less than or equal to the change in Zeeman energy, HM_{FC}. This accounts for the rapid change of the magnetization (so-called reversible part) upon cutting the magnetic field H to zero. For longer times, the diffusion process from occupied states with M_{FC} with energy barriers larger than HM_{FC} to the states with zero magnetization occurs. This leads to the slow decay of the so-called irreversible part of the magnetization (TRM). For longer waiting times, the weight of the populated FC phase space bounded by energy barriers larger than the change in Zeeman energy increases, and consequently, the magnitude of the TRM should increase. Moreover, because of a larger fraction of states surrounded by higher energy barriers for longer waiting time, it takes a longer time for the system to leave these states and decay towards the "sink"among low-barrier heights which have been overcome by HM_{FC}. This explains why the decay of the TRM is slower for longer waiting times.

The existence of the ultrametrically organized phase space in a spin glass can also be evidenced by studying the TRM decay as a function of the cooling field H, which should be in the low-field region where the ZFC and FC magnetizations differ substantially.[30] The decay of the TRM for $t_w = 3600$ s at $T_m = 4.8$ K $= 0.62T_f$ and $T_m = 6.0$ K $= 0.77T_f$ as a function of the cooling field H is shown in Fig. 7. It is clear from Fig. 7 that the magnitude of the TRM increases with the cooling field. The TRM dependence on H observed here is exactly *opposite* to that observed for a canonical spin glass where the TRM decreases with H. The decrease of the TRM with H is expected for the ultrametrically organized phase space in a spin glass[30]: the larger the cooling field H, the smaller the region of populated states bounded by barriers of height $\Delta(t_w) > HM_{FC}$, so that a smaller TRM remains after $H \longrightarrow 0$. We thus have to conclude that the observed increase of the TRM with H in the i-$Zn_{77}Fe_7Sc_{16}$ QC is inconsistent with the ultrametrically organized phase space. This result contradicts the spin-glass nature of the ground state in the i-$Zn_{77}Fe_7Sc_{16}$ QC in the sense of a canonical spin glass.

3. ac magnetic susceptibiity

The in-phase component χ' and the out-of-phase component χ'' of the ac magnetic susceptibility for i-$Zn_{77}Fe_7Sc_{16}$ QC, measured in the temperature range from 2 to 30 K and for selected frequencies between 20 Hz and 10 kHz, are shown in Figs. 8(a) and 8(b), respectively. Both $\chi'(T)$ and $\chi'(T)$ curves show maxima whose amplitudes and positions depend on the frequency f of the applied ac magnetic field. There is a sharp peak in $\chi'(T)$ which can be used to define T_f. $\chi'(T)$ attains a maximum at T_f that shifts towards higher temperatures with higher frequencies, which is typical for conventional spin glasses.[25] Below the maximum, the magnitude of χ' is frequency dependent, but it becomes independent of frequency at temperatures just above T_f. This behavior is qualitatively similar to that of conventional spin glasses.[25] The out-of-phase component χ'' is vanishing above T_f, but is nonzero for temperatures just below T_f, which implies dissipation not only at the freezing transition but also for temperatures below it, a common feature of spin glasses.[25]

The frequency dependence of T_f, which was determined from the maximum of the data in Fig. 8(a), obtained by curve fitting, is shown in Fig. 9. A quantitative measure of the change of the freezing temperature with frequency in spin glasses is represented by the relative change in T_f per decade change in f defined as[25]

$$K = \frac{\Delta T_f}{T_f \Delta \log f}. \tag{3}$$

From a linear fit of the data in Fig. 9, and using the average value of $T_f = 8.08$ K for the range of frequencies used, we find that $K = 0.016(1)$. This value is a factor of 3 greater than that observed for the canonical $Cu_{1-x}Mn_x$ spin glass but comparable to that of several other canonical spin glasses.[25] We note that the value of K reported for another i-$Tb_9Mg_{34}Zn_{57}$ QC is 0.049.[39]

There are basically two different interpretations of the spin freezing phenomenon in spin glasses[25]: one is a cluster model in which the system is considered as a set of interacting superparamagnetic clusters and the other is a model which assumes the occurrence of a true phase transition. The frequency dependence of T_f in spin glasses is described within the cluster model by the phenomenological Vogel-Fulcher law[25,40]

$$f = f_0 \exp\left[-E_a/k_B\left(T_f - T_0\right)\right], \tag{4}$$

where f_0 is a characteristic frequency, E_a is the activation energy, and T_0 is the Vogel-

Fulcher temperature which is a measure of the interaction strengths between clusters in the spin glass.[41] Equation (4) implies a linear dependence of $1/(T_f - T_0)$ with $\log(f)$. The best fit of the $T_f(f)$ data to Eq. (4) (Fig. 10) yields $f_0 = 7.20(22) \times 10^{11}$ Hz, $E_a/k_B = 25.1(2.6)$ K, and $T_0 = 6.87(47)$ K. Similarly to what was observed for other spin glasses,[40] $T_0 < E_a/k_B$. The values of f_0, E_a/k_B, and T_0 obtained for the i-$Zn_{77}Fe_7Sc_{16}$ QC are in general agreement with similar parameters reported for other spin-glass systems.[25,39,40]

The frequency-dependent maximum of $\chi'(T)$ indicates the freezing temperature T_f where the maximum relaxation time, τ, of the system is equal to the characteristic time $1/f$ set by the frequency of the ac-susceptibility measurement. The scaling theory near a phase transition at T_c predicts that the temperature dependence of τ obeys the power-law divergence[25,42]

$$\tau = \tau_0 \left(\frac{T_f - T_c}{T_c} \right)^{-z\nu}, \quad T_f > T_c, \tag{5}$$

where τ_0 is the microscopic relaxation time, z is the dynamic exponent relating the correlation length ξ and τ as $\tau \propto \xi^z$, and ν is the critical exponent for the correlation length $\xi \propto \left(\frac{T_f}{T_c} - 1\right)^{-\nu}$. The best fit of the $T_f(f)$ data to Eq. (5) (Fig. 11) gives $\tau_0 = 1.47(32) \times 10^{-12}$ s, $T_c = 7.72(8)$ K, and $z\nu = 6.77(1.14)$. The derived values of τ_0 and $z\nu$ are similar to those for the canonical $Cu_{1-x}Mn_x$ spin glass.[25,43]

C. Mössbauer spectroscopy

The Mössbauer spectra of the i-$Zn_{77}Fe_7Sc_{16}$ QC recorded at temperatures at which no magnetic dipole hyperfine interaction[44] is present are shown in Fig. 12. All the spectra consist of a broadened doublet which results from the distribution of the quadrupole splittings, $P(\Delta)$.[45] A quadrupole splitting

$$\Delta = \frac{1}{2} eQ|V_{zz}|\sqrt{1 + \eta^2/3}, \tag{6}$$

where e is the proton charge and Q is the electric quadrupole moment of the ^{57}Fe nucleus. The asymmetry parameter $\eta = |(V_{xx} - V_{yy})/V_{zz}|$, $(0 \leq \eta \leq 1)$, where V_{xx}, V_{yy}, and V_{zz} are the eigenvalues of the electric field gradient (EFG) tensor in order of increasing magnitude.[44] The distribution $P(\Delta)$ is the consequence of the distributions of the EFG and of the asymmetry parameter. The Mössbauer spectra in Fig. 12 were fitted with the Voigt-based quadrupole distribution method of Rancourt and Ping.[46] To account for a small asymmetry of the spectra, a linear coupling between the centre shift,δ, and Δ for the elementary

Lorentzian doublets was assumed. The best fits of the Mössbauer spectra in Fig. 12 could be obtained with the probability quadrupole splitting probability distribution functions $P(\Delta)$ shown in Fig. 13.

The determined distributions $P(\Delta)$ (Fig. 13) clearly have a bimodal character. This is in contrast to the unimodal distribution $P(\Delta)$ observed for the thermodynamically stable i-$Al_{62.5}Cu_{24.5}Fe_{13}$ QC.[47] The bimodal character of $P(\Delta)$ may be indicative of the presence of two classes of Fe sites in the structure of the i-$Zn_{77}Fe_7Sc_{16}$ QC. The lack of *ab initio* calculations of the distribution of the EFG in the i-$Zn_{77}Fe_7Sc_{16}$ QC inhibits a comparison of the experimentally determined $P(\Delta)$ with theory. Such calculations are very desirable since the experimentally determined shape of $P(\Delta)$ could be directly used to determine which of the possible structural models of the i-$Zn_{77}Fe_7Sc_{16}$ QC is the most appropriate.

The average value of the quadrupole splitting, $\overline{\Delta}$, at a given temperature was calculated from the $P(\Delta)$ distribution at that temperature (Fig. 13). One can note a small increase of $\overline{\Delta}$ with decreasing temperature (Fig. 14). The temperature dependence of $\overline{\Delta}$ could be fitted well (Fig. 14) to the empirical equation

$$\overline{\Delta}(T) = \overline{\Delta}(0)\left(1 - BT^{3/2}\right), \tag{7}$$

where $\overline{\Delta}(0)$ is the value of $\overline{\Delta}$ at 0 K and B is a constant. Such a $T^{3/2}$ temperature dependence has been observed in many metallic noncubic crystalline alloys,[48] in some metallic amorphous alloys,[49,50] and recently in QCs[47,50,51] over temperature ranges from a few K to the melting point. This seemingly universal $T^{3/2}$ dependence is not well understood. Its origin seems to be associated with a strong temperature dependence of mean-square lattice displacements and, to a lesser extent, with the temperature dependence of lattice expansion.[52] The values of $\overline{\Delta}(0)$ and B determined from the fit for the i-$Zn_{77}Fe_7Sc_{16}$ QC are, respectively, 0.527(1) mm/s and $8.87(44) \times 10^{-6}$ $K^{-3/2}$. The value of B is similar to that found for other metallic amorphous alloys and QCs.[49,51]

The Mössbauer spectra of the i-$Zn_{77}Fe_7Sc_{16}$ QC measured at temperatures at which the magnetic dipole hyperfine interaction[44] is present are shown in Fig. 15. They were fitted with the Voigt-based hyperfine magnetic field, H_{hf}, distribution method of Rancourt and Ping.[46] A linear coupling between δ and H_{hf}, and the quadrupole shift[44], ϵ, and H_{hf}, for the elementary sextets was assumed. The best fits of the Mössbauer spectra in Fig. 15 were obtained with the hyperfine magnetic field probability distribution functions $P(H_{hf})$ shown

in Fig. 16.

Similarly to the case of the $P(\Delta)$ distributions, the $P(H_{hf})$ distributions are also bimodal (Fig. 16). This is suggestive of two classes of Fe sites in the structure of the i-$Zn_{77}Fe_7Sc_{16}$ QC. The average value of the hyperfine magnetic field, $\overline{H}_{hf}$, at a given temperature was calculated from the $P(H_{hf})$ distribution at that temperature (Fig. 16). The temperature dependence of $\overline{H}_{hf}$ is presented in Fig. 17. The temperature at which $\overline{H}_{hf}$ vanishes, that was estimated from the extrapolation of the $\overline{H}_{hf}(T)$ data in Fig. 17, is 9.87(5) K. If one defines the freezing temperature of a spin glass determined from MS, T_f^M, as the temperature at which the magnetic dipole hyperfine interaction disappears, then $T_f^M = 9.87(5)$ K. Clearly, T_f^M is significantly larger than the freezing temperature $T_f = 7.75(2)$ K determined from the dc magnetic susceptibility data. The systematically higher values of T_f^M than T_f have been observed for many other spin-glass systems.[25,53] The inequality $T_f^M > T_f$ results from a time window τ_{exp} of an experimental technique used to determine the freezing temperature. For MS, τ_{exp} is given by the Larmor precession time τ_L of the nuclear magnetic moment in the hyperfine magnetic field. In the case studied here, $\tau_L = 1.2 \times 10^{-7}$ s ($f_L = 8.4$ MHz) for $\overline{H}_{hf} = 106.2$ kOe at 1.9 K. With a wide distribution of the relaxation times τ of fluctuating spin clusters in a spin glass,[25,53,54] those clusters fluctuating with τ larger than τ_{exp} of a given experimental technique will appear frozen and will be discerned at a higher temperature than by the experimental technique characterized by a smaller τ_{exp}. Thus, one expects to observe an increase of T_f with decreasing τ_{exp}, which is indeed universally observed in spin glasses.[25,53]

The average centre shift at temperature T, $\overline{\delta}(T)$, determined from the fits of the spectra in Figs. 12 and 15 is given by

$$\overline{\delta}(T) = \delta_0 + \delta_{\mathrm{SOD}}(T), \tag{8}$$

where δ_0 is the intrinsic isomer shift and $\delta_{\mathrm{SOD}}(T)$ is the second-order Doppler (SOD) shift which depends on lattice vibrations of the Fe atoms.[44] In terms of the Debye approximation of the lattice vibrations, $\delta_{\mathrm{SOD}}(T)$ is expressed[44] by the Debye temperature, Θ_D, as

$$\delta_{\mathrm{SOD}}(T) = -\frac{9}{2}\frac{k_B T}{Mc}\left(\frac{T}{\Theta_D}\right)^3 \int_0^{\Theta_D/T} \frac{x^3 dx}{e^x - 1}, \tag{9}$$

where M is the mass of the Mössbauer nucleus and c is the speed of light. By fitting the experimental data (Fig. 18) to Eq. (9), the quantities δ_0 and Θ_D were found to be,

respectively, 0.226(1) mm/s and 443(8) K. The value of Θ_D found here is comparable to the values of Θ_D found for other i QCs.[47,50,51]

IV. SUMMARY

A new thermodynamically stable i QC $Zn_{77}Fe_7Sc_{16}$ has been studied with x-ray diffraction, dc and ac magnetic susceptibility, and ^{57}Fe Mössbauer spectroscopy. It has a primitive six-dimensional Bravais lattice at room temperature with the six-dimensional hypercubic lattice constant of 7.087(1) Å. Based on dc magnetization measurements, no evidence is found for a transition to a ground state with long-range magnetic order in the temperature range between 2 and 300 K. The temperature dependence of the dc magnetic susceptibility follows the modified Curie-Weiss law with the paramagnetic Curie temperature of 10.6(2) K and an effective magnetic moment of 3.55(1) μ_B per Fe atom. The dc zero-field-cooled and field-cooled susceptibilty data indicate that the studied QC is a spin glass with the freezing temperature $T_f = 7.75(2)$ K. This spin-glass state of the i QC $Zn_{77}Fe_7Sc_{16}$ is further confirmed by observing ageing effects through the dc zero-field-cooled magnetization and the thermoremanent magnetization time decays, and by the analysis of the frequency dependence of T_f using the Vogel-Fulcher law and the dynamic scaling behavior near T_f. However, the observed increase of the thermoremanent magnetization with the magnetic field in the low-field regime is incompatible with the ultrametrically organized phase space of a canonical spin glass. The nature of the spin-glass state of the i QC $Zn_{77}Fe_7Sc_{16}$ is thus fundamentally different from that of a canonical spin glass. The bimodal distribution of the electric quadrupole splitting and of the hyperfine magnetic field derived from Mssbauer spectra indicates the existence of two classes of Fe sites. The average quadrupole splitting decreases with temperature as $T^{3/2}$. The hyperfine magnetic field sets in at a temperature of 9.87(5) K, which is significantly higher than T_f. The lattice vibrations of the Fe atoms are well described by a Debye model, with the Debye temperature of 443(8) K.

Acknowledgments

This work was supported by the Natural Sciences and Engineering Research Council of Canada. Support from the Polish Ministry of Science and Higher Education and the

Structural Funds of the European Commission, Project No. SPO WKP 1.4.3 is gratefully acknowledged.

---

* Electronic address: stadnik@uottawa.ca

[1] *Physical Properties of Quasicrystals*, edited by Z.M. Stadnik (Springer-Verlag, Berlin, 1999); *Quasicrystals, an Introductions to Structure, Physical Properties, and Applications*, edited by J.-B. Suck, M. Schreiber, and P. Häussler (Springer-Verlag, Berlin, 2002).

[2] R. Lifshitz, in *Proceedings of the 5th International Conference on Quasicrystals*, edited by C. Janot and E. Mosseri (World Scientific, Singapore, 1995), p. 43; Phys. Rev. Lett. **80**, 2717 (1998); Mater. Sci. Eng. A **294-296**, 508 (2000); S. E-D. Menden and R. Lifshitz, Acta Crystallogr. Sect. A **60**, 179 (2004).

[3] C. Godrèche, J.M. Luck, and H. Orland, J. Stat. Phys. **45**, 777 (1986); S.M. Bhattacharjee, J.-S. Ho, and J.A.Y. Johnson, J. Phys. A **20**, 4439 (1987); Y. Okabe and K. Niizeki, J. Phys. Soc. Jpn. **57**, 16 (1988); M. Duneau, F. Dunlop, A. Jagannathan, and C. Oguey, Mod. Phys. B **5**, 1895 (1991; S. Matsuo, T. Ishimasa, and H. Nakano, Mater. Sci. Eng. A **294-296**, 633 (2000); S. Matsuo, T. Ishimasa, and H. Nakano, J. Magn. Magn. Mater. **246**, 223 (2002); S. Matsuo, H. Nakano, S. Motomura, and T. Ishimasa, J. Phys. Soc. Jpn. **74**, 1036 (2005); S. Matsuo, S. Motomura, and T. Ishimasa, Philos. Mag. **87**, 51 (2007).

[4] D. Ledue, J. Teillet, J. Carnet, and J. Dujardin, J. Non-Cryst. Solids **153-154**, 403 (1993); R.W.Reid, K. Bose, and B. Mitrović, J. Phys.: Condens. Matter **10**, 2303 (1998); J. Hermission, J. Phys. A **33**, 57 (2000).

[5] S. Wessel, A. Jagannathan, and S. Haas, Phys. Rev. Lett. **90**, 177205 (2003); E.Y. Vedmedenko, H.P. Oepen, and J. Kirschner, Phys. Rev. Lett. **90**, 137203 (2003); A. Jagannathan, Phys. Rev. Lett. **92**, 047202 (2004); E.Y. Vedmedenko, U. Grimm, and R. Wiesendanger, Phys. Rev. Lett. **93**, 076407 (2004); E.Y. Vedmedenko, Ferroelectrics **305**, 129 (2004); A. Jagannathan, Phys. Rev. B **71**, 115101 (2005); E.Y. Vedmedenko, U. Grimm, and R. Wiesendanger, Philos. Mag. **86**, 733 (2006).

[6] A. Jagannathan and H. Schulz, Phys. Rev. B **55**, 8045 (1997); K. Hida, Phys. Rev. Lett. **86**, 1331 (2001).

[7] Z.M. Stadnik, G. Stroink, H. Ma, and G. Williams, Phys. Rev. B **39**, 9797 (1989); K. Fukamichi,

in *Physical Properties of Quasicrystals*, edited by Z.M. Stadnik (Springer-Verlag, Berlin, 1999), p. 295; Z.M. Stadnik, Acta Phys. Pol. A **114**, 1475 (2008).

[8] B. Charrier, B. Ouladdiaf, and D. Schmitt, Phys. Rev. Lett. **78**, 4637 (1997).

[9] T.J. Sato, H. Takakura, A.P. Tsai, and K. Shibata, Phys. Rev. Lett. **81**, 2364 (1998); D.R. Noakes, G.M. Kalvius, R. Wäppling, C.E. Stronach, M.F. White Jr., H. Saito, and K. Fukamichi, Phys. Lett. A **238**, 197 (1998); Z. Islam, I.R. Fisher, J. Zarestky, P.C. Canfield, C. Stassis, and A.I. Goldman, Phys. Rev. B **57**, R11047 (1998).

[10] T.J. Sato, H. Takakura, A.P. Tsai, K. Shibata, K. Ohoyama, and and K.H. Andersen, Phys. Rev. B **61**, 476 (2000); T.J. Sato, H. Takakura, A.P. Tsai, K. Ohoyama, K. Shibata, and K.H. Andersen, Mater. Sci. Eng. A **294-296**, 481 (2000); T.J. Sato, H. Takakura, J. Guo, A.P. Tsai, and K. Ohoyama, J. Alloys Comp. **342**, 365 (2002); T.J. Sato, Acta Crystllogr. Sect. A **61**, 39 (2005); T.J. Sato, H. Takakura, A.P. Tsai, and K. Shibata, Phys. Rev. B **73**, 054417 (2006).

[11] Q. Lin and J.D. Corbett, Philos. Mag. Lett. **83**, 755 (2003); R. Maezawa, S. Kashimoto, and T. Ishimasa, Philos. Mag. Lett. **84**, 215 (2004).

[12] Q. Lin and J.D. Corbett, Inorg. Chem. **43**, 1912 (2004).

[13] H. Takakura, C.P. Gómez, A. Yamamoto, M. de Boissieu, and A.P. Tsai, Nature Mater. **6**, 58 (2007).

[14] S. Kashimoto, S. Motomura, R. Maezawa, S. Matsuo, and T. Ishimasa, Jpn. J. Appl. Phys. B **43**, L526 (2004); S. Kashimoto, S. Motomura, S. Francoual, S. Matsuo, and T. Ishimasa, Philos. Mag. **86**, 725 (2006).

[15] D.L. Bish and S.J. Chipera, Powder Diffract. **4**, 137 (1989).

[16] W. Wong-Ng and C.R. Hubbard, Powder Diffract. **2**, 242 (1987).

[17] *Standard Reference Material 640c, Silicon Powder Line Position and Line Shape Standard for X-ray Diffraction*, Natl. Inst. Stand. Techn. (U.S., Gaithersburg, 2000).

[18] Certificate of Calibration, Iron Foil Mössbauer Standard, Natl. Bur. Stand. (U.S.) Circ. No. 1541, edited by J.P. Cali (U.S. GPO, Washington, D.C., 1971).

[19] R. Jenkins and W.N. Schreiner, Powder Diffract. **4**, 74 (1989).

[20] W.N. Schreiner and R. Jenkins, Adv. X-ray Anal. **26**, 141 (1983).

[21] J.W. Cahn, D. Shechtman, and D. Gratias, J. Mater. Res. **1**, 13 (1986).

[22] V. Elser, Acta Cryst. Sect. A **42**, 36 (1986).

[23] P.A. Bancel, P.A. Heiney, P.W. Stephens, A.I. Goldman, and P.M. Horn, Phys. Rev. Lett. **54**,

2422 (1985).

[24] Y. Ishii, K. Nozawa, and T. Fujiwara, Philos. Mag. **86**, 693 (2006).

[25] J.A. Mydosh, *Spin Glasses: An Experimental Introduction* (Taylor & Francis, London, 1993).

[26] L. Lundgren, P. Svedlindh, P. Nordblad, and O. Beckman, Phys. Rev. Lett. **51**, 911 (1983).

[27] R.V. Chamberlin, G. Mozurkewich, and R. Orbach, Phys. Rev. Lett. **52**, 867 (1984); R. Hoogerbeets, W.-L. Luo, and R. Orbach, Phys. Rev. Lett. **55**, 111 (1985); M.A. Continentino and A.P. Malozemoff, Phys. Rev. B **33**, 3591 (1986).

[28] R.V. Chamberlin, Phys. Rev. B **30**, 5393 (1984).

[29] M. Lederman, R. Orbach, J.M. Hammann, M. Ocio, and E. Vincent, Phys. Rev. B **44**, 7403 (1991).

[30] D. Chu, G.G. Kenning, and R. Orbach, Philos. Mag. B **71**, 479 (1995).

[31] G. Parisi, Phys. Rev. Lett. **50**, 1946 (1983).

[32] M. Mézard, G. Parisi, N. Sourlas, G. Toulouse, and M. Virasoro, J. Phys. (Paris) **45**, 843 (1984).

[33] S. Kirkpatrick and D. Sherrington, Phys. Rev. B **17**, 4384 (1978).

[34] S.F. Edwards and P.W. Anderson, J. Phys. F **5**, 965 (1975).

[35] D.J. Thouless, P.W. Anderson, and R.G. Palmer, Philos. Mag. **35**, 593 (1977).

[36] A.J. Bray and M.A. Moore, J. Phys. C **13**, L469 (1980).

[37] M. Mèzard and M.A. Virasoro, J. Phys. (Paris) **46**, 1293 (1985).

[38] V.S. Dotsenko, J. Phys. C **18**, 6023 (1985).

[39] I.R. Fisher, K.O. Cheon, A.F. Panchula, P.C. Canfield, M. Chernikov, H.R. Ott, and K. Dennis, Phys. Rev. B **59**, 308 (1999).

[40] J.L. Tholence, 1980 Solid State Commun. **35**, 113 (1980).

[41] S. Shtrikman and E.P. Wohlfarth, Phys. Lett. A **85**, 467 (1981).

[42] P.C. Hohenberg and B.I. Halperin, Rev. Mod. Phys. **49**, 435 (1977).

[43] J. Souletie and J.L. Tholence, Phys. Rev. B **32**, 516 (1985).

[44] N.N. Greenwood and T.C. Gibb, *Mössbauer Spectroscopy* (Chapman and Hall, London, 1971); P. Gütlich, R. Link, and A. Trautwein, *Mössbauer Spectroscopy and Transition Metal Chemistry* (Springer, Berlin, 1978).

[45] Z.M. Stadnik, in *Mössbauer Spectroscopy Applied to Magnetism and Materials Science*, edited by G.J. Long and F. Grandjean (Plenum, New York, 1996), Vol. 2, p. 125.

[46] D.G. Rancourt and J.Y. Ping, Nucl. Instrum. Methods Phys. Res. B **58**, 85 (1991).

[47] Z.M. Stadnik, T. Takeuchi, N. Tanaka, and U. Mizutani, J. Phys.: Condens. Matter **15**, 6365 (2003).

[48] E.N. Kaufmann and R.H. Vianden, Rev. Mod. Phys. **51**, 161 (1979), and references therein.

[49] P. Deppe and M. Rosenberg, Hyperfine Interact. **15-16**, 735 (1993); M. Kopcewicz, B. Kopcewicz, and U. Gonser, J. Magn. Magn. Mater. **66**, 79 (1987); M. Mao, D.H. Ryan, and Z. Altounian, Hyperfine Interact. **92**, 2163 (1994).

[50] Z.M. Stadnik, J. Saida, and A. Inoue A, Ferroelectrics **250**, 297 (2001); Z.M. Stadnik, Ö. Rapp, V. Srinivas, J. Saida, and A. Inoue, 2002 J. Phys.: Condens. Matter **14**, 6883 (2002).

[51] R.A. Brand, J. Voss, and Y. Calvayrac, 2000 Mater. Sci. Eng. A **294-296**, 666 (2000); Z.M. Stadnik and G. Zhang, J. Phys.: Condens. Matter **17**, 6599 (2006).

[52] P. Jena, Phys. Rev. Lett. **36**, 418 (1976); K. Nishiyama, F. Dimmling, Th. Kornrumph, and D. Riegel, Phys. Rev. Lett. **37**, 357 (1976); J. Christiansen, P. Heubes, R. Keitel, W. Klinger, W. Loeffler, W. Sandner, W. Witthuhn, Z. Phys. B **24**, 177 (1976).

[53] A.P. Murani, J. Magn. Magn. Mater. **5**, 95 (1977); A.P. Murani, J. Magn. Magn. Mater. **22**, 271 (1981); H.G. Wagner and U. Gonser, J. Magn. Magn. Mater. **31-34**, 1343 (1983); C. Meyer, F. Hartmann-Boutron, Y. Gros, and I.A. Campbell, J. Magn. Magn. Mater. **46**, 254 (1985); H. Aruga, T. Tokoro, and A. Ito, 1988 J. Phys. Soc. Jpn. **57**, 261 (1988); J. Bogner, M. Reissner, W. Steiner, and S.M. Dubiel, J. Phys.: Condens. Matter **10**, 9849 (1988).

[54] L. Lundgren, P. Svedlindh, and O. Beckman, J. Phys. F **12**, 2663 (1982).

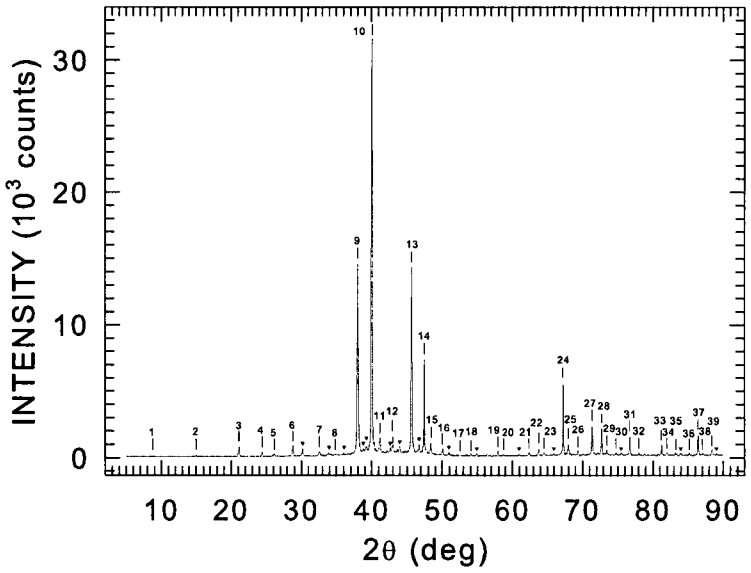

FIG. 1: The XRD spectrum of the i-$Zn_{77}Fe_7Sc_{16}$ quasicrystal at 298 K corrected for the Cu $K\alpha_2$ lines. The vertical lines labeled with intigers above all detected i Bragg peaks correspond to the positions calculated for the Cu $K\alpha_1$ radiation, as explained in the text. The position, full width at half maximum, and relative area of each detected i peak are given in Table 1 together with the corresponding index. The symbol ▼ indicates the peak positions corresponding to an unidentified second phase.

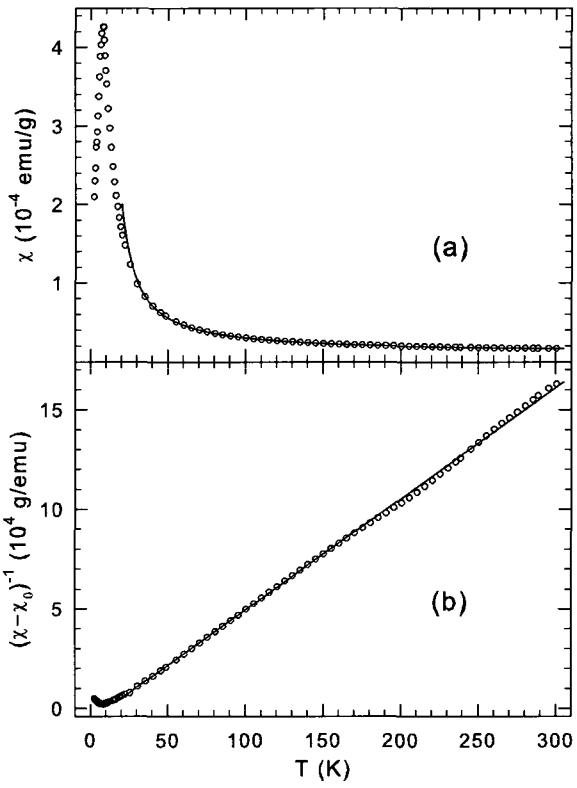

FIG. 2: (Color online) (a) The temperature dependence of the magnetic susceptibility of the *i*-$Zn_{77}Fe_7Sc_{16}$ quasicrystal, measured in an external magnetic field of 50 Oe. The solid line is the fit to Eq. (1) in the temperature range 40–300 K, as explained in the text. (b) The inverse magnetic susceptibility corrected for the contribution χ_0, $(\chi - \chi_0)^{-1}$ versus temperature T of the *i*-$Zn_{77}Fe_7Sc_{16}$ quasicrystal. The solid line is the fit to Eq. (1).

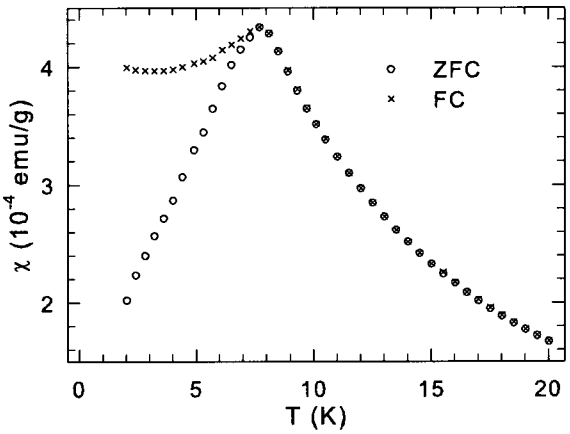

FIG. 3: (Color online) The temperature dependence of the zero-field-cooled (ZFC) and field-cooled (FC) magnetic susceptibility of the i-$Zn_{77}Fe_7Sc_{16}$ quasicrystal, measured in an external magnetic field of 50 Oe.

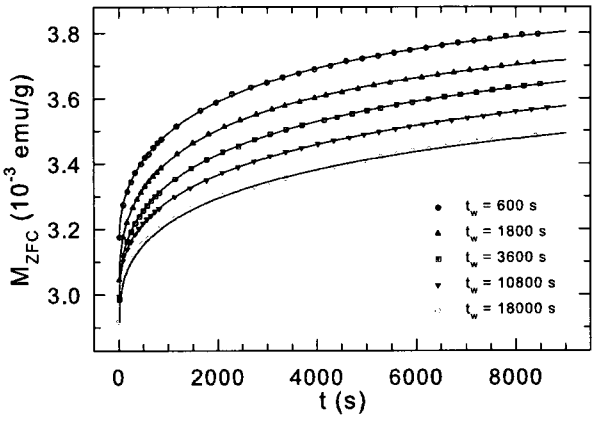

FIG. 4: (Color online) The time dependence of the ZFC magnetization for an applied magnetic field of 20 Oe at 4.8 K for different waiting times t_w of the i-$Zn_{77}Fe_7Sc_{16}$ quasicrystal. The solid lines are the fits to Eq. (2).

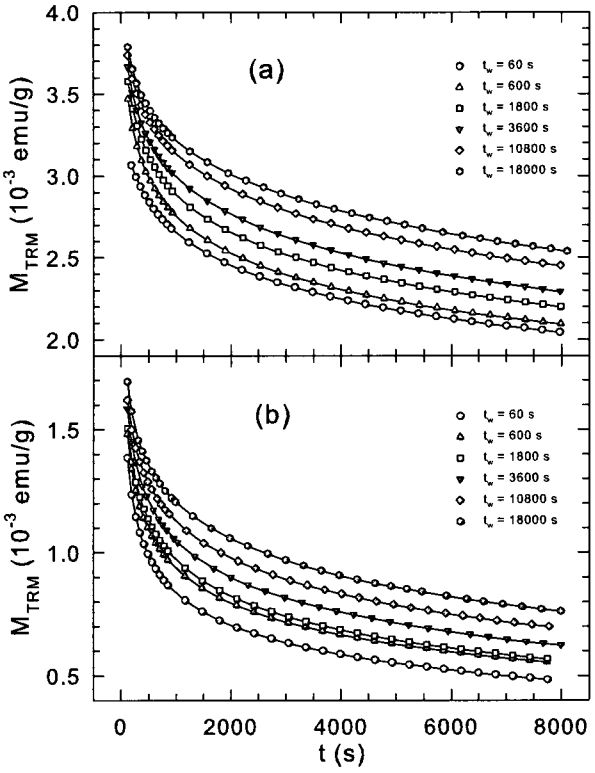

FIG. 5: (Color online) The TRM time decays at $H = 50$ Oe for the different waiting times t_w at (a) 4.8 K and (b) 6.0 K of the i-$Zn_{77}Fe_7Sc_{16}$ quasicrystal. The solid lines are guides for the eye.

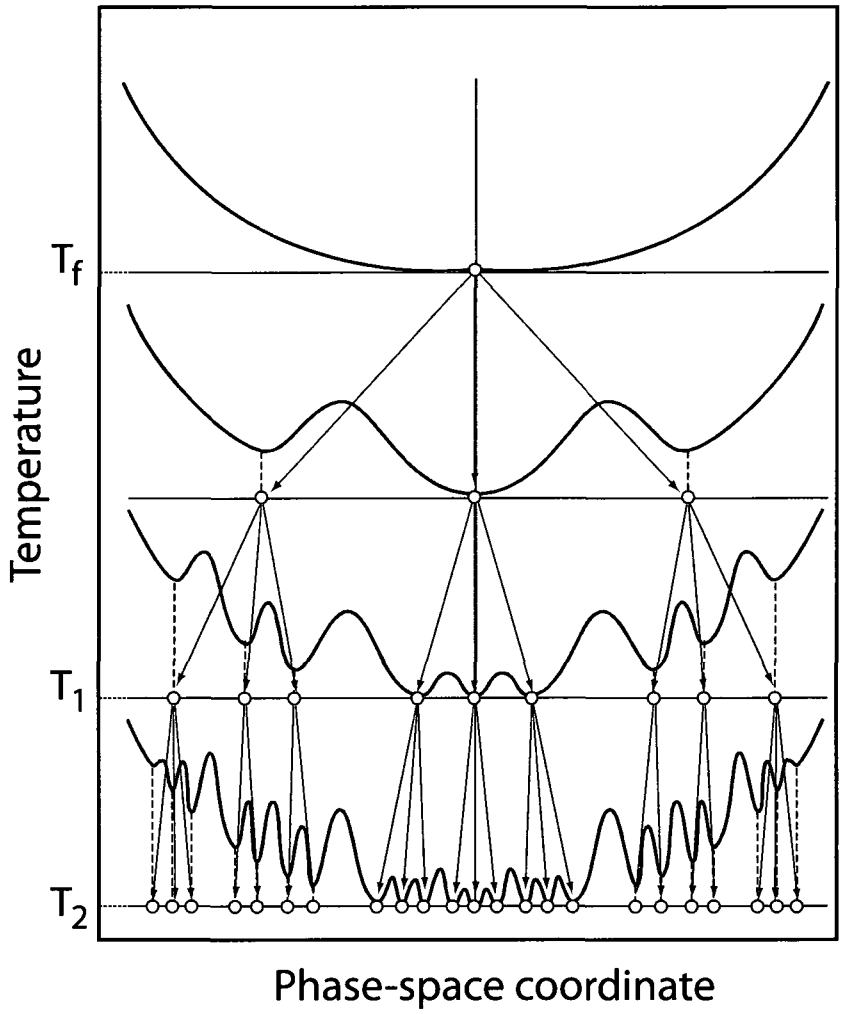

FIG. 6: (Color online) The hierarchical organization of the metastable states in a spin glass. The coarse-grained free-energy surface is represented at each level corresponding to a given temperature. When the temperature is decreased ($T_2 < T_1 < T_f$), each valley subdivides into others. Ageing refers to jumping of the system over ever increasing energy barriers during the waiting time t_w.

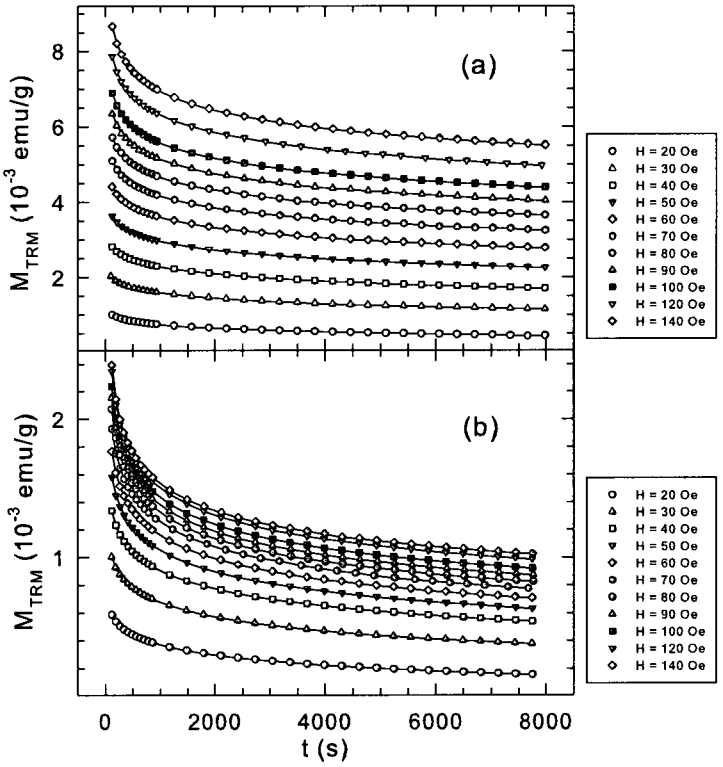

FIG. 7: (Color online) The TRM time decays for t_w = 3600 s at (a) 4.8 K and (b) 6.0 K for different cooling fields H of the i-$Zn_{77}Fe_7Sc_{16}$ quasicrystal. The solid lines are guides for the eye.

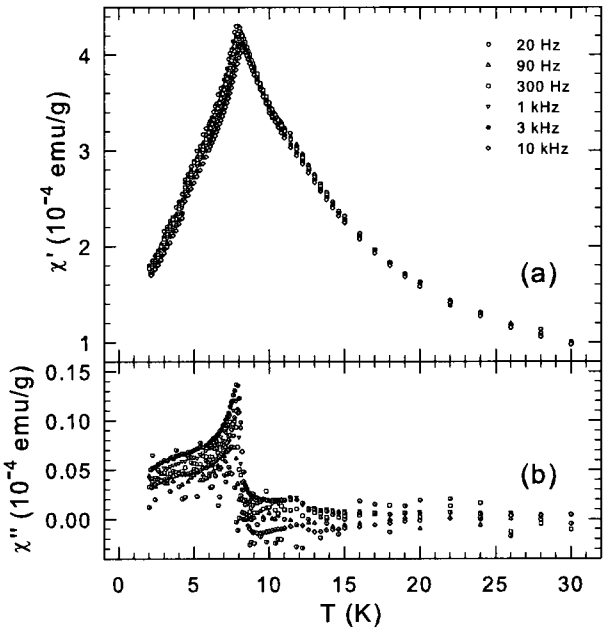

FIG. 8: (Color online) The temperature dependence of the in-phase magnetic susceptibility χ' (a) and out-of-phase magnetic susceptibility χ'' (b) measured for different applied frequencies from 20 Hz to 10 kHz for the i-$Zn_{77}Fe_7Sc_{16}$ quasicrystal.

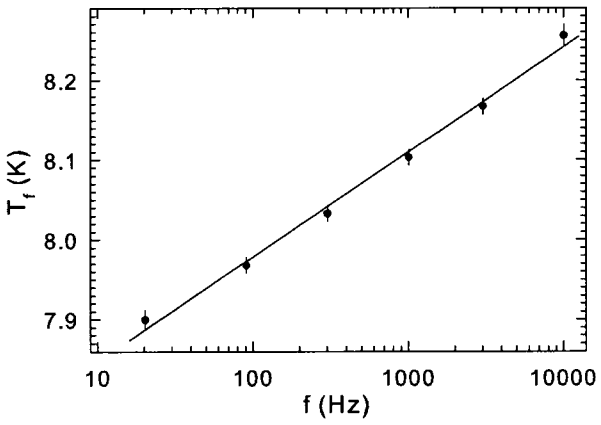

FIG. 9: (Color online) The frequency dependence of the freezing temperature T_f for the *i*-$Zn_{77}Fe_7Sc_{16}$ quasicrystal. The solid line is the best linear fit to the T_f data.

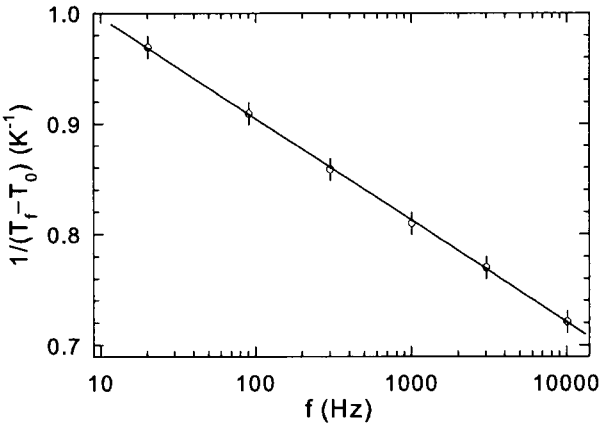

FIG. 10: (Color online) The frequency dependence of the freezing temperature T_f for the *i*-$Zn_{77}Fe_7Sc_{16}$ quasicrystal. The solid line is the best fit to Eq. (4).

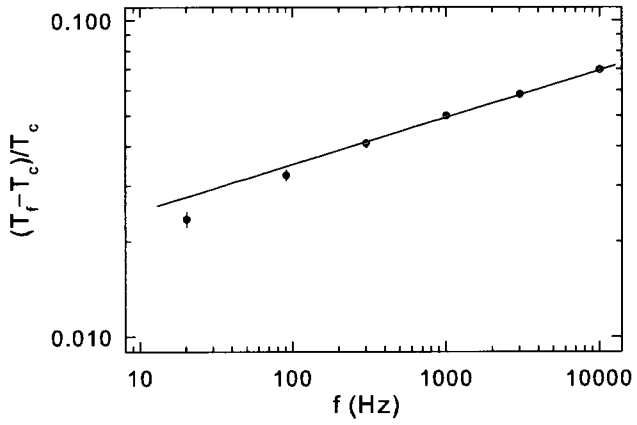

FIG. 11: (Color online) The frequency dependence of the freezing temperature T_f for the *i*-$Zn_{77}Fe_7Sc_{16}$ quasicrystal. The solid line is the best fit to Eq. (5).

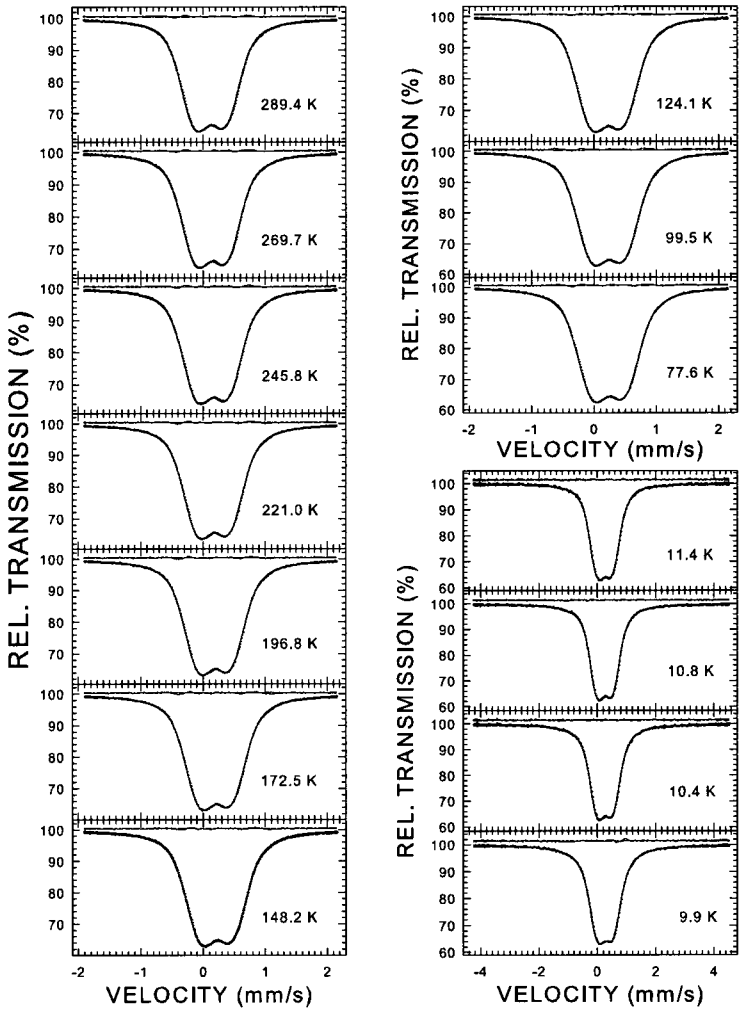

FIG. 12: (Color online) The ^{57}Fe Mössbauer spectra of the i-$Zn_{77}Fe_7Sc_{16}$ quasicrystal obtained at the indicated temperatures fitted (solid lines) with the quadrupole splitting distributions $P(\Delta)$ shown in Fig. 13. The residuals are shown above each spectrum. The zero-velocity origin is relative to α-Fe at room temperature.

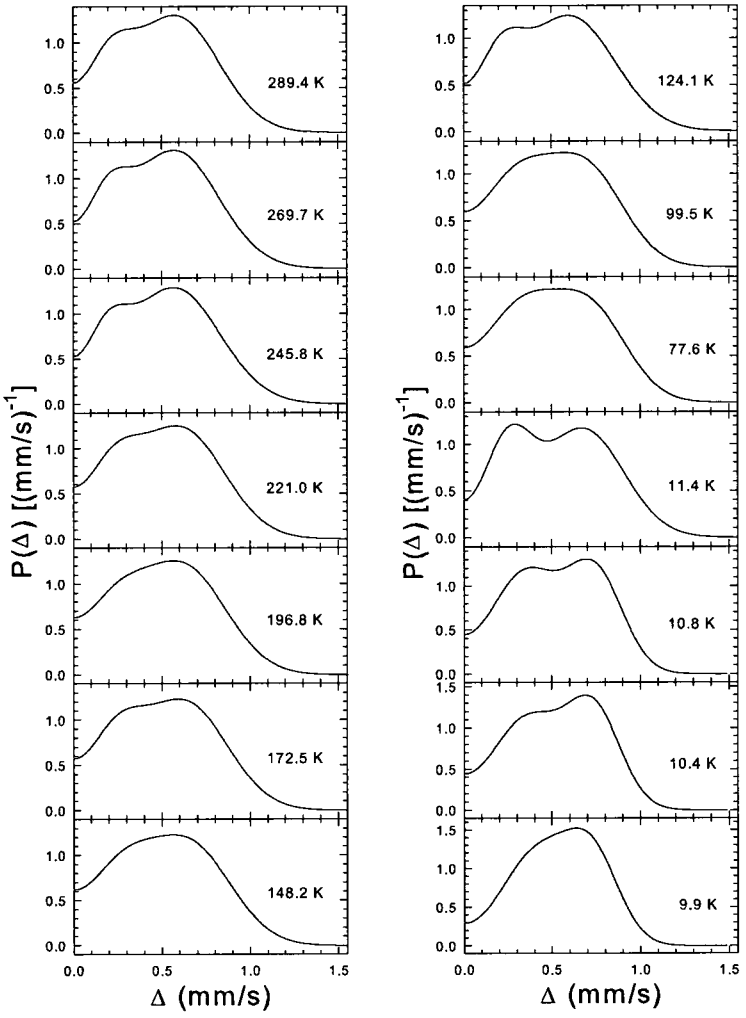

FIG. 13: (Color online) The quadrupole splitting distributions $P(\Delta)$ which fit the best the ^{57}Fe Mössbauer spectra in Fig. 12.

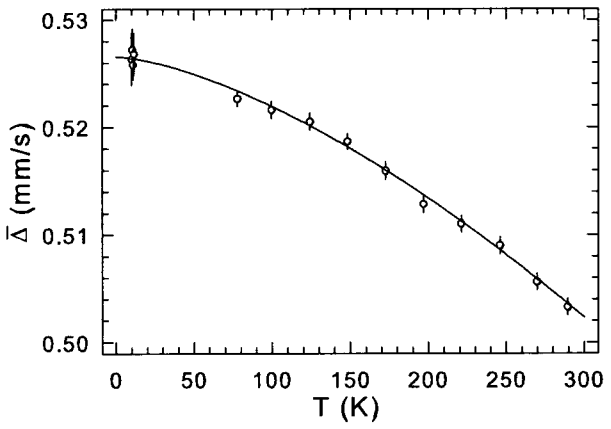

FIG. 14: (Color online) The temperature dependence of the average quadrupole splitting of the i-$Zn_{77}Fe_7Sc_{16}$ quasicrystal. The solid line is the fit to Eq. (7).

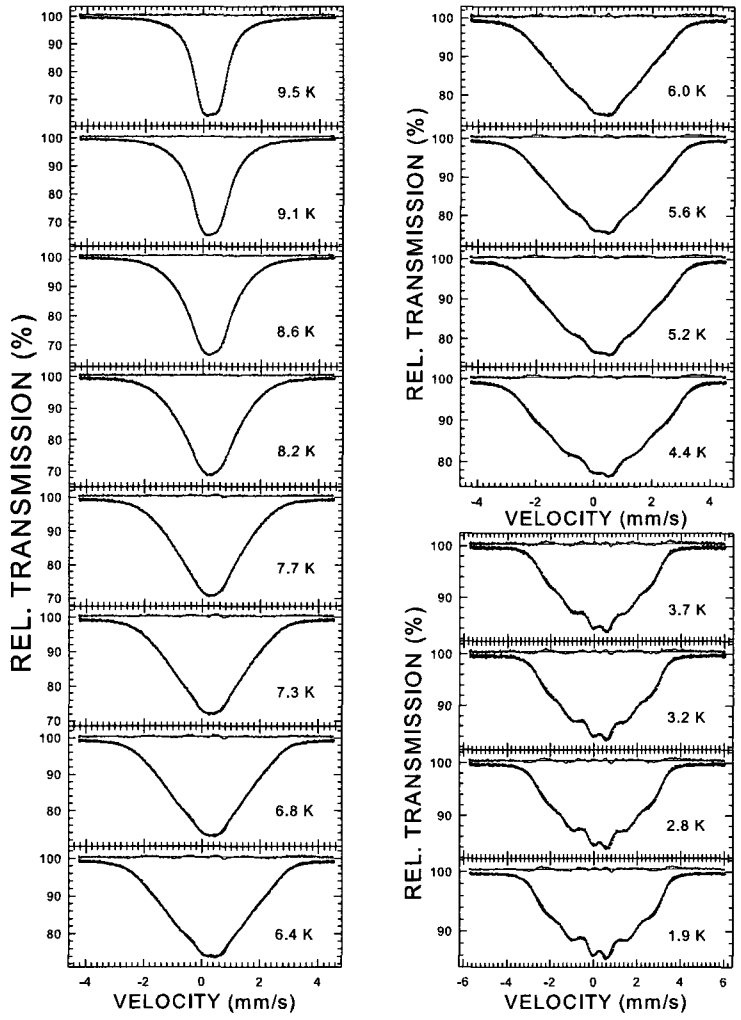

FIG. 15: (Color online) The ^{57}Fe Mössbauer spectra of the i-$Zn_{77}Fe_7Sc_{16}$ quasicrystal obtained at the indicated temperatures fitted (solid lines) with the hyperfine magnetic field distributions $P(H_{hf})$ shown in Fig. 16. The residuals are shown above each spectrum. The zero-velocity origin is relative to α-Fe at room temperature.

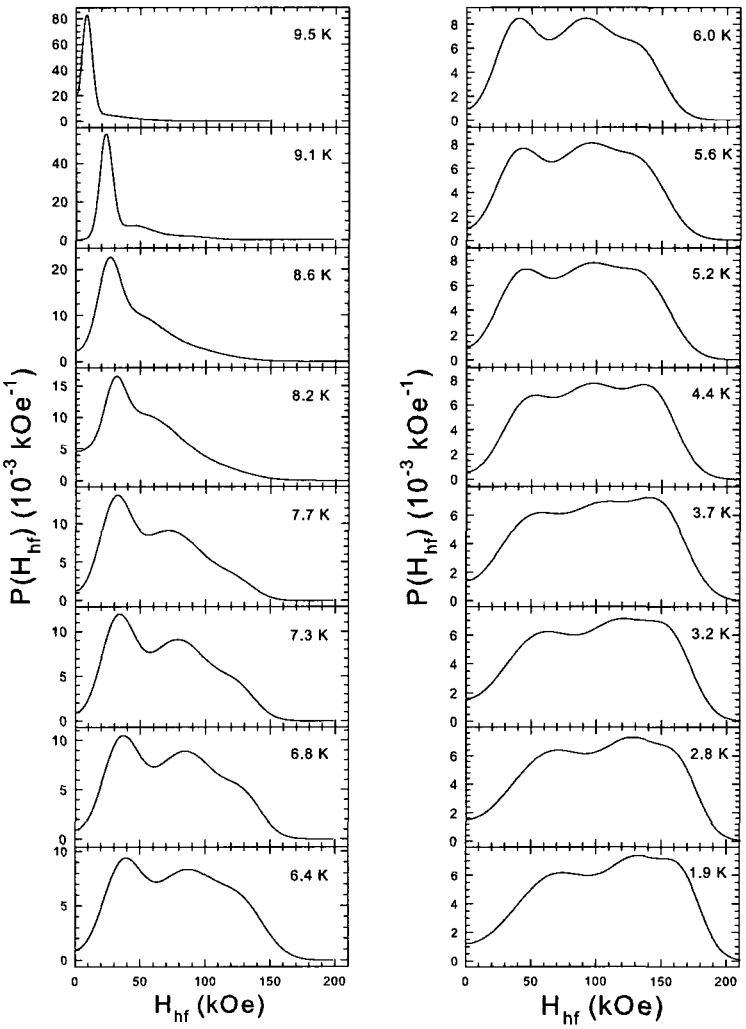

FIG. 16: (Color online) The hyperfine magnetic field distributions $P(H_{hf})$ which fit the best the ^{57}Fe Mössbauer spectra in Fig. 15.

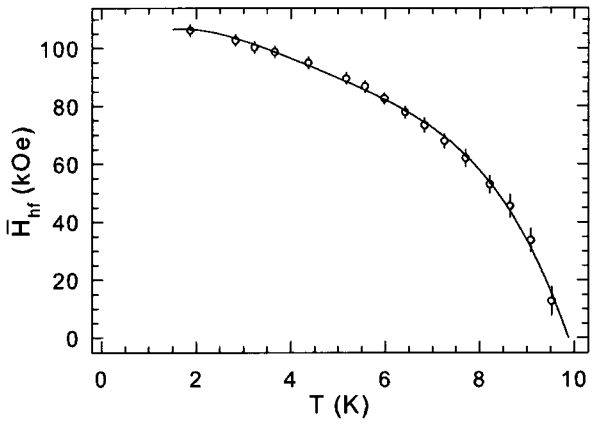

FIG. 17: (Color online) The temperature dependence of the average hyperfine magnetic field of the i-$Zn_{77}Fe_7Sc_{16}$ quasicrystal. The solid line is a guide for the eye.

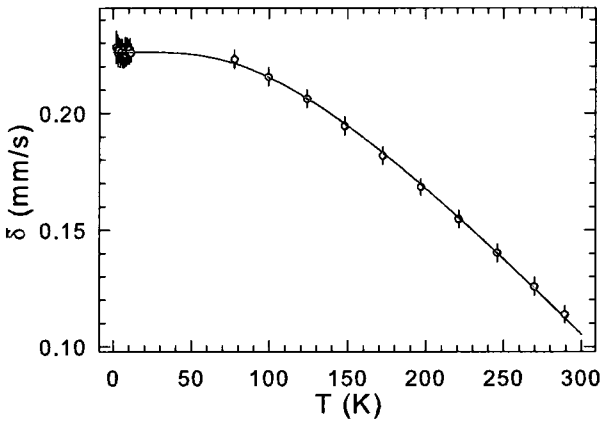

FIG. 18: (Color online) The temperature dependence of the average center shift of the i-$Zn_{77}Fe_7Sc_{16}$ quasicrystal. The solid line is the fit to Eq. (8), as explained in the text.

TABLE I: Positions in terms of $2\theta_1$ (in degrees) corresponding to Cu $K\alpha_1$ radiation and Q_{exp} (in $\AA^{-1}$), full width at half maximum Γ_Q (in $\AA^{-1}$), and relative area A normalized to 100.0 of all detected icosahedral Bragg peaks. Q_{exp} (in $\AA^{-1}$) is the calculated Q value by taking the position of the ninth line with the $I1$ index 18/29 as the reference line. $I1$ and $I2$ are the indices (N/M) and (h/h',k/k',l/l') based on the indexing scheme of Cahn *et al.* (Ref. 21), whereas $I3$ and $I4$ are the indices corresponding, respectively, to the indexing schemes of Elser (Ref. 22) and Bancel *et al.* (Ref. 23).

Label	$2\theta_1$	Q_{exp}	Q_{cal}	Γ_Q	A	$I1$	$I2$	$I3$	$I4$
1	8.791	0.625	0.627	0.016	0.1	2/1	011000	100000	$21\bar{1}\bar{1}1$
2	15.002	1.065	1.067	0.011	0.3	4/4	000200	110000	$2200\bar{1}1$
3	21.098	1.493	1.495	0.014	3.0	6/9	011200	111000	110001
4	24.401	1.724	1.726	0.011	1.2	8/12	002200	111100	$1100\bar{1}0$
5	26.108	1.842	1.836	0.017	0.9	10/13	122100	111110	$2210\bar{2}0$
6	28.791	2.028	2.029	0.008	1.9	12/16	022200	211000	$31\bar{1}\bar{1}1$
7	32.547	2.286	2.283	0.015	1.5	14/21	102300	211100	$2100\bar{1}1$
8	34.792	2.439	2.441	0.007	0.2	16/24	222200	211110	$210\bar{1}\bar{1}1$
9	38.002	2.656	2.656	0.014	51.5	18/29	122300	211111	100000
10	40.017	2.791	2.792	0.012	100.0	20/32	002400	221001	110000
11	41.145	2.866	2.862	0.015	5.0	22/33	012410	221101	$2210\bar{1}1$
12	42.970	2.988	2.989	0.010	3.7	24/36	022400	222000	$221\bar{1}1$
13	45.677	3.166	3.167	0.011	43.6	26/41	013400	222100	111101
14	47.473	3.283	3.283	0.008	5.7	28/44	222400	311111	210001
15	48.368	3.342	3.342	0.009	2.6	30/45	102500	321001	$3200\bar{1}1$
16	50.041	3.450	3.452	0.010	1.3	32/48	004400	321101	$320\bar{1}\bar{1}1$
17	52.564	3.612	3.607	0.015	0.3	34/53	122500	321111	220001
18	54.057	3.707	3.709	0.008	0.3	36/56	013510	322100	$2210\bar{1}0$
19	57.878	3.947	3.949	0.009	0.8	40/64	242400	322111	111100
20	58.713	3.999	3.999	0.014	0.3	42/65	104500	322200	$310\bar{1}\bar{1}1$
21	62.383	4.224	4.222	0.010	1.0	46/73	013600	332001	$2110\bar{1}0$
22	63.765	4.308	4.310	0.009	1.3	48/76	233510	332101	$2110\bar{1}1$
23	64.520	4.354	4.355	0.010	0.7	50/77	213600	332111	320002
24	67.248	4.517	4.518	0.009	12.0	52/84	004600	332002	101000
25	67.994	4.561	4.562	0.011	2.4	54/85	253400	422111	221101
26	69.361	4.641	4.642	0.007	0.6	56/88	024600	333100	$3100\bar{1}1$
27	71.375	4.758	4.759	0.010	7.5	58/93	233600	333101	210000
28	72.718	4.836	4.837	0.008	5.4	60/96	224600	422211	$210\bar{1}00$
29	73.430	4.876	4.877	0.009	0.9	62/97	015600	432101	$320\bar{1}\bar{1}0$
30	74.755	4.952	4.953	0.006	0.2	64/100	253510	432111	$3210\bar{1}1$
31	76.706	5.061	5.062	0.009	4.0	66/105	104700	432002	$2111\bar{1}1$
32	78.010	5.134	5.135	0.005	0.2	68/108	114710	432102	221001
33	81.243	5.311	5.312	0.008	1.7	72/116	244600	433101	200000
34	81.953	5.349	5.348	0.009	0.6	74/117	235600	433111	$2220\bar{1}0$
35	83.229	5.417	5.418	0.007	0.4	76/120	015710	433200	320001
36	85.128	5.517	5.518	0.010	0.5	78/125	344601	433201	211001
37	86.399	5.584	5.585	0.007	3.2	80/128	004800	442002	220000
38	87.055	5.618	5.620	0.007	0.2	82/129	144700	442102	$3211\bar{1}1$
39	88.367	5.685	5.686	0.008	1.3	84/132	024800	522221	$320\bar{1}02$

TABLE II: Results of a fit to Eq. (2) of ZFC magnetization decays at $T = 4.8$ K and $H = 20$ Oe for different waiting times t_w.

t_w (s)	M_0 (10^{-3} emu/g)	M_r (10^{-3} emu/g)	τ_r (10^3 s)	n
600	3.93(3)	0.77(8)	3.08(2)	0.467(95)
1800	3.87(3)	0.83(5)	3.14(2)	0.519(43)
3600	3.90(3))	0.92(4)	5.08(8)	0.555(23)
10800	3.87(4)	0.88(4)	7.53(11)	0.550(23)
18000	3.80(5)	0.88(4)	7.84(12)	0.576(27)

Chapter 11 Conclusions

Structural and magnetic properties and hyperfine interactions of five crystalline alloys Cu_2GdIn, CrNiP, CrNiAs, $EuCu_2Si_2$, Cr_2FeSe_4 and three icosahedral quasicrystals $Al_{60}Cr_{19.9}Fe_{0.1}Ge_{20}$, $Ag_{50}In_{36}Gd_{14}$, $Zn_{77}Fe_7Sc_{16}$ have been studied with x-ray and neutron diffraction, DC and AC magnetic susceptibility, and ^{155}Gd, ^{61}Ni, ^{57}Fe Mössbauer effect techniques.

The rare-earth Heusler alloy Cu_2GdIn has the $L2_1$ crystal structure with a lattice constant of 6.6643(3) Å. Gd magnetic moments order antiferromagnetically with a Néel temperature T_N = 9.6(1) K. The temperature dependence of the magnetic susceptibility above T_N follows the Curie-Weiss law with an effective magnetic moment of 7.98(4) μ_B per Gd atom and a paramagnetic Curie temperature of −41.2(9) K. The Debye temperature of Cu_2GdIn is 229(5) K. The temperature dependence of the hyperfine magnetic field at the ^{155}Gd nuclei follows a J = 7/2 Brillouin function and the saturation hyperfine magnetic field is −23.68(25) T. It is shown that the total contribution to the hyperfine magnetic field at the ^{155}Gd nuclei in Gd-containing Heusler compounds resulting from the conduction electron polarization is +9.8(2.5) T.

The ternary phosphide NiCrP has an orthorhombic Co_2P-type structure (space group *Pnma*) with the lattice parameters a = 5.7965(1) Å, b = 3.5337(1) Å, and c = 6.8123(2) Å. The Curie temperature T_C is found to be 135.1(1) K and the three critical exponents are determined to be β = 0.355(22), γ = 1.241(18), and δ = 4.585(20). The values of these critical exponents are close to those of a three-dimensional Heisenberg ferromagnet. The temperature dependence of the magnetic susceptibility above T_C follows the modified Curie-Weiss law with a paramagnetic

Curie temperature of 142.9(6) K and an effective magnetic moment per transition metal atom of 1.70(2) μ_B. The magnetic moment per formula unit at 4.2 K is found to be 0.816(13) μ_B. The hyperfine magnetic field of 32.3(1.3) kOe at the ^{61}Ni nuclei at 4.2 K implies that the Ni atoms carry a magnetic moment of 0.14(8) μ_B, and that the moment carried by the Cr atoms is 0.68(9) μ_B. The Debye temperature of NiCrP is 261(3) K.

The ternary arsenide NiCrAs has the hexagonal Fe_2P-type structure (space group $P\bar{6}2m$) with the lattice parameters a = 6.1128(1) Å and c = 3.6585(1) Å. The Curie temperature T_C is found to be 171.9(1) K and the three critical exponents are determined to be β = 0.514(18), γ = 1.010(16), and δ = 2.922(10). The values of these critical exponents are close to those of a mean-field ferromagnet. The temperature dependence of the magnetic susceptibility above T_C follows the modified Curie-Weiss law with a paramagnetic Curie temperature 176.0(3) K and an effective magnetic moment per transition metal atom 2.42(1) μ_B. The magnetic moment per formula unit at 4.2 K is found to be 1.114(33) μ_B. The hyperfine magnetic field of 41.5(1.0) kOe at ^{61}Ni nuclei at 4.2 K implies that the Ni atoms carry a magnetic moment of 0.15(3) μ_B, and that the moment carried by the Cr atoms is 0.95(6) μ_B. The Debye temperature of NiCrAs is 221(3) K.

The ^{151}Eu Mössbauer effect study in the temperature range 2.2–299.5 K on a ternary alloy $EuCu_2Si_2$ synthesized from an In flux has been presented. The values of the electric quadrupole coupling constant eQ_gV_{zz} and the asymmetry parameter η are, respectively, 6.11(8) mm/s and η = 1.0(1). The Debye temperature of the studied alloy is 236(4) K. The Eu atoms are shown to be a stable divalent state in the temperature range 2.2–299.5 K.

Cr_2FeSe_4 is found to have antiferromagnetism with weak ferrimagnetism due to the two different distortions of the Cr^{3+} octahedral and of the Fe^{2+} octahedral. A negative magnetization

is found in a magnetic field of 5 Oe and below due to the coercive-field magnetization reversal, which was not studied in the low field limit. The magnetization of this sample is -3×10^{-4} emu/g-Oe in a magetic field of 40 Oe at 80 K. The magnetization reversal disappears in a magnetic field larger than 65 Oe.

The icosahedral quasicrystal $Al_{60}Cr_{19.9}Fe_{0.1}Ge_{20}$ has a simple six-dimensional Bravais lattice with the six-dimensional lattice constant of 6.558(2) Å. The observed broadening of the diffraction Bragg peaks reflects the presence of the topological/chemical disorder. The distribution of the electric quadrupole splitting derived from Mössbauer spectra indicates the existence of a multiplicity of Fe sites. The average quadrupole splitting decreases with temperature as $T^{3/2}$. The vibrations of the Fe atoms are well described by a Debye model, with the Debye temperature of 463(15) K. The temperature dependence of the magnetic susceptibility follows the Curie-Weiss law with the effective magnetic moment of 0.312(3) μ_B per Cr/Fe atom. The origin of the presence of the magnetic moment, and its absence in similar crystalline alloys, is elucidated. The temperature dependence of the electrical conductivity can be successfully fitted with the use of theories of quantum interference effects, and values for spin-orbit and inelastic scattering times are extracted from the fits. The scattering process in the studied quasicrystal is dominated by inelastic electron-electron scattering.

The icosahedral quasicrystal $Ag_{50}In_{36}Gd_{14}$ has a simple six-dimensional Bravais lattice with the six-dimensional hypercubic lattice constant of 7.805(2) Å. The observed broadening of the diffraction Bragg peaks reflects the presence of the topological/chemical disorder. The temperature dependence of the magnetic susceptibility follows the Curie-Weiss law with the effective magnetic moment of 8.15(1) μ_B per Gd atom and the paramagnetic Curie temperature of −37.1(2) K. The quasicrystal $Ag_{50}In_{36}Gd_{14}$ is a spin glass with a freezing temperature of 4.25(5)

K. The presence of the distribution of the electric quadrupole splitting in the Mössbauer spectra indicates the existence of a multiplicity of Gd sites. The values of the principal component of the electric field gradient tensor and the asymmetry parameter at these sites are, respectively, $-4.91(10) \times 10^{21}$ V cm^{-2} and $\eta = 1.00(20)$. The Debye temperature of this studied quasicrystal is 199(2) K. The hyperfine magnetic field sets in at a temperature higher than the freezing temperature.

The icosahedral quasicrystal $Zn_{77}Fe_7Sc_{16}$ has a primitive six-dimensional Bravais lattice at room temperature with the six-dimensional hypercubic lattice constant of 7.087(1) Å. Based on DC magnetization measurements, no evidence is found for a transition to a ground state with long-range magnetic order in the temperature range between 2 and 300 K. The temperature dependence of the DC magnetic susceptibility follows the modified Curie-Weiss law with a paramagnetic Curie temperature of 10.6(2) K and an effective magnetic moment of 3.55(1) μ_B per Fe atom. The DC zero-field-cooled and field-cooled susceptibilty data indicate that the studied QC is a spin glass with a freezing temperature T_f = 7.75(2) K. This spin-glass state of this quasicrystal is further confirmed by observing ageing effects through the DC zero-field-cooled magnetization and the thermoremanent magnetization time decays, and by the analysis of the frequency dependence of T_f using the Vogel-Fulcher law and the dynamic scaling behavior near T_f. However, the observed increase of the thermoremanent magnetization with a magnetic field in the low-field regime is incompatible with the ultrametrically organized phase space of a canonical spin glass. The nature of the spin-glass state of the quasicrystal $Zn_{77}Fe_7Sc_{16}$ is thus fundamentally different from that of a canonical spin glass. The bimodal distribution of the electric quadrupole splitting and of the hyperfine magnetic field derived from Mössbauer spectra indicates the existence of two classes of Fe sites. The average quadrupole splitting decreases

with temperature as $T^{3/2}$. The hyperfine magnetic field sets in at a temperature of 9.87(5) K, which is significantly higher than T_f. The lattice vibrations of the Fe atoms are well described by a Debye model, with the Debye temperature of 443(8) K.